INFORMATION TO USERS

This manuscript has been reproduced from the microfilm master. UMI films the text directly from the original or copy submitted. Thus, some thesis and dissertation copies are in typewriter face, while others may be from any type of computer printer.

The quality of this reproduction is dependent upon the quality of the copy submitted. Broken or indistinct print, colored or poor quality illustrations and photographs, print bleedthrough, substandard margins, and improper alignment can adversely affect reproduction.

In the unlikely event that the author did not send UMI a complete manuscript and there are missing pages, these will be noted. Also, if unauthorized copyright material had to be removed, a note will indicate the deletion.

Oversize materials (e.g., maps, drawings, charts) are reproduced by sectioning the original, beginning at the upper left-hand corner and continuing from left to right in equal sections with small overlaps.

Photographs included in the original manuscript have been reproduced xerographically in this copy. Higher quality 6" x 9" black and white photographic prints are available for any photographs or illustrations appearing in this copy for an additional charge. Contact UMI directly to order.

ProQuest Information and Learning
300 North Zeeb Road, Ann Arbor, MI 48106-1346 USA
800-521-0600

UMI®

Thermal Properties of Framework Materials:

Selected Zeolites, Clathrates and an Organic Diol

Liyan Qiu

Submitted in partial fulfillment of the requirements for the degree of

Doctor of Philosophy in Chemistry

at

Dalhousie University

Halifax, Nova Scotia

December 2000

National Library
of Canada

Acquisitions and
Bibliographic Services

395 Wellington Street
Ottawa ON K1A 0N4
Canada

Bibliothèque nationale
du Canada

Acquisitions et
services bibliographiques

395, rue Wellington
Ottawa ON K1A 0N4
Canada

Your file Votre référence

Our file Notre référence

0-612-66643-3

Canadä

DALHOUSIE UNIVERSITY

FACULTY OF GRADUATE STUDIES

The undersigned hereby certify that they have read and recommend to the Faculty of Graduate Studies for acceptance a thesis entitled "Thermal Properties of Framework Materials: Selected Zeolites, Clathrates and an Organic Diol"

by Liyan Qiu

in partial fulfillment of the requirements for the degree of Doctor of Philosophy.

Dated: December 15, 2000

External Examiner [redacted]
Research Supervisor
Examining Committee

DALHOUSIE UNIVERSITY

Date: December, 2000

AUTHOR: Liyan Qiu

TITLE: Thermal Properties of Framework Materials: Selected Zeolites, Clathrates and an Organic Diol

DEPARTMENT OF SCHOOL: Department of Chemistry

DEGREE: Ph.D. CONVOCATION: Spring YEAR: 2001

Permission is herewith granted to Dalhousie University to circulate and to have copied for non-commercial purposes, as its discretion, the above title upon the request of Individuals or institutions.

[redacted]

Signature of Author

THE AUTHOR RESERVES OTHER PUBLICATION RIGHTS, AND NEITHER THE THESIS NOR EXTENSIVE EXTRACTS FROM IT MAY BE PRINTED OR OTHERWISE REPRODUCED WITHOUT THE AUTHOR'S WRITTEN PERMISSION.

THE AUTHOR ATTESTS THAT PERMISSION HAS BEEN OBTAINED FOR THE USE OF ANY COPYRIGHTED MATERIAL APPEARING IN THIS THESIS (OTHER THAN BRIEF EXCEPRTS REQUIRING ONLY PROPER ACKNOWLEDGEMENT IN SCHOLARLY WRITING) AND THAT ALL SUCH USE IS CLEARLY ACKNOLEGED.

Dedicated to my family and friends

TABLE OF CONTENTS

List of Figures

List of Tables

Abstract

Thermal properties including heat capacity, thermal expansion, thermal conductivity and the Grüneisen parameter are fundamental characteristics of materials. They provide important information such as thermodynamic stability, anharmonicity of lattice vibrations, interatomic interactions and the utility of materials for various applications.

The thesis is concerned with determination of thermal properties, especially low-temperature (below room temperature) heat capacities of some selected framework materials including zeolites, clathrates and a channel-forming diol. The determination of thermal properties of these novel materials has several purposes. First, these materials display various physical (*e.g.* thermal, electrical, optical) properties which can be tailored by doping with different guest molecules or atoms. Some are industrially important catalysts and others are possible thermoelectric materials for cooling devices and power generation. Secondly, thermodynamic properties such as ΔG, ΔH and ΔS are necessary to understand the stability and explore the applications of novel materials. Thermodynamic properties are especially important to design and synthesize new framework materials. Finally, heat capacities are required to understand thermal conductivity, which is indispensable to determine the utility and limitations of materials, especially thermoelectric materials.

The heat capacities of three zeolites with different frameworks and compositions, NaA, NaX and NaY, were determined by adiabatic calorimetry; the complete thermodynamic properties below 300 K were determined and no solid-solid phase transitions were found in the experimental temperature range. A linear relationship between the Gibbs energy of formation and the Al/(Al + Si) molar ratio was found. These results show that thermodynamic stability of zeolites is enthalpic but not entropic. These findings are useful in the estimation of thermodynamic properties and synthesis of new zeolites.

The heat capacities of five type I clathrates, Na_8Si_{46}, $Ba_8Ga_{16}Si_{30}$, $Sr_8Ga_{16}Ge_{30}$, $Sr_8Zn_8Ge_{38}$ and $Cs_8Ga_8Sn_{38}$, were investigated. No solid-solid phase transitions were found between 30 and 300 K and the related thermodynamic properties were derived. Grüneisen parameters indicate that anharmonicity correlates with resonant scattering and the amorphous-like thermal conductivities of Si and Ge clathrates but the Sn clathrate shows strong host-guest interactions.

The low-temperature heat capacity of a solvent-free diol, 2,6-dimethyl-bicyclo[3.3.1]nonane-*exo*-2, *exo*-6-diol was determined. The linear relationship between heat capacity and temperature shows the existence of many high-frequency modes. The high fusion entropy indicates that this chemical compound is an ordered molecular crystal rather than plastic crystal, likely due to strong hydrogen bonding.

List of Symbols

(in order of appearance)

C_P	heat capacity at constant pressure
C_V	heat capacity at constant volume
C_{lat}	heat capacity due to lattice vibration
C_{lib}	heat capacity due to librational vibration
C_{vib}	heat capacity due to intramolecular vibration
Q	heat
T	absolute temperature
H	enthalpy
H_0	enthalpy at 0 K
H_T	enthalpy at T K
S	entropy; Seebeck coefficient
S_0	entropy at 0 K
S_T	entropy at T K
G	Gibbs free energy
U	internal energy
P	external pressure
V	volume
α	thermal expansion coefficient
κ_T	isothermal compressibility
K	bulk modulus

C	heat capacity per unit volume
γ	Grüneisen parameter
ν	vibrational frequency of lattice
R	gas constant
T_{trs}	phase transition temperature
$\Delta_{trs}H$	enthalpy of phase transition
$\Delta_{trs}S$	entropy of phase transition
$\Delta_{trs}V$	volume change at phase transition
ω	angular frequency
N_A	Avogadro's constant
N	number of atom
k	Boltzmann constant
ν_{E}	Einstein characteristic frequency
h	Planck constant
θ_{E}	Einstein temperature
θ_{D}	Debye temperature
$g(\nu)$	density of state
ν_D	Debye characteristic frequency
Θ_{D}	apparent Debye temperature
C_E	Einstein heat capacity function
C_D	Debye heat capacity function

$V(x)$	potential of harmonic oscillator
$\bar{x}$	average displacement of atoms or molecules
l	mean free path of phonons
v	sound velocity
ρ	density
κ	thermal conductivity
$\mathbf{k}$	wave vector
V_h	heating voltage
R_h	resistance of the heater
Q_P	electrical energy input
t	time
C_{sat}	heat capacity under the saturated vapor pressure of a sample
$\Delta_f H$	enthalpy of formation
$\Delta_f H^\circ$	enthalpy of formation at 298.15 K
$\Delta_f S$	entropy of formation
$\Delta_f S^\circ$	entropy of formation at 298.15 K
$\Delta_f G$	Gibbs energy of formation
$\Delta_f G^\circ$	Gibbs energy of formation at 298.15 K
Ω	the number of microscopic states
V	voltage
ΔV	voltage difference

Π	the Peltier coefficient
I	electrical current
Z	the thermoelectric figure of merit
η	Carnot efficiency
L	the Lorenz number, 2.44×10^{-8} V^2 K^2
c_{ij}	elastic constant
κ_L	lattice component of thermal conductivity
κ_e	electronic component of thermal conductivity
a, b, c	lattice constant
α, β, γ	crystallographic angles

Acknowledgements

First of all, I gratefully acknowledge my supervisor Professor Mary Anne White for her guidance and assistance in countless ways, to whom I am indebted.

I sincerely thank the Faculty of Graduate Studies and the Department of Chemistry of Dalhousie University, and the Canadian Bureau for International Education for their financial support during my Ph.D. program.

I would like to thank Dr. G. S. Nolas, Dr. J. S. Tse, Professor R. Bishop, Dr. J. J. Dong, Professor O. F. Sankey for their kind supply of samples and discussions in the writing of the thesis.

I also acknowledge Andy George and the members of Dr. Burford's group for their assistance in the preparation of samples.

I would also like to thank Professor T. S. Cameron and Katherine Robertson for their help in the determination of crystal structures of zeolites.

I thank Brian Millier and Gino Ranieri, Rick Conrad and Ross Shortt for their technical assistance.

I am grateful to the past and present members in Professor Mary Anne White's group for their various assistance. I express my sincere appreciation to Paul W. R. Bessonatte, Chris Smith, Shane Harnish, G. R. MacKay, Vladimir Murashov, Doug Maclaren, Cathy Kennedy, Rob Marriott and Dr. Bi-Zeng Zhan.

Finally, I would like to thank my fellow graduate students in the Department of Chemistry, especially, Guy Bernard and Zhong-Ping Lin for their assistance in the past years.

Chapter 1 Thermal Properties of Solids

1.1 Introduction

Thermal properties are among the fundamental characteristics of materials. They generally refer to heat capacity, thermal expansion, thermal conductivity and the Grüneisen parameter.

The research of the thesis is concerned with determination of thermal properties, especially low-temperature (below room temperature) heat capacities of some selected materials including zeolites and semiconductor clathrates. The determination of thermal properties of these novel materials is based on several purposes. First, these materials display various physical properties (*e.g.* thermal, electrical, optical) which can be tailored by doping different guest molecules or atoms. They are industrially important catalysts and possible thermoelectric materials in cooler devices and power generation. Secondly, thermodynamic properties such as ΔG, ΔH and ΔS are necessary to understand the stability and explore the applications of novel materials. Thermodynamic properties are especially important to design and synthesize new framework materials. For example, thermodynamics can explain why some zeolites such as zeolite A and zeolite NaX can be easily synthesized without templates while others not, and why natural zeolites usually have low Si/Al ratios. The reliable thermodynamic functions can be determined from heat capacity data. In addition, heat capacities are required to calculate thermal conductivity, which is indispensable to determine the usefulness and limitations of materials, to reveal host-guest interactions and relationships between structure and properties.

In the following sections, heat capacity, thermal expansion, thermal conductivity, the Grüneisen parameter and their relationships are introduced. Their applications will be discussed in more detail in the following chapters.

1.2 Heat Capacity of Solids

1.2.1 Heat Capacity and Thermodynamic Functions

Heat capacity is one of the fundamental properties of matter. It can be defined as the energy required to raise the temperature 1 K for a substance under certain conditions, expressed as[1]

$$C_x = \left(\frac{\partial Q}{\partial T}\right)_x, \tag{1.2.1}$$

where ∂Q is the infinitesimal energy input, ∂T is the infinitesimal change of temperature and x denotes the controlled conditions which generally refer to constant volume or constant pressure.

For a closed system undergoing an infinitesimal reversible change of state the heat (Q) absorbed by the system can be represented as

$$dQ = T\,dS, \tag{1.2.2}$$

where S is the entropy of the system. The isobaric heat capacity (C_P) and the isochoric heat capacity (C_V) at temperature T are given by[2]

$$C_P = \left(\frac{\partial Q}{\partial T}\right)_P = T\left(\frac{\partial S}{\partial T}\right)_P, \tag{1.2.3}$$

and

$$C_V = \left(\frac{\partial Q}{\partial T}\right)_V = T\left(\frac{\partial S}{\partial T}\right)_V . \tag{1.2.4}$$

Generally, C_V is more useful than C_P in the theoretical analysis of thermal properties of solids. For isotropic materials C_V can be derived from C_P by the equation[2]

$$C_P - C_V = \frac{TV\alpha^2}{\kappa_T}, \tag{1.2.5}$$

where V is the molar volume, α is the thermal expansion coefficient defined as

$$\alpha = \frac{1}{V}\left(\frac{\partial V}{\partial T}\right)_P , \tag{1.2.6}$$

and κ_T is the isothermal compressibility, defined as

$$\kappa_T = -\frac{1}{V}\left(\frac{\partial V}{\partial P}\right)_T . \tag{1.2.7}$$

The reciprocal of κ_T is also called bulk modulus, $K = 1/\kappa_T$. For pressures to about 1 GPa, the compressibility of a solid can be approximated as constant.[3]

For ideal gases, it can be shown that $C_P - C_V = R$, in which R is the gas constant. For very hard solids below room temperatures, $C_P \approx C_V$ is a good approximation. At room temperature, $(C_P - C_V)$ for a typical solid is about 1 ~ 8 J K^{-1} mol^{-1} and it reaches a maximum at the melting point with a value of about 10% of C_P.[4]

$(C_P - C_V)$ also can be expressed as

$$C_P - C_V = T\alpha\gamma C_V , \tag{1.2.8}$$

in which the dimensionless γ denotes the Grüneisen parameter[5,6]

$$\gamma = -\left(\frac{\partial \ln \nu}{\partial \ln V}\right)_T, \tag{1.2.9}$$

and ν is the vibration frequency of the lattice.

An exact calculation of $C_P - C_V$ requires complete temperature-dependent data of volume, thermal expansion coefficients and isothermal compressibility (and their directional dependence). In the absence of experimental data, the Nernst-Lindemann empirical equation[7]

$$C_P - C_V = AC_P^2 T \tag{1.2.10}$$

can be used where $A = V\alpha^2 / C_P^2 \kappa_T$ reflects the anharmonicity of solids and is a temperature-independent constant[8,9] which usually has the magnitude ~ 10^{-6} mol J^{-1}.

Heat capacity is necessary for the determination of thermodynamic functions. Principally, if accurate heat capacities at different temperatures are determined, the enthalpy (H) of a system is given by

$$H = H_0 + \int_0^T C_P dT, \tag{1.2.11}$$

where H_0 is the enthalpy at $T = 0$ K.

The entropy (S)

$$S = S_0 + \int_0^T \frac{C_P}{T} dT, \tag{1.2.12}$$

and the Gibbs energy (G)

$$G = H - TS \tag{1.2.13}$$

can also be derived. Here S_0 is the entropy at $T = 0$ K.

Low-temperature heat capacity measurements provide an important method of investigating order-disorder and residual entropies of materials. According to the third law of thermodynamics, the entropy of any perfect crystal of a pure substance vanishes as the temperature approaches absolute zero. However, some materials, such as carbon monoxide, exhibit residual entropy at $T = 0$ K because they freeze in disordered conformations that are thermodynamically accessible at higher temperatures. By comparison with spectroscopically determined statistical-mechanical entropies and calorimetrically determined thermodynamic entropies, residual entropies can be obtained. For example, the statistical entropy of carbon monoxide is 4.69 J K^{-1} mol^{-1} higher than the calorimetric value.[10] In the perfect solid state, CO molecules would be all aligned in one direction, for example, CO CO CO CO. In fact, two possible arrangements exist in solid carbon monoxide at relatively high temperatures because of the small energy difference between CO CO CO CO and CO OC OC CO. When the solid is cooled to a temperature at which the molecules do not have enough energy to rotate, the disordered configuration is frozen. According to the Boltzmann principle, $S = R \ln\Omega$, where Ω is the number of microscopic states. The maximum residual entropy due to the orientation disorder is $S = R \ln 2 = 5.76$ J K^{-1} mol^{-1}, which is larger than the observed residual entropy of 4.69 J K^{-1} mol^{-1} for CO. The discrepancy indicates that the orientations of carbon monoxide molecules are not completely disordered.[10]

It is well known that glass is a non-equilibrium amorphous solid and it inherits its "structure" from the liquid state. One of the important determining properties of the glass state is the very slow relaxation of the enthalpy and other thermodynamic quantities that occur around the glass transition temperature. The measurement of heat capacity is particularly powerful for the investigation of the dynamics of glass materials.[11,12,13]

Heat capacity is a measure of thermal excitation of available energy levels. As the temperature goes below ambient, heat capacity can change by several orders of magnitude as the number of excited high-energy vibrational modes is reduced while low-energy vibrational modes become dominant. Hence, heat capacity can be used to analyze the various vibrational modes and to determine the Debye temperature of solids. For example, low-temperature heat capacity investigations revealed that the low-energy optic modes are the dominant mechanism driving the negative thermal expansion of ZrW_2O_8.[14]

The importance of heat capacity is also displayed in many material applications, from energy storage to heat conduction. For example, heat capacity data are required to convert thermal diffusivity (the quantity usually determined experimentally) to thermal conductivity, which is one quantity required to assess the thermoelectric figure of merit (See Chapter 4).

1.2.2 Heat Capacity and Phase Transitions

Heat capacity provides an important technique to discover the phase transitions of materials. The third law of thermodynamics predicts that the entropy of a perfect crystal in thermodynamic equilibrium is equal to zero at $T = 0$ K, *i.e.*, $S_0 = 0$. From equation (1.2.12)

$$S = \int_0^T \left(\frac{C_P}{T}\right) dT, \qquad (1.2.14)$$

and, in order to converge the integral at low temperature, C_P / T must be a finite number as $T \rightarrow 0$ and hence the heat capacities of solids are expected to approach zero in this limit. Most solids show a smooth reduction of their heat capacity as the absolute temperature decreases. However, some materials[15-17] show an abrupt change in heat capacity at low temperatures. This is generally called a heat capacity anomaly.

According to Ehenfest,[18] heat capacity anomalies can be classified based on the derivatives of Gibbs energy at a phase transition. He defined the "order" of a transition as being the order of the lowest derivative of the Gibbs energy which shows a discontinuity at the transition and can be derived from the strict thermodynamic equation

$$dG = -S\,dT + V\,dP. \tag{1.2.15}$$

In a first-order transition, there is no discontinuity in Gibbs energy at the phase-transition temperature T_{trs}. However, such transitions show abrupt changes in

$$V = \left(\frac{\partial G}{\partial P}\right)_T, \tag{1.2.16}$$

and

$$S = -\left(\frac{\partial G}{\partial T}\right)_P, \tag{1.2.17}$$

which lead to the transition enthalpy $\Delta_{trs}H = T_{trs}\Delta_{trs}S \neq 0$ where $\Delta_{trs}S$ is the transition entropy. The heat capacity at the transition point is infinite since non-zero latent heat is absorbed by the system with no temperature change. Many solid-solid phase transitions are first order.

A second-order phase transition is one for which the first-order derivatives of

Gibbs energy are continuous with a change of slope at the transition temperature, but the second-order derivatives of Gibbs energy such as $(\partial V/\partial T)_P$, $(\partial V/\partial P)_T$ are discontinuous. Thus, there are no discontinuities in S ($\Delta_{trs}S = 0$), V ($\Delta_{trs}V = 0$) and H ($\Delta_{trs}H = 0$). Heat capacity, thermal expansion coefficient and isothermal compressibility are finite at the transition temperature. However, the second-order structural phase transitions are rather rare. Some metals such as Hg, Sn, Pb undergo a second-order transition at low temperatures.[19]

1.2.3 Theoretical Models of Heat Capacity

1.2.3.1 Dulong-Petit Law

The study of heat capacity can be traced back to the early nineteenth century when Dulong and Petit[20] first revealed the characteristics of heat capacities of elements in the solid state. They found that the molar heat capacity at constant volume of each element is about $3R$, which is the well-known Dulong-Petit law.

In the middle of the nineteenth century, the Dulong-Petit law was extended to solid state compounds, leading to the Neumann-Kopp law which states that the heat capacity of a compound is the sum of the atomic heat capacities of the constituent elements.[21]

Both empirical rules are understood in terms of the theorem of energy equipartition developed by Boltzmann in the 1870's. However, experiments revealed that some materials have much lower heat capacities at room temperature than those predicted by the Dulong-Petit law, although they reach the limit $3R$ at high temperatures. For example, the value of C_p for diamond is about 1/3 of the Dulong-Petit value of $3R$ at room temperature but approaches $3R$ at 1300 K.[4] Generally, Dulong-Petit and Neumann-Kopp laws are useful for estimating the heat capacities of simple solids such as binary compounds and alloys but are not applicable for complex solid compounds[22] because the chemical properties (determined by the chemical bonds) and hence the physical properties (such as lattice dynamics) of elements are significantly changed upon formation of compounds. Moreover, low-temperature heat capacities strongly depend on temperature, decreasing with lowered temperature, reaching zero at 0 K. Classical statistical mechanics fails to explain the temperature dependence of heat capacity.

1.2.3.2 Einstein Model

As early as 1907, Einstein[23] applied the concept of energy quanta developed by Planck to derive the relation between heat capacity and temperature. He assumed that the vibrations of N atoms in the crystal lattice could be considered as $3N$ independent harmonic oscillators with the same fundamental vibration frequency ν_E. By applying statistical thermodynamic principles, Einstein derived the heat capacity equation

$$C_V = 3Nk\frac{x^2 e^x}{(1-e^x)^2}. \qquad (1.2.18)$$

where $x = \theta_E / T$ and $\theta_E = h\nu_E / k$ is the Einstein temperature. The significance of the Einstein model is that it was the first to quantitatively predict the variation of heat capacity with the universal function θ_E/T and that the quantization of lattice vibrations explains the reduction of heat capacity at low temperatures.

At high temperatures ($T >> \theta_E$), the heat capacity of equation (1.2.18) reaches the limit $C_V = 3Nk$ which agrees with the Dulong-Petit value.

As $T \rightarrow 0$, C_V approaches zero according to equation (1.2.18), in agreement with experimental observation. However, at low temperature ($T << \theta_E$), the predicted heat capacity decreases much faster than that determined by experiment. This is the result of oversimplified assumptions of the model, since in the tightly coupled lattice, the motion of one atom affects the vibrations of the others and atoms can vibrate with different frequencies. Nevertheless, the Einstein model is one of the early successes of quantum mechanics. Moreover, the harmonic oscillator is a good approximation for the vibrational heat capacities of most solids at low temperatures. From the experimental point of view, the Einstein model is easy to use and it usually shows reasonable results in dealing with heat capacities from intramolecular vibrations in solids (See Chapter 4).

1.2.3.3 Debye Model

A more sophisticated treatment of heat capacity of solids is the Debye model[24] which assumed that a solid is an isotropic elastic continuum for all possible vibrational modes. This model considers the concept of density of states which is defined such that the number of modes with frequencies $\nu \rightarrow \nu + d\nu$ is $g(\nu)\,d\nu$, where

$$g(\nu) = \left(\frac{9N}{\nu_D^3}\right)\nu^2 \qquad (0 \leq \nu \leq \nu_D) \qquad (1.2.19)$$

and

$$g(\nu) = 0. \qquad (\nu > \nu_D) \qquad (1.2.20)$$

Here ν_D is the Debye characteristic frequency. The derived heat capacity from the Debye model can be expressed as:

$$C_V = 9Nk\left(\frac{T}{\theta_D}\right)^3 \int_0^{\frac{\theta_D}{T}} \frac{x^4 e^x}{(e^x - 1)^2} dx, \qquad (1.2.21)$$

where $x = h\nu_D / kT$ and $\theta_D = h\nu_D / k$ is the Debye characteristic temperature. The integral can be evaluated by numerical methods.[25]

In equation (1.2.21), θ_D is related to the elastic constant and the velocity of sound. The Debye temperature approximately marks the beginning of the rapid reduction in C_V with decreasing temperature, as the high frequency vibrations begin to "freeze out" and no longer contribute to either the internal energy or the heat capacity.[11] Several methods have been suggested to evaluate the Debye temperature from the experimental data of various physical properties, such as the speed of sound and the Grüneisen parameter.[21]

At high temperatures, $T >> \theta_D$, the Debye model has the limit $C_V = 3Nk$ which is equal to the Dulong-Petit value. At low temperatures ($T << \theta_D$), equation (1.2.21) gives

$$C_V = \frac{12}{5} Nk\pi^4 \left(\frac{T}{\theta_D}\right)^3. \qquad (1.2.22)$$

Equation (1.2.22) is called the Debye T^3-law, *i.e.*, the heat capacity goes to zero as T^3, in agreement with experimental observations for insulating materials. However, the Debye model does not work as well over the entire temperature range ($T < 300$ K) due to the temperature dependence of θ_D.

In general, the Einstein model works well for optic modes while the Debye model fits experimental data well for acoustic modes. In monatomic crystals, the heat capacity comes from three acoustic modes. In a polyatomic crystal with N atoms in each unit cell, the heat capacity from three acoustic modes can be calculated from the Debye model and those from $3N - 3$ optic modes can be derived from the Einstein model. Hence, the Einstein and Debye models are usually combined for the analysis of the vibrational modes in solids.[26,27,28]

1.2.4 Extrapolations and Interpolations of Heat Capacity

Heat capacity can be determined by various calorimetric methods.[4] However, sometimes extrapolation is necessary to obtain complete thermodynamic properties in the cases that experimental data are not available. On the other hand, the accurate representation of the relation between heat capacity and temperature is important in order to interpolate heat capacity conveniently within experimental temperatures and to calculate other thermodynamic properties.

One method to represent the relation between heat capacity of solids and temperature is through the empirical equations[29,30]

$$C_P = a_0 + a_1 T + a_2 T^{-2} + \ldots, \tag{1.2.23}$$

and

$$C_P = a_0' + a_1' T + a_2' T^2 + \ldots, \tag{1.2.24}$$

where the parameters a_0, a_1, a_2 and a_0', a_1', a_2' are determined by a least-squares procedure from the heat capacity at different temperatures. Equations (1.2.23) and (1.2.24) can be modified according to individual systems.[31,32] Generally they are good for fits of the heat capacity above room temperature in the absence of heat capacity anomalies. However, extreme caution should be taken when these empirical equations are used to extrapolate heat capacity to high temperature outside the range of temperature for which they were derived.[33]

At high temperatures, the heat capacity of a harmonic solid at constant volume has the Dulong-Petit value, $3R$. The heat capacity of a cubic solid at constant pressure can be given by[34]

$$C_P = 3NR + \frac{\alpha^2 VT}{\kappa_T}. \tag{1.2.25}$$

The difficulty with equation (1.2.25) is that the thermal expansion coefficient α and compressibility κ_T of most solids are not available. In this case, the heat capacity can be fitted with equation (1.2.10) with $C_V = 3NR$.

At low temperatures, it is not easy to find a general way to fit the experimental heat capacity at different temperatures. According to lattice dynamics, the overall heat capacity of a solid with N atoms in its unit cell is given by the equation

$$C_P = C_{lat}(3) + C_{lib}(3) + C_{vib}(3N-6) + (C_P - C_V), \tag{1.2.26}$$

where $C_{lat}, C_{lib}, C_{vib}$ are the heat capacities due to lattice (translational) vibration, rotational (librational) vibration and intramolecular vibration. The parenthetic numbers indicate the degrees of freedom. The last term gives the correction for the heat capacity difference $(C_P - C_V)$ which can be presented as equation (1.2.5). The heat capacity from the three acoustic modes, C_{lat}, can be represented by equation (1.2.21) and the remaining 3*N*-3 optic modes are described by equation (1.2.18). Equation (1.2.26) is very useful when the optic modes have been assigned completely by IR and Raman spectroscopies. If the spectral data are not accessible, the heat capacity is usually expressed as[35]

$$\frac{C_V}{3R} = mC_E + nC_D, \tag{1.2.27}$$

where *m* and *n* are adjustable parameters; C_E and C_D are the Einstein and Debye heat capacity functions respectively, giving by equations (1.2.18) and equation (1.2.21). In general, the coefficient $m + n$ is equal or close to the number of atoms in each unit cell.[35] Equation (1.2.27) is widely used to extrapolate experimental heat capacity to $T = 0$ K and can be further modified to better represent low-temperature heat capacity.[36,37]

When the temperature is very low ($T < 0.01\ \theta_D$), equation (1.2.27) is generally simplified as the Debye T^3 equation

$$C_V = \frac{12}{5} N\pi^4 R \left(\frac{T}{\theta_D}\right)^3. \tag{1.2.28}$$

In the practical applications, equation (1.2.28) is often represented as[38]

$$C_V = aT^3, \tag{1.2.29}$$

where a is an empirical parameter, which can be determined by a plot of C_V / T^2 against T at very low temperatures ($T < 0.01\ \theta_D$), allowing a determination of the Debye temperature.

In the above discussion, electronic and magnetic contributions to heat capacities are neglected. Equation (1.2.29) can be modified as[21]

$$C_V = aT^3 + \gamma T + \delta T^{3/2}, \tag{1.2.30}$$

where a, γ, and δ terms represent the lattice, electronic, and magnetic contributions, respectively. More contributions to heat capacity can be found elsewhere.[21]

Since the lattice heat capacity at very low temperature depends on T^3, heat capacity below room temperature can also be used to extrapolate T = 0 K with the equation[39]

$$\frac{C_V}{T^3} = a' + b'T^2 + c'T^4 + \ldots, \tag{1.2.31}$$

where a', b', c' are fitting parameters.

1.3 Thermal Expansion

Generally, materials expand when they are heated. The magnitude of the expansion can be measured by the thermal expansion coefficient as defined in equation (1.2.6). In order to account for the thermal expansion of a real crystal in detail, additional terms higher than quadratic (*i.e.* anharmonic terms) of the potential energy should be included[40], *i.e.*,

$$V(x) = ax^2 - gx^3 - fx^4, \tag{1.3.1}$$

where a, g, f, are constants corresponding to harmonic vibration, asymmetry repulsion, and the softening of vibration, respectively. The average displacement, $\bar{x}$ of atoms or molecules from the minimum energy separation can be derived from the Boltzmann distribution law to give[40]

$$\bar{x} = \frac{3}{4}\frac{g}{a^2}kT . \tag{1.3.2}$$

This result illustrates that the thermal expansion of solids increases as temperature increases and vanishes as the temperature approaches absolute zero, which is consistent with observed experimental results and the third law of thermodynamics. It is evident that the average displacement of a harmonic oscillator does not change with temperature since $g = 0$ in that case.

For cubic solids, the volume thermal expansion coefficient can be expressed by equation (1.2.6). For non-cubic solids, thermal expansion generally varies in different directions. It is necessary to define the thermal expansion according to the dimensions of the unit cell of a solid. For example, the thermal expansion coefficient α_a along the a-axis of the unit cell is defined as

$$\alpha_a = \frac{1}{a}\left(\frac{\partial a}{\partial T}\right)_P . \tag{1.3.3}$$

Thermal expansion coefficients can be determined by several methods. Generally, diffraction techniques (X-ray or neutron) have less accuracy (with an error of 2%) than dilatometers (with an error less than 1%).[3]

Thermal expansion can be a complicated physical phenomenon. In many cases, although the overall volume of a solid displays positive expansion on heating, the coefficient in the different directions can be either positive (expansion) or negative (contraction).[41,42] Moreover, not all materials exhibit thermal expansion on heating. The well known liquid with negative thermal expansion is water below 277.15 K.[43] Solid-state examples of this anomalous behavior include ice Ih below 100 K[44] and amorphous

SiO_2 below room temperature.[45]

Recently, several framework materials have been found to exhibit negative thermal expansion. Among them are the AM_2O_7 family (A = Ti, Zr, Hf, Sn; M = P, V),[46,47,48] the $A_2M_3O_{12}$ family (A = Ti, Sc, Lu, Y; M = P, W)[49-54] and the AMO_5 family[55] where A and M are octahedral and tetrahedral cations. Various kinds of zeolites also show thermal contraction (Section 3.1.3). The most interesting material in the research of negative thermal expansion is the cubic material ZrW_2O_8, which shows isotropic negative thermal expansion over a wide temperature range, 0.3 to 1050 K.[14,56,57] The negative thermal expansion of these framework materials is attributed to the transverse thermal motions of oxygen atoms in A-O-M. They lead to coupled rotations of the essentially rigid polyhedral building blocks of the structure.[53, 57]

Positive and negative thermal expansion of materials can be either a liability or an advantage. On one hand, thermal expansion or contraction is a disadvantage for devices or instruments (*e.g.*, electronic components, optical systems, and computer hard disk storage systems) which must work in a large temperature range. On the other hand, thermal expansion or thermal contraction in liquids and in solids permits some applications such as in thermometers. Negative thermal expansion of materials also provides some potential applications both as pure phases or as the components of composite materials with overall thermal expansion coefficients adjusted to a desired value, including zero thermal expansion.[59] In fact, some materials like Invar ($Fe_{0.65}Ni_{0.35}$), which almost has no thermal expansion[59,60] ($\alpha = 2\times10^{-8}$ K^{-1}) from –50°C to 150°C, have been used in optic devices and hulls of supertankers.[61] The study of thermal expansion of materials can provide information about the relationship between structure and properties, and molecular interactions as well the motion of the guest in the lattice.[41,42] This information is vital to the development of novel materials.

1.4 Thermal Conductivity

Kinetic theory gives the Debye equation[40]

$$\kappa = \frac{1}{3} C \rho \, \mathrm{v} \, l, \tag{1.4.1}$$

where κ is the thermal conductivity, C is the heat capacity per unit volume, ρ is the density of the solid, v is the sound velocity, and l is the mean free path of phonons, the quanta of electromagnetic radiation with energy of $\hbar\omega$, where $\hbar = h/2\pi$ and ω is angular frequency. As a first approximation, ρ and v are independent of temperature. Therefore, the variation of thermal conductivity of a solid at different temperatures is governed mainly from the temperature dependence of the heat capacity and the mean free path of phonons.

For ideal harmonic solids without imperfections, the flow of heat associated with phonon flow is likely unchanged. Hence, the thermal resistance is zero and κ is expected to be infinite. However, lattice vibrations in real crystals are not perfectly harmonic and phonon-phonon interactions occur, which can result in the reversing of group velocity ($d\omega/d\mathbf{k}$, where $\mathbf{k}$ is a wave vector with magnitude $2\pi/\lambda$ and λ is the wavelength) of the phonon, in so-called U-processes. Thus thermal resistance can occur.[40] Although the calculation of the effect of phonon-phonon coupling on κ is quite complicated, a qualitative outline can be presented. The temperature dependence of the thermal conductivity for a typical crystal and a glass are shown in Figures 1.1. For most simple crystals, the differential, $\partial\kappa/\partial T$, changes from a negative value to a positive value as temperature decreases. On the other hand, amorphous materials always have a positive $\partial\kappa/\partial T$ in the whole temperature range.

Considering crystals at high temperatures ($T > \theta_D$), the number of excited phonons increases with increasing temperature, which results in the increasing probability of collisions of phonons and the reduction of mean free path, *i.e.*, $l \sim T^{-1}$ On the other hand, the heat capacity given by the Dulong-Petit law is temperature independent at high temperatures. Therefore, the thermal conductivity from equation (1.4.1) varies as T^{-1} for $T > \theta_D$.

At low temperatures, few phonons have sufficient energy for U-processes. The mean free path for phonon-phonon collisions becomes very long as the temperature decreases, and eventually depends only on the boundaries or imperfections in the crystal. Therefore, l can be treated as a constant and the only temperature dependence of thermal conductivity comes from the heat capacity, which obeys the Debye T^3 law, *i.e.*, thermal conductivity has a T^3 dependence at low temperatures.

In noncrystalline substances like glass, the thermal conductivity is generally proportional to T^n ($n > 0$)[63] and relatively independent of the chemical composition of the material. This behavior is related to the random structure of these materials, which is dominant even at high temperatures. The mean free path of phonons in these materials is

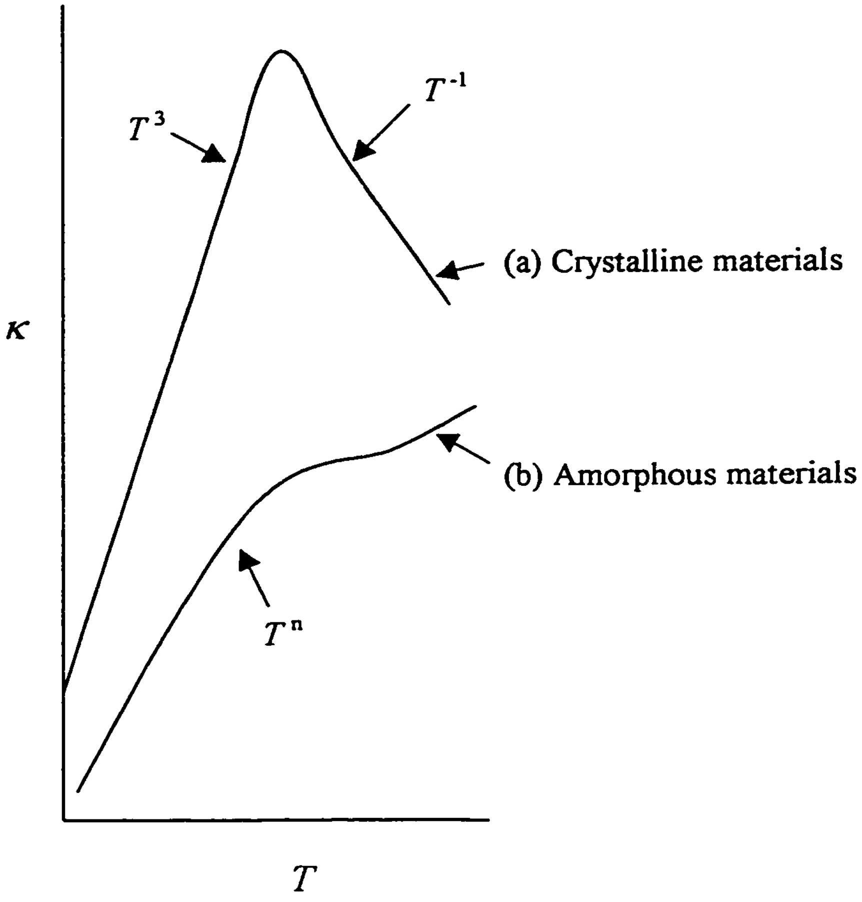

Figure 1.1. Temperature dependence of the thermal conductivity for (a) crystalline materials and (b) amorphous materials.[62] For typical crystalline materials, $\kappa \propto T^{-1}$ at higher temperatures and $\kappa \propto T^3$ at low temperatures. For amorphous materials, $\kappa \propto T^n$.

limited by the average interatomic spacing. Thus, the much shorter l of an amorphous material results in its smaller κ than that of crystalline materials.

Thermal conductivity is also a complicated physical property of solid materials. Some crystalline materials like the hexadecane-urea inclusion compound[63] show a temperature dependence of thermal conductivity between crystalline and amorphous materials. Such intermediate behavior is considered a result of weaker guest-host interactions. Other interesting examples are the clathrate hydrates which are well-defined crystalline host-guest systems based on a framework composed of water molecules. Their thermal conductivities exhibit similar behavior to that of amorphous materials with low κ and positive $\partial\kappa/\partial T$.[64] Recently, very low thermal conductivities also have been found in the skutterudite family and various Group 14 semiconductor clathrates (Chapter 4). The glass-like thermal conductivity of crystalline materials is one of the necessary requirements for applications of semiconductor thermoelectric materials. Studies[65] of the thermal conductivity of the inclusion compound HPTB.2CBr$_4$ revealed the possible generality of glass-like thermal conductivity in crystalline molecular solids.

1.5 Grüneisen Parameter

Like thermal expansion and thermal conductivity, the Grüneisen parameter is an important quantity for the measurement of the anharmonicity in solid-state materials, as shown in equation (1.2.9) in which it is assumed that all phonons vibrate at one frequency. In fact, a solid that has N atoms in its unit cell has $3N$ vibrational degrees of freedom, many with different frequencies. Thus, a stricter expression of the Grüneisen parameter is[66]

$$\gamma_i = -\left(\frac{\partial \ln \omega_i}{\partial \ln V}\right)_T, \tag{1.5.1}$$

and

$$\gamma = \frac{\sum_i \gamma_i C_{V,i}}{\sum_i C_{V,i}}, \tag{1.5.2}$$

where ω_i and $C_{V,i}$ are the angular frequency and the heat capacity of the ith vibration mode, respectively. The summation is taken over all the modes in the first Brillouin zone. In principle, the overall Grüneisen parameter can be evaluated from all the vibration modes if sufficient spectroscopic data are available.

For cubic solids, the Grüneisen parameter can be expressed with physically more accessible quantities:

$$\gamma = \frac{\alpha V}{\kappa_T C_V}. \tag{1.5.3}$$

For anisotropic solids, the calculation of γ requires other parameters such as adiabatic compressibilities, adiabatic elastic constants and the thermal expansion coefficients in different directions.

In harmonic solids, there is no thermal expansion and the vibrational frequency is independent of the spacing of the crystal lattice, $\gamma_i = 0$ and hence $\gamma = 0$. For most non-metallic solids, the overall Grüneisen parameter is of the order of unity near room temperature. It generally decreases with decreasing temperature and reaches zero at absolute zero because of the requirement of the third law of thermodynamics. Some materials such as tetrahydrofuran clathrate hydrates[67] show the opposite behavior due to the presence of low-frequency librational modes. For materials with thermal contraction, the Grüneisen parameter can be negative.

Although many materials display very similar shape in temperature-dependent heat capacity and thermal expansion coefficients, their Grüneisen parameter-temperature curves can be significantly different. In this respect, the Grüneisen parameter is more sensitive to the anharmonicity of vibration in solids.

1.6 Summary

Thermal properties are closely related to each other and they are necessary for both theoretical research interest and practical applications. Among the thermal properties, heat capacity is the most fundamental from which thermal conductivity, Grüneisen parameter, phase transition and thermodynamic properties, *etc.* can be obtained. The low-temperature heat capacity can be determined by adiabatic calorimetry which is discussed in Chapter 2.

In this thesis, the low-temperature thermal properties, especially heat capacity, of nine materials with different frameworks will be presented. They are zeolites (Chapter 3), semiconductor clathrates (Chapter 4) and 2, 6-dimethylbicyclo[3.3.0]nonane-*exo*-2, *exo*-6-diol (Chapter 5).

Chapter 2 Measurement of Heat Capacity

2.1 Introduction

Accurate heat capacity is necessary to determine thermodynamic properties including entropy, enthalpy and Gibbs energy as discussed in the previous chapter. This is especially important for many supramolecular materials such as clathrates and other inclusion compounds. These materials generally have the absolute values of small entropies and enthalpies of formation.[68]

Several techniques have been developed to determine the heat capacity especially for small samples in the last 30 years. The mid-1960's brought the introduction of differential scanning calorimetry (DSC) to determine the heat capacity of solids.[69] This is based on the principle that the output signal of the DSC instrument depends on the heat capacity difference between the sample and a reference.[70] One of the advantages of the commercially available DSC instruments over the classic adiabatic calorimeter is that it requires only a few milligrams of sample. This is especially useful for materials that are difficult to obtain in large quantities. In the absence of heat capacity anomalies, it is possible to use DSC to obtain the heat capacity with an accuracy of 3% and a precision better than 1%.[71,72] Other advantages of DSC over the traditional adiabatic calorimeter are the convenient loading and quick acquisition of heat capacity data.

However, commercial DSC's cannot presently determine the heat capacity or other thermal properties of materials below 100 K, although there is no technological problem in reaching this temperature range.[73] Careful selection of a reference material and knowledge of its heat capacity are also very important in the acquisition of accurate heat capacity from DSC.

One of the significant breakthroughs in the measurement of heat capacity was the introduction of alternating current (a.c.) calorimetry, developed by Sullivan and Seidel,[74] which depended on the well-developed commercially available lock-in amplifier. One of the advantages of a.c. calorimetry is that much less sample (*ca.* 20 mg) is used.[75,76] This method has very high temperature resolution (within 1 mK) and is particularly useful for the study of heat capacity anomalies in the limited temperature ranges.[77] Careful operation can achieve the accuracy on the order of 2%,[75] but a. c. calorimetry is more commonly used for relative heat capacities not for absolute heat capacities. The major disadvantage of a.c. calorimetry is the inaccuracy caused by the uncertainty of the heat capacity contributions from the addenda, including the thermometer, heater and wires.[70,78] This and other factors, often mean that a.c. calorimetric heat capacities are not known with high accuracy.[70] Unlike differential scanning calorimeters, a.c. calorimeters are not commercially available.

Additional calorimetric techniques are summarized elsewhere.[4,70] The remainder of this section concentrates on the adiabatic calorimetry.

Among the various types of calorimetry, adiabatic calorimetry is the most widely used technology to determine accurate heat capacities of materials.[4] Strictly speaking, an adiabatic calorimeter is an apparatus used to directly determine the heat capacity of a sample and its addenda (calorimeter cell, heater/thermometer assembly, etc.) without heat exchange between the system and the surroundings. The actual operating conditions are approximately close to the adiabatic state. The concept for evaluating the heat capacity of condensed phases by determining the temperature rise, which accompanies the input of a measured quantity of electrical energy, was first exploited by Gaede[79] in the early 20th century. Euken[80] and Nernst[81] developed Gaede's method and their apparatus was the precursor for the modern adiabatic calorimeter which remains one of the most important methods for determining the heat capacities of solids.

In early experiments, accurate measurement of heat capacity relied on an ample amount of the sample being available. The internal volume[82] of the sample cell was as large as 150 cm^3. This greatly limited the application of adiabatic calorimetry for materials which are difficult to obtain in large quantities but valuable for study.

The development of electronics, particularly the introduction of the computer in the early 1970's, significantly improved the field of classical adiabatic calorimetry. At the same time, the sizes of traditional platinum resistance thermometers were greatly reduced. These factors not only increased the efficiency of the experiment and the accuracy of heat capacity data but also made it possible to construct small-sample adiabatic calorimeters.[83-86] They can be used to measure heat capacity from room temperature down to about 10 K with a temperature resolution of better than 1 mK. The use of a sample vessel of 5 cm^3 is now routine.

Adiabatic calorimetry has a simple principle and almost no additional assumptions introduced in the determination of heat capacity. Since adiabatic calorimetry is an equilibrium method rather than a dynamic method, the heat capacity and phase transition data obtained from an adiabatic calorimeter directly give absolute, equilibrium thermodynamic information, provided that the sample is in an equilibrium state.

Generally, adiabatic calorimetry takes a longer time for measurement than other methods such as scanning calorimeters to determine heat capacity since it is an equilibrium method. In addition, the heat leaks from the necessary electrical connections can be significant at low temperatures (below 30 K). However, the major disadvantage of most adiabatic calorimeters is that a relatively large amount of sample, *ca.* 1~5 g, is required to obtain suitable accuracy. To decrease the sample size and retain the advantages of the adiabatic calorimeter, the volume of calorimeter must be reduced such that the heat capacity contribution from the sample is not too low relative to the overall heat capacity. The second important consideration is the selection of a miniaturized thermometer with high stability, sensitivity and accuracy since a large thermometer occupies a large space and contributes significantly to the heat capacity in the heater/thermometer assembly. As the sample size decreases, the thermal equilibrium time and hence the time to acquire data will also decrease.

In the following sections, the principles and the operation procedures of an automatic small sample adiabatic calorimeter is introduced. This apparatus was used to determine the low-temperature heat capacities of porous materials and thermoelectric materials in this thesis.

2.2 Principles of Adiabatic Calorimetry

The isobaric heat capacity is calculated by the operational equation

$$C_P = \frac{Q_P}{\Delta T}, \qquad (2.2.1)$$

where ΔT is the temperature change during heating, and Q_P is the electrical energy input at constant pressure by the heat pulse method:

$$Q_P = \frac{V_h^2 t}{R_h}, \tag{2.2.2}$$

where V_h is the heating voltage, t is the time interval of heating, and R_h is the resistance of the heater. In equation (2.2.1), C_P is the total heat capacity including the heat capacities of the sample, calorimeter, heater/thermometer assembly, and any sealants or grease.

Experimentally, the first step is to determine the heat capacity of the empty calorimeter. The heat capacity of a sample is determined from the difference between the heat capacity of sample-loaded calorimeter and that of the empty calorimeter. The minor heat capacity contributions from any variance in masses (e.g. sealant or grease) can be corrected.

Equation (2.2.1) indicates that the accuracy of the heat capacity data depends on the accuracy of determination of the input electrical energy and of the temperatures before heating and after heating. Generally, it is easier to obtain accurate Q than T.

To calculate $\Delta T = T_2 - T_1$, the pre-heating temperature (T_1) and post-heating temperature (T_2) are required. They can be determined by extrapolation of the pre-heating temperature-time curve forward and post-heating temperature-time curve backward to the midpoint of heating as indicated in Figure 2.1. These determinations would be made under adiabatic (or more realistically, quasiadiabatic) conditions. The temperature T of the heat capacity is taken as the average of T_1 and T_2:

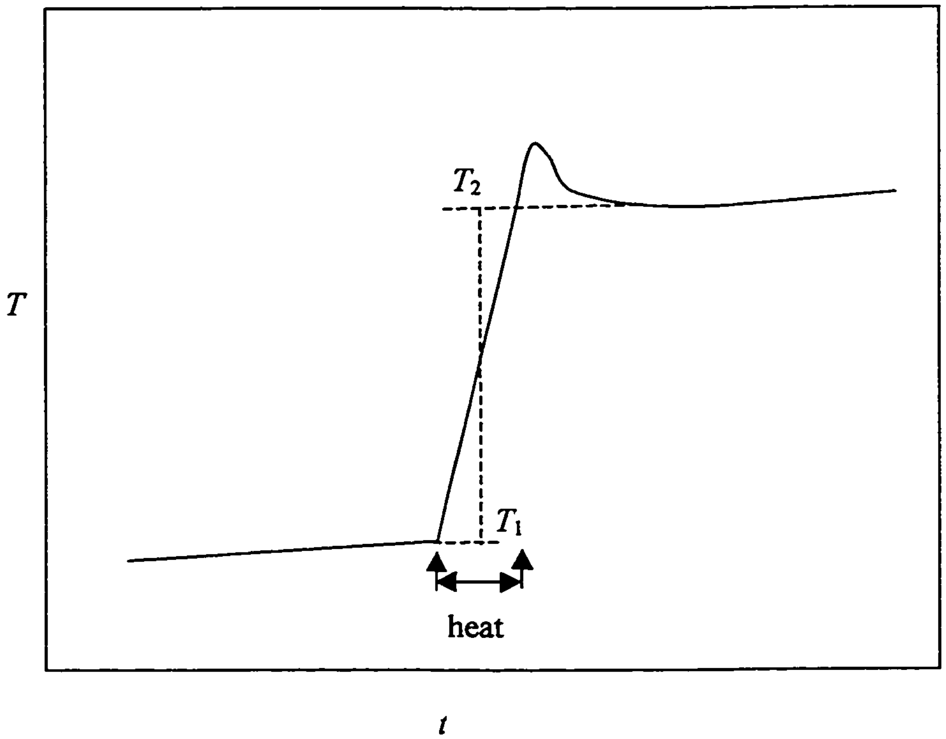

Figure 2.1. Determination of preheating temperature T_1 and post-heating temperature T_2. They are determined by extrapolation of preheating temperature-time curve forward and post-heating temperature-time curve backward to the midpoint of the heating.

$$T = \frac{1}{2}(T_1 + T_2). \tag{2.2.3}$$

It should be noted that the heat capacity of the sample, C_{sat}, is determined under its own saturated vapor pressure, P, which is related to the isobaric heat capacity C_P by:[87]

$$C_{sat} - C_P = \alpha TV\left(\frac{dP}{dT}\right)_{sat}. \tag{2.2.4}$$

Below ambient temperature, the difference between C_{sat} and C_P usually can be ignored due to the low vapor pressure and small thermal expansion coefficient of most solids.

2.3 A Small Sample Adiabatic Calorimeter

The apparatus used in this research is an immersion-type adiabatic calorimeter,[88] as shown in Figure 2.2. It uses liquid nitrogen or liquid helium as a refrigerant depending on the desired temperature range. The sample calorimeter shown in Figure 2.3, is a thin-walled cylinder (0.3 mm thick) made from gold-plated copper. The overall mass and volume of the calorimeter are about 10 g and 5 cm^3, respectively. The calorimeter sits in a heater/thermometer assembly.

The heater/thermometer assembly is made from thin-walled copper with a central well to hold a miniaturized capsule platinum resistance thermometer, described further below. The heater is a 2.6 m double silk-wound Karma wire (540 Ω at room temperature) wound bifilarly around the heater/thermometer assembly and varnished with GE 7031 low-temperature varnish. At the bottom of the assembly is a thermocouple (copper-constantan) with a resistance of 28 Ω at room temperature. The temperature difference

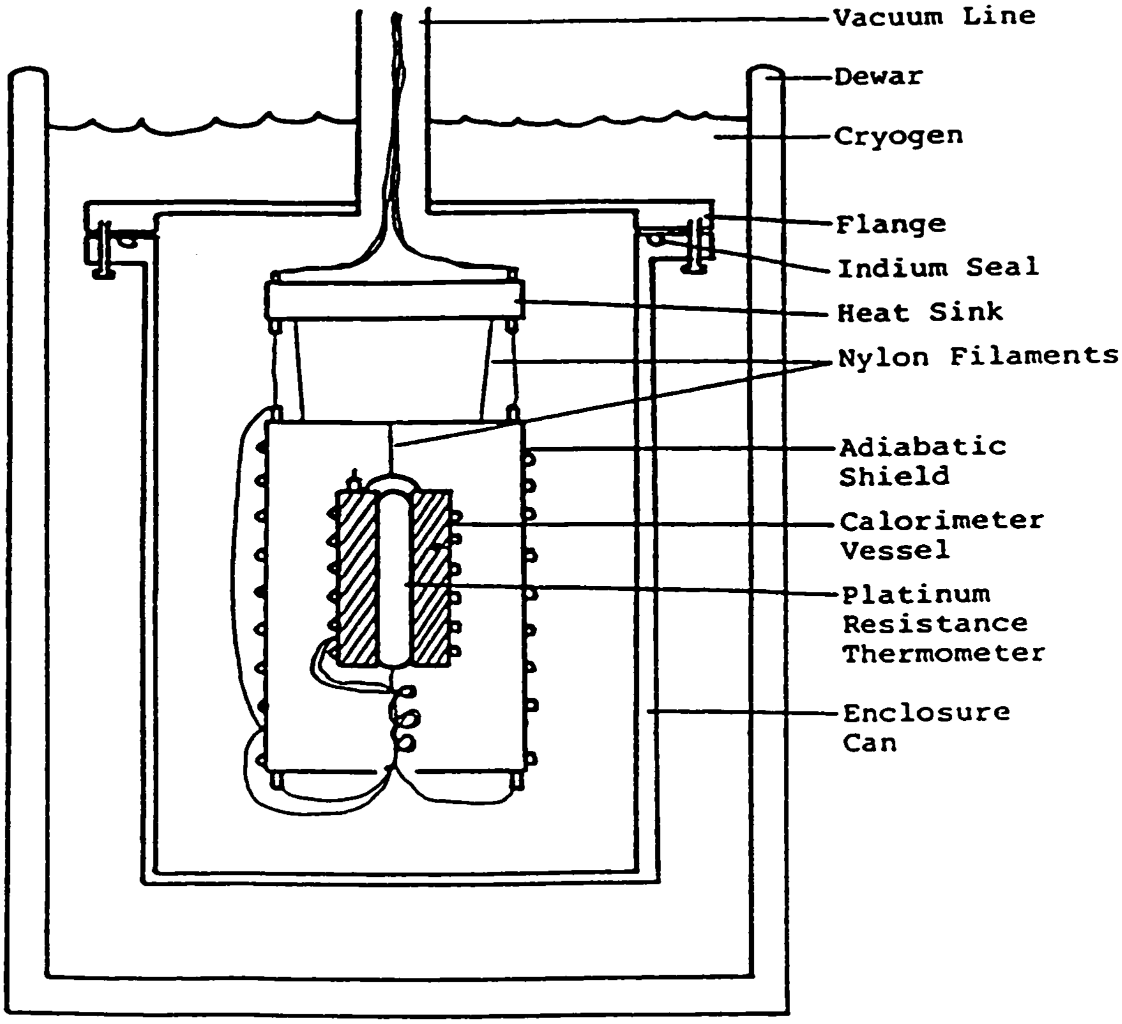

Figure 2.2. Schematic representation of an immersion-type adiabatic calorimeter.[88]

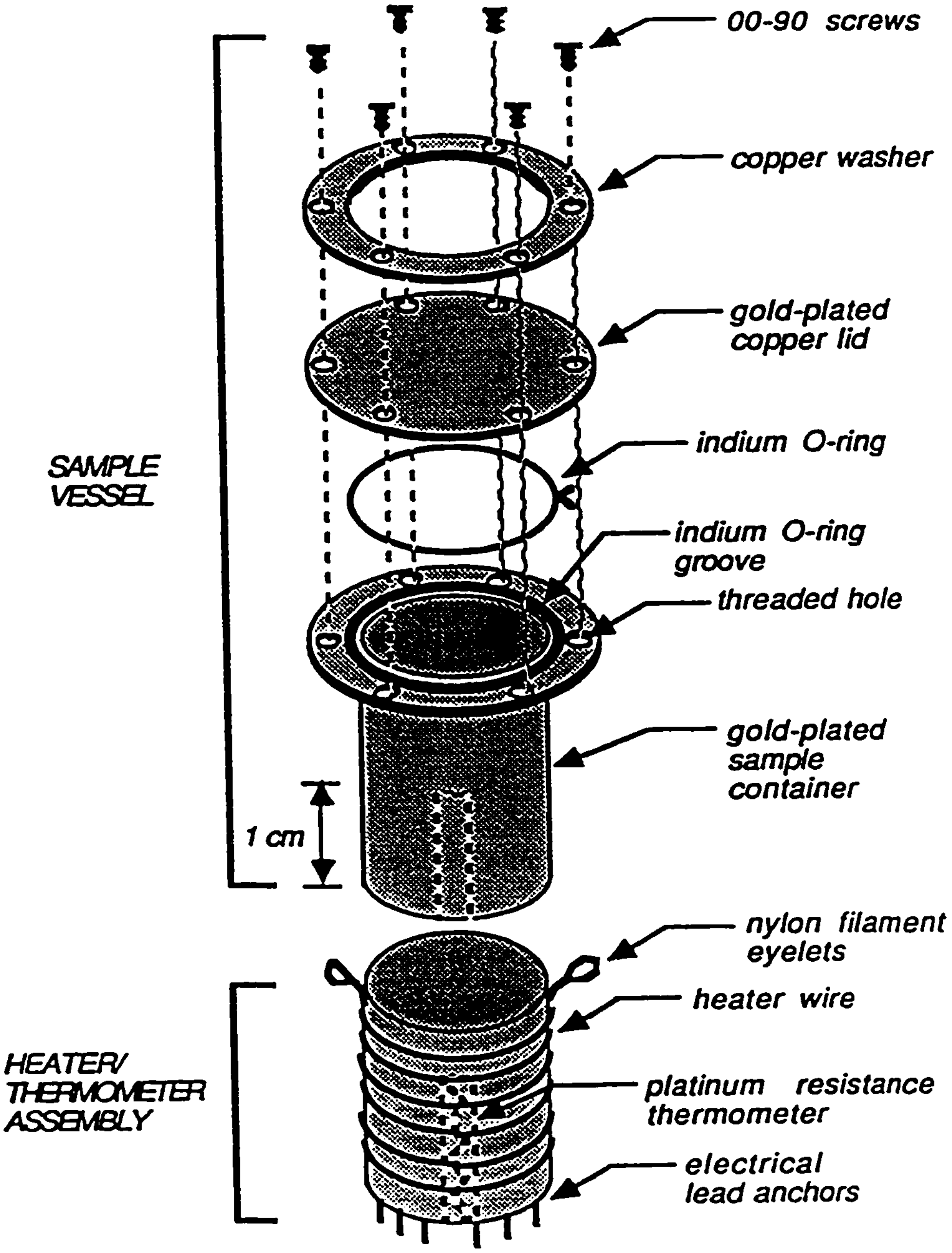

Figure 2.3. Schematic diagram of the calorimeter cell.[88]

between the adiabatic shield and sample cell is monitored by the thermocouple which is connected to an Artronix 5301-E shield controller.

The adiabatic shield, made from a thin-walled copper cylinder, is used to decrease the temperature gradient between the calorimeter and the refrigerant and has enough space to surround the heater/thermometer assembly. The shield heater is a 15 m manganin wire with a resistance of about 100 Ω which is wound bifilarly on the surface of the shield. The ceramic pins on the top and the bottom of the shield are used to connect cables coming from the heat sink and those from heater/thermometer assembly. The power to the shield is provided by the shield controller through the shield heater.

The electrical energy is supplied to the calorimeter by a d.c. constant-voltage power supply. The resistance and potential drop across calorimeter heater are measured by a Hewlett Packard 3456A digital voltmeter. The time interval of heating is measured by an internal clock in the computer.

A commercial PT-103 (Lake Shore) thermometer was used to determined the temperature of the calorimeter. It was calibrated by the manufacturer from 4 to 380 K with the asserted accuracy of ± 10 mK above 27 K and ± 15 mK below 27 K. The resistance of the thermometer was determined by comparing the potential drop across the thermometer with that across an approximate 100 Ω standard resistor. The potential drops are measured by the digital voltmeter. To increase the sensitivity, 1 mA constant current is passed through the thermometer and the standard resistor. Hence their voltage ratio is equal to the resistance ratio, which is measured with the current in the forward direction and in the reverse direction, so that the thermal electromotive force at the junctions can be cancelled.

The heat capacity of the empty calorimeter was determined and the data were stored in the computer. The accuracy of the calorimeter had been tested with Calorimetry Conference Standard benzoic acid, and the agreement with the known value was within ± 0.5%.[88] A most recent investigation of heat capacity of NaOH showed that the result agreed with literature value within 1.5%,[13] indicating that the accuracy of this apparatus is rather stable.

2.4 Operation of the Adiabatic Calorimeter

Before loading a sample, the calorimeter vessel was cleaned and dried, and its mass was determined. The sealing gasket, a piece of indium wire with a diameter of 0.5 mm, was put in the grove of the calorimeter vessel. The mass of the indium wire is about 85 mg and indium's heat capacity has been measured.[89,90] Sample loading was performed under a dry nitrogen atmosphere and the calorimeter was sealed under a dry helium atmosphere. The He was necessary to increase the thermal conductivity between the sample and the calorimeter. The sample was about 1 ~ 5 g depending on its availability. To enhance the thermal contact between the calorimeter and the thermometer/heater assembly, the outside of the calorimeter was greased slightly with weighed amount of Apiezon T grease, usually about 10 mg. Its heat capacity at low temperatures has been determined.[91] The calorimeter and thermometer/heater assembly were then hung by a nylon filament attached to a hook on the top of the adiabatic shield. The latter was hung on the three hooks from the heat sink (See Figure 2.2). All the leads from the corresponding instruments outside of the vacuum system were wrapped around the heat sink to reduce the thermal leaks from the surroundings to the system.

To minimize the thermal electromotive force all electrical connections were soldered with thermal-free solder (70.44% Cd + 29.56 Sn).[92] The copper enclosure can was sealed with an indium wire with a diameter of 1 mm to obtain suitable vacuum and was immersed in a glass Dewar vessel filled with refrigerant. In the acquisition of data below about 80 K, two Dewars were used: the inner Dewar for liquid helium and the outside one for liquid nitrogen.

To achieve adiabatic conditions the system is pumped down to a pressure of less than 10^{-5} Pa by running a roughing pump and an oil diffusion pump connected to the vacuum system. A small amount of helium gas was introduced to the enclosure can to cool the system down to the desired temperature and then pumped out until the vacuum was restored. After turning on the power to the shield and adjusting the set point manually to the desired value so that the temperature drift of the calorimeter was within ± 1 mK min^{-1}, the shield controller was set to automatic mode. The data acquisition and analysis were automatically done by the computer.

The time required to obtain one point of heat capacity ranges from 30 to 100 minutes depending on the temperature. During the heating period, the temperature step was adjusted to about 10% of the experimental absolute temperatures up to a maximum of 7 K to obtain maximum accuracy.

In the following chapters, the above small sample adiabatic calorimeter was used to determine the heat capacities of various materials.

Chapter 3 Thermal Properties of Zeolites

3.1 Introduction

Zeolites are aluminosilicates with various cavities and channels in their crystalline structures. The name zeolite comes from the Greek 'zein' meaning 'to boil' and 'lithos' meaning 'stone'. Hence, zeolites are also called boiling stones in reference to their peculiar frothing characteristics when heated. Zeolites exist in nature as fine crystals of hydrothermal genesis in geodes and in fissures of volcanic rocks, or as microcrystalline masses of sedimentary origin.[93]

The first natural zeolite, now known as stilbite with typical chemical composition $Ca_{1.09}Na_{0.136}K_{0.006}\ Al_{2.18}Si_{6.82}O_{18}\cdot 7.33H_2O$,[94] was discovered by a Swedish mineralogist Cronstedt in 1756.[93] During the next hundred years or so these boiling stones received little attention. The pioneering work of Wiegel and Steinhof[95] revealed that dehydrated zeolitic crystals selectively adsorb small organic molecules but reject larger ones. Thus zeolites received their other name, "molecular sieve". Although many zeolites are "molecular sieves", not all "molecular sieves" are zeolites.[96]

The early attempts to synthesize zeolites can be traced back to the 1860's, but most of them were unsuccessful. Large scale preparation of synthetic zeolites started in the late 1940's. The synthesis of the first generation of zeolites, including zeolite A, zeolite X and zeolite Y, was performed using reactive aluminosilicate gels with alkali and alkaline earth metal hydroxides. These zeolites contain a low silica to alumina ratio with $SiO_2:Al_2O_3 < 5$. They exhibit a high ion exchange capacity, an extremely hydrophilic surface and have many acid sites with a wide variety of acid strengths. The frameworks of these novel materials show different thermal stabilities depending on the structure and composition.

The second generation of synthetic zeolites was prepared from organic quaternary ammonium ions such tetramethylammonium (TMA) as structural directing agents instead of alkali metal ions. These organic cations have a larger size than alkali metal ions and template large cavities in the aluminosilicate framework. Zeolites with high Si/Al ratio ($SiO_2:Al_2O_3 > 10$) such as ZSM-5 can be successfully synthesized by this method.[97] The end member of ZSM-5, also known as a pure silica molecular sieve, shows the hydrophobic and organophillic properties of the internal surface.

In the last two decades, the application of large organic species as structure-directing templates or pore-filling agents led to new zeolite-like materials with different framework ions, such as Ga^{3+}, $Ge^{4+}$and P^{5+} replacing the traditional silicon and aluminum.[98] Generally, these zeolitic-like materials have no ion exchange capacity.

In this chapter, the general properties and the research purposes of zeolites are summarized. The determined thermal properties of three important zeolites are discussed.

3.1.1 Framework Topology, Cations, Water and Si/Al ratio

The typical empirical formula of a zeolite can be expressed as:[99]

$$M_{2/n}O\cdot Al_2O_3\cdot xSiO_2\cdot yH_2O,$$

where M usually is an alkali metal or alkaline earth metal ion although many other cations such as NH_4^+, H^+, or Ag^+ may be inserted instead by ion exchange or synthetic processes, and n represents the valence of cation M^{n+}. In general, $x \geq 2$. The physical and chemical properties of zeolites rely on three components: the aluminosilicate framework, the exchangeable cations, and the zeolite water.

The aluminosilicate framework is the most conserved and stable component, and defines the structure type. The framework topology describes the connectivity of the tetrahedral atoms (or T-atoms) of the framework in the highest possible space group, neglecting the framework composition, the observed symmetry and the unit cell dimensions.[100] Therefore, many different zeolitic materials can be classified under one framework topology designation. The framework topology can consist of channels and cages which have approximately molecular diameter and can host the charge-compensating cations, water or other molecules and salts. The topology of the framework, the numbers and distribution of charges, and the stacking faults are all formed at the crystal growth stage and define a series of technologically important properties of zeolites. The framework is generally considered as open because communication between the interior and exterior of the crystals is through the openings, with a typical diameter larger than 4 Å circumscribed by at least eight corner-shared AlO_4 and SiO_4. These TO_4 (T = Al, Si) tetrahedra are the basic units of the framework and are called the primary building units. Compared with other framework materials, zeolites have a low tetrahedral TO_4 density in the framework, less than 20 (TO_4) / 1000 $Å^3$, due to their large pore volume.[101] Different combinations and arrangements of TO_4 construct the various structural units in the zeolite framework from the simple β-cage of sodalite to the supercage of faujasite and from the one-dimensional channel in the mordenite framework to the three-dimensional channels in zeolite X and zeolite Y.[101]

Indeed, the primary building units are not enough to describe the complicated structures of zeolitic materials and the concept of secondary building units (SBU) was proposed. Some selected SBUs are shown in Figure 3.1. The complete and unique framework of a particular zeolite can generally be obtained by linking SBUs. For example, the framework of sodalite ($Na_6Al_6Si_6O_{24}\cdot 2NaCl$) can be obtained by joining the body-centered truncated octahedra, β-cages, through single 4-rings and 6-rings, as shown in Figure 3.2. About 800 different zeolites can be classified by 119 framework topologies.[102] They are not only helpful for classification purposes and for deducing rules relative to these structures but also are important for the assignment of vibrational spectra.[101]

Nonframework cations not only are necessary to balance the negative charges of the AlO_2^- terahedra in the framework but also contribute to the thermodynamic stability of zeolites which will be discussed in Section 3.5. The cations determine many important applications of zeolites such as ion exchange, separation and metal inclusion compounds. For example, in noncryogenic air separation, the lithium ion in Li-zeolite LSX exhibits strong affinity for N_2 instead of O_2 because the former has a quadrupolar moment three times larger than the latter.[103] The cations are distributed in various sites, such as β-cages (See Figure 3.2) and hexagonal prisms. However, their precise locations remain uncertain and are of both practical and theoretical research interest.

Water is important in the formation of zeolites and in the ion exchange process. The water molecules generally are loosely bound to the zeolitic framework through hydrogen bonds due to the large voids of the zeolite. It is found that the entropy[104] of

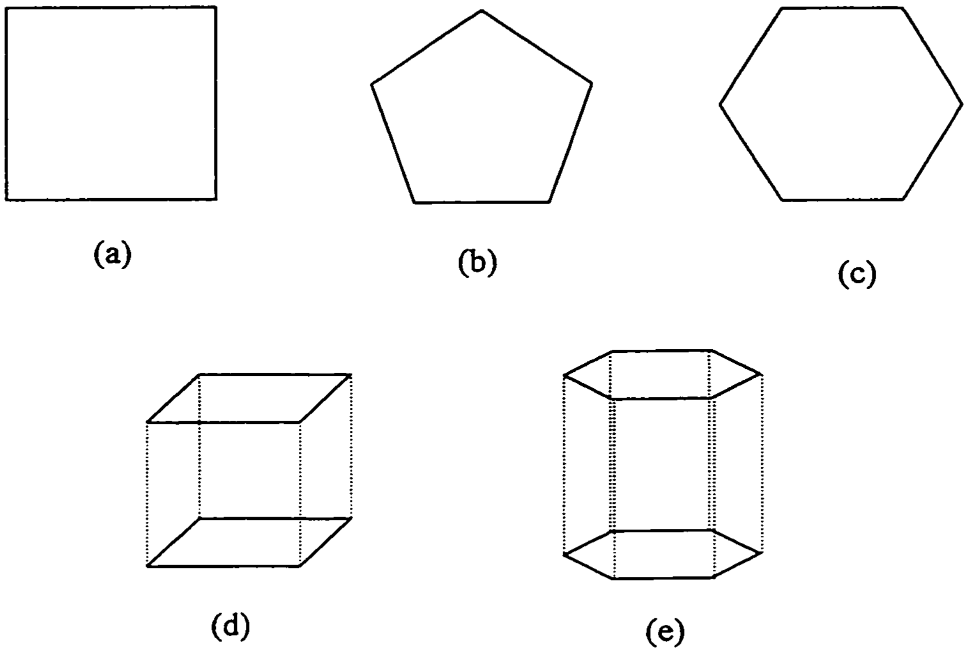

Figure 3.1. Some selected secondary building units (SBU) of zeolite frameworks. (a) Single four-ring (S4R), b) single five-ring (S5R), (c) single six-ring (S6R), (d) double four-ring (D4R) and (e) double six-ring (D6R). All the vertices represent the T atoms and the oxygen atoms in T–O–T bonds are omitted.

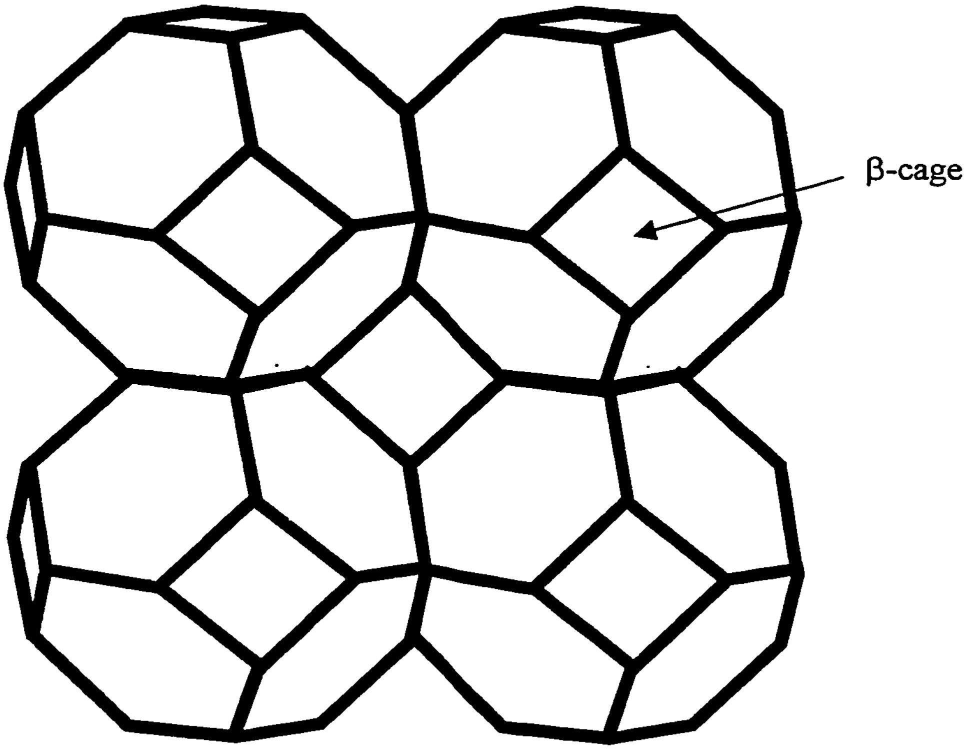

Figure 3.2. Framework of sodalite. It can be constructed by joining body-centred cubic octahedra, β-cages (or sodalite cages), through single 4-rings and 6-rings. The β-cages can also be obtained by linking 4-rings and 6-rings.

zeolitic water is between that of ice and liquid water, with a value of 45 ± 10 J mol^{-1} K^{-1}. The incorporation of water is exothermic in most cases and hydration can stabilize zeolites with respect to their anhydrous phases but the effect diminishes at high temperatures especially above 373 K due to the large negative entropy effect from water.[105] The water content varies depending on the character of the exchangeable cations and the conditions of crystallization. Ideally, if the water molecules completely fill the free volume of channels and cages in the zeolites, the free inner volume of the zeolite can be determined by measuring the volume of the water released while heating in *vacuo*. The dehydration procedure is reversible and the dehydrating temperature ranges from 200 to 450°C depending on the zeolite. For instance, it is generally accepted that the dehydration of faujasite is complete at 400°C under vacuum conditions[106] while the dehydrating temperature of the crystals of ZSM-5 is only 200°C.[107]

Apparently, framework topology, cations, and water molecules influence each other. Since the cations are mobile, the framework can influenced by dehydration.[108] The distribution of water molecules depends upon both the framework and the character, quantity and location of cations, which in turn are defined by the density and distribution of anionic sites in the framework. Concurrently, the presence of cations and negative charges of the framework can produce a cooperatively strong electric field to stabilize or activate the molecular species inside the cages and channels.[109]

In fact, one of the most fundamental parameters to determine the physical and chemical properties of a zeolite is the Si/Al ratio. In natural zeolites, the Si/Al ratio lies within the limits of 1 to 6 while in synthetic zeolites the value can vary from 1 to ∞. The lower limit of Si/Al is determined by Löwenstein's rule,[110] which states that an AlO_4 tetrahedron cannot be connected with another AlO_4 tetrahedron by a common oxygen atom. Hence, at Si/Al =1, the silicon and aluminum tetrahedron alternate to form an ordered framework. As the Si/Al ratio increases, the ordering of Si and Al become complex and both ordered and disordered frameworks are possible.[111] It is common that the Si/Al ratio can significantly change not only in the zeolites with different framework topologies, but also in those with the same framework topologies such as zeolite X and zeolite Y. Generally, the lattice parameters of zeolites increase with the decrease of the Si/Al ratio and an approximately linear relationship exists between the lattice parameter and the Al content,[112] *i.e.*, the lattice parameters decrease as the Si/Al ratio increases because Si-O has a shorter bond length than Al-O. In addition, the stability of zeolites also strongly depends on the Si/Al ratio; this will be presented in more detail in Section 3.5.

3.1.2 Techniques for Investigating Physical Properties of Zeolites

One of the most common techniques in zeolite research is diffraction, including X-ray diffraction and neutron diffraction. These techniques are sensitive to long-range order and can provide the structural parameters of the lattice at different temperatures. Hence, phase transitions, the mechanical properties (such as bulk modulus) and the thermal expansion parameter can be determined. In general, it is very difficult to obtain single crystals of synthetic zeolites with adequate quality and sufficient dimensions for single crystal diffraction. Thus, powder diffraction methods are commonly used. Since X-rays are scattered by the electrons around the nuclei and the scattering factors are directly proportional to atomic number, distributions of Al atom and Si atom are not well distinguished owing to their close scattering factors,[113] although X-ray diffraction provides an accurate overall framework for the zeolites. Unlike X-rays, neutrons are scattered by the nuclei. The advantage of neutron diffraction over X-ray diffraction is that the former can distinguish atoms with similar numbers of electrons such as Al and Si.

Solid-state NMR spectroscopy plays a very important role in the research of structure and property of zeolites.[114] Both ^{29}Si and ^{27}Al NMR spectroscopy provide information about the local distribution of Si and Al and hence the immediate environment of a particular tetrahedral site.[115] Solid-state NMR spectroscopy is especially powerful in the study of dynamics and site distribution of various guests in the channels and cages of zeolites.

Vibrational spectroscopic techniques including IR and Raman spectroscopy are powerful methods for the characterization of zeolites.[116,117] The vibrational frequencies also can be used to estimate the heat capacity of optic modes and the Grüneisen parameter. However, the successful application of vibrational techniques requires reliable assignments of observed vibrational modes. A definite interpretation of spectral data is usually rather difficult due to the complicated frameworks of zeolites which contain hundreds of atoms per unit cell. Moreover, the vibrational spectra of zeolites generally exhibit a limited number of broad, strongly overlapped bands. Hence the application of vibrational spectroscopic techniques is greatly limited in the determination of thermal properties of zeolites.

In the past few decades, computational simulations such as Monte Carlo calculations[118] and molecular dynamics[119] have proven to be useful methods of studying the structural stability and various properties of zeolites. However, these techniques are generally restricted to fragments of zeolitic structures and further there remain many problems associated with the selection of appropriate potentials.[118] Quantum mechanical calculations can be computationally expensive because of the large unit cell and low symmetry.[120]

On the other hand, adiabatic calorimetry is considered one of the most powerful techniques to determine thermodynamic properties (Section 2.1) and hence to understand the thermodynamic stability of zeolites with different Si/Al ratios and to predict the experimental conditions that will lead to zeolite syntheses. Furthermore, calorimetric investigation can reveal whether the thermodynamic stabilities of zeolites are enthalpic or entropic. However, experimental data especially below 300 K only exist for the heat capacities and related thermodynamic properties for a few synthetic zeolites. The applications of an adiabatic calorimeter in some selected synthetic zeolites will be presented from Section 3.2 to 3.4.

3.1.3 Thermal Expansion

Thermal expansion behavior of zeolites is of great academic interest and industrial importance since expansion and contraction of the pores and channels can significantly influence the rate of diffusion and sorption, and hence the formation of reaction products.

The open structure and low framework density of the unit cell can result in unusual thermal properties for zeolites. X-ray diffraction[121] and lattice energy calculations[122] revealed that zeolite X exhibits significant thermal contraction below 200 K. Negative thermal expansion also was found in zeolite A[123] and many siliceous zeolites, including siliceous faujasite,[124] ITQ-1, ITQ-3 and SSZ-23,[125] ITQ-4 and chabazite.[126] The aluminophosphate, $AlPO_4$-17, was identified as the most strongly contracting zeolite-like material with a volume expansion coefficient -3.51×10^{-5} K^{-1} over a temperature range from 18 K to 300 K.[127] However, the similar framework material sodalite exhibits typical positive thermal expansion.[121] Theoretical calculations[122] further predict that thermal contraction depends on the Si/Al ratio and that the more siliceous zeolites have much greater contraction or expansion. It had been proposed that the highly porous framework and three-dimensional channels in zeolites allow expansion into the pores and channels upon heating and result in its negative thermal expansion.[122] However, X-ray diffraction of siliceous faujasite indicates that the bond lengths and bond angles of the rigid TO_4 remain essentially constant between 25 and 573 K.[124] Thus, it was supposed that the strong negative thermal expansion in siliceous zeolites is due to the transverse vibrations of the bridging oxygen atoms in O-Si-O.[126] A similar mechanism has been suggested to explain the negative thermal expansion of ZrW_2O_8.[56,57]

Although several mechanisms have been suggested to explain thermal contraction of various materials,[128,129] it is not completely understood yet why some zeolites show negative thermal expansion while others with similar structures show a positive thermal expansion. Even if only one zeolite is considered, the property of thermal expansion depends on the temperature region. For example, $AlPO_4$-17 shows a strong thermal contraction below ambient temperatures,[128] but displays positive thermal expansion between 320 and about 770 K.[125] A similar phenomenon also has been found for dehydrated zeolite NaX.[121]

3.1.4 Research Objectives

As mentioned above, the open framework and high stability of zeolites lead to many industrial applications including ionic exchangers, molecular sieves and catalysis or catalyst support. Zeolites are also closely associated with the daily life of humans. For example, zeolite 4A (Linde Type A) is commonly used in soap powders and in water treatment plants for the removal of heavy metal ions. Recently, zeolites have been used in photochemistry,[130] solid state batteries and solar energy converters.[98,131]

To inclusion chemists, the existence of various intersecting channels and cavities with definite shape and uniform size makes zeolites ideal materials for the study of the host-guest interactions. Unlike most host structures such as urea and thiourea,[132] zeolites exhibit high stability, with or without guests. The stabilizing interactions in zeolite inclusion compounds can be guest-guest interactions, Coulombic interactions between cations and anions in the framework, or guest-framework interactions from van der Waals forces to hydrogen bonds.[133,134] In alkali-metal zeolite inclusion compounds, dehydrated zeolites behave as solid solvents and the alkali atoms form clusters with the extra framework cations.[135] By including various guests, the properties of zeolites can be tailored, for example, from insulator to conductor and from many novel composite materials to advanced molecular-scale electronic and optic devices such as optical transistors.[135] The urgent need for thermodynamic data on zeolite inclusion compounds is clear.[136]

As discussed in Section 1.2, heat capacity is a fundamental property of a material, from which information concerning such matters as phase transitions can be obtained and thermodynamic functions such as ΔH, ΔG, and ΔS can be determined. Thermodynamic information can enhance our understanding of the relationships between structure and properties of zeolitic materials, especially the effect of aluminum concentration on the thermodynamic stability of zeolites to develop new methodologies for the syntheses of these novel framework materials. While a few natural zeolites including analcime,[137] sodalite,[138] erionite,[139] epistilbite,[140] natrolite, mesolite and scolecite,[104] heulandite,[141,142] mordenite and gibbsite,[143] and stilbite[94] have been investigated by calorimetry, lack of compositional uniformity is a major problem encountered in accurately determining heat capacity and other thermodynamic functions of these natural zeolites. Moreover, investigation of the behaviour of dehydrated zeolites is important since catalytic properties and adsorption, such as molecular sieve effects, sorptive and catalytic properties, depend on the dehydrated forms.

In the following sections, the thermal properties, especially the low-temperature heat capacities of three zeolites, *i.e.*, zeolite 4A, zeolite NaX and zeolite NaY, are reported. The selection of these materials was based on several considerations. First, as discussed above, they are academically and industrially important in ion exchange, catalysis, separations, etc. Secondly, the high purity of these commercially available materials is especially helpful to acquire accurate thermodynamic properties. In addition, the effects of different frameworks and compositions of these synthetic zeolites on thermodynamic properties can be revealed through the investigation of heat capacities. Finally, the heat capacities of these zeolites could be useful to convert experimental thermal diffusivities to thermal conductivities.

3.2 Heat Capacity and Thermodynamic Properties of Zeolite 4A

3.2.1 Structure

The unit cell of zeolite 4A can be constructed by arrangement of β-cages[144] through the double four-rings, which results in the formation of α-cages as shown in Figure 3.3. The framework of zeolite 4A is more open than that of sodalite. There are eight α-cages (11 Å diameter) and eight β-cages (7 Å diameter) in each unit cell.[145,146] The negative charged framework is balanced by the presence of cations such as sodium ions. The crystal structure of dehydrated zeolite 4A has been determined with greater precision than that of hydrated zeolite 4A because of the difficulty in distinguishing crystallographically the water oxygen and the sodium ions.[146] The average T-O bond length is 1.66 Å and the average O-T-O bond angle is 109.4°.[147,148] Single crystal X-ray diffraction indicates strong ordering of Si and Al into alternate tetrahedra.[148] Depending on the report, two chemical formulae of zeolite 4A are widely used: $Na_{12}Al_{12}Si_{12}O_{48}$ has a pseudocell with a unit cell parameter 12.29 Å and cubic space group *Pm*3*m*[147] while the true unit cell has the chemical formula $Na_{96}Al_{96}Si_{96}O_{384}$ with a unit-cell parameter of 24.56 Å, space group *Fm*3*c*.[148]

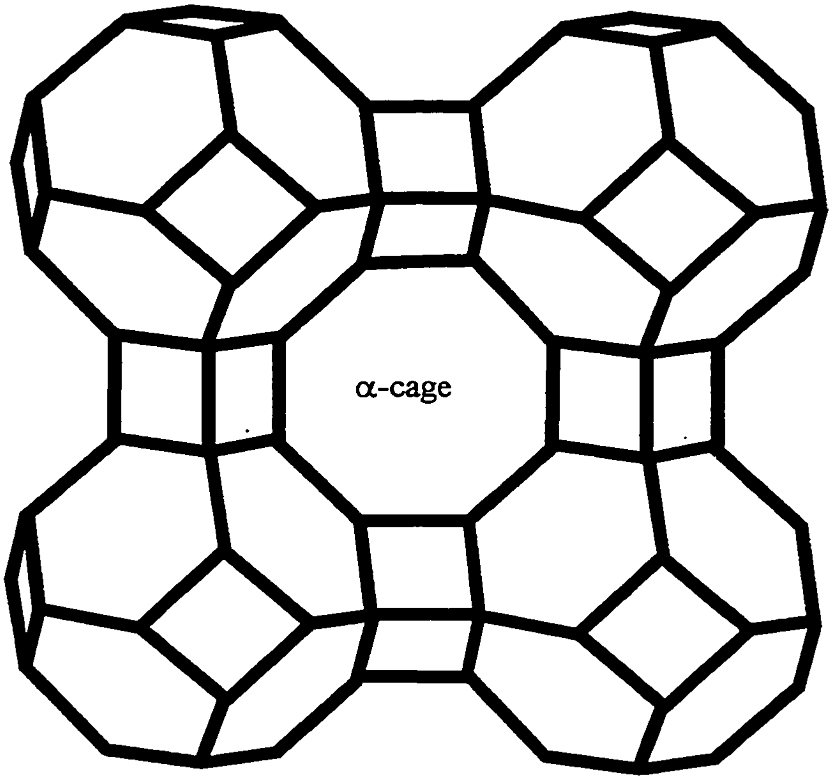

Figure 3.3. Framework of zeolite 4A. It can be described by linking the β-cages through double four-rings. This results in the formation and α-cage with a diameter of 11 Å.

3.2.2 Experimental Methods and Characterization

Zeolite 4A (molecular sieve 4A) powder was purchased from Aldrich Chemical Company. The sample was heated in a quartz tube to 453 K under vacuum conditions for 10 hours to achieve essentially complete dehydration. DSC was used to detect the possible water in the dehydrated sample in the temperature range 350-600 K. A scanning rate of 5 K $\mathrm{min^{-1}}$ was used. The limit of detection of water in the DSC experiment is 0.1% and there was no detectable water within this limit.

The lattice parameter of the dehydrated powder sample was determined by X-ray diffraction (Cu Kα radiation with wavelength 1.54056 Å) at 298 K. It revealed that the sample was highly crystalline with a cubic unit cell parameter of 24.51(3) Å, in very good agreement with published values.[148,149]

To determine the composition about 1 g of the sample was analyzed by X-ray fluorescence. The compositions of all oxides in the dehydrated sample are shown in Table 3.1. The Si/Al mole ratio was found to be 0.98 ± 0.02. The unit cell of zeolite 4A is considered to have an ideal chemical formula, $Na_{96}Al_{96}Si_{96}O_{384}$.

The dehydrated sample was handled exclusively in a dry nitrogen atmosphere in a glove box to avoid the adsorption of moisture. The sample was sealed in the calorimeter under a helium atmosphere to facilitate thermal equilibrium. The heat capacity of a 2.3039 g sample of zeolite 4A was determined over the temperature range 37 K to 310 K by using an automated adiabatic calorimeter which was operated in the heat pulse mode as described in Section 2.4.

Table 3.1. X-ray Fluorescence Analysis of Components in Zeolite 4A.

Components	mass%(exp.)	mass%(theor.)*
SiO_2	41.8±0.8	42.3
TiO_2	0.02±0.01	
Al_2O_3	36.1±0.7	35.9
Fe_2O_3	0.02±0.01	
MgO	0.07±0.00	
CaO	0.12±0.00	
Na_2O	21.3±0.42	21.8
K_2O	0.56±0.01	

* The mass% (theor.) is based on the ideal formula $Na_{96}Al_{96}Si_{96}O_{384}$.

3.2.3 Results and Discussion

3.2.3.1 Heat Capacity

The experimental heat capacities of zeolite 4A are given in Table 3.2 and shown in Figure 3.4. The heat capacity of the sample comprised about 20% of the total (sample + vessel) heat capacity at 300 K and 15% at 37 K. Although the full temperature evolution of the heat capacity of zeolite 4A does not appear to have been determined previously, the heat capacity at T = 300 K has been determined,[150] and is within 5% of the present data.

The heat capacity is smooth over the experimental temperature range. Although it has been proposed that subtle changes in the rhombohedral distortion of the lattice of zeolite 4A are associated with a phase transition at 335 K,[151] neither anomalous pretransitional heat capacity nor any sharp anomalous features near T = 335 K was detected by differential scanning calorimetry.

The experimental heat capacities are essentially those at constant pressure, C_P, but the more meaningful heat capacity can be that at constant volume, C_V. Since zeolite 4A is a cubic solid, C_P and C_V can be related by equation (1.2.5). The volume of the unit cell of zeolite 4A has been reported for only two temperatures, *viz.* 5 K and 290 K,[152] but this allows an estimate of the thermal expansion. Combined with the isothermal compressibility results[153] for zeolite 4A, this leads to an estimate of $(C_P - C_V)/C_P$ at room temperature of 0.005%. As this would be expected to decrease with decreasing temperature, it is assumed that $C_P - C_V \approx C_V$.

Table 3.2. Experimental Heat Capacity of Zeolite 4A, $Na_{96}Al_{96}Si_{96}O_{384}$.

T/K	C_P/J K^{-1} g^{-1}	T/K	C_P/J K^{-1} g^{-1}	T/K	C_P/J K^{-1} g^{-1}
37.02	0.0936	130.37	0.495	230.82	0.780
42.26	0.141	133.09	0.497	234.42	0.783
46.91	0.159	136.67	0.508	237.95	0.796
51.16	0.174	140.82	0.529	241.38	0.810
55.24	0.186	145.94	0.547	244.83	0.813
58.90	0.201	148.56	0.553	248.40	0.821
62.88	0.222	153.61	0.568	251.72	0.830
67.99	0.249	156.23	0.572	255.37	0.834
73.67	0.267	161.27	0.586	258.69	0.840
79.35	0.291	163.87	0.592	262.02	0.851
81.08	0.301	170.10	0.618	265.44	0.858
84.96	0.323	171.48	0.622	268.42	0.862
86.55	0.325	176.53	0.641	272.18	0.863
87.47	0.330	179.02	0.641	274.92	0.871
90.58	0.343	183.99	0.654	278.81	0.873
92.08	0.352	186.63	0.664	281.30	0.878
96.26	0.367	190.97	0.685	283.67	0.885
97.62	0.374	194.13	0.682	287.09	0.895
101.25	0.388	198.31	0.696	287.65	0.889
103.22	0.390	201.56	0.701	290.74	0.901
106.80	0.406	205.64	0.712	294.30	0.904
109.88	0.417	208.95	0.723	294.36	0.901
112.40	0.438	212.89	0.735	298.71	0.915
117.61	0.448	216.26	0.742	301.39	0.921
118.04	0.452	220.15	0.753	305.13	0.935
123.68	0.466	223.56	0.766	307.57	0.938
125.36	0.470	227.29	0.768	311.41	0.948

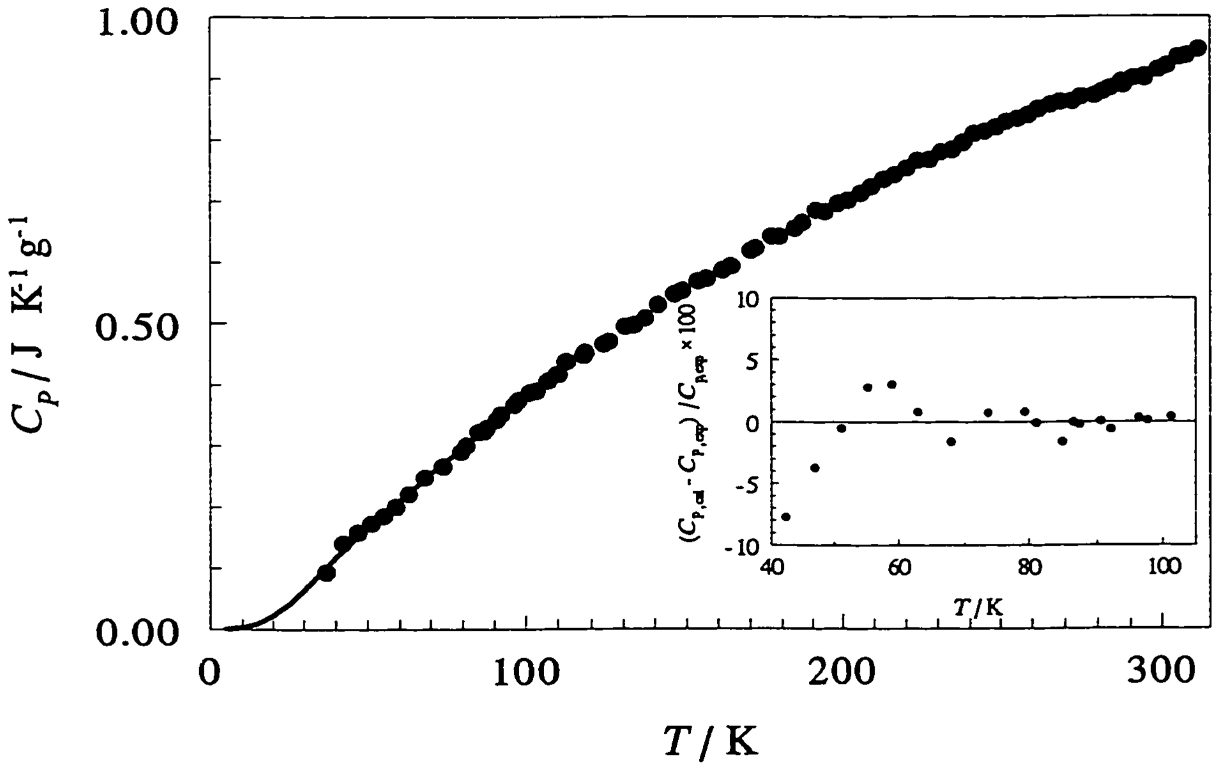

Figure 3.4. Heat capacity of zeolite 4A. •, experimental heat capacity and —, extrapolated value ($T < 100$ K) from equation (1.2.27), described in the text. The inset diagram indicates the difference between the experimental and fitted heat capacity data. See text for details.

From the chemical formula of the unit cell of zeolite 4A, it is clear that the major contribution to the heat capacity is from the optical modes while the heat capacity from acoustic modes is very small. From the Dulong-Petit value, it appears that about 75% of the maximum heat capacity has been achieved at 300 K.

The temperature dependence of the apparent Debye temperature, Θ_D, based on the conversion of the total heat capacity to the Debye model, equation (1.2.21), is shown in Figure 3.5. Like many other solid materials, the apparent Θ_D from zeolite 4A is a temperature-dependent function. Around $T = 42$ K, the apparent Θ_D has a minimum value of 363 K. It reaches a maximum value of 750 K at $T = 290$ K. Θ_D slightly decreases above $T = 300$ K, likely due to anharmonic vibrations of the lattice. The relatively high Θ_D explains why the heat capacity of zeolite 4A did not reach the Dulong–Petit value at room temperature.

3.2.3.2 Constituent Additivity

As discussed in Section 1.2.3, the Neumann-Kopp law is based on additivity of the properties of the elements to estimate heat capacity of a solid. Another approach, namely consideration of thermodynamic contributions from the "constituent groups" of a compound has been used with the considerable success to estimate heat capacity and other thermodynamic properties of complex inorganic compounds.[22,33,35,104,138]

For example, sodalite, ($Na_8Al_6Si_6O_{24}Cl_2$), can be considered to have the constituent compounds ($3Na_2O + 3Al_2O_3 + 6SiO_2 + 2NaCl$). The heat capacity of sodalite

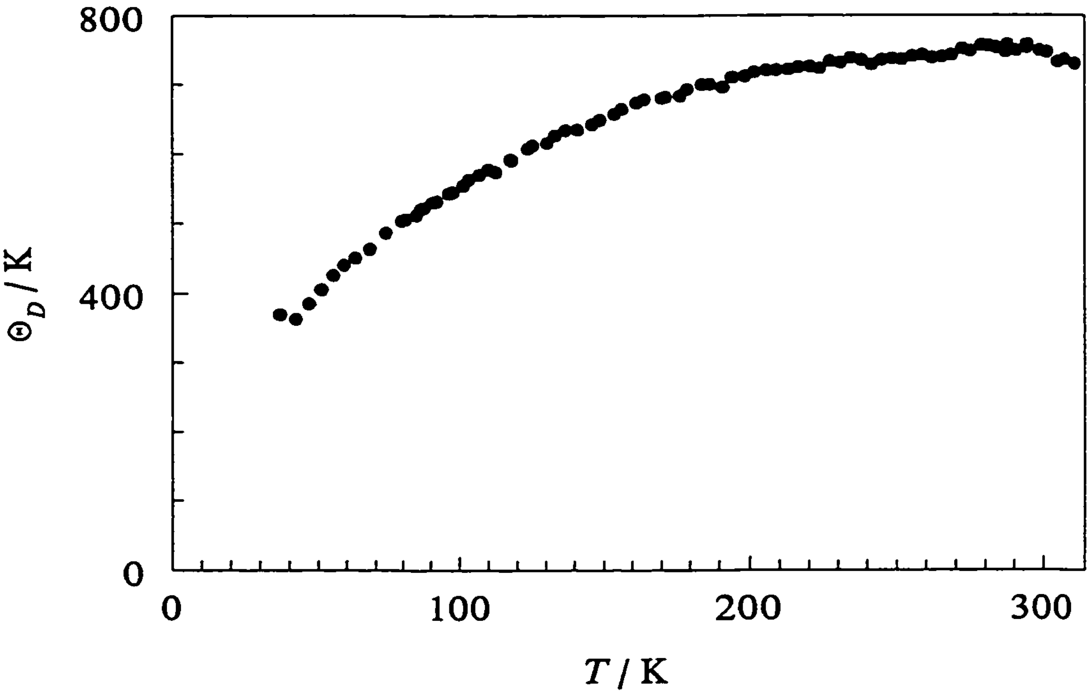

Figure 3.5. Apparent Debye temperature of zeolite 4A. It was calculated from overall experimental heat capacity based on the Debye model, equation (1.2.21), described in the text.

can be estimated from the contributions of its constituents, *i.e.* $C_P = \sum_i \nu_i C_{P,i}$ in which $C_{P,i}$ is the heat capacity of a constituent i and ν_i is the number of moles of the constituent compound i in sodalite. At 298.15 K, the calculated heat capacity of sodalite from those of constituents[154] is 815 J K^{-1} mol^{-1} while the Neumann-Kopp value is 1147 J K^{-1} mol^{-1}. The value from constituent additivity agrees well with the experimental value, 812 J K^{-1} mol^{-1},[138] and is much better than that from the Neumann-Kopp law. More examples can be found elsewhere.[22]

With similar methods, other thermodynamic functions, such as Gibbs energy of formation of many inorganic materials can also be estimated. For example, the Gibbs energies of formation of various zeolites at 298.15 K calculated from constituent additivity agree with experimental results usually within a deviation of 0.5%.[155]

Generally, the estimation of thermodynamic functions from constituent additivity methods works well, provide that: (1) the experimental data for the constituent solids are reliable, (2) the coordination within the constituent solids is similar to the complex solids and (3) there are no solid-solid phase transitions.[22]

Under favorable conditions, the reasonably accurate thermodynamic functions generally can be obtained. In this chapter, the constituent additivity method was used to estimate the Gibbs energies of formation of zeolite 4A, NaX and NaY at 298.15 K.

3.2.3.3 Thermodynamic Stability

The thermodynamic data allow an understanding of the relative contribution of enthalpy and entropy to the stability of zeolite 4A. To calculate the thermodynamic functions, the complete low-temperature C_P is required. As discussed in Section 3.1.2, ideally, if the full vibrational spectrum was known and correctly assigned, the optic contributions to the heat capacity could be calculated. However, reliable vibrational assignments are not available for zeolite 4A. Hence, a least-squares procedure was used to fit the low temperature (< 100 K) experimental data to equation (1.2.27) and extrapolate the heat capacity to $T = 0$ K, as shown in Figure 3.4. It is found that the best fit (generally within 1% of the experimental data) has a $m = 224$ and $n = 448$ with $\theta_D = 211$ K and $\theta_E = 528$ K. Thermodynamic function increments relative to 0 K were calculated from the heat capacity fit and are listed in Table 3.3.

Although Caullet *et al.*[156] reported $\Delta_f G^\circ$, the standard Gibbs energy of formation of zeolite 4A at 298.15 K from solubility studies, they were not able to obtain temperature-dependent data to determine $\Delta_f H^\circ$ or $\Delta_f S^\circ$. However, by using their data,[156] $\Delta_f G^\circ(\mathrm{Na_2Al_2Si_{2.12}O_{8.24}}) = -4078$ kJ mol^{-1} and $\Delta_f G^\circ(\mathrm{SiO_2})$,[155] and the assumption of constituent additivity, the value of $\Delta_f G^\circ$ $(\mathrm{Na_{96}Al_{96}Si_{96}O_{384}})$ was determined here to be $(-1.908 \pm 0.005)\times 10^5$ kJ mol^{-1}. From the present results for $S_T - S_0$ with the assumption that $S_0 = 0$, and the data for the constituent elements Al,[157] Si,[158] $\mathrm{O_2}$,[154,159] Na,[160] $\Delta_f S^\circ(\mathrm{Na_{96}Al_{96}Si_{96}O_{384}})$ has the value of (-35.80 ± 0.07) kJ K^{-1} mol^{-1}, which results in $\Delta_f H^\circ$ $(\mathrm{Na_{96}Al_{96}Si_{96}O_{384}}) = (-2.015 \pm 0.005)\times 10^5$ kJ mol^{-1}. The thermodynamic functions of formation of zeolite 4A below 300 K are listed in Table 3.4. From these data, it can be clearly found that the stability of zeolite 4A stems from enthalpic, not entropic

Table 3.3. Thermodynamic Functions (I) of Zeolite 4A, $Na_{96}Al_{96}Si_{96}O_{384}$.

T/K	C_P/J K^{-1} mol^{-1}	(H_T-H_0)/kJ mol^{-1}	(S_T-S_0)/J K^{-1} mol^{-1}	(G_T-G_0)/kJ mol^{-1}
5	4.83	0.0121	2.41	0.000
10	38.6	0.121	14.5	-0.024
15	130	0.542	45.8	-0.145
20	303	1.63	105	-0.482
25	562	3.79	200	-1.20
30	885	7.41	330	-2.48
35	1240	12.7	492	-4.50
40	1610	19.8	681	-7.39
45	1940	28.7	889	-11.3
50	2270	39.3	1110	-16.2
55	2570	51.4	1340	-22.3
60	2890	65.0	1580	-29.8
65	3180	80.2	1820	-38.1
70	3480	96.8	2070	-48.1
75	3780	115	2320	-59.0
80	4060	135	2570	-71.0
85	4360	156	2830	-85.0
90	4650	178	3080	-99.1
95	4930	202	3340	-115
100	5200	227	3600	-133
105	5460	254	3860	-151
110	5710	282	4120	-171
115	5960	311	4380	-193
120	6200	342	4640	-215
125	6440	373	4900	-239
130	6670	406	5160	-265
135	6900	440	5410	-291
140	7140	475	5670	-319
145	7370	511	5920	-347
150	7600	549	6170	-377
155	7810	587	6430	-409
160	8020	627	6680	-442

Continued...

Table 3.3. (continued).

T/K	C_P/J K^{-1} mol^{-1}	$(H_T\text{-}H_0)$/kJ mol^{-1}	$(S_T\text{-}S_0)$/J K^{-1} mol^{-1}	$(G_T\text{-}G_0)$/kJ mol^{-1}
165	8210	667	6930	-476
170	8400	709	7180	-512
175	8590	751	7420	-547
180	8790	795	7670	-586
185	8980	839	7910	-624
190	9160	885	8150	-664
195	9340	931	8390	-705
200	9510	978	8630	-748
205	9710	1030	8870	-788
210	9900	1080	9100	-831
215	10090	1125	9340	-883
220	10280	1176	9570	-929
225	10430	1228	9810	-979
230	10600	1280	10040	-1029
235	10760	1334	10270	-1079
240	10920	1388	10490	-1130
245	11070	1443	10720	-1183
250	11240	1499	10950	-1239
255	11370	1555	11170	-1293
260	11510	1612	11390	-1349
265	11640	1670	11610	-1407
270	11750	1729	11830	-1465
275	11860	1788	12050	-1526
280	11980	1847	12260	-1586
285	12110	1907	12480	-1650
290	12250	1968	12690	-1712
295	12400	2030	12900	-1776
298.15	12490	2069	13030	-1816
300	12550	2092	13110	-1841

Table 3.4. Thermodynamic Functions (II) of Zeolite 4A, $Na_{96}Al_{96}Si_{96}O_{384}$.

T/K	$\Delta_f H$/kJ mol^{-1}	$\Delta_f G$/kJ mol^{-1}	T/K	$\Delta_f H$/kJ mol^{-1}	$\Delta_f G$/kJ mol^{-1}
0	-200500	-200500	155	-201300	-195900
5	-200600	-200500	160	-201300	-195700
10	-200600	-200400	165	-201300	-195600
15	-200600	-200300	170	–201300	–195400
20	-200700	-200200	175	–201300	–195200
25	-200700	-200000	180	-201400	-195000
30	-200700	-199900	185	–201400	–194900
35	-200700	-199800	190	-201400	-194700
40	-200800	-199600	195	-201400	-194500
45	-200800	-199500	200	-201400	-194300
50	-200800	-199300	205	-201400	-194200
55	-200800	-199200	210	-201400	-194000
60	-200900	-199000	215	–201400	–193800
65	-200900	-198900	220	-201400	-193600
70	-200900	-198700	225	-201400	-193400
75	-201000	-198600	230	-201500	-193300
80	-201000	-198400	235	-201500	-193100
85	-201000	-198300	240	-201500	-192900
90	-201000	-198100	245	-201500	-192700
95	-201000	-197900	250	-201500	-192600
100	-201100	-197800	255	-201500	-192400
105	-201100	-197600	260	-201500	-192200
110	-201100	-197400	265	-201500	-192000
115	-201100	-197300	270	-201500	-191800
120	-201200	-197100	275	-201500	-191700
125	-201200	-196900	280	-201500	-191500
130	-201200	-196800	285	-201500	-191300
135	-201200	-196600	290	-201500	-191100
140	-201200	-196400	295	-201500	-191000
145	-201200	-196300	298.15	-201500	-190800
150	-201300	-196100	300	-201500	-190800

contributions. Indeed, the latter are destabilizing ($\Delta_f S^\circ < 0$). It is apparent that the thermodynamic stability of zeolite 4A is mainly from the strong T-O bonds of the primary building units.

3.2.3.4 $\Delta_f H^\circ$ of $NaAlSiO_4$ in Zeolites

Komada *et al.* [138] reported the standard enthalpy of formation of sodalite, which, as discussed above, can be considered to be the "parent structure" from which zeolite 4A is derived. To compare the enthalpy of formation of their common constituent $NaAlSiO_4$ at 298.15 K, the standard enthalpy of $NaAlSiO_4$ from sodalite can be calculated from:

$$2NaCl(s) + 6NaAlSiO_4(s) = Na_8Al_6Si_6O_{24}Cl_2(s), \qquad (3.2.1)$$

where the NaCl data is from the literature.[154] The result indicates that $\Delta_f H^\circ$ ($NaAlSiO_4$) from sodalite is -2106 kJ mol^{-1}, while $\Delta_f H^\circ$ ($NaAlSiO_4$) from zeolite 4A is -2099 kJ mol^{-1}. Robie *et al.*[161] reported that the standard enthalpy of formation of $\Delta_f H^\circ$($NaAlSiO_4$, crystal, nepheline) was -2092 kJ mol^{-1}. The values of $\Delta_f H^\circ$($NaAlSiO_4$) from the three considerations (zeolite 4A, sodalite and nepheline), deviate by only 0.3%. These rather remarkable results are understandable because all three of these materials are composed of similar TO_4 tetrahedral groups and all have the same cations in their structure. Hence, their T-O bonds have very similar strengths. In their studies of zeolitic silicas, Petrovic *et. al.*[162] found a similarly small range of differences in stability, only 4.9 kJ mol^{-1}, between the densest and least dense frameworks. These results indicate that enthalpy changes associated with zeolites have a rather weak dependence on their structure. The importance of this consideration is that materials scientists can use known values of thermodynamic functions to predict the stability of structures and the synthetic conditions for preparation of new zeolites and other framework materials.

3.2.4 Conclusions

The low-temperature heat capacities of zeolite 4A, $Na_{96}Al_{96}Si_{96}O_{384}$, below ambient temperature were determined by using an adiabatic calorimeter. The heat capacity of zeolite 4A is mainly from the optic modes due to its large number of atoms in the unit cell. At room temperature, about 75% of the maximum possible heat capacity is achieved. The apparent Debye temperature of zeolite 4A is a temperature-dependant function with a minimum of 363 K at $T = 42$ K and a maximum of 750 K at $T = 290$ K.

The standard thermodynamic functions below ambient temperature were derived from the heat capacity. At $T = 298.15$ K, C_P, $S_T - S_0$, $\Delta_f H$, $\Delta_f G$ of zeolite 4A are 1.249×10^4 J K^{-1} mol^{-1}, 1.303×10^4 J K^{-1} mol^{-1}, -2.015×10^5 kJ mol^{-1} and -1.908×10^5 kJ mol^{-1}, respectively. From these data, it is found that zeolite 4A is enthalpically stabilized, as are several other zeolitic materials.[137,141-143] It is found that the enthalpy of formation of $NaAlSiO_4$ in zeolite 4A is -2099 kJ mol^{-1} which agrees within 0.3% with those values obtained from sodalite and nepheline. It is concluded that the thermodynamic stability of zeolite 4A results from the strong T-O bonds in the primary building units, with bond strengths very close to those in similar materials.

3.3 Thermal and Thermodynamic Properties of Zeolite NaX

3.3.1 Structure

Zeolite NaX (also called zeolite X, NaX, Linde X) is an analogue of the natural zeolite faujasite. The unit cell of zeolite X can be considered to be built up by tetrahedrally connecting the β-cages through hexagonal prisms, creating a large three-dimensional supercage with a diameter of 13Å and a three-dimensional channel with a diameter of 7.5 Å,[163-165] shown in Figure 3.6. There are eight sodalite cages and eight supercages in each unit cell of NaX.[166] This framework topology gives NaX a more open structure than that of zeolite 4A (Linde A). Unlike zeolite 4A in which the Si/Al ratio is close to 1, the typical Si/Al ratio in NaX varies from 1.1 to 1.5. When Si/Al = 1, the SiO_4 and AlO_4 terahedra alternate as required by the Löwenstein law and the framework of NaX has long-range order with space group *Fd*3.[163] However, if the Si/Al ratio is greater than one, the long-range order may be lost and the space group changes to *Fd3m.*[167] The crystalline structure of NaX has been determined by X-ray diffraction[163,167] and neutron diffraction.[168] The lattice parameter of the cubic unit cell ranges from 24.80 Å to 25.10 Å, depending on the Si/Al ratio and the temperature. The T-O bond length ranges from 1.619 Å to 1.722 Å and the average O-T-O bond angle[168] is 109.5°. Sodium ions can occupy several nonequivalent positions in the framework.[167-169]

3.3.2 Experimental Methods and Characterization

Zeolite NaX (molecular sieve 13X or Linde X) powder was purchased from Aldrich Chemical Company. It was dehydrated in a quartz tube under vacuum conditions

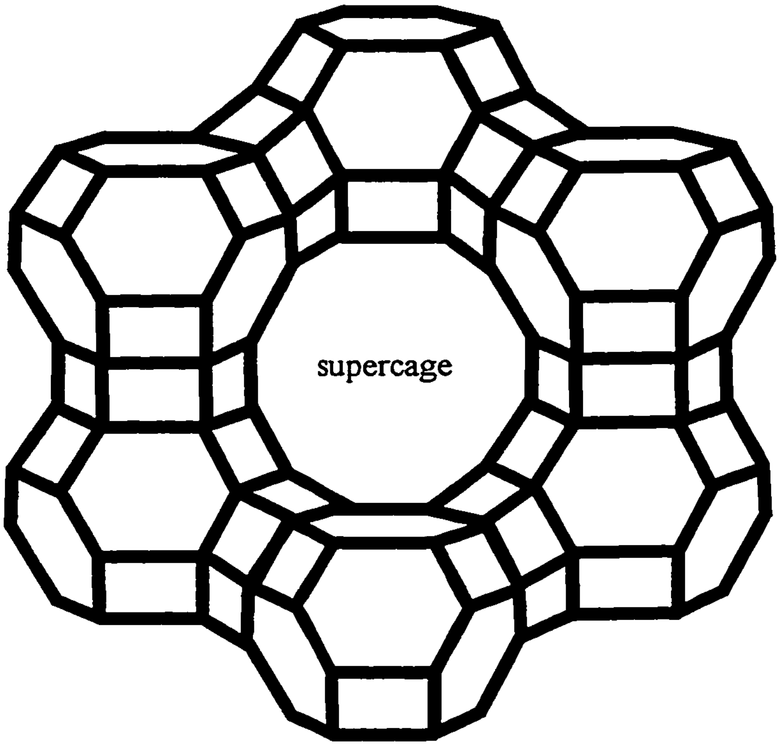

Figure 3.6. Framework of zeolite NaX and of faujasite. The unit cell is constructed by connecting the sodalite cages through hexagonal prisms, creating a three dimensional supercage 13 Å in diameter.

for 24 hours at 673 K and sealed at room temperature. The dehydration was examined by DSC between 300 and 670 K with a scanning rate of 5 K min^{-1}. DSC did not find detectable peaks, indicating the dehydration was complete to better than 0.1% water.

Powder X-ray diffraction was used to determine the lattice parameter of the unit cell at 298 K as for zeolite 4A. X-ray diffraction showed that NaX is a well-defined crystalline material with cubic lattice parameter of 24.7701(1) Å. It was confirmed that NaX dehydrated at 673 K has the same pattern as the sample before heating.[170]

To determine the composition of NaX about 1 g of sample was analyzed by X-ray fluorescence. The contents of constituent oxides in NaX are listed in Table 3.5. The dehydrated NaX has a Si/Al mole ratio of 1.207 ± 0.001, which agrees with that from chemical and solid-state NMR analysis.[171] The uncertainty is estimated from two runs. The unit cell of NaX is considered to have the ideal chemical formula, $Na_{87}Al_{87}Si_{105}O_{384}$. Hence, there are total 192 T-atoms in the unit cell of NaX.

The dehydrated sample of 2.908 g was loaded with the same procedure as discussed for zeolite 4A. The heat capacity was determined for the temperature range 33 to 310 K by the automated adiabatic calorimeter, described in Section 2.3.

3.3.3 Results and Discussion

3.3.3.1 Heat Capacity

The experimental heat capacities of NaX increase smoothly with temperature and are shown in Table 3.6 and Figure 3.7. The heat capacity of the sample comprised about 25% of the total (sample + calorimeter vessel) heat capacity at room temperature and

Table 3.5. X-ray Fluorescence Analysis of Components in NaX.

Components	mass%(exp.)	mass%(theor.)**
SiO_2	47.1±0.1	46.9
TiO_2	0.03±0.00	
Al_2O_3	33.1±0.0	33.0
Fe_2O_3	0.04±0.01	
MgO	0.05±0.00	
CaO	0.09±0.00	
Na_2O	19.4±0.1	20.0
K_2O	0.17±0.00	
P_2O_5	0.01±0.00	

* The mass%(exp.) is the average value of two runs. The deviation is estimated from the two runs.

** The mass%(theor.) is based on the ideal formula $Na_{87}Al_{87}Si_{105}O_{384}$.

Table 3.6. Experimental Heat Capacity of NaX, $Na_{87}Al_{87}Si_{105}O_{384}$.

T/K	C_P/J K^{-1} g^{-1}	T/K	C_P/J K^{-1} g^{-1}	T/K	C_P/J K^{-1} g^{-1}
33.70	0.0653	122.16	0.432	212.38	0.687
37.14	0.0830	125.38	0.436	215.47	0.691
39.44	0.100	127.60	0.446	219.27	0.704
43.13	0.118	131.57	0.471	222.36	0.709
48.55	0.127	133.11	0.471	226.31	0.718
53.94	0.146	137.00	0.492	229.38	0.722
54.01	0.151	139.59	0.495	233.31	0.729
59.18	0.178	143.42	0.515	236.35	0.731
64.43	0.194	147.21	0.516	240.40	0.753
69.70	0.215	150.90	0.530	243.33	0.755
74.94	0.240	154.71	0.534	247.48	0.768
80.27	0.259	158.26	0.546	254.39	0.777
84.16	0.287	162.18	0.556	257.70	0.785
86.50	0.289	165.63	0.570	262.21	0.789
87.92	0.303	169.66	0.578	265.26	0.793
91.89	0.316	172.91	0.595	270.92	0.801
93.28	0.320	176.98	0.601	273.63	0.813
97.33	0.330	180.15	0.609	278.83	0.822
98.59	0.351	184.24	0.615	282.13	0.825
103.88	0.364	187.55	0.632	287.09	0.838
105.79	0.367	191.58	0.635	290.87	0.852
109.26	0.387	194.79	0.646	295.39	0.853
111.24	0.392	198.74	0.647	298.86	0.858
114.69	0.410	201.89	0.668	303.86	0.858
116.72	0.411	205.87	0.673	307.04	0.869
120.14	0.428	208.66	0.678	312.27	0.879

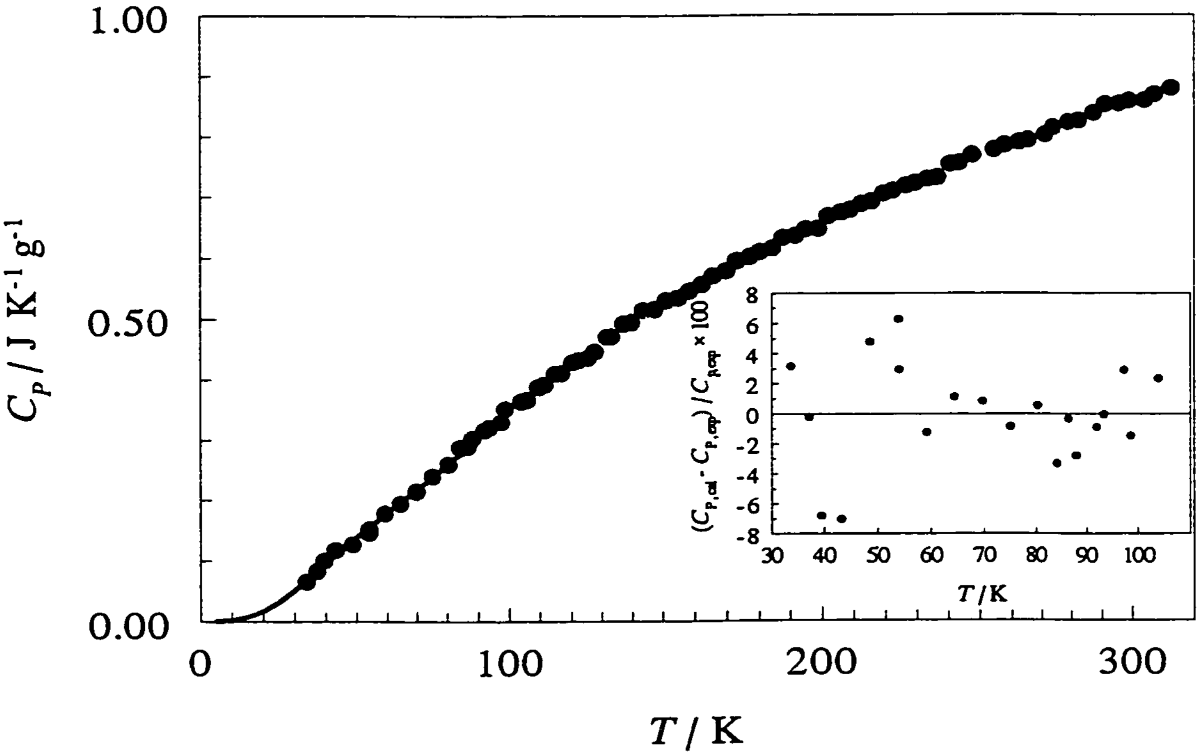

Figure 3.7. Heat capacity of zeolite NaX. ●, Experimental heat capacity and —, extrapolation result from equation (1.2.27), as discussed in the text. The inset diagram indicates the difference between the experimental and fitted heat capacity data.

15% at 35 K. This appears to be the first determination of heat capacity of NaX.

To calculate the physically more interesting heat capacity C_V from C_P, the value $C_P - C_V$ was estimated from equation (1.2.5). The thermal expansion coefficient of NaX was derived from the experimental lattice parameters (unit in Å) between 44 K and 293 K[121] by least squares fitting a polynomial equation:

$$a = a_0 + a_1 T + a_2 T^2 + a_3 T^2 + a_4 T^3 \tag{3.2}$$

where the fitted parameters are $a_0 = 24.8081$, $a_1 = -2.4 \times 10^{-5}$, $a_2 = -4.96 \times 10^{-7}$, $a_3 = 2.73 \times 10^{-9}$, $a_4 = -3.73 \times 10^{-12}$. The results are shown in Figure 3.8. At 298.15, the thermal expansion is estimated to be $(1.8 \pm 0.6) \times 10^{-6}$ K. The uncertainty is estimated from the error of the experimental lattice parameter.

The bulk modulus, K, of NaX has not been reported yet. Since NaX and zeolite 4A have very similar frameworks, K for zeolite 4A, 22 ± 2 GPa,[153] was used to estimate $C_P - C_V$ for NaX. At 300 K, $(C_P - C_V)/C_P$ for NaX is 0.00006 and $C_P \approx C_V$ is used, hereafter.

It is interesting to compare the experimental heat capacity with the Dulong-Petit value 663x3R. About 70% of the total heat capacity is achieved at 298.15 K. This value is 5% lower than that of zeolite 4A at same temperature, likely due to the higher Si/Al ratio in NaX and more Si-O bonds, which vibrate at a higher frequency than Al-O bonds.

The apparent Debye temperature, Θ_D, for NaX, calculated from the total heat capacity, is presented in Figure 3.9. It is a temperature dependent function. At room

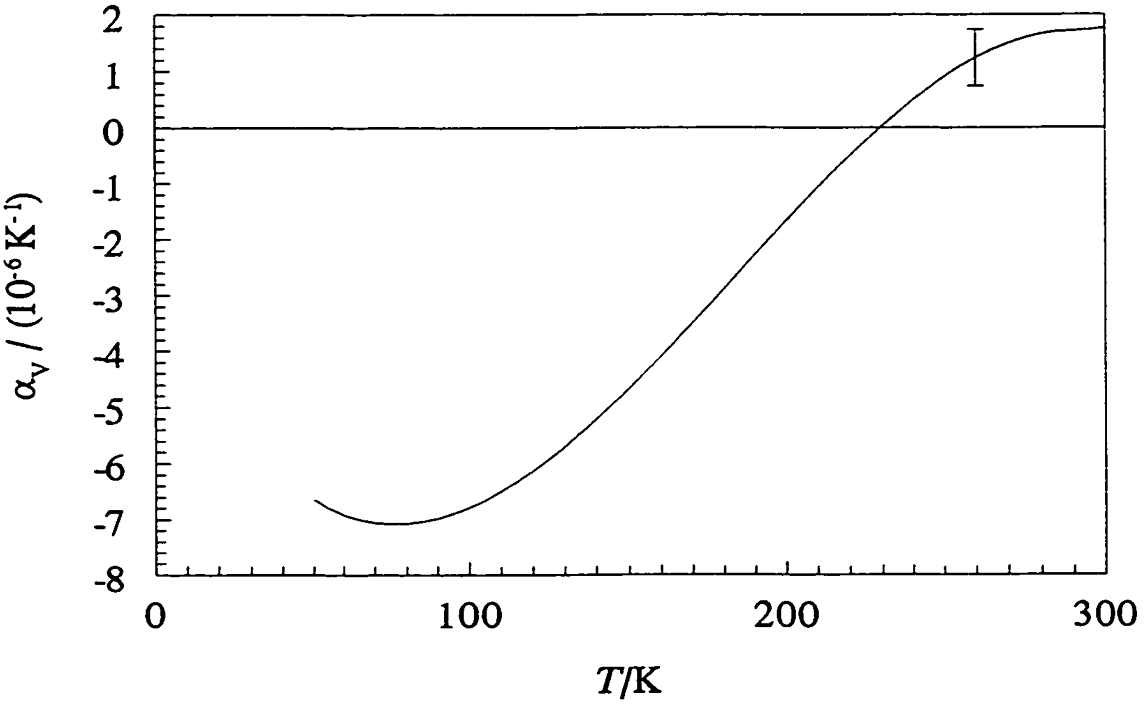

Figure 3.8. Volume thermal expansion coefficient of NaX, calculated from experimental lattice parameters[121] by fitting equation (3.7.1), as described in the text. The error bar indicates the uncertainty in α_v, based on the error of the lattice parameter.

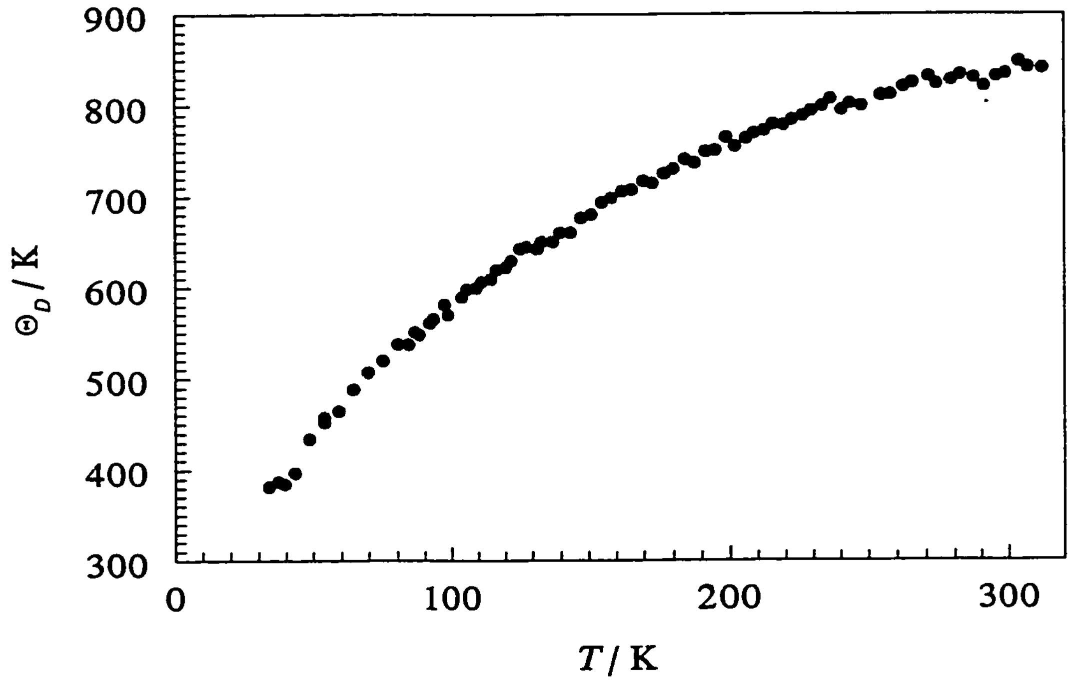

Figure 3.9. Apparent Debye temperature of zeolite NaX, calculated from the overall experimental heat capacity and the Debye model equation (1.2.21).

temperature, the apparent Θ_D reaches a maximum value of 840 K. NaX has a higher maximum apparent Θ_D and hence a lower heat capacity than zeolite 4A at 300 K.

Due to the large number of atoms in the unit cell (663) of NaX it is evident that the heat capacity contribution from the acoustic modes is small compared to the overall heat capacity. This means that there are some low-frequency optic modes which are excited even at very low temperatures. The energy of weakly dispersive optic modes can be approximately described with the equation,[14] $\omega_A \propto (k_f / m_A)^{1/2}$, where ω_A is the wave number, k_f is the interatomic force constant and m_A is the atomic mass. In NaX, the oxygen atom has the smallest atomic mass and is the most likely to be excited at low temperature. The low-energy modes can be the transverse motions of oxygen atoms in Si-O-Si and Al-O-Si, which have lower energy than longitudinal modes and hence are easier to vibrate at low temperatures. This factor is important in the next section.

3.3.3.2 Grüneisen Parameter

The Grüneisen parameter is important to understand the abnormal negative thermal expansion of NaX at low temperatures. It has been known since the late 1950s that the transverse modes can result in the negative thermal expansion of solids.[172,173] These modes are shown for T-O-T in Figure 3.10. From equation (1.5.3), the sign of the thermal expansion coefficient is always the same as that of the Grüneisen parameter, which is associated with the vibrational modes through equation (1.5.1) and (1.5.2). Below 220 K, the low-frequency transverse vibrations of oxygen atoms might dominate the overall Grüneisen parameter and their frequencies could decrease as the volume

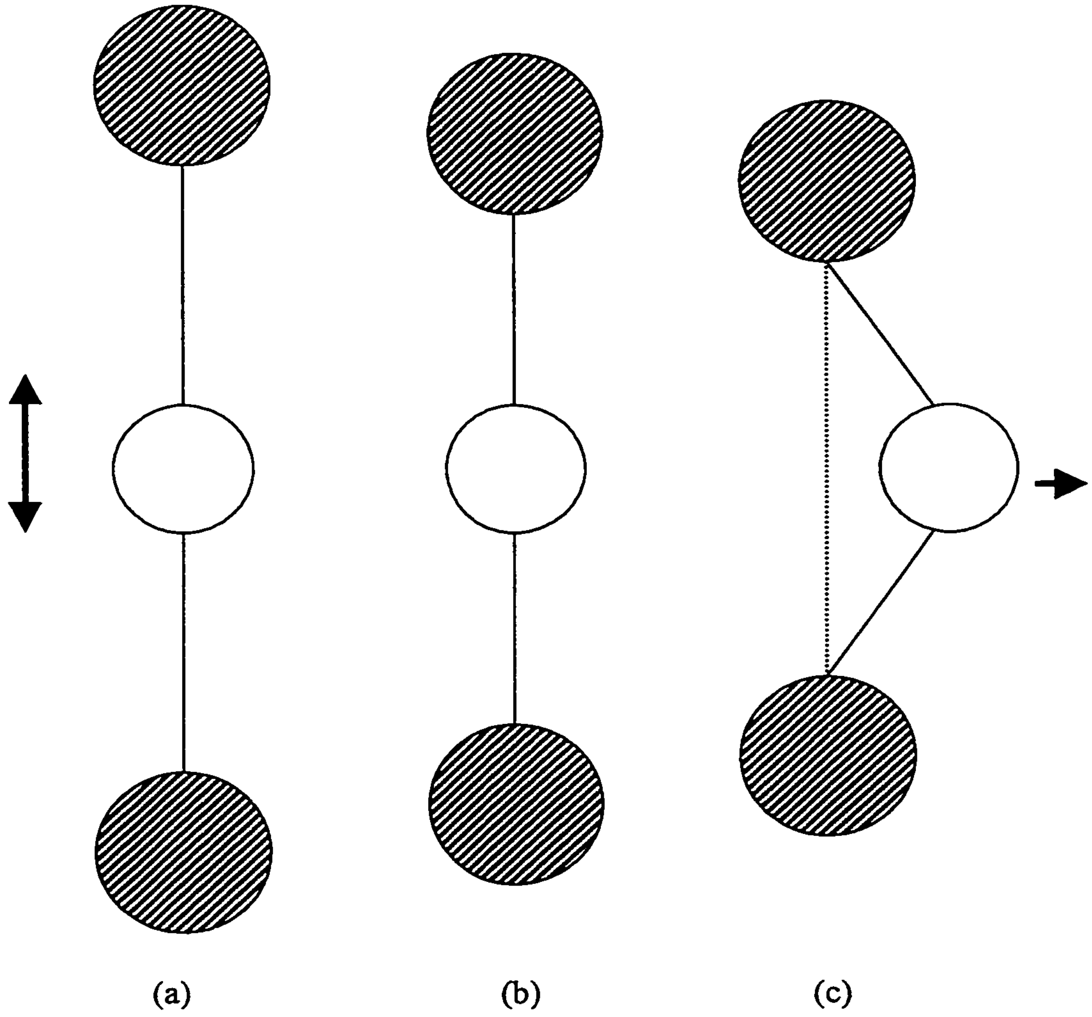

Figure 3.10. Vibrational modes in T-O-T bonds: (a) longitudinal vibration, resulting in the expansion of lattice; (b) equilibrium state; (c) transverse vibration resulting in the contraction of the lattice on excitation.

decreases. The overall Grüneisen parameter would be negative and the lattice would contract on heating. This is observed for NaX at low temperature (Figure 3.8).

As the temperature increases above 220 K, the high-energy longitudinal modes that tend to expand the lattice could dominate the overall Grüneisen parameter and positive thermal expansion would result, as observed for NaX in Figure 3.8.

With the thermal expansion coefficient, bulk modulus of zeolite 4A[153] and present heat capacity, the overall Grüneisen parameter of NaX was estimated from equation (1.5.3) and it is presented in Figure 3.11. Although the approximation concerning the bulk modulus can result in uncertainty of the Grüneisen parameter, the most uncertain quantity is the thermal expansion coefficient. Nevertheless, the estimated Grüneisen parameter still can provide information about the anharmonicity of the lattice vibrations. The result is shown in Figure 3.11. (The uncertainty of the Grüneisen parameter is estimated to be 0.03 independent of temperature). The relative small Grüneisen parameter, especially around room temperature, indicates that NaX has a rather stiff lattice which is important for its applications such as in ion exchange and catalysis.

Since the framework of NaX can be constructed from sodalite, it is helpful to compare the overall Grüneisen parameter of these framework materials. The thermal properties (thermal expansion,[121] heat capacity[138] and compressibility[153]) of sodalite have been studied thoroughly. From these data, the derived Grüneisen parameter is 1.0 ± 0.2 at 300 K, higher than that of NaX due to the larger thermal expansion of sodalite.

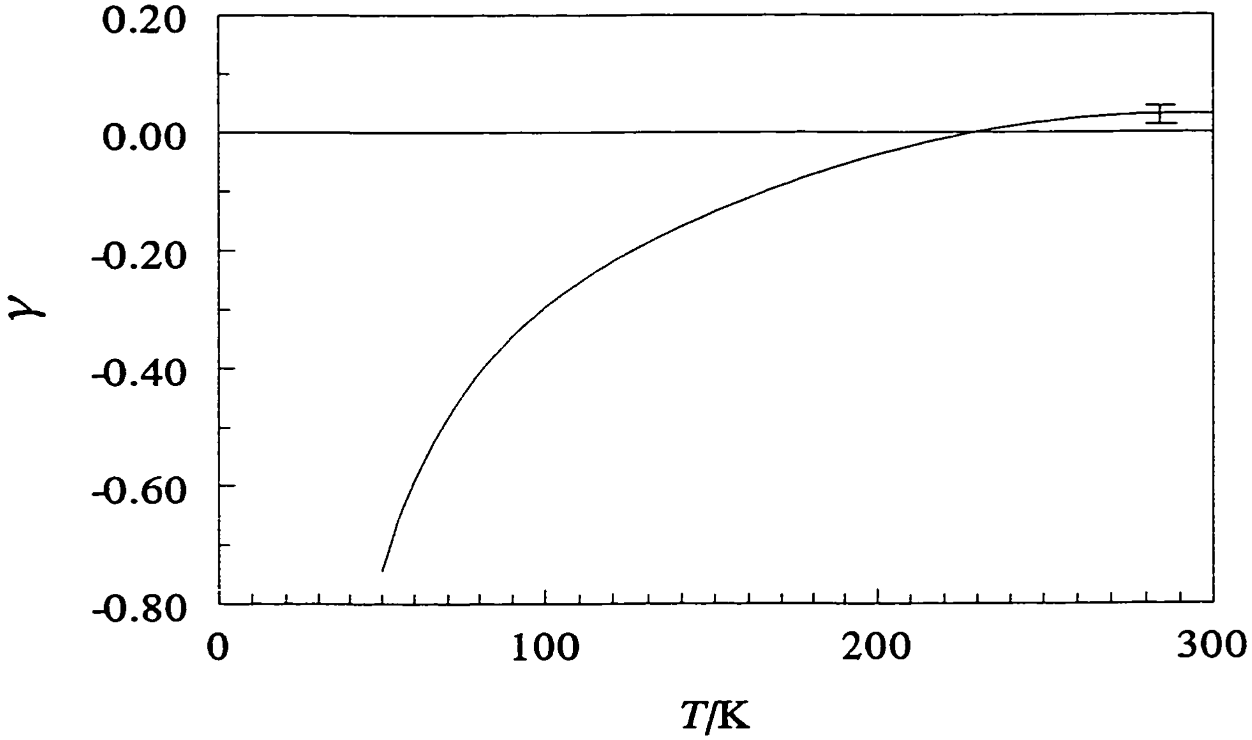

Figure 3.11. Grüneisen parameter of NaX, derived from the lattice parameter,[121] compressibility of zeolite 4A[153] and present heat capacity. The error bar indicates the uncertainty of γ, as discussed in the text.

3.3.3.3 Thermodynamic Stability

Thermodynamic properties are necessary to understand the stability of NaX. They require complete heat capacity data below room temperature. Reliable vibrational assignments and elastic properties of NaX are not available. Hence, the Debye model and Einstein model were used to fit experimental data below 100 K through equation (1.2.27). The least-square fitting parameters were found to be $\theta_D = 227 \pm 2$ K, $\theta_E = 579 \pm 5$ K, m = 166 and n = 497 with fitting error of 2.5%. ^{23}Na NMR showed that θ_D of NaX is 250 ± 20 K.[174] The result is quite close to the value from the heat capacity. The heat capacities below 35 K were derived from the extrapolation of equation (1.2.27). Other thermodynamic function increments relative to 0 K were calculated from the heat capacity. They are listed in Table 3.7.

Although the standard Gibbs energy of formation of NaX has been determined from solubility studies[156] at 298.15 K, the data do not allow calculation of enthalpy of formation, $\Delta_f H^\circ$ and entropy of formation, $\Delta_f S^\circ$. From the experimental value[156] of Gibbs energy of formation of NaX with an empirical chemical formula, $Na_2Al_2Si_{2.48}O_{8.96}$, $\Delta_f G^\circ(Na_2Al_2Si_{2.48}O_{8.96})$ = - 4392 kJ mol^{-1} and $\Delta_f G^\circ(SiO_2)$[155] combined with the assumption of constituent additivity, the Gibbs energy of NaX with a chemical formula $Na_{87}Al_{87}Si_{105}O_{384}$, $\Delta_f G^\circ[Na_{87}Al_{87}Si_{105}O_{384}] = (-1.886 \pm 0.002) \times 10^5$ kJ mol^{-1} was obtained. With the assumption of $S_0 = 0$ and the absolute entropy, $S_T - S_0$, determined from the heat capacity of NaX and the entropies of the elements at 298.15 K,[154,155,157-160] the entropy of formation and enthalpy of formation of NaX are $\Delta_f S^\circ[Na_{87}Al_{87}Si_{105}O_{384}]$ = -36.53 ± 0.06 kJ K^{-1} mol^{-1} and $\Delta_f H^\circ[Na_{87}Al_{87}Si_{105}O_{384}] = (-1.995 \pm 0.002) \times 10^5$ kJ mol^{-1},

Table 3.7. Thermodynamic Functions (I) of NaX, $Na_{87}Al_{87}Si_{105}O_{384}$.

T/K	C_P/J K^{-1} mol^{-1}	(H_T-H_0)/kJ mol^{-1}	(S_T-S_0)/J K^{-1} mol^{-1}	(G_T-G_0)/kJ mol^{-1}
5	3.63	0.00906	1.81	0.000
10	29.0	0.0906	10.9	-0.018
15	97.8	0.408	34.4	-0.108
20	229	1.23	79.4	-0.362
25	431	2.88	151	-0.903
30	689	5.67	252	-1.88
35	979	9.84	379	-3.42
40	1280	15.5	529	-5.66
45	1540	22.6	695	-8.71
50	1810	30.9	871	-12.6
55	2090	40.7	1060	-17.6
60	2380	51.9	1250	-23.1
65	2670	64.5	1450	-29.8
70	2960	78.6	1660	-37.6
75	3260	94.1	1880	-46.9
80	3550	111	2100	-56.9
85	3840	130	2320	-67.6
90	4120	150	2550	-80.0
95	4400	171	2780	-93.3
100	4680	194	3010	-108
105	4950	218	3240	-123
110	5210	243	3480	-140
115	5470	270	3720	-158
120	5710	298	3960	-178
125	5960	327	4190	-197
130	6190	357	4430	-219
135	6420	389	4670	-242
140	6640	421	4910	-266
145	6850	455	5140	-290
150	7060	490	5380	-317
155	7260	526	5610	-344
160	7460	562	5850	-374

Continued...

Table 3.7. (continued).

T/K	C_P/J K^{-1} mol^{-1}	$(H_T\text{-}H_0)$/kJ mol^{-1}	$(S_T\text{-}S_0)$/J K^{-1} mol^{-1}	$(G_T\text{-}G_0)$/kJ mol^{-1}
165	7640	600	6080	-403
170	7830	639	6310	-434
175	8010	678	6540	-466
180	8180	719	6770	-500
185	8350	760	6990	-533
190	8520	802	7220	-570
195	8680	845	7440	-606
200	8840	889	7660	-643
205	9000	934	7890	-684
210	9150	979	8100	-722
215	9300	1025	8320	-764
220	9450	1072	8540	-807
225	9600	1120	8750	-849
230	9740	1168	8960	-893
235	9890	1217	9170	-938
240	10030	1267	9380	-984
245	10170	1317	9590	-1033
250	10300	1369	9800	-1081
255	10440	1420	10000	-1130
260	10570	1473	10210	-1182
265	10700	1526	10410	-1233
270	10830	1580	10610	-1285
275	10960	1634	10810	-1339
280	11080	1689	11010	-1394
285	11200	1745	11210	-1450
290	11320	1801	11400	-1505
295	11430	1858	11600	-1564
298.15	11500	1894	11720	-1600
300	11540	1916	11790	-1621

respectively. These data were used to calculate the standard thermodynamic functions of formation of NaX below ambient temperatures, as listed in the Table 3.8. Comparing the enthalpy and entropy of formation of NaX, it can be concluded that the thermal stability of NaX is from the enthalpy contribution, $\Delta_f H^o$, while the entropy term, $T\Delta_f S^o$, slightly decreases the thermodynamic stability of NaX. The high thermal stability of NaX is a consequence of strong T-O bonds of the primary building units. Similar results have been obtained in considering zeolite 4A.

3.3.4 Conclusions

The heat capacities of zeolite NaX with chemical formula $Na_{87}Al_{87}Si_{105}O_{384}$ were determined from 33 to 310 K by an automatic adiabatic calorimeter. About 70% of the maximum heat capacity of NaX is achieved at room temperature, 5% lower than that of zeolite 4A. The heat capacity of NaX mainly comes from the contribution of optic modes because of the large number of atoms in the unit cell. The apparent Debye temperature is a temperature dependent function and is approximately 840 K at $T = 300$K.

The standard thermodynamic functions of formation of NaX from $T = 0$ to 300 K were calculated. At 298.15 K, C_P and $S_T - S_0$ are 1.150×10^4 J K^{-1}mol^{-1} and 1.172×10^4 J K^{-1}mol^{-1}; $\Delta_f H$ and $\Delta_f G$ are -1.995×10^5 kJ mol^{-1} and -1.886×10^5 kJ mol^{-1}, respectively. The high thermal stability of NaX is due to the large dissociation energy of the T-O bonds.

The negative thermal expansion of NaX might be due to the domination of the low-energy transverse motions of the oxygen atoms in T-O-T bonds. The small

Table 3.8. Thermodynamic Functions (II) of NaX, $Na_{87}Al_{87}Si_{105}O_{384}$.

T/K	$\Delta_f H$/kJ mol^{-1}	$\Delta_f G$/kJ mol^{-1}	T/K	$\Delta_f H$/kJ mol^{-1}	$\Delta_f G$/kJ mol^{-1}
0	-198400	-198400	155	-199200	-193700
5	-198400	-198400	160	-199200	-193600
10	-198500	-198300	165	-199200	-193400
15	-198500	-198200	170	-199200	–193200
20	-198500	-198000	175	-199300	–193000
25	-198600	-197900	180	-199300	-192900
30	-198600	-197800	185	-199300	–192700
35	-198600	-197600	190	-199300	-192500
40	-198600	-197500	195	-199300	-192300
45	-198700	-197400	200	-199300	-192100
50	-198700	-197200	205	-199300	-192000
55	-198700	-197100	210	-199300	-191800
60	-198800	-196900	215	-199400	–191600
65	-198800	-196800	220	-199400	-191400
70	-198800	-196600	225	-199400	-191200
75	-198800	-196400	230	-199400	-191100
80	-198900	-196300	235	-199400	-190900
85	-198900	-196100	240	-199400	-190700
90	-198900	-196000	245	-199400	-190500
95	-198900	-195800	250	-199400	-190300
100	-199000	-195600	255	-199400	-190200
105	-199000	-195500	260	-199400	-190000
110	-199000	-195300	265	-199400	-189800
115	-199000	-195100	270	-199500	-189600
120	-199100	-195000	275	-199500	-189400
125	-199100	-194800	280	-199500	-189300
130	-199100	-194600	285	-199500	-189100
135	-199100	-194400	290	-199500	-188900
140	-199100	-194300	295	-199500	-188700
145	-199200	-194100	298.15	-199500	-188600
150	-199200	-193900	300	-199500	-188500

Grüneisen parameter indicates that NaX has a very stiff lattice which is important to its applications.

3.4 Thermodynamic Properties of Zeolite NaY

3.4.1 Structure

Zeolite Y has the same framework topology as the natural zeolite faujasite and zeolite X, shown in Figure 3.6. The Si/Al ratio and hence the numbers of cations in the unit cell of synthetic zeolite Y vary from sample to sample. The difference between zeolite Y and zeolite X is that the former has a higher Si/Al ratio, typically in the range of 1.5 ~ 3.0 and the latter has Si/Al ratio ranging from 1.1 to 1.5. Thus, zeolite Y has fewer exchangeable cations. The structure of dehydrated sodium zeolite Y (NaY) has been investigated by many researchers.[170,175-177] It displays a cubic crystalline structure with space group $Fd\bar{3}m$. The lattice parameter of NaY ranges from 24.60 Å to 25.12 Å, depending on the Si/Al ratio.[179] The average O-T-O angle is around 109° and the T-O bond length varies between 1.64 and 1.70 Å.[170,177,180] Like zeolite X, the framework of NaY is composed of β-cages that are connected together through a tetrahedral arrangement of hexagonal prisms, which result in supercages with a diameter of about 13 Å and three-dimensional channels with a diameter of 7.5 Å.[170]

3.4.2 Experimental Methods and Characterization

The NaY (molecular sieve Y) powder was purchased from Aldrich Chemical Company. The dehydration procedure, analysis of compositions and lattice parameter determination of the sample were the same as for NaX (Section 3.3.2).

DSC was run between 300 K and 670 K and it did not shown any detectable peaks due to water in NaY. X-ray diffraction showed that NaY is well-defined crystalline solid with a lattice parameter of 24.6609(5) Å.

The compositions of oxides in NaY are listed in Table 3.9. The Si/Al mole ratio is 2.65 ± 0.02 which agrees well with that from chemical and solid-state NMR analysis.[171] The uncertainty is estimated from two runs. The unit cell of NaY is considered to have the ideal chemical formula $Na_{53}Al_{53}Si_{139}O_{384}$.

The dehydrated sample of 2.062 g was loaded in the calorimeter as for zeolite 4A (Section 3.2.2). The heat capacity was determined in the temperature range 30 K to 300 K. The measurement of heat capacity was carried out by the automated adiabatic calorimeter as described in Section 2.3.

3.4.3 Results and Discussion

3.4.3.1 Heat Capacity

The heat capacity of NaY increases monotonically with temperature and is shown in Table 3.10 and Figure 3.12. The heat capacity of the sample comprised of about 20% of the total (sample + calorimeter vessel) heat capacity at room temperature and 10% at 30 K. The heat capacity of NaY appears not to be determined previously.

To determine the heat capacity at constant volume from the heat capacity at constant pressure, the heat capacity difference was estimated from equation (1.2.5). The lattice parameters[176] at $T = 4$ and 298.15 K were used to estimate the thermal expansion

Table 3.9. X-ray Fluorescence Analysis of Compositions in NaY

Components	mass%(exp.)*	mass%(theor.)**
SiO_2	65.6±0.2	65.8
TiO_2	0.06±0.00	
Al_2O_3	21.0±0.1	21.3
Fe_2O_3	0.07±0.00	
MgO	0.10±0.00	
CaO	0.03±0.01	
Na_2O	13.1±0.2	12.9
K_2O	0.03±0.01	
P_2O_5	0.01±0.00	

* The mass%(exp.) and deviations were determined by two runs.

** The mass%(theor.) was calculated from the ideal formula $Na_{53}Al_{53}Si_{139}O_{384}$.

Table 3.10. Experimental Heat Capacity of NaY, $Na_{53}Al_{53}Si_{139}O_{384}$.

T/K	C_P/J K^{-1} g^{-1}	T/K	C_P/J K^{-1} g^{-1}	T/K	C_P/J K^{-1} g^{-1}
30.80	0.0405	124.50	0.383	215.04	0.616
35.94	0.0823	126.58	0.392	218.68	0.626
39.63	0.0924	130.21	0.407	222.43	0.637
43.71	0.107	132.16	0.409	226.05	0.642
48.47	0.119	136.87	0.422	229.77	0.657
53.13	0.131	138.77	0.431	233.37	0.660
54.34	0.137	144.68	0.447	236.98	0.666
57.72	0.151	146.53	0.458	240.53	0.668
62.24	0.172	152.50	0.468	244.05	0.684
67.45	0.193	154.33	0.471	247.60	0.686
73.03	0.203	158.24	0.486	251.01	0.688
78.59	0.223	160.30	0.492	254.41	0.695
84.15	0.248	162.03	0.489	257.97	0.697
88.71	0.270	168.04	0.506	261.21	0.702
89.72	0.274	169.67	0.512	265.94	0.710
94.32	0.284	175.71	0.526	268.10	0.719
96.38	0.292	177.36	0.535	268.47	0.719
101.24	0.314	183.40	0.547	274.69	0.725
103.54	0.320	185.00	0.552	275.51	0.727
107.47	0.333	191.06	0.566	282.25	0.742
109.70	0.348	192.56	0.563	283.49	0.746
109.80	0.343	194.42	0.564	289.86	0.752
113.17	0.358	198.66	0.574	291.98	0.762
115.39	0.363	203.96	0.590	298.54	0.781
118.83	0.372	206.10	0.597		
120.95	0.377	211.85	0.607		

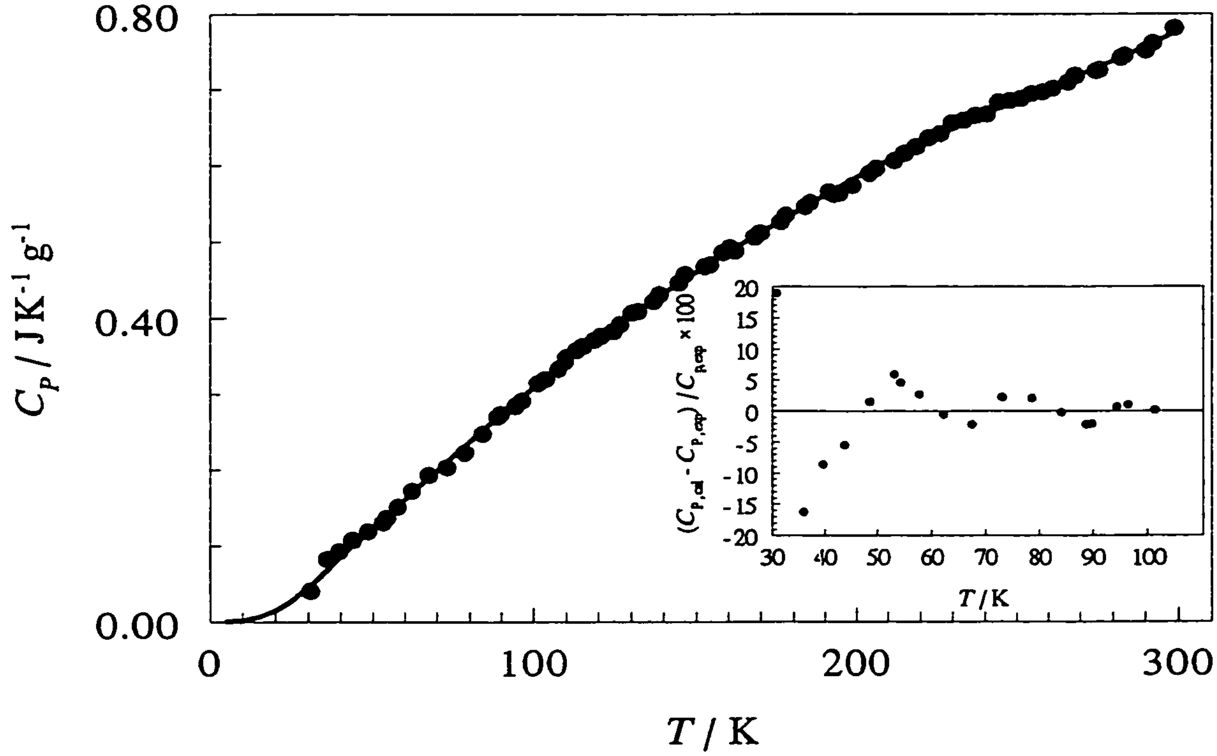

Figure 3.12. Heat capacity of NaY. ●, experimental heat capacity and —, extrapolated result (below 100 K) from equation (1.2.27), described in the text. The inset diagram indicates the difference between the experimental and fitted heat capacity data. See text for details.

coefficient for NaY. Due to the absence of experimental data, the bulk modulus, K = 22 GPa for zeolite 4A[153] was used. The calculated value of $(C_P - C_V)/C_P$ at 298.15 K is 0.003% of C_P and the approximation $C_P \approx C_V$ is used in the discussion hereafter.

There are 629 atoms in the ideal unit cell of NaY. The experimental heat capacity of NaY at 298.15 K is 63% of the Dulong-Petit value (629×3R). Comparing the heat capacity of zeolite 4A, NaX and NaY, heat capacities at 298.15 K decrease with the increasing Si/Al ratio, which indicates that the stronger Si-O bond requires higher energy (higher temperature) than the Al-O bond to achieve the same heat capacity.

Like zeolite NaX, the phonon spectrum of NaY is mainly composed of optic modes due to the large numbers of atoms in the unit cell. Hence, the low-energy optic modes are important to the heat capacity at low temperature.

The apparent Debye temperature calculated from total heat capacity at different temperatures, shown in Figure 3.13, displays a shape typical of solids. It has a minimum of Θ_D = 376 K at T = 35 K and reaches a maximum of 950 K at 273 K.

3.4.3.2 Thermodynamic Stability

Thermodynamic functions are important to understand the stability of NaY, which require complete heat capacity data. Due to the lack of reliable vibrational data and elastic properties of NaY to calculated heat capacity, equation (1.2.27) was used to fit the experimental data below 100 K through the least-squares procedure. The best fitting parameters were θ_D = 236 ± 3 K and θ_E = 629 ± 8 K with the coefficients m = 157 and n = 472. Igarashi *et al.*[174] reported a Debye temperature of 230 ± 20 K for NaY from

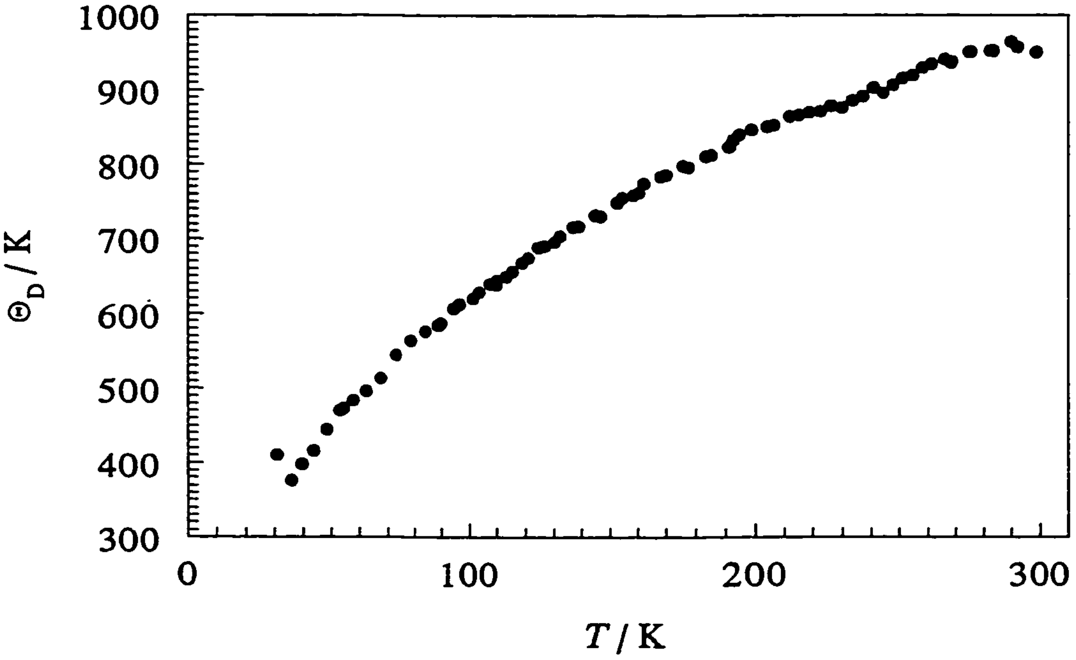

Figure 3.13. Apparent Debye temperature of NaY. It is derived from overall heat capacity and the Debye model, equation (1.2.21).

^{23}Na NMR spectroscopy which suggests that equation (1.2.27) reflects the low-temperature heat capacity well. The heat capacities below 30 K were derived from the extrapolation of equation (1.2.27), shown in Figure 3.12. The enthalpy increment, H_T-H_0, and entropy increment, $S_T - S_0$, were calculated from the heat capacity. They are listed in Table 3.11. At 298.15 K, the heat capacity, enthalpy and entropy of NaY relative to T = 0 K are 9.84×10^3 J K^{-1} mol^{-1}, 1.59×10^6 J mol^{-1} and 9.85×10^3 J K^{-1} mol^{-1}, respectively.

There are no complete low-temperature experimental thermodynamic functions available for NaY. The Gibbs energy of formation of NaY can be estimated from those of NaX[156] and SiO_2[155] with the assumption of constituent additivity. At 298.15 K, the Gibbs energy of formation of NaY is calculated to be $(-1.791 \pm 0.002)\times10^5$ kJ mol^{-1}. The entropy of formation is -38.44 ± 0.06 kJ K^{-1} mol^{-1}, which is calculated from the entropies of the elements[154,155,157–160] and the present entropy of NaY with the assumption $S_0 = 0$. These values were used to calculate the enthalpy of formation of NaY to be $(-1.906 \pm 0.002)\times10^5$ kJ mol^{-1}. The complete thermodynamic properties of NaY between T = 0 and 300 K are listed in Table 3.12. The results show that the thermodynamic stability of zeolite Y is mainly from the enthalpy term and not from entropy term. The latter actually makes a slightly negative contribution to the thermodynamic stability of zeolites.

3.4.4 Conclusions

The low-temperature heat capacity of NaY, $Na_{53}Al_{53}Si_{139}O_{384}$, was determined by an automatic adiabatic calorimeter from 30 to 300 K. The heat capacity of NaY mainly

Table 3.11. Thermodynamic Functions (I) of NaY, $Na_{53}Al_{53}Si_{139}O_{384}$.

T/K	C_P/J K^{-1} mol^{-1}	(H_T-H_0)/kJ mol^{-1}	(S_T-S_0)/J K^{-1} mol^{-1}	(G_T-G_0)/kJ mol^{-1}
5	2.90	0.00724	1.45	0.000
10	23.2	0.0724	8.69	-0.015
15	78.2	0.326	27.5	-0.087
20	184	0.981	63.5	-0.290
25	349	2.31	121	-0.721
30	566	4.60	204	-1.51
35	818	8.07	309	-2.76
40	1090	12.9	436	-4.59
45	1320	18.9	578	-7.12
50	1560	26.1	729	-10.4
55	1800	34.5	889	-14.4
60	2040	44.1	1060	-19.5
65	2290	54.9	1230	-25.0
70	2530	66.9	1410	-31.8
75	2770	80.2	1590	-39.1
80	3010	94.6	1780	-47.8
85	3240	110	1970	-57.2
90	3470	127	2160	-67.4
95	3700	145	2350	-78.3
100	3920	164	2550	-91.0
105	4130	184	2740	-104
110	4340	205	2940	-118
115	4550	228	3140	-134
120	4740	251	3340	-150
125	4940	275	3530	-166
130	5130	300	3730	-185
135	5320	326	3930	-204
140	5500	353	4120	-224
145	5670	381	4320	-245
150	5850	410	4520	-268
155	6020	440	4710	-290
160	6190	470	4900	-314

Continued...

Table 3.11. (continued).

T/K	C_P/J K^{-1} mol^{-1}	(H_T-H_0)/kJ mol^{-1}	(S_T-S_0)/J K^{-1} mol^{-1}	(G_T-G_0)/kJ mol^{-1}
165	6350	502	5100	-340
170	6510	534	5290	-366
175	6670	567	5480	-392
180	6830	600	5670	-420
185	6980	635	5860	-449
190	7140	670	6050	-479
195	7280	706	6230	-509
200	7430	743	6420	-541
205	7570	781	6610	-574
210	7710	819	6790	-607
215	7850	858	6970	-641
220	7980	897	7150	-676
225	8110	938	7340	-714
230	8240	978	7520	-751
235	8360	1020	7690	-787
240	8480	1060	7870	-829
245	8600	1110	8050	-862
250	8710	1150	8220	-905
255	8820	1190	8400	-952
260	8930	1240	8570	-988
265	9040	1280	8740	-1040
270	9150	1330	8910	-1080
275	9260	1370	9080	-1130
280	9370	1420	9250	-1170
285	9490	1470	9410	-1210
290	9610	1510	9580	-1270
295	9750	1560	9740	-1310
298.15	9840	1590	9850	-1350
300	9890	1610	9910	-1360

Table 3.12. Thermodynamic Functions (II) of NaY, $Na_{53}Al_{53}Si_{139}O_{384}$.

T/K	$\Delta_f H$/kJ mol^{-1}	$\Delta_f G$/kJ mol^{-1}	T/K	$\Delta_f H$/kJ mol^{-1}	$\Delta_f G$/kJ mol^{-1}
0	-189500	-189500	155	-190200	-184500
5	-189500	-189400	160	-190200	-184400
10	-189500	-189300	165	-190300	-184200
15	-189500	-189200	170	-190300	-184000
20	-189600	-189100	175	-190300	-183800
25	-189600	-188900	180	-190300	-183600
30	-189600	-188800	185	-190300	-183400
35	-189700	-188600	190	-190300	-183200
40	-189700	-188500	195	-190300	-183000
45	-189700	-188300	200	-190400	-182900
50	-189700	-188200	205	-190400	-182700
55	-189800	-188000	210	-190400	-182500
60	-189800	-187900	215	-190400	-182300
65	-189800	-187700	220	-190400	-182100
70	-189800	-187500	225	-190400	-181900
75	-189900	-187400	230	-190400	-181700
80	-189900	-187200	235	-190500	-181500
85	-189900	-187000	240	-190500	-181300
90	-189900	-186900	245	-190500	-181200
95	-190000	-186700	250	-190500	-181000
100	-190000	-186500	255	-190500	-180800
105	-190000	-186300	260	-190500	-180600
110	-190000	-186200	265	-190500	-180400
115	-190100	-186000	270	-190500	-180200
120	-190100	-185800	275	-190500	-180000
125	-190100	-185600	280	-190500	-179800
130	-190100	-185400	285	-190500	-179600
135	-190100	-185300	290	-190600	-179400
140	-190200	-185100	295	-190600	-179200
145	-190200	-184900	298.15	-190600	-179100
150	-190200	-184700	300	-190600	-179000

comes from the optic modes due to its large numbers of atoms in unit cell. At 298.15 K the heat capacity and entropy of NaY are 9.84×10^3 J K^{-1} mol^{-1} and 9.85×10^3 J K^{-1} mol^{-1}, respectively, while the estimated $\Delta_f H$ and $\Delta_f G$ of NaY are -1.906×10^5 kJ mol^{-1} and -1.791×10^5 kJ mol^{-1}, respectively.

3.5 Thermodynamic Stability and the Concentration of Aluminum in Zeolites

It is known that the thermal stability of zeolites depends on the Si/Al ratio,[181] however, it appears that there are few quantitative discussions about the relationship between $\Delta_f G^\circ$ and the concentration of aluminum in zeolites. Table 3.13 and Figure 3.14 show the values of $\Delta_f G^\circ$ of some dehydrated synthetic zeolites, natural zeolites with different Al/(Al + Si) ratios, and related materials, for the purposes of comparison. $\Delta_f G^\circ$ is calculated from the experimental values based on the empirical chemical formula containing $Na_xAl_xSi_{(1-x)}O_2$. The Gibbs energy and enthalpy of formation[155,182] of zeolitic water are known. Analbite, nepheline and jadeite are non-zeolitic aluminosilicate materials, included for comparison with zeolites.

The thermodynamic functions of aluminosilicate materials depend mainly on the Al/(Al + Si) ratio. For example, the natural zeolite analcime has almost the same Gibbs energy of formation as the non-zeolitic jadeite. Both have the same Al/(Al + Si) ratio. Similar results have been obtained for pure SiO_2-zeolite materials and quartz.[162] ($\Delta_f G^\circ$) and the Al/(Al + Si) ratio can be expressed in kJ mol^{-1} as:

$$\Delta_f G^\circ = -859.6 - 268.4\,[\mathrm{Al}/(\mathrm{Al} + \mathrm{Si})]. \qquad (3.5.1)$$

Table 3.13. $\Delta_f G^\circ$ and $\Delta_f H^\circ$ of Zeolites with Different Al/(Al + Si) at 298.15 K.*

Zeolite	Composition	Al/(Al + Si)	$\Delta_f G^\circ$/kJ mol^{-1}	$\Delta_f H^\circ$/kJ mol^{-1}	Ref.
Analbite**	$NaAlSi_3O_8$	0.250	-926.8	-983.8	183
Analcime	$NaAlSi_2O_6$	0.333	-950.3	-1008	183
Analcime	$NaAl_{0.96}Si_{2.04}O_6$	0.320	-946.6	-1004	184
Jadeite**	$NaAlSi_2O_6$	0.333	-950.3	-1010	185
Na-Clinoptilolite	$Na_{3.6}Al_{3.6}Si_{14.4}O_{36}$	0.200	-911.6		182
Na-phillipsite	$Na_6Al_6Si_{14}O_{40}$	0.300	-938.7	-1003	186
Natrolite	$Na_2Al_2Si_3O_{10}$	0.400	-968.4	-1025	143
Nepheline**	$NaAlSiO_4$	0.500	-988.5	-1046	187
Zeolite 4A	$Na_2Al_2Si_{2.12}O_{8.24}$	0.485	-989.8		154
Zeolite 4A	$Na_{96}Al_{96}Si_{96}O_{384}$	0.500	-994.0	-1050	***
Zeolite NaX	$Na_2Al_2Si_{2.48}O_{8.96}$	0.446	-982.6		154
Zeolite NaX	$Na_{87}Al_{87}Si_{105}O_{384}$	0.453	-982.3	-1039	***
Zeolite NaY	$Na_{53}Al_{53}Si_{139}O_{384}$	0.276	-932.8	-992.7	***

* The values of $\Delta_f G^\circ$ and $\Delta_f H^\circ$ are based on the formula $Na_xAl_xSi_{(1-x)}O_2$, and expressed per mole of T (T = Si or Al).

** Analbite, jadeite and nepheline are non-zeolitic aluminosilicates materials, included for comparison with zeolites.

*** This work.

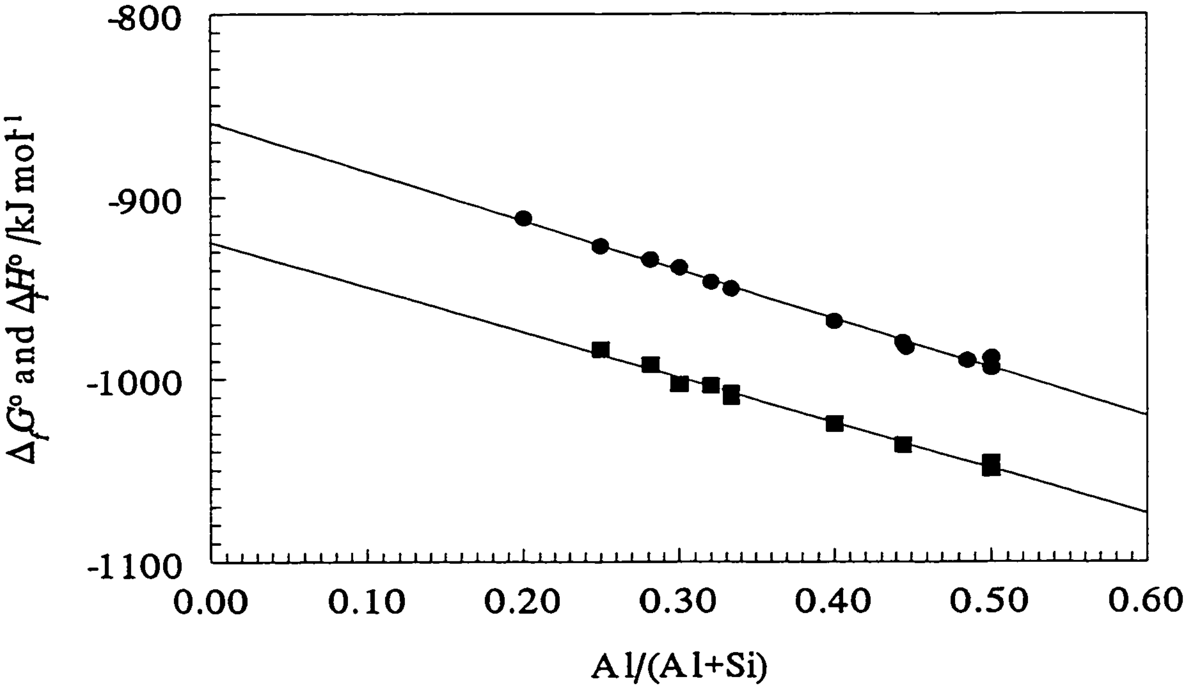

Figure 3.14. Dependence of $\Delta_f G^o$ (●) and $\Delta_f H^o$ (■) of zeolites versus Al/(Al + Si) at 298.15 K. The thermodynamic functions of formation are based on the formula $Na_xAl_xSi_{(1-x)}O_2$.

The intercept at Al/(Al + Si) = 0, -860 ± 7 kJ mol^{-1}, corresponds to the $\Delta_f G^0_{298}$ of the constituent SiO_2 in the zeolites, very close to $\Delta_f G^0_{298} = -856.4$ kJ mol^{-1} of quartz.[154]

The enthalpy of formation of zeolites also exhibits a linear relationship with the Al/(Al + Si) ratio, which can be expressed in kJ mol^{-1} as:

$$\Delta_f H^o = -921.4 - 258.3\ [Al/(Al + Si)]. \qquad (3.5.2)$$

The intercept at Al/(Al + Si) = 0, -921 ± 7 kJ mol^{-1}, corresponds to the $\Delta_f H^0_{298}$ of constituent SiO_2 in the zeolites, close to $\Delta_f H^0_{298} = -910.0$ kJ mol^{-1} of quartz.[154]

From Figure 3.14, increasing the content of aluminum increases the thermodynamic stability of zeolites. As silicon atoms are replaced by aluminum, the framework charges require more non-framework cations, Na^+, to compensate, *i.e.*, Si^{4+} is replaced with Al^{3+} and Na^+. Since the Gibbs energy of formation of one mol of SiO_2 (quartz, -856.4 kJ mol^{-1})[154] is larger than that (-980.7 kJ mol^{-1}) of (0.5 mol α-Al_2O_3 + 0.5 mol Na_2O),[154] increasing the concentration of aluminum decreases the Gibbs energy and hence increases the thermodynamic stability of zeolites. Similar results were found for the dehydrated sodium faujasite frameworks with different Si/Al ratios at 977 K.[171] One immediate application of the result is that zeolitic scientists generally use templates to synthesize high Si zeolites because they are not thermodynamically as favorable as low Si zeolites. This further illustrates that natural zeolites generally have higher Al/(Al + Si) molar ratio as discussed in Section 3.1.1.

In Figure 3.14 the difference between $\Delta_f H$ and $\Delta_f G$ represents the entropy changes in the formation of zeolites, which are negative and hence decreases the thermal stability of zeolites. Thus, thermodynamic stability of zeolites comes from the enthalpic effect not from the entropic effect. Furthermore, equations (3.5.1) and (3.5.2) indicate that the entropic effect is almost independent of Al to Si ratio.

Similar results are found for the thermodynamic functions of formation of zeolites relative to Na_2O, Al_2O_3 and SiO_2.

One phenomenon related to the above discussion is the decomposition of zeolites. DTA experiments[171] show that the decomposition temperature of zeolites increases with increasing Si/Al mole ratio. This is because the Al-O bonds are weaker than Si-O bonds and are easier to break in the framework. It should be noted that the thermodynamics of formation data in Table 3.13 are relative to the elements, not thermal decomposition.

3.6 Overall Summary

The three commercial zeolites: zeolite 4A, NaX and NaY were characterized. Their low-temperature heat capacities were determined, from which the complete thermodynamic functions between 0 and 300 K were derived. The thermodynamic functions at 298.15 K are summarized in Table 3.14.

The heat capacity of zeolites largely results from the contribution of optic modes due to the large number of atoms in their unit cell. As the Si/Al ratio increases from zeolite 4A to NaY, the apparent Debye temperature increases and hence the total heat capacity at a given temperature decreases. The thermodynamic stabilities of zeolites are an enthalpic effect but not an entropic effect. In fact, the entropic term destabilizes the zeolite framework.

The thermodynamic stabilities of zeolites strongly depend on the concentration of Al but less so on the framework of zeolites, *i.e.*, the higher the Al/(Al + Si) ratio, the lower the $\Delta_f G^0_{298.15}$ and hence, thermodynamically more stable the zeolite.

Table 3.14. Summary of Thermodynamic Properties of ZeoliteA, NaX, and NaY at 298.15 K.*

Zeolites	C_P/J K^{-1}mol^{-1}	$(H_T\text{-}H_0)$/kJmol^{-1}	$(S_T\text{-}S_0)$/J mol^{-1}K^{-1}	$\Delta_f H$/kJmol^{-1}	$\Delta_f G$/kJmol^{-1}
Zeolites 4A	12490	2069	13030	-201500	-190800
Zeolite NaX	11500	1894	11720	-199500	-188600
Zeolite NaY	9840	1590	9850	-190600	-179100

* The thermodynamic functions are based on the ideal chemical formulae, *i.e.*, zeolite 4A ($Na_{96}Al_{96}Si_{96}O_{384}$), zeolite NaX ($Na_{87}Al_{87}Si_{105}O_{384}$) and zeolite Y ($Na_{53}Al_{53}Si_{139}O_{384}$).

Chapter 4 Thermal Properties of Clathrates

4.1 Introduction

Clathrates in this chapter refer to those in which Group 14 elements or Group 14 elements and other elements form a framework with the metal atoms occupying the cages in the framework. The details of the structures of these novel materials will be discussed in Section 4.1.2.

Clathrates can display various thermal, electrical and even optical properties by doping different guests or adjusting the concentration of guests in the cages.[188,189] One of the interesting properties of clathrates of Group 14 elements is that they generally exhibit much lower thermal conductivity than most crystalline materials, and many of them show the thermal conductivity typical of amorphous materials. This is summarized in Section 4.1.3. The amorphous-like thermal conductivity makes clathrates of Group 14 elements poor heat conductors and hence one of the most promising thermoelectric materials in cooling devices which do not use refrigerants.

In this chapter, the thermal properties, especially low-temperature heat capacities and the related thermodynamic properties enthalpy, entropy and Gibbs energy of five novel clathrates of Group 14 elements are determined. They are Na_8Si_{46}, $Sr_8Ga_{16}Ge_{30}$, $Sr_8Zn_8Ge_{38}$, $Cs_8Ga_8Sn_{38}$ and $Ba_8Ga_{16}Si_{30}$. In addition to their remarkable properties mentioned above, the objectives of investigating the thermal properties of clathrates of Group 14 elements in this thesis rely on several considerations. First, heat capacity data are required to convert thermal diffusivity to thermal conductivity and hence to determine the efficiency of thermoelectric materials, as discussed in the following section.

Secondly, measurements of thermal properties are necessary to understand phonon-phonon interactions and anharmonicity of lattice vibrations in clathrates, which are important to understand the amorphous-like thermal conductivities of these crystalline materials. Finally, the investigation of heat capacity can provide information such as why a clathrate framework of Group 14 elements is stable with or without guests in the cages, which is important for their applications. In this chapter, the background of thermoelectric properties of materials is briefly introduced first.

4.1.1 Thermoelectric Materials

Thermoelectricity deals with the relationship between electricity and heat. The Seebeck and Peltier effects are typical thermoelectric phenomena.

The Seebeck effect was discovered by Thomas Seebeck[190] in 1822. When a material is placed in a temperature gradient, an electrical potential, known as the thermal electromotive force (emf), develops between the hot and cold ends. The origin of the Seebeck effect in a material can be explained by the electron-gas model,[190] as shown in Figure 4.1. As long as the temperature gradient exists, the electrons at the hot end will diffuse towards the cold end to produce an electrical potential gradient, ΔV. At the same time the electrons at the cold end will diffuse at a relatively slow velocity towards the hot end because of the electrical potential gradient. Consequently, an equilibrium of diffusion between cold and hot ends is established. The rate of change of thermal emf with respect to temperature is called the thermoelectric power or Seebeck coefficient, S, defined as $S = dV/dT$, where V is the electric potential.[191] Generally, the Seebeck coefficients of pure

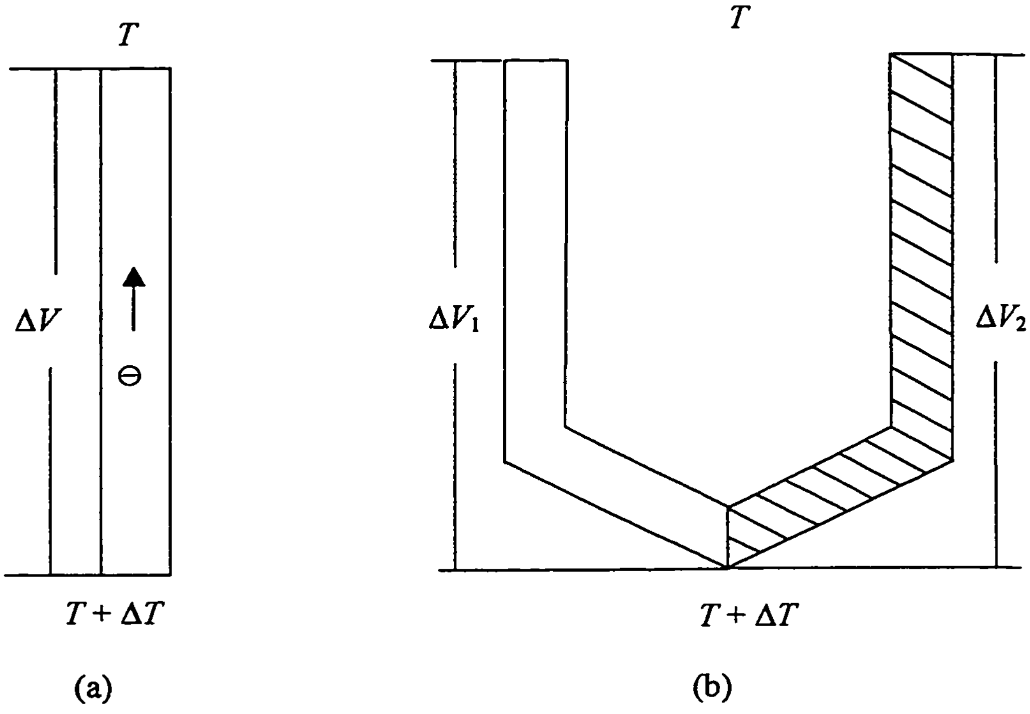

Figure 4.1. Seebeck effect. (a) When a temperature gradient exists, electrons disperse from the high temperature ($T+\Delta T$) end to the low temperature end (T), producing an electrical potential gradient, ΔV. (b) When two dissimilar materials are used, as shown, a net voltage, $\Delta V = \Delta V_1 + \Delta V_2$, develops.

metals are less than 10 μV/K while alloys have much higher Seebeck coefficients (10 ~ 10^2 μV/K).[190,191] Hence, alloys are widely used in temperature measurement and control.

The Peltier effect is exhibited when a current flows across a junction between two dissimilar materials and a temperature increase or decrease at the junction occurs, depending on the direction of the current. The mechanism[192] of the Peltier effect again can be understood by the free-electron gas model, as shown by a cooling device in Figure 4.2. When a current flows through the device, electrons in the *n*-type semiconductor and holes in the *p*-type semiconductor carry heat away from one surface, making it cooler than the other surface. If the direction of the current is reversed, the flow of the electrons and holes and hence the heat effect are reversed. Commercially available devices contain from 18 to 128 couples of *n*-type and *p*-type thermoelectric materials.[192] Heat (Q) flows away from the junction in unit time (t) defined as[190] $dQ/dt = \Pi I$, where Π and I are the Peltier coefficient and electrical current, respectively.

Lord Kelvin discovered in 1854 that there is a relation between the Peltier and Seebeck effects given by the equation,[192] $\Pi = (S_A - S_B)T$, where S_A and S_B are the Seebeck coefficients of the thermoelectric materials A and B, respectively.

Apart from thermoelectric power, the Peltier effect depends on the electrical resistance and thermal conductivity of the materials. As electrical current flows through the device, the Joule heat I^2R increases the temperature of the device. Meanwhile, heat will flow back to the low temperature end as long as a temperature gradient, ΔT, exists. The heat can be calculated from the Debye equation[193] $dQ/dt = \kappa A\ dT/dl$ where κ is the thermal conductivity of the material, A is its cross–section area material, and dT/dl is the

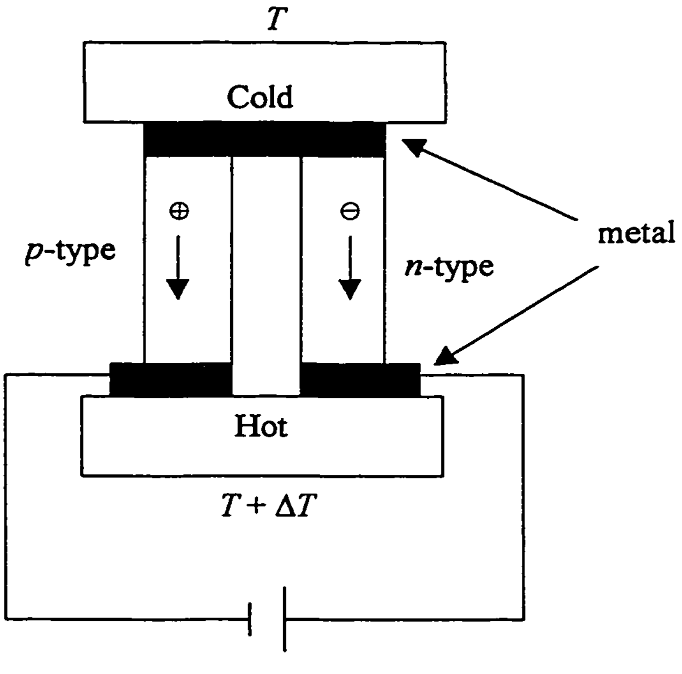

Figure 4.2. Thermoelectric cooler device. As electrical current flows through the device, electrons (⊖) in the *n*-type semiconductor and holes (⊕) in the *p*-type semiconductor carry heat away from the upper surface, making it cooler than the lower surface. If the current direction is reversed, heat (and electrons and holes) will flow in the opposite direction and the device is a thermoelectric heater. Similarly, a temperature gradient can give rise to a current flow, for thermoelectric power generation.

temperature gradient along the material.

The thermoelectric efficiency of a material can be quantified[192] by $Z = S^2\sigma/\kappa$, where σ is the electrical conductivity. Since Z has the dimension of K^{-1}, a dimensionless figure of merit, ZT, is commonly used. Hence an ideal thermoelectric material has a large Seebeck coefficient, a high electrical conductivity and a low thermal conductivity. The most challenging work in searching for efficient thermoelectric materials is to balance the three parameters S, σ and κ because they are not independent of each other. For example, pure metals have high electrical conductivity, but their Seebeck coefficient is low and their thermal conductivity is high. On the other hand, insulators are characterized by high Seebeck coefficients and low thermal conductivity but low electrical conductivity. Semiconductors have moderately high Seebeck coefficients, high electrical conductivity and relatively low thermal conductivity. They are possible thermoelectric materials. Examples of commercial thermoelectric materials are bismuth telluride (Bi_2Te_3), antimony telluride (Sb_2Te_3) and their alloys,[194] with a ZT of about 1 at room temperature. Over the past 30 years, commercial thermoelectric cooling devices have primarily relied on these semiconductor materials[195] with about 10% Carnot efficiency, $\eta = T_{cold} / (T_{hot} - T_{cold})$. Theoretically, there is no fundamental maximum limit to ZT. If ZT is increased to the value of 4, thermoelectric solid-state cooling devices, which do not use refrigerants, could replace refrigeration units with 30% Carnot efficiency.[192]

On the basis of investigations of thermal conductivities of clathrate hydrates and the role of the guest species,[64,67] Slack[196, 197] proposed that cage-type compounds with a large unit cell containing encapsulated atoms that can rattle inside the voids could be useful thermoelectrics. They would have low thermal conductivities but rattling would not scatter the conduction electrons as long as the electrical conductivity takes place mostly through the framework. Slack[196,197] called such a material "a phonon-glass and an electron-crystal" (PGEC). One of the possible candidates for PGEC's is filled skutterudite compounds.

Filled skutterudite compounds[198] can be represented by the formula RM_4X_{12} where R is La, Ce, Pr, Nd or Eu, M is Fe, Ru or Os and X is P, As, or Sb. They can be prepared by direct reaction from the elements at around T = 1000 K under vacuum conditions.[199] Skutterudite compounds have a cubic structure and a space group of $Im3$. The unit cell[200] consists of eight MX_3 groups and has two cages that can hold various metal atoms. One example is $CeFe_4Sb_{12}$. It has a thermal conductivity of 1.7 W m^{-1} K^{-1} at 300 K and shows only a weak temperature dependence between 300 and 900 K.[199] The low thermal conductivity is predominantly attributed to the scattering of heat-carrying phonons through the rattling of Ce atoms in cages.[201] In general, empty skutterudite compounds MX_3, (M = Co, Rh, or Ir; X = P, As or Sb) such as $CoAs_3$, are not efficient thermoelectric materials because of their high thermal conductivity although they have large Seebeck coefficients and high electrical conductivity.

Recently, clathrates of Group 14 elements have shown promise in extending the ZT range. Like skutterudite compounds, these novel materials have voids that can accommodate various guests including alkali, alkali-earth and rare-earth atoms. This is discussed in more detail in the following sections.

4.1.2 Structures of Clathrates

Clathrates are a type of inclusion compound, having a cage structure capable of holding guests. The history of clathrates can be traced back to as early as 1778 when Priestley observed the sulfur dioxide clathrate hydrate.[202] It was Powell[203,204] who not only proposed the structures for these host-guest compounds but also coined the term *clathrate* to indicate the situation where the molecule is completely enclosed by the host and cannot escape from its surroundings. Like many other inclusion compounds, the existence of clathrates is due to the presence of guests in the voids. The empty or even partially filled framework of clathrates is generally unstable. However, some empty clathrates (the *clathrands*) such as Dianin's compound and Si_{136} indeed exist.[205,206]

Metal-doped clathrates with Group 14 elements, Si, Ge and Sn as host atoms were first developed in 1965.[207] However, the rapid development of these novel materials has occurred only in recent years. They display the same framework topology as type I and type II clathrate hydrates, and are similarly named as type I and II clathrates.

In type I clathrates of Group 14 elements, 46 framework atoms, Q, combine to form a simple primitive cubic structure, shown in Figure 4.3, with a general chemical formula of M_xQ_{46} and space group $Pm\overline{3}n$, where M is an alkali metal, alkali-earth metal or rare-earth metal atom and Q is Si, Ge or Sn.[208,209] These clathrates are isostructural with type I clathrate hydrates, such as $Cl_8(H_2O)_{46}$. Each unit cell contains two small cages (dodecahedra), Q_{20}, formed by 20 framework atoms, and six large cages (tetrakaidecahedra), Q_{24}, formed by 24 framework atoms.[210] The cages are linked to each other by shared pentagonal or hexagonal faces. Alkali or alkali-earth metal atoms occupy

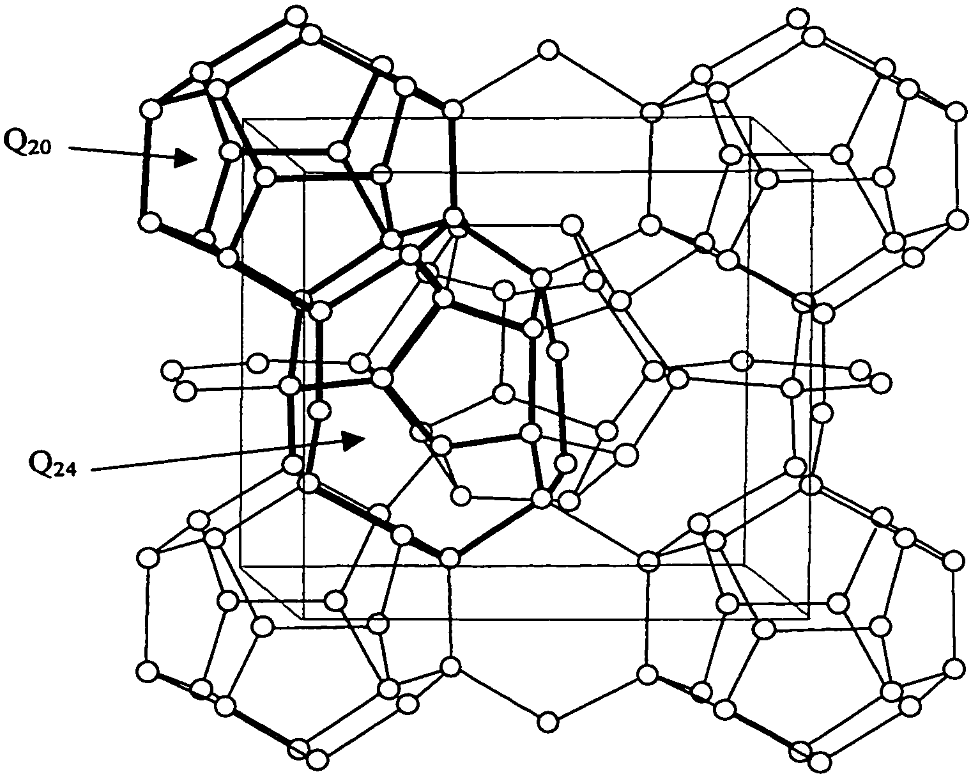

Figure 4.3. Type I clathrate structure. 20-atom cages and 24-atom cages combine in a two-to-six ratio to form the unit cell, Q_{46}.

the cages, with the maximum occupancy of eight per unit cell.

In type II clathrates, 136 host atoms (Q) form a face-centred cubic structure, shown in Figure 4.4, with a general chemical formula of M_xQ_{136} and space group $Fd\bar{3}m$. They are isostructural with type II clathrate hydrates,[208] such as $(CCl_4)_8(H_2O)_{136}$ or $(H_2S)_{16}(CCl_4)_8(H_2O)_{136}$. There are sixteen smaller 20-atom cages (pentagonal dodecahedra), Q_{20}, and eight large 28-atom cages (hexakaidecahedra), Q_{28}, in the unit cell.[211,212] The maximum guest occupancy is 24.

In both structures, the framework atoms have sp^3 hybridization and form the same covalent network as their diamond phases. The bond lengths between framework atoms are only slightly greater than in the crystalline diamond phase structure.[207] X-ray diffraction[213,214] and theoretical calculations[215] revealed that the bond angles range from 105° to 125° but the average bond angle is close to an ideal angle of 109.5°. The internal energies of type I and type II empty clathrate structures are slightly higher than those of the diamond phase, by ~ 1 kJ mol^{-1}.[216,217]

Si, Ge and Sn atoms not only form the uniform framework such as in M_8Q_{46} and $M_{24}Q_{136}$ but also form multicomponent frameworks, which greatly increases the number of clathrates. In these framework topologies, the Group 14 atoms are partially replaced by other atoms. The general formula of type I clathrates can be expressed as $M_8N_xQ_{46-x}$ where M is the metal atom and N and Q are framework atoms. In many cases, the number of replaced framework atoms is 8 with chemical formula, $M_8N_8Q_{38}$, where M is Na, K, Rb or Cs; N is Al, Ga, or In and Q is Si, Ge or Sn. When x = 16, type I clathrates have the chemical formula $M_8N_{16}Q_{30}$, where M is Ba or Sr, N is Al, Ga or In and Q is Si, Ge, or

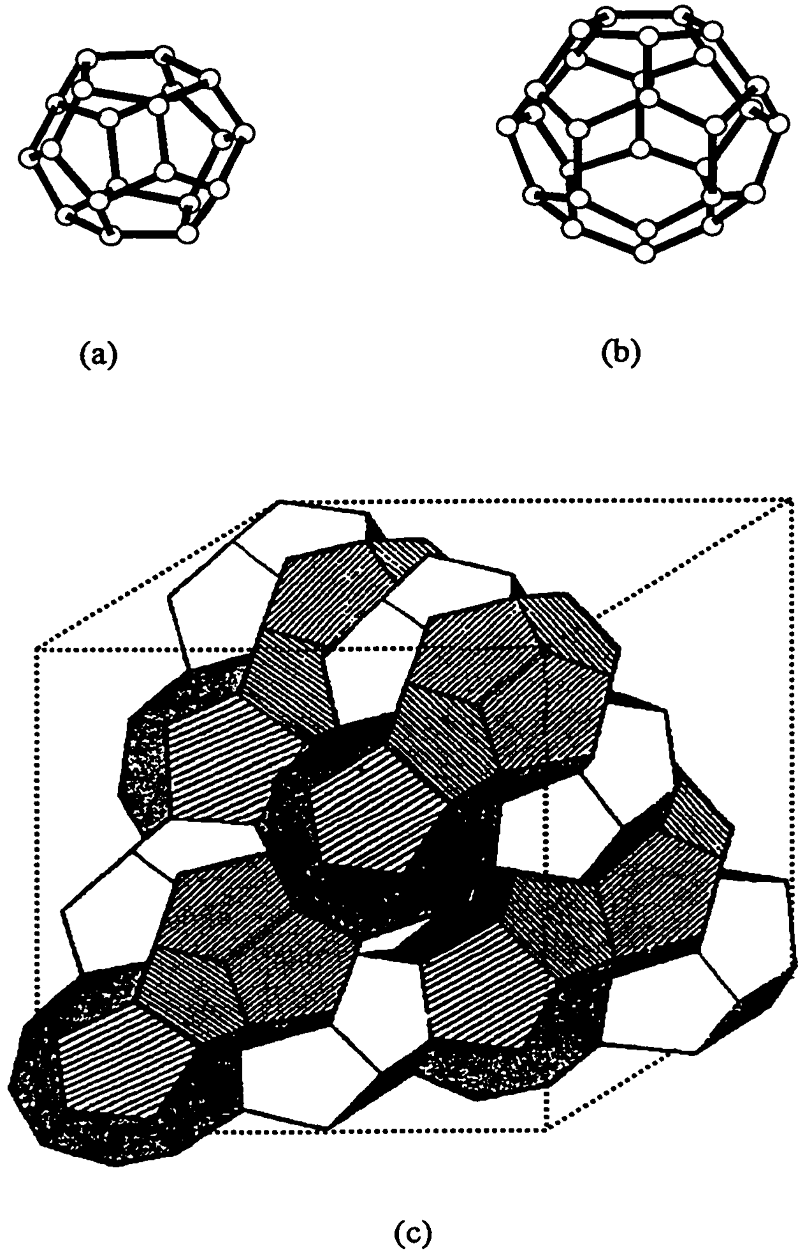

Figure 4.4. Type II clathrate structure: (a) 20-atom cages and (b) 28-atom cages. (c) 20-atom cages and 28-atom cages combine in a sixteen-to-eight ratio to form the unit cell, Q_{136}.

Sn. A few examples[218-220] of these clathrates are $K_8Ga_8Si_{38}$, $Rb_8Al_8Ge_{38}$, $Rb_8Al_8Sn_{38}$ and $Rb_8In_8Ge_{38}$. The numbers of clathrates can be further extended by doping with different guests in the cages.

The electronic states of metal guests in Si and Ge clathrates have been investigated.[212,216,221-224] It has been suggested that metal atoms in uniform framework clathrates be regarded as neutral or partially ionized.[212,221] In the multicomponent framework clathrates, the alkali metal or alkaline earth metal atoms are ionized by transferring their valence electrons to the framework.[216] For example, Sr atoms can provide 16 electrons to the framework of $Sr_8Ga_{16}Ge_{30}$.[216] As a consequence, $Ga_{16}Ge_{30}$ has the same valence electron configuration as the Ge_{46} clathrate. Such a method makes it easy to understand the electronic structures of multicomponent frameworks and helpful to design new frameworks. However, the real electronic state of metal atoms in frameworks is not completely understood. For example, a recent theoretical calculation indicates there is little charge transfer between metal atoms and the framework.[222] To a first approximation, the metal atoms in the cages are neutral and the main contribution to the electrical conductivity comes from the framework electrons.[223] On the other hand, significant charge transfer from the metal to the clathrate framework has also been proposed.[224]

4.1.3 Thermal Properties of Si, Ge and Sn Clathrates

Thermal properties are necessary to select efficient thermoelectric materials and to understand the mechanism of their glass-like thermal conductivity. The thermal properties of some clathrates of Group 14 elements have been investigated recently. For example, the thermal expansion of both powder and single crystal samples[225] of $Sr_8Ga_{16}Ge_{30}$ have been determined by neutron diffraction below room temperature. The Grüneisen parameter and compressibility of Na_xSi_{136} also were determined at room temperature.[206,226] The results[206,226] indicated that silicon clathrates are about 10% less compressible than the diamond phase.

The thermal conductivities of clathrates of Group 14 elements have been widely investigated in the past five years. Among the clathrates of Group 14 elements, the thermal conductivity of Cs_8Sn_{44} is typical of a crystalline insulator, exhibiting a maximum at low temperatures and depending on T^{-1} at high temperatures.[227] However, the thermal conductivity[213] of $Cs_8Zn_4Sn_{42}$ is less temperature-dependent than Cs_8Sn_{44}. At room temperature, the lattice component of the thermal conductivity, κ_L, of Sn clathrates[213,227] is about 1.0 W m^{-1} K^{-1}. According to the Wiedemann-Franz law,[228] $\kappa_e = L\sigma T$, where $L = 2.44 \times 10^{-8}$ V^2 K^2 is the Lorenz number, the electronic component of the thermal conductivity, κ_e, of Sn clathrates is less than 2% of the total thermal conductivity.[213] The structures of several other Sn clathrates[229,230] also were reported, but their thermal properties have not been investigated yet.

The thermal conductivity of the Si clathrate $Ba_8Ga_{16}Si_{30}$ was investigated.[227] The lattice component of the thermal conductivity of $Ba_8Ga_{16}Si_{30}$ is less than that of $Cs_8Zn_4Sn_{42}$ below 100 K. At higher temperatures, both have very similar thermal conductivity. At room temperature, $Ba_8Ga_{16}Si_{30}$ has a higher *ZT* than Sn clathrates because of its much higher electrical conductivity.[213,227]

The thermal conductivities of Ge clathrates such as $Sr_8Ga_{16}Ge_{30}$, $Eu_8Ga_{16}Ge_{30}$ and $Sr_4Eu_4Ga_{16}Ge_{30}$, have been determined[227,231] and are found to have typical characteristics of amorphous materials.[227] The lattice component of thermal conductivity of these clathrates at room temperature approaches the minimum based on a theoretical model.[227]

Generally, the clathrates of Group 14 elements have much lower thermal conductivities than their diamond phases due to the rattling guests strongly scattering the heat-carrying acoustic phonons.[227,231] This is reasonable because the coupling of optic phonons and acoustic phonons could result in Umklapp processes and hence decrease the thermal conductivity, as discussed in Section 1.4. A similar mechanism has been used to explain the thermal conductivity of other clathrates[232] and is supported by molecular dynamics calculations.[233]

The efficiency of scattering of heat-carrying phonons depends on the size difference between the cage and guest, $U = r_{cage} - r_{guest}$, where r is the radius. Generally the larger the cages, the lower the vibrational frequency.[213] The rattle frequencies of the guests in the cages can be determined from the atomic displacement parameters (ADP).[234] This measures the mean-square displacement amplitude of an atom about its equilibrium position in a crystal. For example, the rattle frequencies of Sr in $Sr_8Ga_{16}Ge_{30}$ are 95 cm^{-1} in 20-atom cages and 20 ~ 60 cm^{-1} in the 24-atom cages.[224,235]

In the following sections, the results of thermal properties determined for Si, Ge and Sn clathrates are presented and discussed.

4.2 Thermal Properties of the Clathrate Na_8Si_{46}

4.2.1 Structure

Silicon clathrates form isostructures of type I and type II clathrate hydrates. Each Si framework atom is *sp*^{3} hybridized with a mean bond angle of 109.4° and covalent bond length of about 2.38 Å, slightly greater than 2.35 Å in the crystalline diamond phase.[209,236] Theoretical calculations reveal that the silicon clathrands have an internal energy about 7 kJ mol^{-1} higher than that of the diamond phase.[237,238]

In type I silicon clathrates, M_xSi_{46}, where M represents the guest metal atoms, 46 silicon atoms form the unit cell of a simple cubic structure[208,209] with space group $Pm\bar{3}n$ and lattice parameter of about 10.235 Å. Each unit cell contains two small 20-atom cages, pentagonal dodecahedra, Si_{20} (I_h) and six large 24-atom cages, tetrakaidecahedra, Si_{24} (D_{6d}). Metal atoms can be trapped in both these cages. The numbers of trapped metal atoms depend on their sizes. When all the available cavities are occupied, the clathrate has the ideal formula M_8Si_{46}. In the cases where the metal atom is too big, only the larger cages are occupied.[214]

The cages of silicon clathrates can be occupied by different metal atoms, which leads to the mixed metal guest clathrates. When all the cages are completely occupied by two different metal atoms, the silicon clathrate has a formula of $M_2M'_6Si_{46}$ where M and M' are different metals. Generally, the smaller metal atoms M occupy the cages of Si_{20} and the larger ones M' occupy the sites formed by Si_{24}.[239,240] Metal atoms in the small and large cages can be investigated by solid-state NMR.[208]

In type II silicon clathrates, M_xSi_{136}, 136 silicon atoms form a face-centred cubic structure, space group[209] $Fd\bar{3}m$ and lattice parameter 14.62 Å. The unit cell consists of 16 smaller 20-atom cages, pentagonal dodecahedra or Si_{20} (I_h), and 8 large 28-atom cages, hexakaidecahedra or Si_{28} (T_d). The maximum occupancy in a unit cell of a type II clathrate is 24 guests.

The electrical conductivity of silicon clathrates can be tailored from semiconductor to conductor by trapping different numbers of metal guests. Generally, M_8Si_{46} is metallic and M_xSi_{136} is an insulator[210] when $x < 9$. Recently, it has been discovered that barium–doped Si clathrates, such as Ba_8Si_{46}[241] and $Na_2Ba_6Si_{46}$[211]show superconductivity below 10 K. Since metal atoms are located inside the cages formed by framework atoms, silicon clathrates are remarkably stable in air, moisture and even in strong acids except HF.[211,241]

4.2.2 Experimental

4.2.2.1 Synthesis

A polycrystalline Na_8Si_{46} sample was supplied by the National Research Council (NRC) of Canada. The sample was prepared from combined batches from two preparations, similar to those described previously.[242,243] Sodium silicide (NaSi) precursor was synthesized by reacting stoichiometric amounts of Na with Si in a stainless vessel (evacuated and sealed) at 873 K for three hours. The air and moisture-sensitive NaSi product was then wrapped in tantalum foil and placed in a quartz tube in an inert atmosphere dry box. This was heated in a furnace to 633 K under active vacuum for 1h. The tube was then closed under vacuum and heated at 720 K for 20 hr to produce Na_8Si_{46}.

Na metal, from the decomposition of NaSi, condensed on the walls of the glass tube outside the furnace.

The purity of the materials was determined by X-ray powder diffraction and ^{23}Na solid state MAS NMR at NRC. ^{23}Na NMR, described elsewhere,[244] showed no traces of Na metal or NaSi, to which NMR is quite sensitive.

X-ray power diffraction patterns were measured by NRC using mononchromatized Co K_α (λ=1.79021 Å) radiation on a Rigaku X-ray diffractometer (model RAD-R). For sample purity analysis the data were collected over the range 5 to 80° in 2θ at 0.04° intervals in continuous scan mode at a scanning speed of 0.5%. The first sample contained traces of crystalline Si (estimated at 1%) and the second sample traces of Na_xSi_{136} (< 4%).

4.2.2.2 Lattice Parameter Determination

The lattice parameter of Na_8Si_{46} was determined by NRC using powder X-ray diffraction from two independent samples at 11 temperatures between 90 and 330 K. The [222], [320], and [321] Bragg peaks were measured between 32-39° in 2θ at intervals of 0.02° at a scanning rate of 0.24°/min. The unit cell size calculated using each peak individually was averaged at each temperature. For the expansion measurements crystalline silicon was included with the powdered samples to provide an interval reference.

4.2.2.3 Heat Capacity Measurement

A 0.9456 g power sample was loaded in the calorimeter in a glove box under dry nitrogen atmosphere. The calorimeter was sealed in a helium atmosphere to increase the heat exchange rate. The heat capacity was determined between 35 and 300 K and the details of the adiabatic calorimeter and its operation have been described in Section 2.4.

4.2.3 Results and Discussion

4.2.3.1 Lattice Parameter and Thermal Expansion

The lattice parameters are listed in Table 4.1. No phase transitions were found in the experimental temperature range.

Table 4.1. Experimental Lattice Parameters of Na_8Si_{46}.

T/K	*a*/Å	*T*/K	*a*/Å
90	10.180	260	10.195
100	10.180	280	10.199
140	10.180	300	10.200
180	10.185	320	10.210
200	10.187	330	10.210
240	10.193		

The volume thermal expansion coefficient, α_V, of a cubic solid can be determined from equation (1.2.6). The lattice parameters were least-squares fitted to a polynomial equation:

$$a = a_0 + a_1 T^2 + a_2 T^3 \qquad (4.2.1)$$

with $a_0 = 10.178$ Å, $a_1 = 6.887 \times 10^{-8}$ Å K^{-2}, and $a_2 = 6.802 \times 10^{-10}$ Å K^{-3}. At 298.15 K, Na_8Si_{46} has a typical α_V of $(6 \pm 1)\times 10^{-5}$ K^{-1}. The temperature dependence of α_V below room temperature is shown in Figure 4.5.

4.2.3.2 Experimental Heat Capacity

The experimental heat capacities are listed in Table 4.2 and they increase smoothly with temperature as shown in Figure 4.6, indicating the presence of a single phase from T = 35 to 300 K in agreement with X-ray diffraction results. The heat capacity from the sample comprised about 10% of total heat capacity over the whole range of experimental temperatures.

To compare with experimental heat capacity, the sum of heat capacity from the constituent elements Na[160] and Si,[158] *i.e.*, C_P (Na) + C_P (Si), was calculated and is shown in Figure 4.6. At 298.15 K, the experimental heat capacity is 1160 J K^{-1} mol^{-1}, 1.2% greater than the value from the Neumann-Kopp value. Around 130 K, the difference increases to approximately 8%. Considering that the energy of the silicon clathrand is calculated to be only slightly higher (7 kJ mol^{-1})[237] than that of the diamond phase, such a difference is reasonable. Furthermore, it probably can be concluded that the Si-Si bond strength in the silicon clathrate is very close to that in the diamond phase of Si and the host-guest interactions are weak, which is reasonable given that the clathrand, Si_{136}, has recently been synthesized.[206]

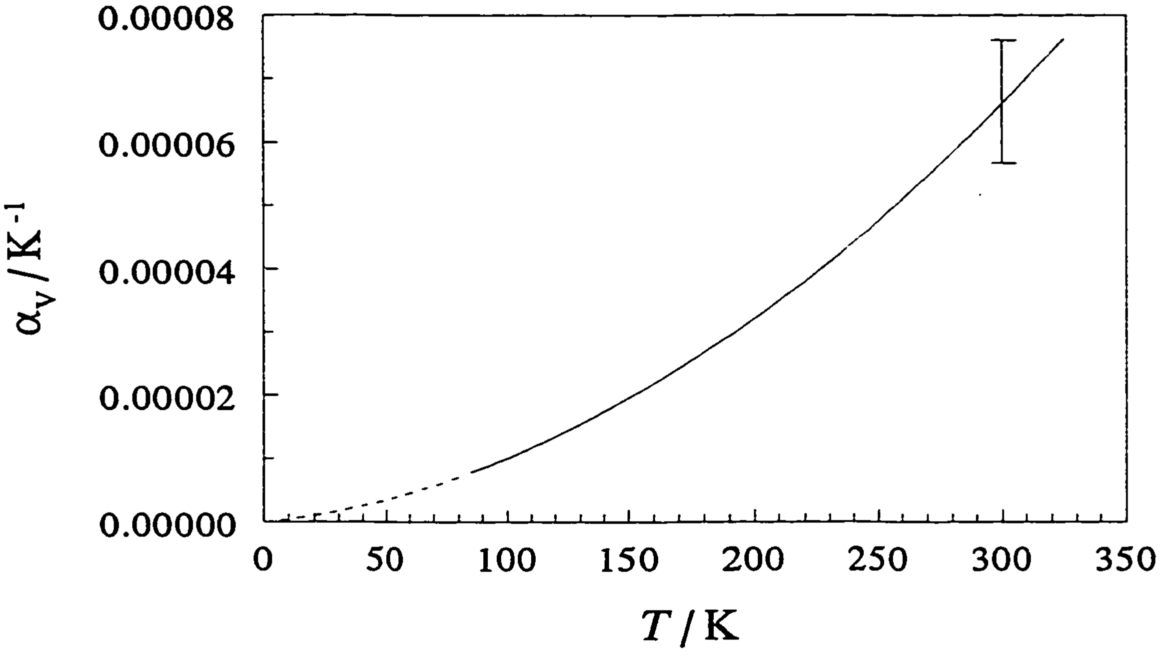

Figure 4.5. Volume thermal expansion coefficient of Na_8Si_{46}, calculated from the experimental lattice parameters as described in the text. The dashed line shows extrapolated values. The error bar indicates the uncertainty of the thermal expansion coefficient, estimated from the uncertainty in the experimental lattice parameters.

Table 4.2. Experimental Heat Capacity of Na_8Si_{46}.

T/K	C_P/J K^{-1} mol^{-1}	T/K	C_P/J K^{-1} mol^{-1}	T/K	C_P/J K^{-1} mol^{-1}
35.87	94.7	97.86	533	208.34	977
36.60	102	99.14	553	211.42	988
40.76	145	104.86	570	216.07	1001
43.24	175	108.67	605	219.01	1009
44.36	183	113.63	632	223.68	1014
45.33	193	116.65	648	226.56	1026
47.01	201	122.20	673	231.24	1027
48.24	208	124.55	693	233.71	1037
50.01	219	129.46	712	238.70	1054
51.27	232	132.55	730	240.99	1060
53.03	243	137.39	747	247.23	1067
53.08	254	140.55	769	253.33	1076
54.02	269	145.31	784	254.59	1078
58.94	303	148.53	803	256.35	1082
60.32	315	153.21	818	260.41	1092
64.42	336	156.80	829	263.45	1093
64.71	342	161.19	838	267.42	1100
70.11	375	164.51	852	270.55	1107
70.45	367	169.11	865	274.36	1115
76.20	401	172.44	872	277.36	1127
81.12	443	176.99	882	281.32	1130
81.92	439	180.78	898	284.27	1136
86.80	467	184.83	912	288.76	1141
87.63	472	188.10	918	290.98	1141
90.05	494	192.66	932	295.00	1154
92.48	521	196.53	938	297.80	1158
92.86	519	200.54	950	301.62	1163
93.38	513	203.74	962		

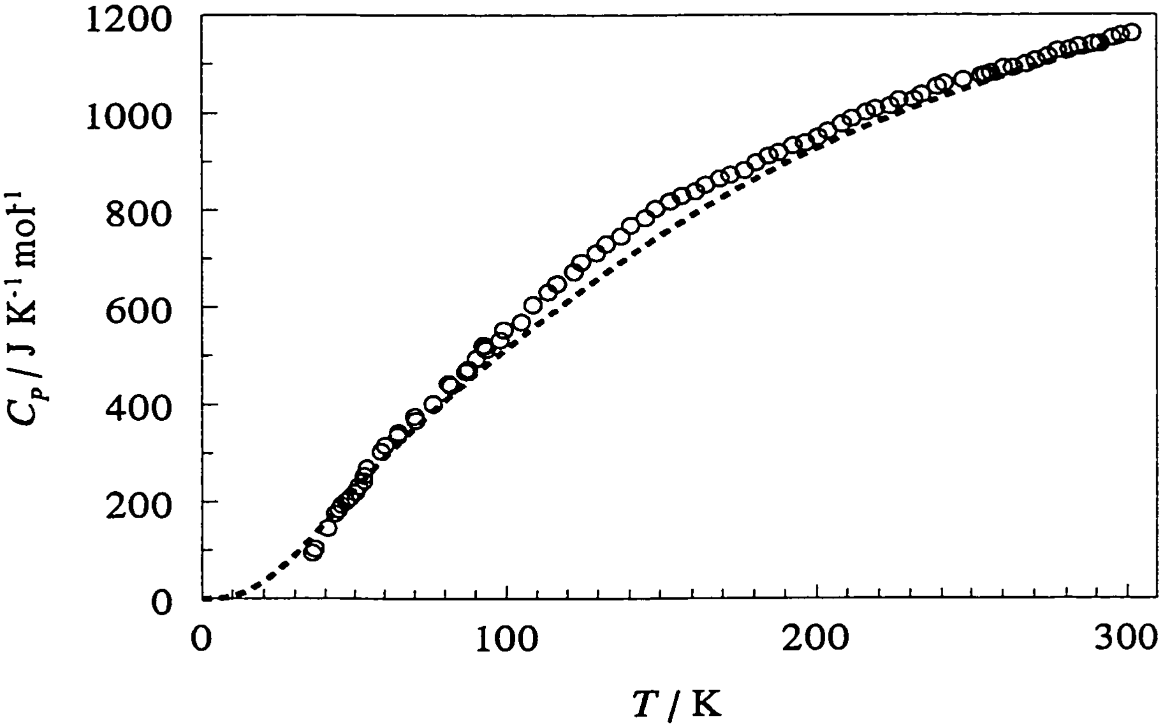

Figure 4.6. Heat capacities of Na_8Si_{46} from experiment (○) and from the Neumann-Kopp law (▪▪▪), as discussed in the text.

4.2.3.3 Heat Capacity from Vibrational Spectroscopy and Lattice Dynamics

The heat capacity contribution from the optic modes can be determined from vibrational spectroscopy if the spectrum is correctly assigned.

In a unit cell composed of N atoms, there are 3 acoustic modes (translational motions or lattice vibrations) and $3N$-3 optic modes (librations and intramolecular vibrations). In the case of Na_8Si_{46}, there are 54 atoms in the unit cell. There should be 159 optic modes. There are several early reports of theoretical[215,245] and experimental[209,246,247] vibrational spectra of silicon clathrates, but the published theoretical Raman frequencies are considerably higher than those determined experimentally. Moreover, of the 20 Raman lines predicted for Na_8Si_{46} on the basis of group theory,[247] 18 lines are associated with the Si framework, but only 15 have been observed experimentally.[247]

A new theoretical assignment[248] of the vibrational spectrum of Na_8Si_{46} was used to calculate the optical contribution to C_V. The acoustic contribution to the heat capacity was calculated with a Debye temperature of 371 K deduced from the experimental density and bulk modulus.[226] An additional term for $(C_P - C_V)$ was given by equation (1.2.5) using the present lattice expansion results and the published bulk modulus.[226] This term is less than 3% of C_P throughout the range of experimental temperatures. The calculated total heat capacity, $C_{P,cal} = C_{V,optical} + C_{V,acoustic} + (C_P - C_V)$, shown in Figure 4.7, matches the experimental results quite well. Above 150 K, the deviation of the spectrally calculated heat capacity from the experimental value could be ascribed to anharmonic vibrations of the optic modes.

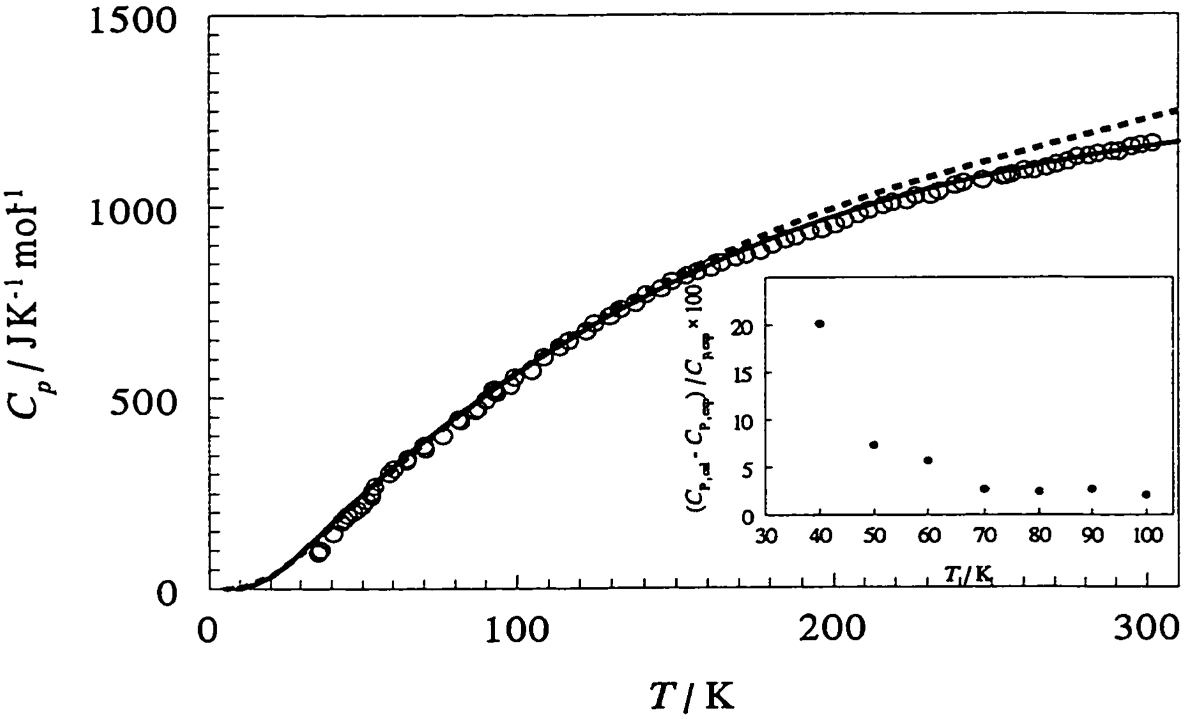

Figure 4.7. Heat capacities of Na_8Si_{46} from experiment, Raman spectroscopy and theoretical calculation. ○, experiment data; ----- calculation from vibrational assignment + Debye modes + empirical $(C_P - C_V)$ correction; — calculation from lattice dynamics. The inset diagram indicates the difference between the experimental and calculated heat capacity data. See text for details.

A direct theoretical calculation[248] of the heat capacity of Na_8Si_{46} from lattice dynamics was done by NRC and is also shown in Figure 4.7. The total theoretical heat capacity of Na_8Si_{46}, $C_V(T)$, is from the sum of all modes over the Brillouin zone:

$$C_V(T) = \sum_{k,n} C_{V,n}(\mathbf{k}, \mathrm{T}) \qquad (4.2.2)$$

where $C_{V,n}(\mathbf{k}, T)$ is the mode contribution to the heat capacity. The quantities required to calculate $(C_P - C_V)$ also were obtained from the theoretical calculation. The agreement between the calculated and experimental heat capacity is remarkably good.

4.2.3.4 Thermodynamic Stability

In order to calculate the complete thermodynamic functions between $T = 0$ and 300 K, the heat capacities below 30 K were obtained from $C_{P,cal}$ discussed in 4.2.3.3. With the assumption of $S_0 = 0$, the entropy of formation of Na_8Si_{46}, $\Delta_f S$, derived from the entropies of Na,[160] Si[158] and Na_8Si_{46}, is shown in Table 4.3. At $T = 298.15$ K, $\Delta_f S$ is 32 ± 7 J K^{-1} mol^{-1}. The uncertainty in $\Delta_f S$ is largely from the error of S_T-S_0 of Na_8Si_{46}. The positive $\Delta_f S$ decreases the Gibbs energy of formation, $\Delta_f G$, and hence increases the thermodynamic stability of Na_8Si_{46}. Due to the higher energy of a silicon clathrate than that of its diamond phase,[237,238] the enthalpy of formation of a silicon clathrate would be expected to be positive (endothermic). Hence, the positive $\Delta_f S$ is important in stabilizing the structure of silicon clathrates. The quantitative calculation of $\Delta_f G$ requires additional experimental thermodynamic data such as enthalpy of formation.

Table 4.3. Thermodynamic Functions of Na_8Si_{46}.

T/K	C_P/J K^{-1} mol^{-1}	(H_T-H_0)/kJ mol^{-1}	(S_T-S_0)/J K^{-1} mol^{-1}	(G_T-G_0)/kJ mol^{-1}	$\Delta_f S$/J K^{-1} mol^{-1}
5	0.323	0.000808	0.162	0.000	-0.18
10	2.59	0.00810	0.970	-0.0016	-0.97
15	8.73	0.0364	3.07	-0.097	-2.8
20	20.7	0.110	7.11	-0.0322	-5.8
25	39.9	0.261	13.7	-0.0808	-9.5
30	67.1	0.529	23.3	-0.169	-13
35	101	0.949	36.1	-0.313	-17
40	137	1.54	51.8	-0.530	-19
45	182	2.34	70.5	-0.832	-21
50	224	3.36	91.8	-1.23	-21
55	261	4.57	115	-1.75	-21
60	296	5.96	139	-2.38	-21
65	334	7.54	164	-3.14	-20
70	371	9.30	190	-4.03	-19
75	404	11.2	217	-5.04	-18
80	435	13.3	244	-6.20	-16
85	465	15.6	271	-7.49	-14
90	494	18.0	299	-8.91	-13
95	525	20.5	326	-10.5	-11
100	555	23.2	354	-12.2	-8.8
105	585	26.1	382	-14.0	-6.7
110	614	29.1	410	-16.0	-4.5
115	641	32.2	438	-18.1	-2.2
120	667	35.5	465	-20.4	0.0
125	693	38.9	493	-22.8	2.3
130	717	42.4	521	-25.3	4.5
135	741	46.1	548	-28.0	6.7
140	763	49.8	576	-30.8	8.9
145	785	53.7	603	-33.7	11
150	804	57.7	630	-36.8	13
155	822	61.7	656	-40.0	15
160	839	65.9	683	-43.4	16

Continued...

Table 4.3. (continued).

T/K	C_P/J K^{-1} mol^{-1}	(H_T-H_0)/kJ mol^{-1}	(S_T-S_0)/J K^{-1} mol^{-1}	(G_T-G_0)/kJ mol^{-1}	$\Delta_f S$/J K^{-1} mol^{-1}
165	856	70.1	709	-46.9	18
170	872	74.4	735	-50.5	19
175	885	78.8	760	-54.2	21
180	897	83.3	785	-58.1	21
185	910	87.8	810	-62.1	22
190	924	92.4	835	-66.2	23
195	937	97.0	859	-70.4	24
200	951	102	883	-74.7	24
205	967	107	906	-79.3	25
210	981	111	930	-83.8	26
215	994	116	953	-88.5	26
220	1006	121	976	-93.3	27
225	1018	126	999	-98.3	27
230	1029	132	1020	-103	28
235	1041	137	1040	-108	28
240	1052	142	1070	-114	28
245	1062	147	1090	-119	29
250	1071	153	1110	-125	33
255	1080	158	1130	-130	30
260	1088	163	1150	-136	30
265	1097	169	1170	-142	30
270	1107	174	1190	-148	31
275	1116	180	1210	-154	31
280	1125	186	1230	-160	31
285	1134	191	1250	-166	31
290	1143	197	1270	-172	31
295	1153	203	1290	-179	32
298.15	1159	206	1310	-183	32
300	1162	208	1310	-185	32

4.2.3.5 Apparent Debye Temperature

The apparent Debye temperature, Θ_D, of Na_8Si_{46} from the total heat capacity, C_V, with the Debye model, equation (1.2.21), is shown in Figure 4.8. Here C_V was derived from the experimental C_P values and $(C_P - C_V)$ as discussed in 4.2.3.3. Like most solids, Θ_D depends on temperature. Around 280 K, Θ_D approaches a maximum with a value of 590 ± 8 K. The result is not unreasonable considering the porous structure of Na_8Si_{46} with a density of 2.309 g cm^{-3}, less than 2.329 g cm^{-3} of pure silicon.[249,250]

X-ray photoemission and X-ray absorption spectroscopy[251] reveal that the Debye temperature of Na_8Si_{46} is close to 640 K of the diamond phase of Si at 300 K. The apparent Θ_D is higher than the Debye temperature θ_D = 373 K calculated from the experimental bulk modulus[226] discussed in Section 4.5.3.4. The reason is that the apparent Θ_D includes all vibrational modes including optic and acoustic modes while θ_D considers only acoustic modes. Since the acoustic modes are usually excited at lower temperatures than the optic modes, the Debye temperature is lower than the apparent Θ_D.

4.2.3.6 Mean Free Path of Phonons

For cubic solids, the sound velocity is given by the equation[21]

$$v = 3^{\frac{1}{3}} (v_1^{-3} + 2\, v_2^{-3})^{-\frac{1}{3}}, \qquad (4.2.3)$$

where v_1, the longitudinal velocity of sound wave is:[252]

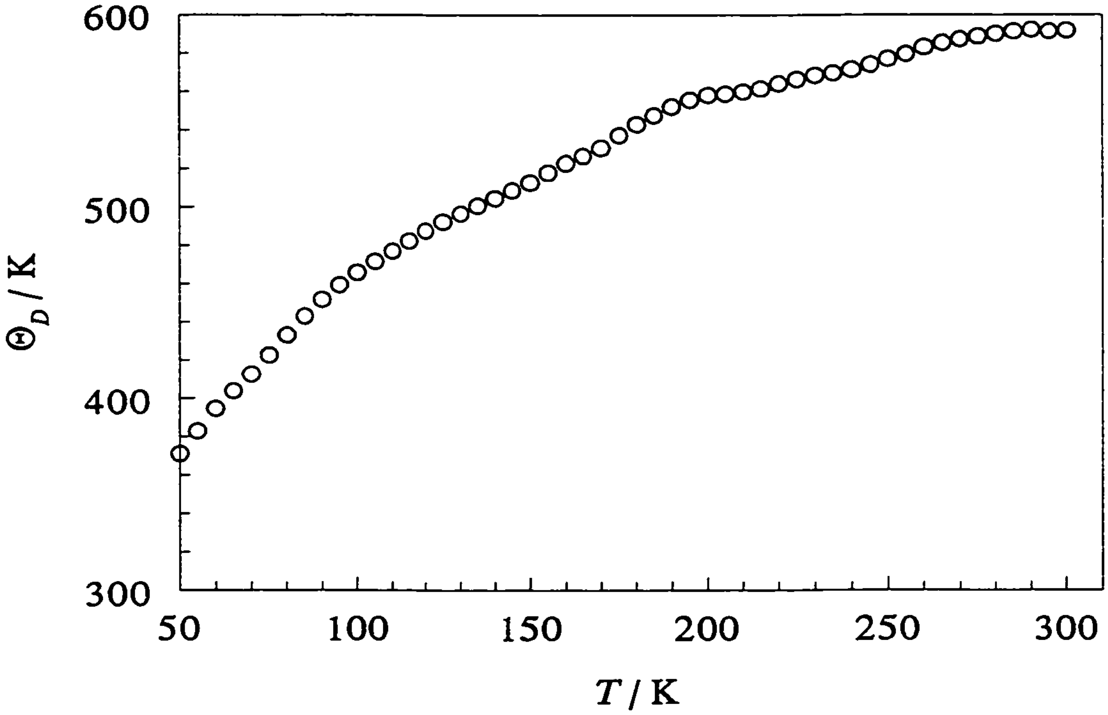

Figure 4.8. Apparent Debye temperature of Na_8Si_{46}, derived from the total heat capacity, C_V, as discussed in the text.

$$v_1 = \left(\frac{c_{11}}{\rho}\right)^{\frac{1}{2}}, \tag{4.2.4}$$

and v_2, the transverse velocity of sound wave is:[252]

$$v_2 = \left(\frac{c_{44}}{\rho}\right)^{\frac{1}{2}}. \tag{4.2.5}$$

Here, c_{11} and c_{44} are elastic constants[253], and ρ is the density of a solid. The calculated sound velocity for Na_8Si_{46} from theoretically determined elastic constants[215] is $(4.9 \pm 0.3)\times10^3$ m/s, which corresponds to a Debye temperature of 540 ± 23 K and agrees with the maximum apparent Debye temperature determined from experimental heat capacity as discussed in Section 4.2.3.6.

With knowledge of the sound velocity and heat capacity, the mean free path of the phonons, l, can be estimated from equation (1.4.1). The thermal conductivity[238] of Na_8Si_{46} below room temperature is almost a temperature-independent quantity with a value of about 0.40 W m^{-1} K^{-1}. Based on the present heat capacity data and the velocity of sound, l has been calculated as a function of temperature. The results are shown in Figure 4.9; l has a value between 1.5 and 6 Å and a temperature-dependence typical of amorphous materials. The value of l in Na_8Si_{46} is quite close to that in tetrahydrofuran clathrate ($THF\cdot17H_2O$).[254] The short mean free path of phonons can be associated with the rattling of sodium atoms in the cages, which results in the low thermal conductivity of Na_8Si_{46}.[238]

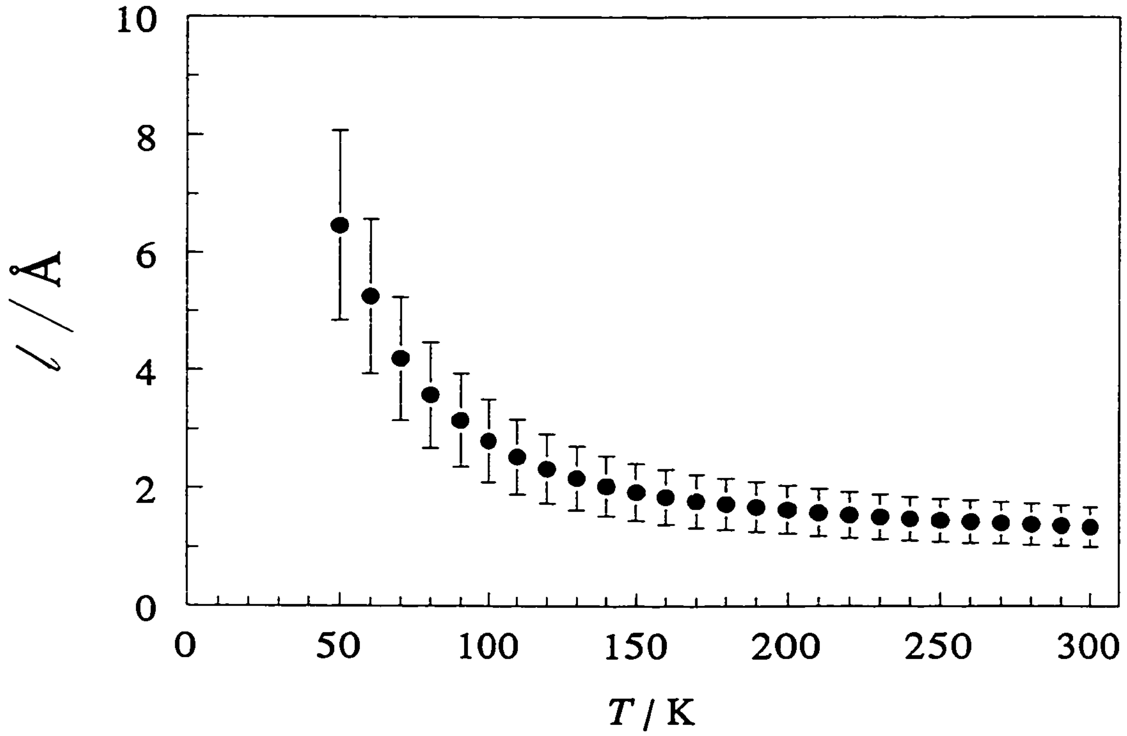

Figure 4.9. Mean free path of phonons in Na_8Si_{46}, calculated as described in the text. The error bars indicate the uncertainty of the mean free path of phonons, which is estimated from the errors in thermal conductivity,[238] elastic properties[215] and the present heat capacity. Most of the uncertainty results from the error in thermal conductivity.

4.2.3.7 Grüneisen Parameter

The Grüneisen parameter measures the anharmonicity of lattice vibrations. A convenient way to obtain γ for cubic phases is given by equation (1.5.3). The γ of Na_8Si_{46} at different temperatures is shown in Figure 4.10. The experimental compressibility,[226] molar volume and thermal expansion coefficient, and isochoric heat capacity are available. At 300 K, it has a value of 3.4 ± 0.5, which is typical of solids. The uncertainty in γ is due largely to the error of thermal expansion coefficients. At very low temperatures, γ increases as temperature decreases, in agreement with experimental thermal conductivity.[238] Similar results have been found for other clathrates,[255] a consequence of the scattering of acoustic phonons through the rattling of guests in the cages.[232]

4.2.4 Conclusions

The low temperature heat capacity of Na_8Si_{46} has been determined using an adiabatic calorimeter and the related thermodynamic functions were calculated. At 298.15 K, Na_8Si_{46} has a C_P of 1159 J K^{-1} mol^{-1}, $S_{298.15}-S_0$ of 1310 J K^{-1} mol^{-1}, and $(H_{298.15}-H_0)$ of 206 kJ mol^{-1}. It exhibits normal thermal expansion and has a volume expansion coefficient of 6×10^{-5} K^{-1} at 298.15 K. The Grüneisen parameter was also calculated and found to have a value of 3.4 at room temperature. The mean free path of phonons of Na_8Si_{46} has a temperature profile typical of an amorphous material and is 1.5 Å ~ 6 Å between 50 K and 300 K.

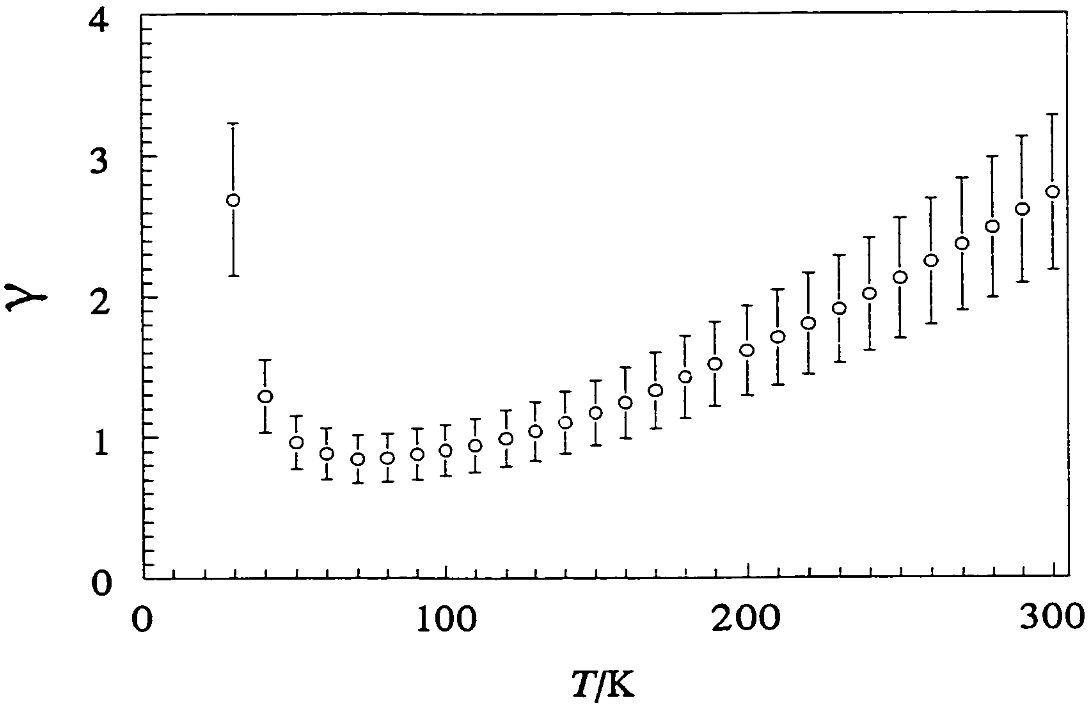

Figure 4.10. Grüneisen parameter of Na_8Si_{46} as a function of temperature. It is calculated from equation (1.5.3) as described in the text. The error bars indicate the uncertainty of the Grüneisen parameter, which is mainly from the uncertainty of the thermal expansion coefficient.

4.3 Thermal Properties of $Sr_8Ga_{16}Ge_{30}$ Clathrate

4.3.1 Structure

Neutron diffraction indicates that both powder and single-crystal samples of $Sr_8Ga_{16}Ge_{30}$ have the structure of type I clathrate hydrates with space group $Pm\bar{3}n$.[225] The Ga and Ge atoms are distributed randomly in the framework.[225] The estimated average radii[225] of Ge_{20} and Ge_{24} cages are 2.2 and 2.4 Å, respectively. The cage size depends only on the framework atoms, not on guest atoms. Theoretical calculations reveal that the energy of a type I Ge clathrate increases by 5 kJ mol^{-1} compared with its diamond phase while the internal energy of the type II Ge clathrate increases by 4.4 kJ mol^{-1}.[216]

The lattice parameter of $Sr_8Ga_{16}Ge_{30}$ is around 10.74 Å at 295 K, which is slightly greater than that[216] of K_8Ge_{46}, 10.66 Å. The Ge-Ge bond length[225] ranges from 2.44 Å to 2.51 Å with an average of 2.50 Å, which is close to 2.45 Å of diamond-structure germanium.[231] Single-crystal X-ray diffraction analysis shows that the Ge-Ge-Ge bond angle ranges from 106 to 125°, and the bond is close to sp^3 hybridization.[231]

4.3.2 Experimental

4.3.2.1 Synthesis

The sample $Sr_8Ga_{16}Ge_{30}$ was synthesized and provided by Marlow Industries, Inc. High purity Sr (99.95%) and Ge (99.999%) were arc-melted together in an argon atmosphere to form nominal $SrGe_2$. The exact composition was determined by weighing the sample before and after melting and assuming the mass loss was due to Sr.

Stoichiometric amounts of $SrGe_2$, Ga, and Ge were loaded in a helium dry box into a carbonized silica tube. It was sealed under vacuum, held at 1320 K for 20 h and then cooled to 920 K, held for several days. The resulting black boule consisted of large single-crystal grains (5-10 mm) of $Sr_8Ga_{16}Ge_{30}$. The detailed procedures of synthesis can be found elswhere.[225]

The melting point of the sample was found to be 1043 K.[225] Electronic-beam microprobe analysis[256] indicates the atomic percentage are 14.7, 29.8, 55.5 for Sr, Ga and Ge, respectively. For $Sr_8Ga_{16}Ge_{30}$, the theoretical atomic percentage are 14.8, 29.6 and 55.5, respectively.

4.3.2.2 Lattice Parameter Determination

Single-crystal neutron diffraction data were collected by Nolas *et al.*[225] from 15 K to 295 K using the HB2a four-circle diffractometer at the High-Flux Isotope Reactor at Oak Ridge National Laboratory.[225] The 331 reflection from a Ge monochromator at a take-off angle of 45° was used, which gives the neutron wavelength of 1.0037 Å for this instrument configuration. More details can be found elswhere.[225]

4.3.2.3 Heat Capacity Measurement

A shiny black boule of 2.6968 g sample was loaded in the adiabatic calorimeter. The sample loading procedure was the same as for Na_8Si_{46}, described in Section 4.2.2.3. The measurement of heat capacity was carried out from the temperature 29 to 302 K by an adiabatic calorimeter operated in a heat-pulse mode as described in Section 2.4.

4.3.3 Results and Discussion

4.3.3.1 Lattice Parameter and Thermal Expansion

The lattice parameters[225] from neutron diffraction are listed in Table 4.4 and agree well with an earlier report.[256] They were fitted by equation (4.2.1) through a least-squares procedure. The best fitting parameters were $a_0 = 10.709$ Å, $a_1 = 8.234 \times 10^{-7}$ A K^{-2} and $a_2 = -1.464 \times 10^{-9}$ Å K^{-3}. The volume thermal expansion coefficients of $Sr_8Ga_{16}Ge_{30}$ were calculated from equation (1.2.6). At 298.15 K, the volume thermal expansion coefficient of $Sr_8Ga_{16}Ge_{30}$ is $(3.0 \pm 0.7)\times10^{-5}$ K^{-1}. The error in thermal expansion coefficient, especially at the high temperature region, is due to the large uncertainty of lattice parameters.[225]

Table 4.4. Experimental Lattice Parameters of $Sr_8Ga_{16}Ge_{30}$. [225]

T/K	a/Å	T/K	a/Å
15	10.708	230	10.734
85	10.715	295	10.743
155	10.723		

4.3.3.2 Experimental Heat Capacity

The experimental heat capacity is given in Table 4.5 and shown in Figure 4.11. There is no heat capacity anomaly in the experimental temperature range. The heat capacity of the sample comprised 15% of the total heat capacity at 300 K and 10% around 30 K.

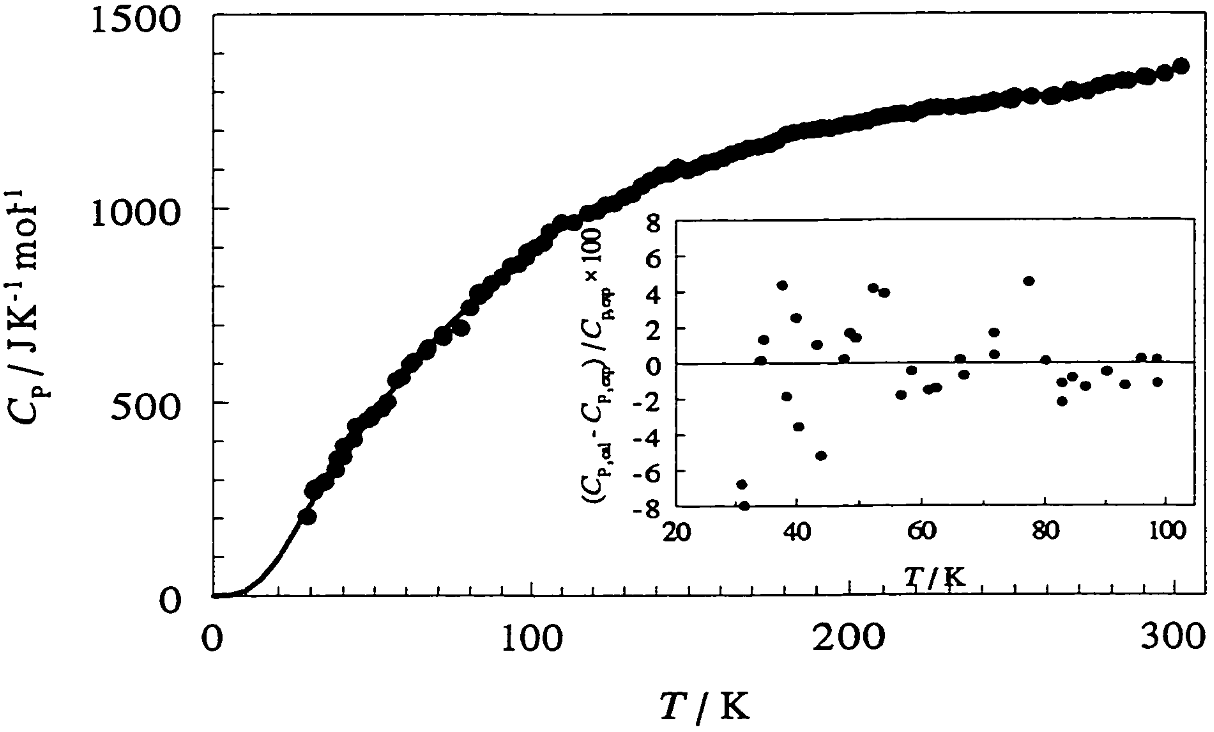

Figure 4.11. Heat capacity of $Sr_8Ga_{16}Ge_{30}$. • and — represent heat capacities from experiment and extrapolation, respectively, as described in the text. The inset diagram indicates the difference between the experimental and fitted heat capacity data. See text for details.

Table 4.5. Experimental Heat Capacity of $Sr_8Ga_{16}Ge_{30}$.

T/K	C_P/J K^{-1} mol^{-1}	*T*/K	C_P/J K^{-1} mol^{-1}
29.01	205	90.16	824
31.07	270	93.06	851
31.49	280	95.79	857
34.14	294	98.48	876
34.61	297	98.59	888
37.66	326	101.42	899
38.36	356	104.22	912
39.99	360	106.00	940
40.37	388	109.88	964
43.39	405	113.85	964
44.02	439	118.43	988
47.68	456	121.61	993
48.66	459	124.07	1009
49.54	470	126.76	1012
52.31	484	129.76	1029
54.01	501	132.40	1037
56.77	558	135.39	1057
58.44	566	138.19	1073
61.19	597	141.07	1085
62.40	608	143.85	1088
66.20	631	145.10	1094
66.81	642	146.69	1106
71.74	668	149.53	1097
71.78	676	152.59	1106
77.27	692	155.21	1116
77.29	692	158.02	1120
80.09	745	160.82	1129
82.80	775	163.53	1140
82.82	784	166.44	1147
84.54	786	169.15	1156
86.72	806	172.09	1158

Continued...

Table 4.5. (continued).

T/K	C_P/J K^{-1} mol^{-1}	T/K	C_P/J K^{-1} mol^{-1}
174.94	1162	237.44	1264
175.36	1164	240.55	1265
177.56	1173	241.17	1269
180.48	1189	242.62	1270
182.98	1195	243.53	1274
186.07	1199	247.75	1277
188.63	1201	248.80	1275
190.60	1203	249.81	1285
191.58	1206	254.88	1285
193.98	1205	260.88	1283
197.07	1211	261.93	1285
199.39	1216	262.05	1288
202.58	1219	266.79	1293
204.93	1222	267.51	1302
208.06	1231	268.61	1297
210.43	1236	272.57	1298
213.51	1240	276.05	1311
215.79	1242	278.88	1319
218.99	1241	282.91	1325
221.09	1249	284.99	1325
224.30	1256	289.99	1336
226.46	1258	291.23	1334
230.24	1259	296.81	1344
234.10	1259	302.03	1362
236.38	1262		

$(C_P - C_V)$ can be calculated from equation (1.2.5). From the thermal expansion coefficients, the theoretical bulk modulus[216] and the experimental lattice parameters,[225] $(C_P - C_V)$ is 10 J K^{-1} mol^{-1} at 300 K, corresponding to 0.7% of C_P.

Figure 4.11 shows that the heat capacity of $Sr_8Ga_{16}Ge_{30}$ increases quickly as the temperature increases. For example, the heat capacity at 150 K is already about 80% of the Dulong-Petit value, $3NR$ (1347 J K^{-1} mol^{-1}). From this, it is concluded that the optic modes of $Sr_8Ga_{16}Ge_{30}$ have low vibrational frequencies and are excited at low temperatures. It is evident that the heat capacity contribution from the optic modes is much more important than from acoustic modes due to the large number of atoms in the unit cell. At 300 K, the heat capacity of $Sr_8Ga_{16}Ge_{30}$ has the classical Dulong-Petit value meaning that optic modes and acoustic modes are virtually fully excited.

One of the interesting properties of $Sr_8Ga_{16}Ge_{30}$ is that the heat capacity closely obeys the Neumann-Kopp law, *i.e.*, $C_P(Sr_8Ga_{16}Ge_{30}) \cong 8C_P(Sr) + 16C_P(Ga) + 30C_P(Ge)$. The calculated heat capacity from Sr,[257] Ge,[158] and Ga[258-260] is shown in Figure 4.12. The additivity property can be ascribed to the similar energy of the clathrate framework and the diamond phase structure, and weak guest-host interactions.

4.3.3.3 Thermodynamic Stability

In order to calculate thermodynamic functions, complete low-temperature heat capacity data are required. Ideally, if the full vibrational spectrum were known and correctly assigned, the optic contribution to the heat capacity could be calculated. However, detailed vibrational assignments of $Sr_8Ga_{16}Ge_{30}$ currently are not available.

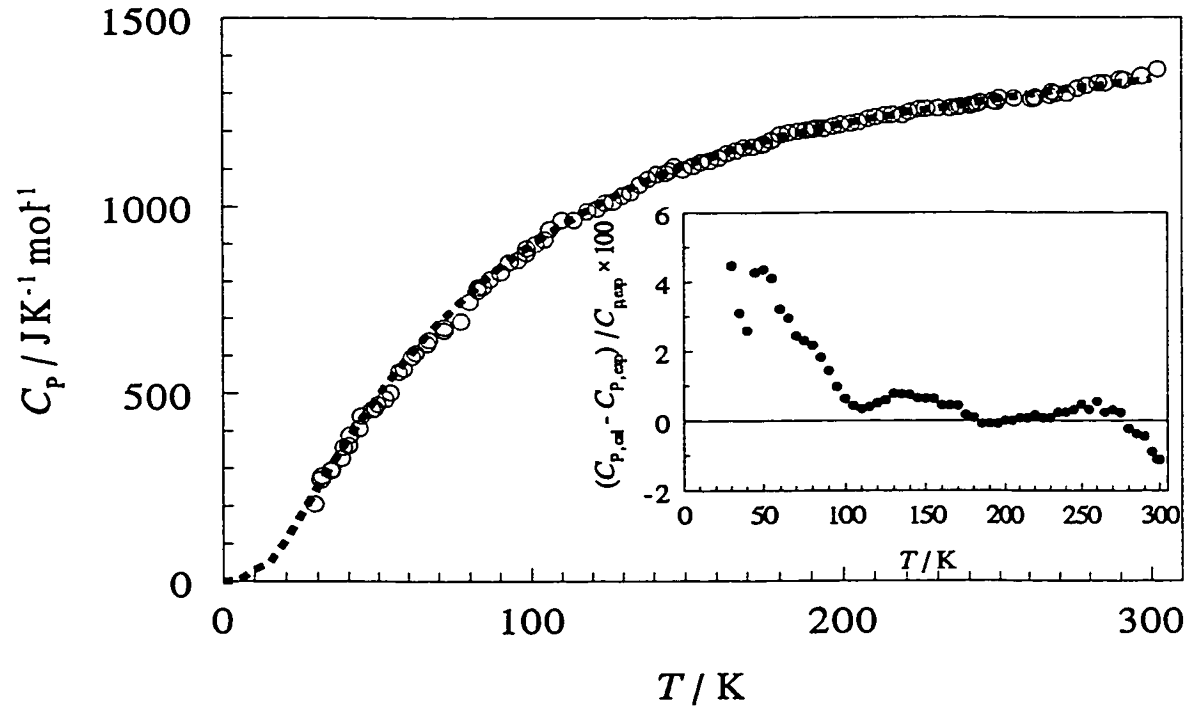

Figure 4.12. Heat capacities of $Sr_8Ga_{16}Ge_{30}$ from experiment and the Neumann-Kopp law. o, experimental data; ▪▪▪, the Neumann-Kopp value, as discussed in the text. The $(C_{p,cal} - C_{p,exp})/C_{p,exp}\times 100$ is the error of calculated heat capacity from the Neumann-Kopp law relative to experimental values. See text for details.

Hence, experimental heat capacity data below 100 K were extrapolated to 0 K with equation (1.2.27) through least-squares fitting procedure, and are as shown in Figure 4.12. The best-fit Debye temperature and the Einstein temperature are θ_D = 164 K and θ_E = 373 K; m = 29 and n = 25. The average fit deviation is 1.7% from the experimental heat capacity. Heat capacities below 30 K were derived from equation (1.2.27).

Thermodynamic function increments relative to 0 K, calculated from heat capacity, are listed in Table 4.6. The entropy of formation of $Sr_8Ga_{16}Ge_{30}$ was calculated from the entropies of the elements[158,257-260] and the absolute entropy of $Sr_8Ga_{16}Ge_{30}$ with the assumption of $S_0 = 0$, and it increases with temperature but is found to be negative below room temperature (Table 4.6). This means the entropy term decreases the thermodynamic stability of the germanium clathrate from its elements below room temperature. At 298.15 K, the entropy of formation of $Sr_8Ga_{16}Ge_{30}$ has the value of -52 ± 11 J K^{-1} mol^{-1}. The entropy change for the reaction, $8Sr + 16Ga + 30Ge \rightarrow Sr_8Ga_{16}Ge_{30}$, is relatively small. The error of S_T-S_0 of $Sr_8Ga_{16}Ge_{30}$ is the major source of uncertainty in $\Delta_f S$. Since Ge clathrates and Si clathrates have energies quite close to those of their diamond phases, the lower $\Delta_f S$ of $Sr_8Ga_{16}Ge_{30}$ compared to that of Na_8Si_{46} ($\Delta_f S^0_{298.15}$ = 32 ± 7 J K^{-1} mol^{-1}, Section 4.2.3.4) and especially the temperature-dependence of $\Delta_f S$ (Table 4.3 and 4.6), reflects the higher synthesis temperature[231] (1170 ~ 1270 K for $Sr_8Ga_{16}Ge_{30}$) compared to that of Na_8Si_{46} (770 ~ 870 K).[215]

Table 4.6. Thermodynamic Properties of $Sr_8Ga_{16}Ge_{30}$.

T/K	C_P/J K^{-1} mol^{-1}	$(H_T$-$H_0)$/kJ mol^{-1}	$(S_T$-$S_0)$/J K^{-1} mol^{-1}	$(G_T$-$G_0)$/kJ mol^{-1}	$\Delta_f S$/J K^{-1} mol^{-1}
5	1.65	0.00412	0.823	0.000	-0.35
10	13.2	0.0412	4.94	-0.0082	-6.2
15	43.8	0.184	15.5	-0.049	-15
20	96.8	0.535	34.9	-0.164	-24
25	165	1.19	63.5	-0.398	-34
30	237	2.19	99.7	-0.801	-43
35	306	3.55	141	-1.40	-51
40	370	5.24	186	-2.21	-57
45	421	7.22	233	-3.26	-61
50	475	9.45	280	-4.54	-65
55	526	12.0	328	-6.05	-67
60	579	14.7	376	-7.81	-69
65	626	17.7	424	-9.81	-70
70	671	21.0	472	-12.1	-71
75	712	24.4	520	-14.5	-71
80	751	28.1	567	-17.3	-72
85	790	31.9	613	-20.2	-72
90	827	36.0	660	-23.4	-72
95	861	40.2	705	-26.8	-72
100	893	44.6	750	-30.4	-72
105	922	49.1	794	-34.3	-72
110	949	53.8	838	-38.4	-72
115	972	58.6	881	-42.7	-72
120	994	63.5	923	-47.2	-71
125	1014	68.5	964	-51.9	-71
130	1032	73.7	1000	-56.9	-70
135	1051	78.9	1040	-62.0	-70
140	1069	84.2	1080	-67.3	-69
145	1086	89.6	1120	-72.7	-69
150	1102	95.0	1160	-78.4	-68
155	1116	101	1190	-84.3	-67
160	1131	106	1230	-90.3	-67

Continued...

Table 4.6. (continued).

T/K	C_P/J K^{-1} mol^{-1}	$(H_T\text{-}H_0)$/kJ mol^{-1}	$(S_T\text{-}S_0)$/J K^{-1} mol^{-1}	$(G_T\text{-}G_0)$/kJ mol^{-1}	$\Delta_f S$/J K^{-1} mol^{-1}
165	1144	112	1260	-96.5	-66
170	1156	118	1300	-103	-66
175	1170	123	1330	-110	-65
180	1182	129	1370	-116	-65
185	1193	135	1400	-123	-64
190	1202	141	1430	-130	-64
195	1211	147	1460	-137	-63
200	1219	153	1490	-145	-63
205	1226	160	1520	-152	-62
210	1232	166	1550	-160	-62
215	1239	172	1580	-168	-61
220	1246	178	1610	-176	-61
225	1252	184	1640	-184	-61
230	1258	191	1660	-192	-60
235	1263	197	1690	-201	-60
240	1268	203	1720	-209	-59
245	1274	210	1740	-218	-59
250	1278	216	1770	-227	-59
255	1286	222	1800	-235	-58
260	1290	229	1820	-245	-58
265	1298	235	1850	-254	-57
270	1303	242	1870	-263	-57
275	1310	248	1890	-272	-56
280	1318	255	1920	-282	-55
285	1326	261	1940	-292	-55
290	1334	268	1960	-302	-54
295	1342	275	1990	-311	-53
298.15	1348	279	2000	-318	-52
300	1351	282	2010	-321	-52

4.3.3.4 Apparent Debye Temperature

The temperature dependence of the apparent Debye temperature, Θ_D, can be derived from the total heat capacity C_V with equation (1.2.21). C_V was calculated from the present experimental C_P and $(C_P - C_V)$ discussed in Section (4.3.3.2). The apparent Θ_D is shown in Figure 4.13. It does not change very much between 50 K and 260 K but decreases drastically at higher temperatures due to the anharmonicity of lattice vibrations. The averaged Θ_D between 50 K and 260 K has the value of 300 ± 12 K.

4.3.3.5 Mean Free Path of Phonons

The mean free path of phonons, l, is important to understand the mechanism of thermal conductivity of materials and is given by equation (1.4.1). The published thermal conductivity,[231] sound speed[225] and present heat capacities are used to estimate l below room temperatures. The results are shown in Figure 4.14. At 300 K, l is 5 ± 1 Å. The uncertainty of l is mainly from thermal conductivity. The mean free path of phonons has the typical behaviour of an amorphous material, which is due to the scattering of heat carrying acoustic phonons by the rattling of guests in the cages.[227]

4.3.3.6 Grüneisen Parameter

For cubic phases, a convenient way to obtain the Grüneisen parameter is given by equation (1.5.3). The values of γ of $Sr_8Ga_{16}Ge_{30}$ at different temperatures are shown in Figure 4.15. Between 50 and 250 K, γ behaves as a constant with an average of 1.7 ± 0.6.

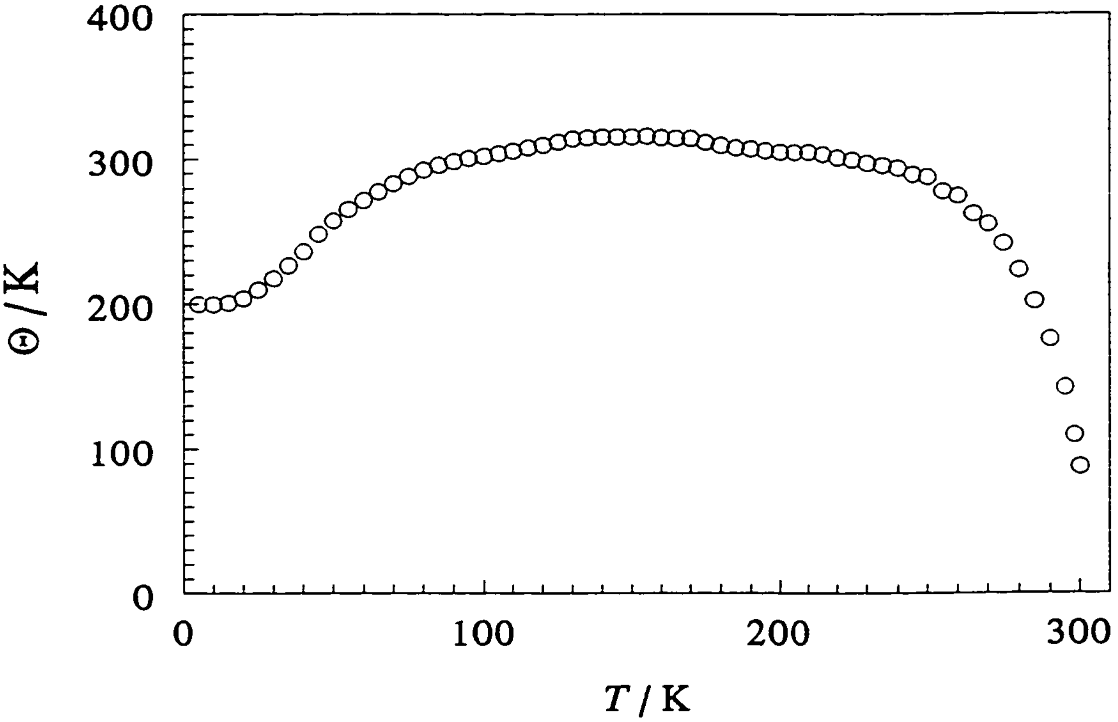

Figure 4.13. Apparent Debye temperature for $Sr_8Ga_{16}Ge_{30}$, calculated from the total heat capacity, C_V, as discussed in the test.

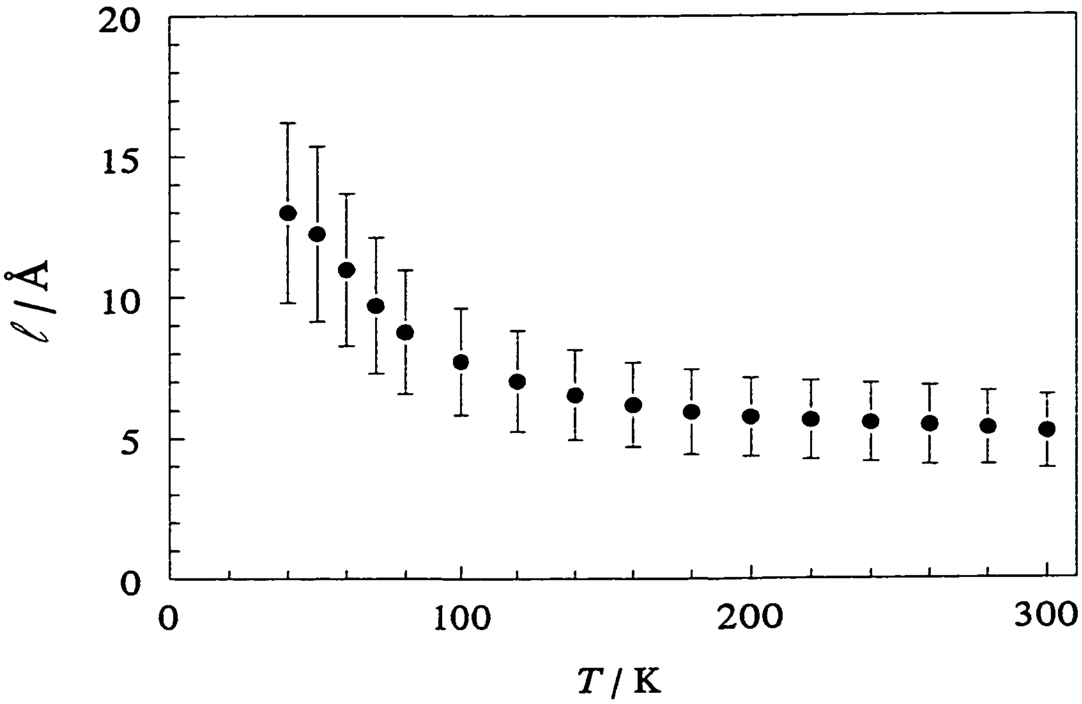

Figure 4.14. Mean free path of phonons of $Sr_8Ga_{16}Ge_{30}$, based on the thermal conductivity data,[231] present heat capacity and the sound velocity.[225] The error bars represent the uncertainty of l, which is estimated from thermal conductivity, sound speed and heat capacity. The uncertainty largely results from the uncertainty in thermal conductivity.

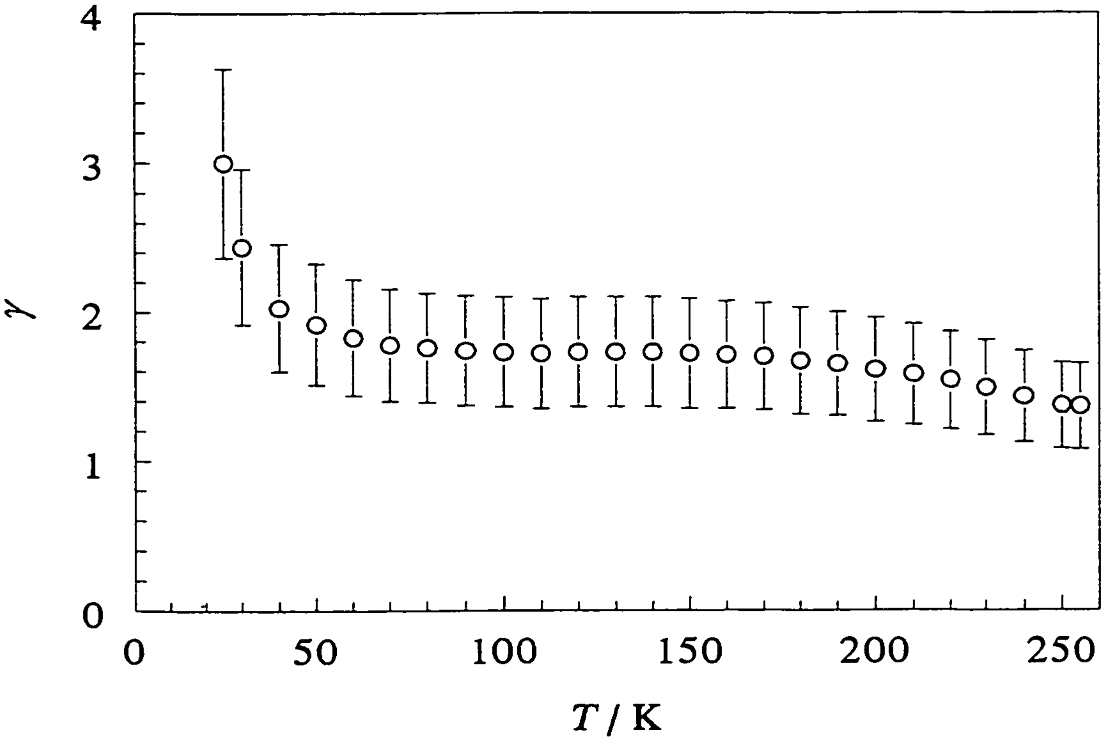

Figure 4.15. Grüneisen parameter for $Sr_8Ga_{16}Ge_{30}$, calculated from equation (1.5.3) as discussed in the text. The error bars indicate the uncertainty of γ, which is largely from the thermal expansion coefficient.

The uncertainty is largely from the thermal expansion coefficient. At lower temperatures γ should tend to zero according to the thermodynamic laws. However, it increases rapidly as temperature decreases. Such behaviour has been observed in Dianin's compound[255] and Na_8Si_{46} in Section 4.2.3.7. It is proposed that the existence of low vibrational frequencies of guests results in the abnormal temperature dependence of the Grüneisen parameter.

4.3.4 Conclusions

The thermal properties of the clathrate $Sr_8Ga_{16}Ge_{30}$ were investigated. The heat capacity below ambient temperature was determined by an adiabatic calorimeter and the entropy and enthalpy relative to 0 K were determined. The isobaric heat capacity, entropy and enthalpy are 1348 J K^{-1} mol^{-1}, 2000 J mol^{-1} K^{-1} and 279 kJ mol^{-1} at 298.15 K, respectively. The heat capacity obeys the Neumann-Kopp law, which can be ascribed to the structural similarity between the clathrate and the diamond phase, and weak guest-host interactions. The apparent Θ_D is a constant with an average value of 300 ± 12 K between 50 and 260 K. The mean free path of phonons is characteristic of amorphous materials indicating that the rattling of guest Sr atoms in the cages of $Sr_8Ga_{16}Ge_{30}$ effectively scatters the phonons. The Grüneisen parameter of $Sr_8Ga_{16}Ge_{30}$ is 1.7 ± 0.6 between 50 K and 250 K.

4.4 Thermal Properties of $Sr_8Zn_8Ge_{38}$ Clathrate

4.4.1 Structure

Neutron powder diffraction reveals that the $Sr_8Zn_8Ge_{38}$ has the structure of a type I clathrate hydrate, space group $Pm\overline{3}n$ and lattice parameter of 10.7055(1) Å at 300 K.[261] This is slightly greater than the lattice parameter for K_8Ge_{46}, 10.66 Å. [216] The zinc and germanium atoms are randomly distributed through the framework.[261]

4.4.2 Experimental Methods and Characterization

4.4.2.1 Synthesis

The sample of $Sr_8Zn_8Ge_{38}$ was provided by Marlow Industries, Inc. It was synthesized in a fashion similar to $Sr_8Ga_{16}Ge_{30}$.[225] The sample contained about 1% of another phase and the detailed analysis of the sample is ongoing.[261]

4.4.2.2 Heat Capacity Measurement

The sample was several shiny black boules with a mass of 3.002 g and they were loaded in the same procedure as for Na_8Si_{46} described in Section 4.2.2.3. The heat capacity was determined from 29 to 303 K. The measurement of heat capacity was carried out by an automated adiabatic calorimeter discussed in the Section 2.4.

4.4.3 Results and Discussion

4.4.3.1 Experimental Heat Capacity

The experimental heat capacity of $Sr_8Zn_8Ge_{38}$ is shown in Figure 4.16 and

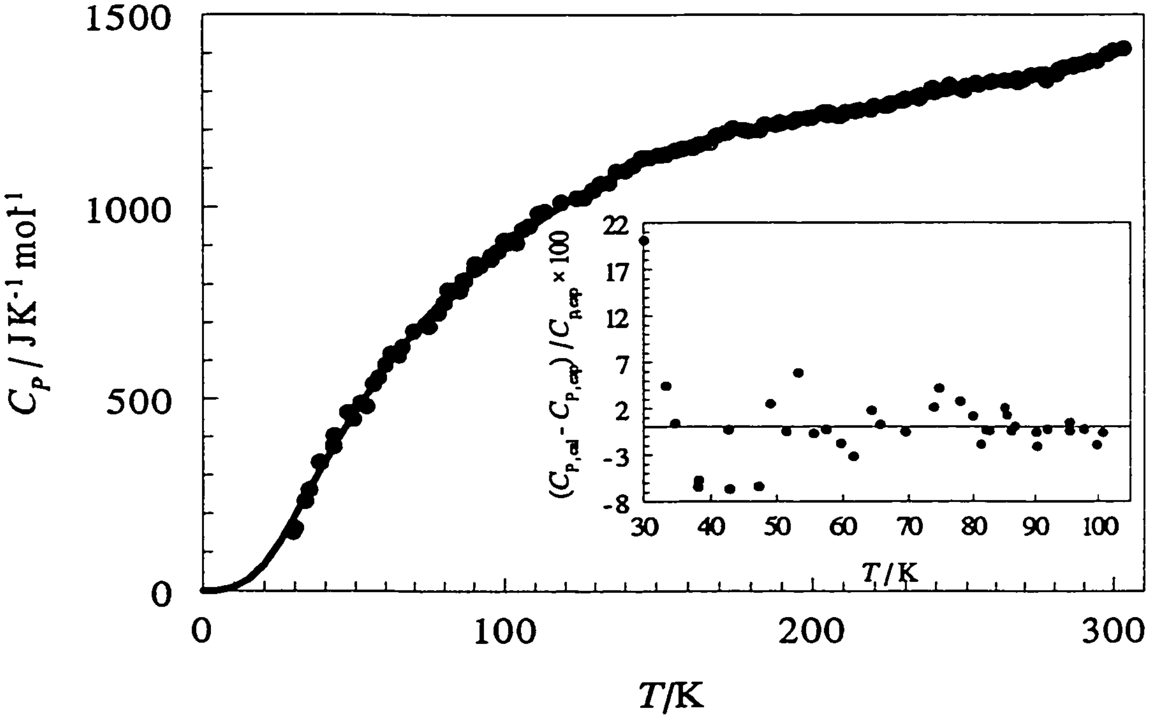

Figure 4.16. Heat capacity of $Sr_8Zn_8Ge_{38}$. ● experimental values and —, extrapolated values (<100 K) from equation (1.2.27) as described in the text. The inset diagram indicates the difference between the experimental and fitted heat capacity data. See text for details.

summarized in Table 4.7. No heat capacity anomalies were observed within the experimental temperature range. The heat capacity of the sample comprised of 15% of the total heat capacity at 300 K and about 10% around 30 K.

The experimental data needed to derive the theoretically more interesting C_V from equation (1.2.5) require thermal expansion coefficient and compressibility. They are not available for $Sr_8Zn_8Ge_{38}$. However, the theoretical compressibility of Ge clathrand has been reported.[216] $Sr_8Zn_8Ge_{38}$ and $Sr_8Ga_{16}Ge_{30}$ have similar frameworks. Their thermal expansions are expected to be very close. As an approximation, the theoretical compressibility 61.3 GPa[216] and the thermal expansion coefficient of $Sr_8Ga_{16}Ge_{30}$ in Section 4.3.3.1 were used to estimate $(C_P - C_V)$ of $Sr_8Zn_8Ge_{38}$. This should not result in significant uncertainty of C_V since $(C_P - C_V)$ is small. With these approximations, $(C_P - C_V)$ of $Sr_8Zn_8Ge_{38}$ corresponds to 0.8% of C_P at 300 K, less at lower temperatures.

The experimental heat capacity approaches the Dulong-Petit value, 3*NR* (= 1347 J K mol^{-1}), at 280 K, which indicates that all vibrational modes are virtually fully excited at this temperature. Due to the large numbers of atoms in the unit cell of $Sr_8Zn_8Ge_{38}$, it can be deduced that the heat capacity contributions are mainly from optic modes.

The heat capacities of $Sr_8Zn_8Ge_{38}$ calculated from those of Sr,[257] Zn[262,263] and Ge[158] (Neumann-Kopp values) are lower than the experimental values by an average of 3.5%, as shown in Figure 4.17. The difference likely results from the fact that Zn-Ge and Ge-Ge bonds have different bond energies.

Table 4.7. Experimental Heat Capacity of $Sr_8Zn_8Ge_{38}$.

T/K	C_P/J K^{-1} mol^{-1}	T/K	C_P/J K^{-1} mol^{-1}
29.28	152	95.43	865
30.06	163	95.43	873
33.39	233	97.68	885
34.74	262	99.75	913
38.15	333	100.69	907
38.22	332	102.95	916
42.62	375	103.85	908
42.81	403	105.90	942
47.24	464	107.92	951
49.04	445	111.11	984
51.47	488	113.15	988
53.31	479	118.48	1012
55.63	537	123.84	1023
57.50	556	126.35	1025
59.72	588	129.19	1044
61.61	617	131.70	1061
64.35	614	134.59	1063
65.71	636	137.08	1092
69.51	677	139.97	1094
73.85	696	142.47	1107
74.69	689	145.37	1127
77.93	725	147.77	1127
79.87	751	150.83	1134
81.16	785	153.10	1136
82.02	779	156.15	1146
82.58	784	158.46	1151
85.06	783	161.51	1154
85.39	791	163.72	1162
86.13	810	166.86	1167
86.70	810	169.06	1185
90.15	839	172.23	1193
90.25	853	174.21	1204
91.91	848	177.53	1200

Continued...

Table 4.7. (continued).

T/K	C_P/J K^{-1} mol^{-1}	T/K	C_P/J K^{-1} mol^{-1}
179.39	1197	243.44	1306
182.89	1199	244.41	1317
184.62	1214	248.28	1306
188.20	1213	249.16	1303
189.43	1219	249.80	1314
189.86	1217	253.10	1322
193.47	1220	253.99	1317
194.60	1225	257.88	1324
195.12	1228	258.71	1326
198.33	1230	262.68	1328
199.72	1231	262.73	1328
203.40	1244	263.74	1328
204.82	1238	267.40	1335
205.48	1245	267.53	1324
208.52	1235	269.43	1331
209.87	1240	272.09	1342
210.64	1246	275.04	1344
213.65	1248	276.81	1344
214.93	1251	277.27	1329
218.76	1253	280.70	1344
219.99	1262	281.50	1357
223.82	1262	283.14	1362
224.81	1265	286.24	1366
225.05	1268	286.50	1369
228.84	1275	288.92	1371
229.65	1277	290.87	1376
230.03	1281	292.17	1380
233.82	1286	294.30	1380
234.53	1282	297.67	1397
235.07	1290	299.64	1407
238.87	1309	303.15	1412
239.48	1298		

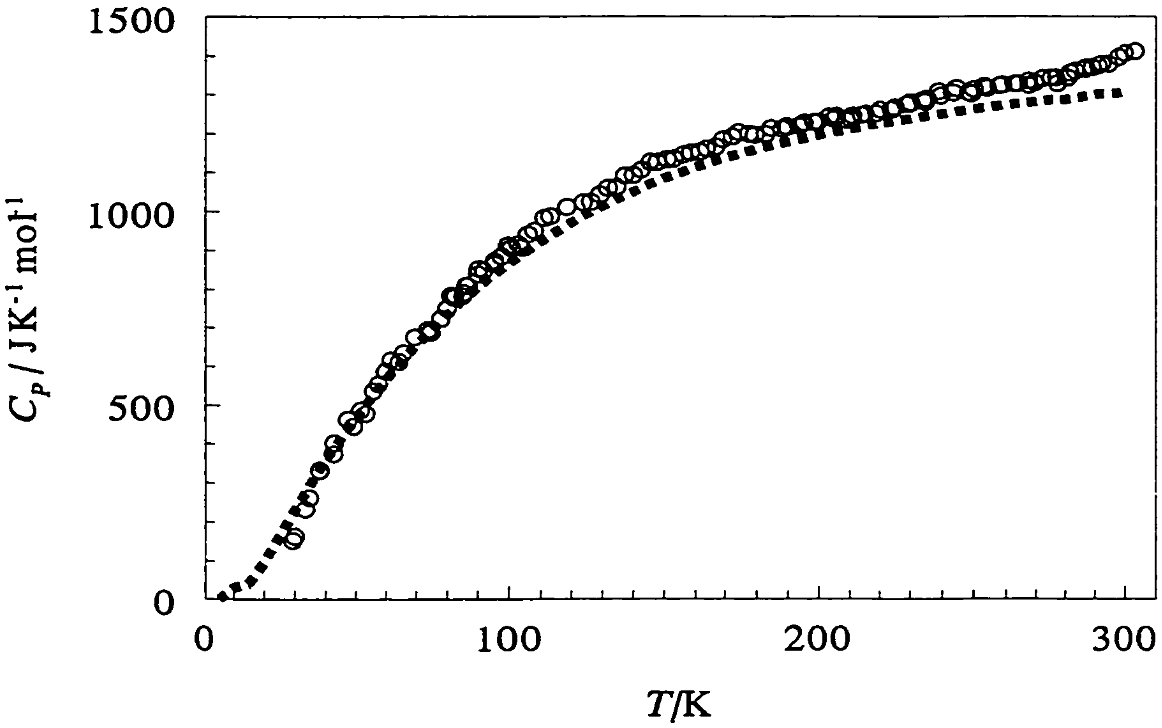

Figure 4.17. Heat capacity of $Sr_8Zn_8Ge_{38}$. ○, from experiment and ▪▪▪, from the Neumann-Kopp law, as described in the text.

4.4.3.2 Thermodynamic Stability

The calculation of complete thermodynamic functions requires heat capacity data below 30 K. Since the vibrational frequencies to determine heat capacity contributions from optic modes are not available, the experimental heat capacities below 100 K were used to fit equation (1.2.27) through a least-squares procedure. The best fit parameters are θ_D = 198 K and θ_E = 382 K; m = 36 and n = 18. The average fitted deviation is 1.9% from the experimental heat capacity. The heat capacities below 30 K were obtained from the extrapolation of equation (1.2.27), shown in Figure 4.16.

The thermodynamic functions derived from the heat capacity are listed in Table 4.8. The entropy of formation of $Sr_8Zn_8Ge_{38}$ can be calculated from those of Sr,[257] Zn,[262,263] Ge[158] and the present data for $Sr_8Zn_8Ge_{38}$ with the assumption of $S_0 = 0$. At 298.15 K, $Sr_8Zn_8Ge_{38}$ has a $\Delta_f S^\circ$ of 18 ± 10 J K^{-1} mol^{-1}, which is quite small. The uncertainty of $\Delta_f S$ mainly results from the uncertainty of $S_T - S_0$ of $Sr_8Zn_8Ge_{38}$.

The positive entropy increment decreases the Gibbs energy of the reaction, $8Sr + 8Zn + 38Ge \rightarrow Sr_8Zn_8Ge_{38}$, and hence stabilizes $Sr_8Zn_8Ge_{38}$ formed from elements. The quantitative calculation of Gibbs energy of reaction requires additional thermodynamic data such as enthalpy of formation.

4.4.3.3 Apparent Debye Temperature

The apparent Debye temperature Θ_D can reveal the anharmonicity of vibration of the lattice. It can be obtained from the total C_V with the Debye model, equation (1.2.21).

Table 4.8. Thermodynamic Properties of $Sr_8Zn_8Ge_{38}$.

T/K	C_P/J K^{-1} mol^{-1}	$(H_T\text{-}H_0)$/kJ mol^{-1}	$(S_T\text{-}S_0)$/J K^{-1} mol^{-1}	$(G_T\text{-}G_0)$/kJ mol^{-1}	$\Delta_f S$/J K^{-1} mol^{-1}
5	1.12	0.00280	0.559	0.000	-0.27
10	8.94	0.0280	3.35	-0.0055	-6.0
15	30.1	0.126	10.6	-0.034	-13
20	69.5	0.375	24.3	-0.112	-18
25	127	0.87	45.7	-0.28	-25
30	195	1.67	74.5	-0.57	-31
35	267	2.82	110	-1.02	-36
40	338	4.33	150	-1.67	-40
45	405	6.19	194	-2.52	-41
50	468	8.38	240	-3.60	-42
55	527	10.9	287	-4.92	-41
60	581	13.6	335	-6.47	-41
65	631	16.7	384	-8.27	-39
70	678	19.9	432	-10.3	-38
75	721	23.4	480	-12.6	-36
80	762	27.1	528	-15.1	-34
85	800	31.0	575	-17.9	-33
90	836	35.1	622	-20.9	-31
95	870	39.4	668	-24.1	-30
100	901	43.8	714	-27.6	-28
105	931	48.4	758	-31.2	-26
110	958	53.1	802	-35.1	-25
115	984	58.0	846	-39.3	-23
120	1009	63.0	888	-43.6	-22
125	1032	68.1	930	-48.1	-20
130	1053	73.3	970	-52.9	-19
135	1073	78.6	1011	-57.9	-17
140	1092	84.0	1050	-63.0	-16
145	1110	89.5	1089	-68.4	-14
150	1126	95.1	1127	-74.0	-13
155	1141	101	1164	-79.6	-12
160	1155	107	1200	-85.5	-10

Continued...

Table 4.8. (continued).

T/K	C_P/J K^{-1} mol^{-1}	(H_T-H_0)/kJ mol^{-1}	(S_T-S_0)/J K^{-1} mol^{-1}	(G_T-G_0)/kJ mol^{-1}	$\Delta_f S$/J K^{-1} mol^{-1}
165	1168	112	1236	-91.6	-9.2
170	1181	118	1271	-97.9	-8.0
175	1192	124	1305	-104	-6.8
180	1202	130	1339	-111	-5.7
185	1212	136	1372	-118	-4.6
190	1221	142	1405	-125	-3.5
195	1229	148	1436	-132	-2.5
200	1237	155	1468	-139	-1.5
205	1244	161	1498	-146	-0.6
210	1251	167	1528	-154	0.3
215	1258	173	1558	-162	1.2
220	1264	180	1587	-170	2.1
225	1271	186	1615	-178	2.9
230	1277	192	1643	-186	3.7
235	1284	199	1671	-194	4.6
240	1290	205	1698	-202	5.4
245	1298	212	1725	-211	6.2
250	1305	218	1751	-220	7.0
255	1313	225	1777	-229	7.9
260	1321	231	1802	-237	8.7
265	1329	238	1828	-247	9.7
270	1338	245	1853	-256	11
275	1347	251	1877	-265	12
280	1357	258	1902	-275	13
285	1367	265	1926	-284	14
290	1377	272	1949	-294	15
295	1387	279	1973	-304	17
298.15	1393	283	1988	-310	18
300	1396	286	1996	-313	18

The calculation of C_V was discussed in Section 4.4.3.1. The derived apparent Θ_D of $Sr_8Zn_8Ge_{38}$ has a maximum value of 300 K at T = 90 K, as shown in Figure 4.18. Compared with maximum apparent Θ_D of germanium (370 K),[158] the decrease of Θ_D of $Sr_8Zn_8Ge_{38}$ can be ascribed to the weaker bond strength between framework atoms, which also can be observed in the bond length in $Sr_8Zn_8Ge_{38}$ and K_8Ge_{46}, as indicated in Section 4.4.1. The apparent Θ_D decreases above T = 250 K due to the anharmonicity of the lattice vibrations.

4.4.3.4 Grüneisen Parameter

The Grüneisen parameter is important to understand the anharmonic vibrations of the lattice especially for clathrates, for which resonant scattering of heat-carrying phonons by the rattling of guests in the clathrate cages can be revealed.

The experimental lattice parameter 10.7055 Å at 300 K was used to calculate the molar volume.[261] The compressibility, 61.3 GPa,[216] the thermal expansion coefficient and the isobaric heat capacity C_V have been discussed in 4.4.3.1. These data were used to calculate the Grüneisen parameter of $Sr_8Zn_8Ge_{38}$ from equation (1.5.3). The approximation (thermal expansion of $Sr_8Ga_{16}Ge_{30}$) used in the calculation might increase the uncertainty of the Grüneisen parameter. Nevertheless, the approximate Grüneisen parameter can provide useful information regarding the anharmonicity of lattice vibrations. The results are shown in Figure 4.19. As expected, $Sr_8Zn_8Ge_{38}$ has a Grüneisen parameter-temperature profile similar to $Sr_8Ga_{16}Ge_{38}$. Below 50 K, the

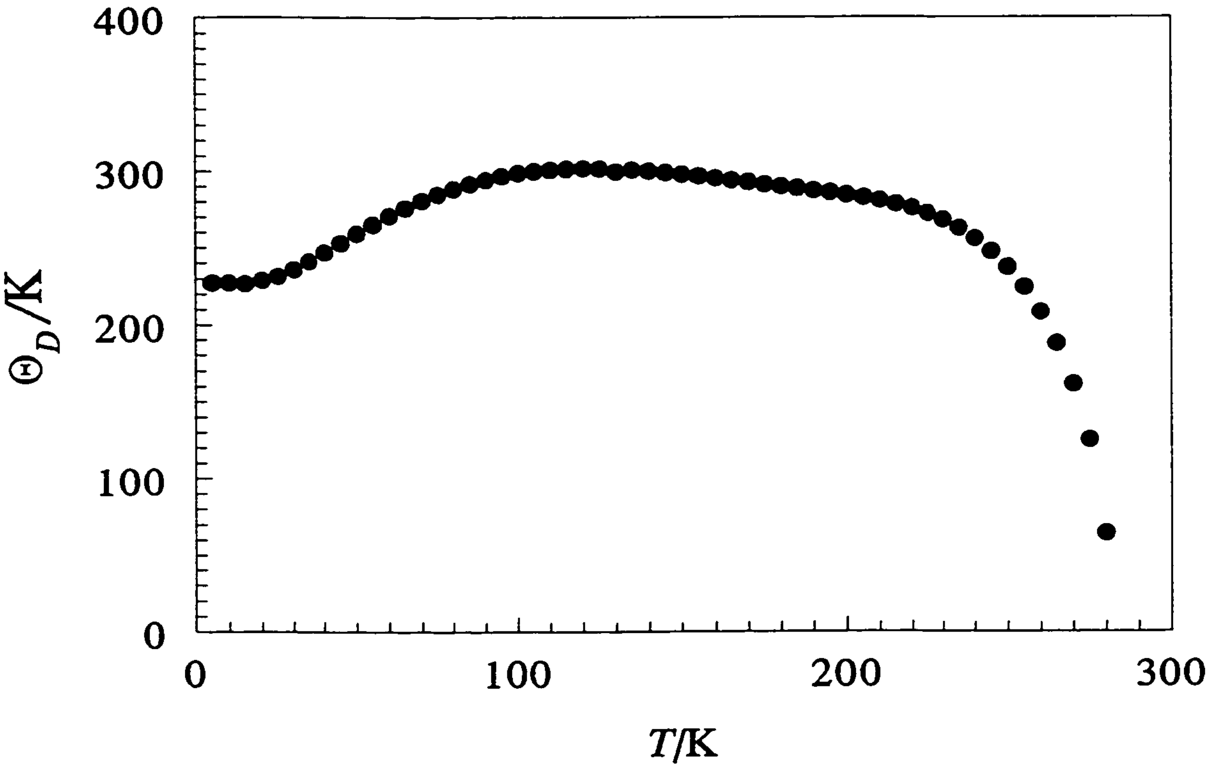

Figure 4.18. Apparent Debye temperature of $Sr_8Zn_8Ge_{38}$, calculated from the total isochoric capacity, C_V, as described in the text.

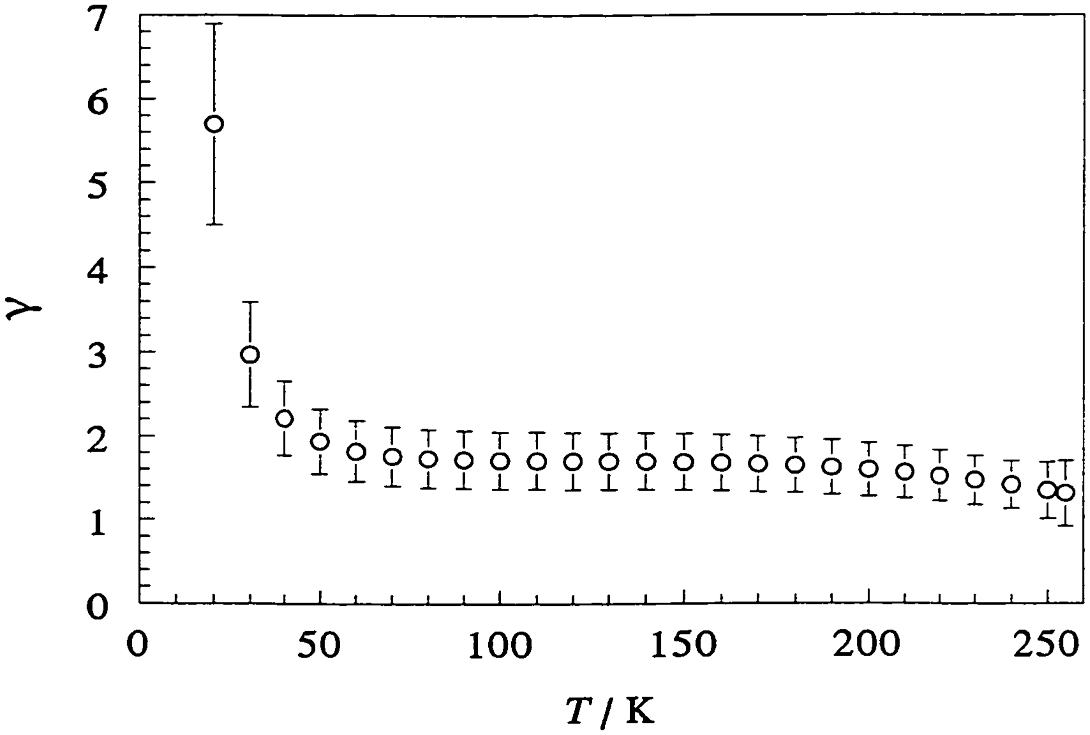

Figure 4.19. Grüneisen parameter of $Sr_8Zn_8Ge_{38}$, calculated from the thermal expansion coefficient of $Sr_8Ga_{16}Ge_{30}$, total C_V of $Sr_8Zn_8Ge_{38}$, compressibility[216] and experimental lattice parameter,[261] as discussed in the text. The error bars indicate the uncertainty of γ which is largely from the uncertainty of the thermal expansion coefficient.

increase of γ is due to the scattering of heat carrying phonons by the rattling of Sr atoms in the cages as discussed in Na_8Si_{46} and $Sr_8Ga_{16}Ge_{38}$.

4.4.4 Conclusions

The thermal properties of $Sr_8Zn_8Ge_{38}$ below room temperature were determined. At 298.15 K, the heat capacity, $H_T - H_0$, and $S_T - S_0$ are 1393 J K^{-1} mol^{-1}, 283 kJ mol^{-1}, and 1988 J K^{-1} mol^{-1}, respectively. The $\Delta_f S^\circ$ has a positive value of 18 J K^{-1} mol^{-1} at 298.15 K, which is important to the thermodynamic stability of $Sr_8Zn_8Ge_{38}$. The maximum apparent Debye temperature is 300 K. The Grüneisen parameter has a temperature profile similar to Na_8Si_{46} and $Sr_8Ga_{16}Ge_{30}$.

4.5 Thermal Properties of $Cs_8Ga_8Sn_{38}$ Clathrate

4.5.1 Structure

Single-crystal X-ray diffraction[264] reveals that $Cs_8Ga_8Sn_{38}$ has the structure of a type I clathrate hydrate. The lattice parameter is 12.0792(1) Å at 300 K with the space group $Pm\bar{3}n$. The Ga and Sn atoms are randomly distributed through the framework. The details can be found elswhere.[264]

4.5.2 Experimental Methods and Characterization

4.5.2.1 Synthesis

The sample was synthesized and supplied by Marlow Industries, Inc. High purity elements were mixed in the appropriate stoichiometric proportions in an argon atmosphere glovebox and reacted for 2 weeks at 823 K inside a tungsten crucible which was itself welded inside a stainless steel canister. The resulting compounds consisted of very small crystals with a shiny, blackish metallic luster that were not visibly reactive in air or moisture. The details can be found elsewhere.[264]

The purity of the sample was analyzed by electron-beam microprobe. The atomic percentages of the sample are 14.9, 14.9, 70.2 for Cs, Ga and Sn, respectively.[264] For $Cs_8Ga_8Sn_{38}$, the ideal atomic percentage are 14.8,14.8 and 70.4, respectively. The directly determined density of the sample agrees well with that from X-ray diffraction.[261]

4.5.2.2 Heat Capacity Measurement

A 1.157 g of a shiny sample of $Cs_8Ga_8Sn_{38}$ was loaded in the calorimeter. The loading procedure was the same as for Na_8Si_{46} described in Section 4.2.2.3. The operation of the adiabatic calorimeter was described in the Section 2.4. The experimental heat capacity data were determined from 37 to 305 K.

4.5.3 Results and Discussion

4.5.3.1 Experimental Heat Capacity

The experimental heat capacity of $Cs_8Ga_8Sn_{38}$ is shown in Figure 4.20 and Table 4.9. It increases smoothly with temperature. The heat capacity of the sample comprised about 5% of the total (sample + vessel) heat capacity in the experimental temperature region. Such a small percentage of heat capacity from the sample does increase the uncertainty of heat capacity especially at low temperatures and makes it difficult to

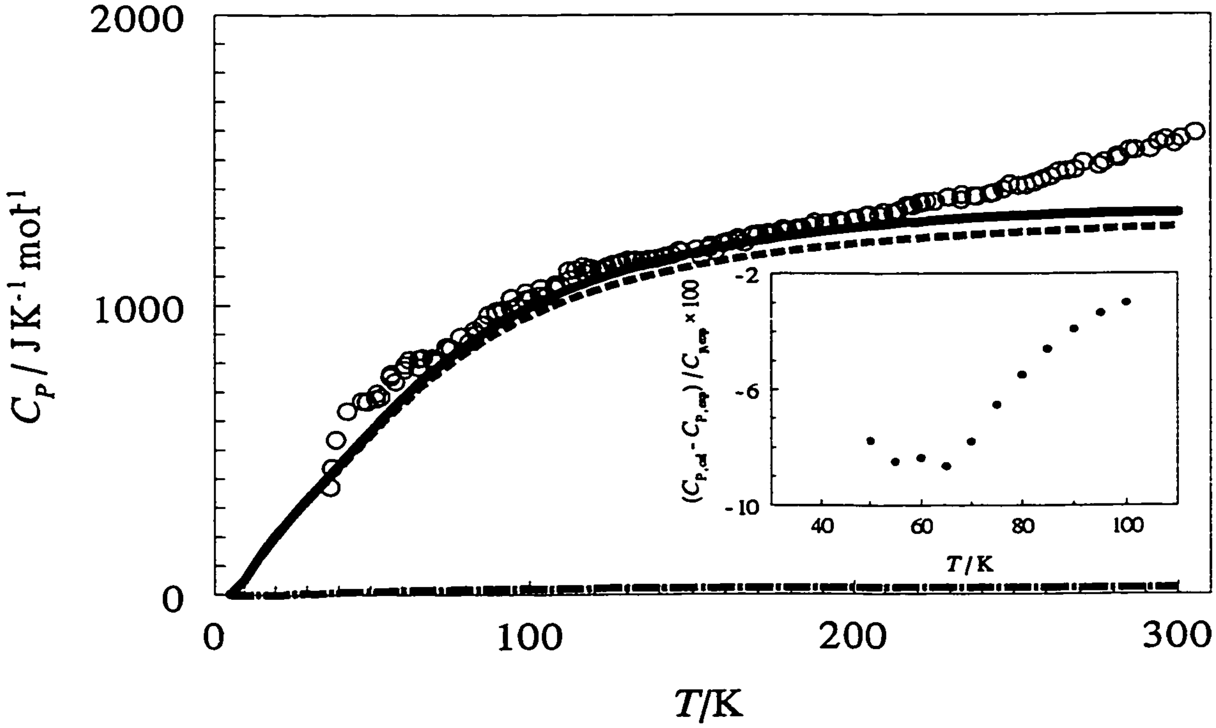

Figure 4.20. Heat capacity of $Cs_8Ga_8Sn_{38}$. ▬ ▪, $C_{acoustic}$; ▪▪▪, C_{optic} ; ▬, C_{cal} and o, experimental heat capacity, as discussed in the text. The inset diagram indicates the difference between the experimental and calculated heat capacity data. See text for details.

Table 4.9. Experimental Heat Capacity of $Cs_8Ga_{16}Sn_{38}$.

T/K	C_P/J K^{-1} mol^{-1}	T/K	C_P/J K^{-1} mol^{-1}	T/K	C_P/J K^{-1} mol^{-1}
37.36	372	89.72	983	136.59	1158
37.94	439	89.89	977	137.31	1158
39.25	536	91.74	986	139.16	1160
42.68	635	94.26	991	141.16	1166
47.40	670	96.12	998	141.88	1169
48.81	668	98.67	1021	143.67	1173
51.75	678	98.83	1044	145.68	1187
52.05	696	100.58	1026	146.52	1184
53.36	684	103.14	1035	151.00	1192
56.34	753	103.40	1060	152.61	1164
56.58	764	105.01	1031	154.85	1195
57.86	737	107.75	1061	155.47	1206
60.82	779	108.07	1073	156.94	1185
61.01	795	109.50	1070	159.35	1213
62.26	813	112.18	1119	159.91	1215
65.23	787	112.64	1090	161.38	1218
65.40	816	114.53	1122	163.87	1230
66.61	819	116.60	1135	164.30	1222
69.60	818	117.16	1113	165.82	1214
69.78	813	118.60	1126	168.38	1238
70.93	806	119.06	1128	168.69	1241
73.97	858	121.73	1120	170.21	1244
74.15	852	123.09	1130	172.82	1242
75.32	854	123.63	1133	173.02	1249
78.33	893	125.63	1141	174.61	1248
81.08	874	127.56	1142	177.32	1255
82.67	914	128.18	1148	177.40	1260
83.22	901	130.15	1155	178.99	1256
85.34	935	132.07	1154	181.73	1260
85.49	936	132.73	1156	181.85	1263
87.00	968	134.68	1153	183.40	1264

Table 4.9. (continued).

T/K	C_P/J K^{-1} mol^{-1}	T/K	C_P/J K^{-1} mol^{-1}
186.21	1272	242.49	1382
187.33	1284	243.56	1385
190.59	1280	246.62	1397
191.71	1281	248.68	1415
195.04	1289	251.30	1409
196.15	1284	253.66	1411
199.50	1294	256.24	1421
200.54	1297	258.61	1432
204.02	1307	261.24	1442
205.04	1309	263.57	1457
208.30	1307	266.14	1461
209.45	1318	268.49	1466
212.61	1315	270.94	1489
214.20	1323	275.69	1479
216.95	1341	277.26	1491
218.53	1340	281.13	1510
220.81	1353	281.70	1503
221.20	1350	284.92	1530
222.82	1355	286.70	1530
225.33	1355	291.36	1534
229.54	1370	293.87	1559
233.64	1361	296.02	1568
233.74	1378	298.67	1553
237.83	1376	300.74	1571
238.35	1372	305.18	1591

reliably extrapolate the experimental heat capacity to 0 K.

The heat capacity of $Cs_8Ga_8Sn_{38}$ increases rapidly with temperature, likely due to the existence of low energy internal vibrational modes. At 220 K, the heat capacity is close to the Dulong-Petit value, $3NR$ (1347 J K^{-1} mol^{-1}).

The Neumann-Kopp value of $Cs_8Ga_8Sn_{38}$ can be calculated from the heat capacity of Cs,[160] Ga,[258-260] and Sn[266] at 298.15 K, the calculated heat capacity is 1492 J K^{-1} mol^{-1}, which is lower than the experimental value by 5%. This is similar to the Si and Ge clathrates already discussed, and likely due to guest-host interactions in $Cs_8Ga_8Sn_{38}$ and the different energies of the clathrate framework and the diamond phase of Sn.

4.5.3.2 Thermal Expansion

The experimentally determined lattice parameter for $Cs_8Ga_8Sn_{38}$ is available only at 300 K.[264] However, the data from 11 K to 300 K were reported for similar clathrates $Cs_8Zn_4Sn_{42}$ and Cs_8Sn_{44}.[264] From these data, it is found that $Cs_8Zn_4Sn_{42}$ and Cs_8Sn_{44} have very close thermal expansion coefficients with a difference of about 1% below 300 K. In order to discuss anharmonic vibration of lattice, it is assumed here that $Cs_8Ga_8Sn_{38}$ has the same thermal expansion as $Cs_8Zn_4Sn_{42}$. Thus the experimental lattice parameters[264] (units in Å) of $Cs_8Zn_4Sn_{42}$ were least-squares fit to equation (4.2.1) with the coefficients of $a_0 = 12.093$ Å, $a_1 = 7.328 \times 10^{-7}$ Å K^{-2} and $a_2 = -1.246 \times 10^{-9}$ Å K^{-3}. At 298.15 K, the thermal expansion coefficient is $(2.5 \pm 0.5) \times 10^{-5}$ K^{-1}. The uncertainty is estimated from the uncertainty in the experimental lattice parameter.

4.5.3.3 Heat Capacity from Raman Spectroscopy

The experimental heat capacity, C_P, is under isobaric conditions. The calculation of the theoretically more interesting heat capacity C_V requires compressibility, thermal expansion coefficients and experimental C_P. The experimental compressibility of $Cs_8Ga_8Sn_{38}$ has not been reported yet. However, it has been confirmed both experimentally and theoretically that the bulk modulus of Ge clathrates and Si clathrates are less than those of their diamond phases by about 10%.[206,226] Hence, the compressibility, 111 GPa,[40] of Sn (cubic) was scaled by 0.9 to estimate the bulk modulus of $Cs_8Ga_8Sn_{38}$ in order to calculate $(C_P - C_V)$ with equation (1.2.5). The required thermal expansion coefficients have been discussed in Section 4.5.3.2. These approximations should not introduce significant uncertainty to $(C_P - C_V)$ which generally is very small for most solids. The molar volume was calculated from experimental lattice parameter[264] of $Cs_8Ga_8Sn_{38}$ and is considered as constant due to its small change (less than 1% for Sn clathrates between 0 K and 300 K).[264] The obtained $(C_P - C_V)$ of $Cs_8Ga_8Sn_{38}$ is less than 2% of C_P below room temperature.

The comparison of heat capacities from vibrational spectroscopy and adiabatic calorimetry can provide a test of lattice dynamical models. Like Na_8Si_{46}, there are 159 optic modes in $Cs_8Ga_8Sn_{38}$ and 3 acoustic modes. The Raman frequencies of $Cs_8Ga_8Sn_{38}$ have been reported recently.[265] Theoretically, there are 18 Raman-active frequencies related to the Sn framework atom vibrations ($3A_{1g}$ + $7E_g$ + $8T_{2g}$) and 2 for the guest vibrations (E_g + T_{2g})[265] where A_{1g} modes are singly degenerate, E_g are doubly degenerate and T_{2g} are triply degenerate. However, the Raman spectroscopy experiment showed only 14 frequencies. The reduced number is likely due to accidental degeneracy given the high symmetry of the structure. Furthermore, the degeneracies of observed frequencies were assigned only for two frequencies based on Raman polarization experiments.[265] They are 132 cm^{-1} (A_{1g}) and 141 cm^{-1} (A_{1g}). The 26 cm^{-1} mode was assigned as T_{2g} based on the similarity of the spectrum to other clathrates.[265] These three frequencies correspond to 5 Raman modes. For the present analysis, the observed other 11 frequencies[265] were considered to evenly share the remaining 41 Raman modes. This means that the 14 observed frequencies represent the 20 expected Raman frequencies. Accounting for degeneracies, the 20 frequencies correspond to 46 modes and are representative of 159 optic modes of $Cs_8Ga_8Sn_{38}$, so the calculated optic contribution to the heat capacity, equation (1.2.18), was taken with a weight of 159/46. A similar method has been successfully used in the discussion of heat capacities of other clathrates.[255]

The calculation of the heat capacity from the acoustic contribution, $C_{acoustic}$, requires the Debye temperature. Due to the lack of knowledge about elastic properties of $Cs_8Ga_8Sn_{38}$, the Debye temperature of Sn at its low temperature limit,[40] 200 K, was used. Such an approximation will not introduce significant error to the total heat capacity due to the large number of atoms in the unit cell. In fact, the heat capacity from the acoustic modes is only 0.4% of total C_P at $T = 10$ K and 1.6% at $T = 300$ K based on the above Debye temperature.

The calculated total heat capacity $C_{p,cal} = C_{optic} + C_{acoustic} + (C_P - C_V)$ is shown in

Figure 4.20. It agrees well with experimental results between 50 K and 200 K but deviates at higher temperatures, possibly due to the anharmonic vibrations of both acoustic and optic modes, or the simplifications in the optic mode treatment.

4.5.3.4 Apparent Debye Temperature

The apparent Debye temperature, Θ_D, is useful to understand the anharmonicity of lattice vibrations and examine lattice dynamic models. It can be calculated from the total isochoric heat capacities, C_V, through the Debye model, equation (1.2.21). C_V can be obtained from $C_P-(C_P-C_V)$ as discussed in Section 4.5.3.3. The calculated apparent Θ_D is a temperature dependent function as shown in Figure 4.21. Above 200 K, the apparent Θ_D decreases as temperature increases, likely due to the anharmonic lattice vibration.

4.5.3.5 Thermodynamic Stability

Thermodynamic properties can be used to understand the thermodynamic stability of $Cs_8Ga_8Sn_{38}$. To calculate the complete thermodynamic functions, the isobaric heat capacity data below 40 K were derived from $C_{P,cal}$ as discussed in Section 4.5.3.3. The thermodynamic functions below ambient temperatures were calculated from C_P and are summarized in Table 4.10. Since the complete entropy data for Sn below room temperature are not available, the entropy of formation of $Cs_8Ga_8Sn_{38}$ below 298.15 K is not listed in Table 4.10.

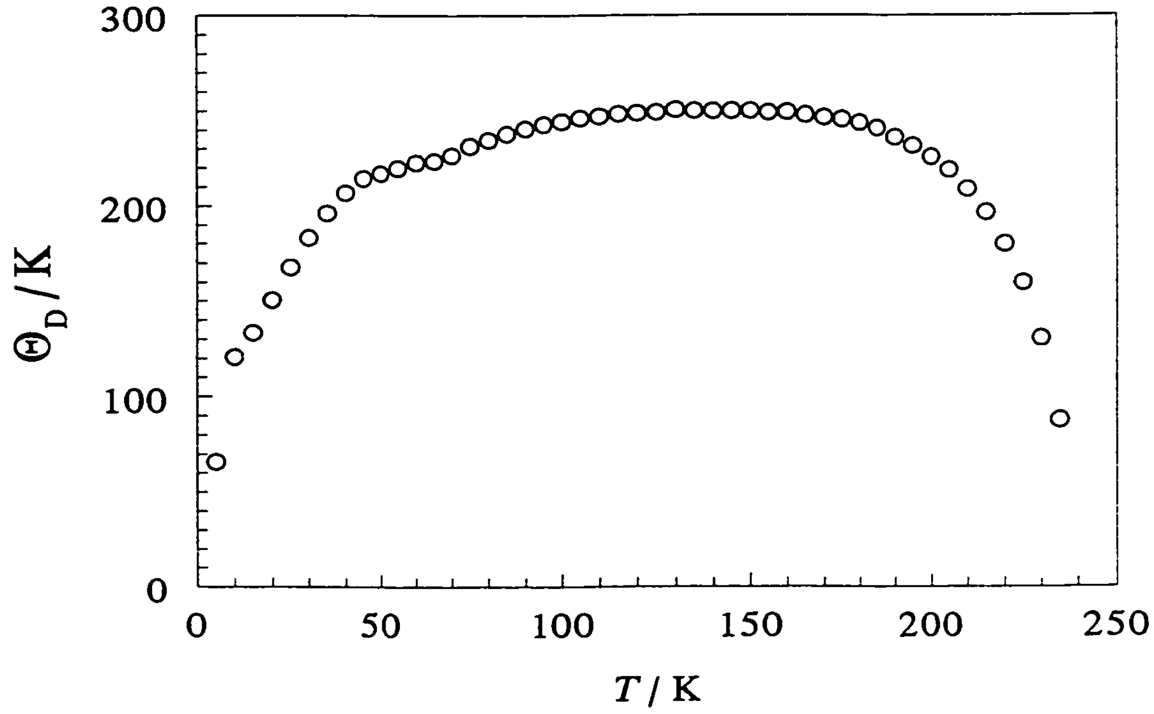

Figure 4.21. Apparent Debye temperature of $Cs_8Ga_8Sn_{38}$, calculated from the total isochoric heat capacity, C_V, as indicated in the text.

Table 4.10. Thermodynamic Properties of $Cs_8Ga_8Sn_{38}$.

T/K	C_P/J K^{-1} mol^{-1}	$(H_T\text{-}H_0)$/kJ mol^{-1}	$(S_T\text{-}S_0)$/J K^{-1} mol^{-1}	$(G_T\text{-}G_0)$/kJ mol^{-1}
5	3.07	0.00768	1.54	0.000
10	52.3	0.146	16.2	-0.015
15	131	0.604	51.0	-0.162
20	204	1.44	98.3	-0.526
25	268	2.62	151	-1.14
30	327	4.11	205	-2.03
35	386	5.89	259	-3.19
40	445	7.96	315	-4.62
45	505	10.3	371	-6.34
50	612	13.1	429	-8.33
55	680	16.4	491	-10.6
60	739	19.9	553	-13.2
65	798	23.8	614	-16.2
70	843	27.9	675	-19.4
75	879	32.2	734	-22.9
80	913	36.6	792	-26.7
85	944	41.3	848	-30.8
90	973	46.1	903	-35.2
95	1000	51.0	957	-39.9
100	1026	56.1	1009	-44.8
105	1049	61.3	1059	-49.9
110	1071	66.6	1108	-55.4
115	1091	72.0	1157	-61.0
120	1110	77.5	1203	-66.9
125	1128	83.1	1249	-73.1
130	1144	88.8	1294	-79.4
135	1159	94.5	1337	-86.0
140	1173	100	1380	-92.8
145	1186	106	1421	-99.8
150	1198	112	1461	-107
155	1210	118	1501	-114
160	1220	124	1539	-122

Continued...

Table 4.10. (continued).

T/K	C_P/J K^{-1} mol^{-1}	$(H_T\text{-}H_0)$/kJ mol^{-1}	$(S_T\text{-}S_0)$/J K^{-1} mol^{-1}	$(G_T\text{-}G_0)$/kJ mol^{-1}
165	1231	130	1577	-130
170	1241	137	1614	-138
175	1250	143	1650	-146
180	1259	149	1685	-154
185	1268	155	1720	-163
190	1278	162	1754	-171
195	1287	168	1787	-180
200	1296	175	1820	-189
205	1305	181	1852	-199
210	1315	188	1884	-208
215	1325	194	1915	-217
220	1336	201	1945	-227
225	1347	208	1976	-237
230	1359	214	2005	-247
235	1371	221	2035	-257
240	1384	228	2064	-267
245	1397	235	2092	-278
250	1411	242	2121	-288
255	1425	249	2149	-299
260	1441	256	2177	-310
265	1456	264	2204	-320
270	1472	271	2232	-332
275	1489	278	2259	-343
280	1505	286	2286	-354
285	1522	293	2312	-366
290	1538	301	2339	-377
295	1554	309	2365	-389
298.15	1564	314	2382	-397
300	1570	317	2392	-401

At 298.15 K, the absolute entropy of $Cs_8Ga_8Sn_{38}$ has the value of 2382 J K^{-1} mol^{-1} with the assumption of $S_0 = 0$. From the entropies of Cs,[160] Ga[258,259] and β-Sn[266] the entropy of formation of $Cs_8Ga_8Sn_{38}$ is -570 ± 10 J K^{-1} mol^{-1} at 298.15 K. The negative entropy of formation can significantly decrease the thermodynamic stability of $Cs_8Ga_8Sn_{38}$. Such a large negative entropy change suggests strong host-guest interactions due to the similar radii of Cs atoms and the cage.[227] The host-guest interactions decrease the degrees of freedom of both the guests and host, and hence the entropy of clathrates. Theoretical calculations suggest that Cs and Sn atoms are rehybridized and strongly interacting in a similar clathrate, Cs_8Sn_{46}, which is significantly different from the case of Na_8Si_{46}.[267]

4.5.3.6 Grüneisen Parameter

The Grüneisen parameter can be derived from equation (1.5.3). The required thermal expansion coefficients, compressibility and total isochoric heat capacities are discussed in Sections (4.5.3.3). The molar volume was calculated from the experimental density at 300 K.[261] The results are shown in Figure 4.22.

It is found that the Grüneisen parameter is essentially independent of temperatures. Between 20 K and 250 K, the variation of γ is within the experimental uncertainty, which is in contrast to Na_8Si_{46} and $Sr_8Ga_{16}Ge_{30}$ discussed in the Sections (4.2.3.7) and (4.3.3.6). This finding indicates that the scattering of acoustic phonons by the rattling of guests in the cages is reduced due to the strong host-guest interactions. Such a conclusion agrees well with experimental thermal conductivity of $Cs_8Ga_8Sn_{38}$[264]

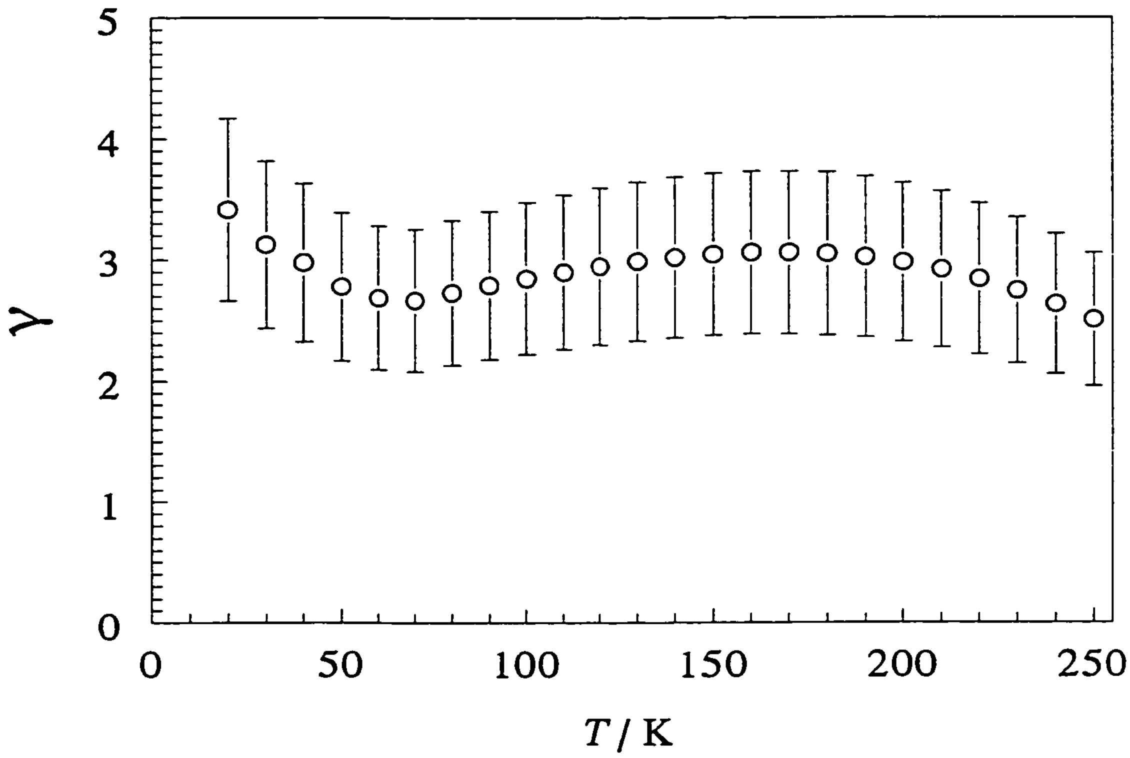

Figure 4.22. Grüneisen parameter of $Cs_8Ga_8Sn_{38}$. Its calculation was discussed in the text. The error bar indicates the uncertainty of γ. The thermal expansion coefficient is the major source of uncertainty of γ.

and theoretical calculations.[267]

4.5.4 Conclusions

The low-temperature heat capacity of $Cs_8Ga_8Sn_{38}$ was determined from 37 to 305 K. At 298.15 K, the heat capacity, $H_T - H_0$, and $S_T - S_0$ are 1564 J K^{-1} mol^{-1}, 314 kJ mol^{-1}, and 2382 J K^{-1} mol^{-1}, respectively. The large negative $\Delta_f S^o$, -570 J K^{-1} mol^{-1}, of $Cs_8Ga_8Sn_{38}$ at 298.15 K indicates the strong host-guest interaction. The heat capacity calculated from Raman frequencies agrees well with experimental data between 50 K and 200 K. The Grüneisen parameters were constant below 250 K which indicates that resonant scattering is not a major effect in the $Cs_8Ga_8Sn_{38}$. This finding agrees well experimental thermal conductivity[264] and theoretical calculation.[267]

4.6 Thermal Properties of $Ba_8Ga_{16}Si_{30}$ Clathrate

4.6.1 Structure

$Ba_8Ga_{16}Si_{30}$ has the type I clathrate structure as for Na_8Si_{46} with the cubic space group $Pm\overline{3}n$ and a lattice parameter[227] of 10.554 Å. The Ga and Si atoms are assumed to be randomly distributed through the framework.[261]

4.6.2 Experimental

4.6.2.1 Synthesis

A 2.409 g sample of $Ba_8Ga_{16}Si_{30}$ was synthesized and supplied by Marlow Industries, Inc. The synthesis of the sample was similar to that of $Sr_8Ga_{16}Ge_{30}$.[227] Powder

X-ray diffraction showed that there is a trace amount of Si in the sample.[227,261]

4.6.2.2 Heat Capacity Measurement

The sample was loaded in the calorimeter as for Na_8Si_{46} (Section 4.2.2.3). The heat capacity data were taken between 29 and 300 K. The detailed operation of the adiabatic calorimeter has been discussed in Section 2.4.

4.6.3 Results and Discussion

4.6.3.1 Experimental Heat Capacity

The experimental heat capacity of $Ba_8Ga_{16}Si_{30}$ is shown in Figure 4.23 and listed in Table 4.11. The heat capacity of the sample comprised about 15 % of the total heat capacity at 300 K and 10% at 30 K.

The experimental heat capacity data are those at constant pressure, C_P. The theoretically more interesting C_V can be determined from C_P through equation (1.2.27). The additional required data include temperature-dependent thermal expansion coefficients and bulk modulus but they are not available for $Ba_8Ga_{16}Si_{30}$. The thermal properties of the similar clathrate Na_8Si_{46} have been discussed in Section 4.2.3. The experimental thermal expansion coefficients and bulk modulus[226] of Na_8Si_{46} were used to estimate $(C_P - C_V)$ for $Ba_8Ga_{16}Si_{30}$. Such an approximation should not introduce significant uncertainty in C_V. At 298 K, $(C_P - C_V)$ of $Ba_8Ga_{16}Si_{30}$ is estimated to be about 5% of C_P.

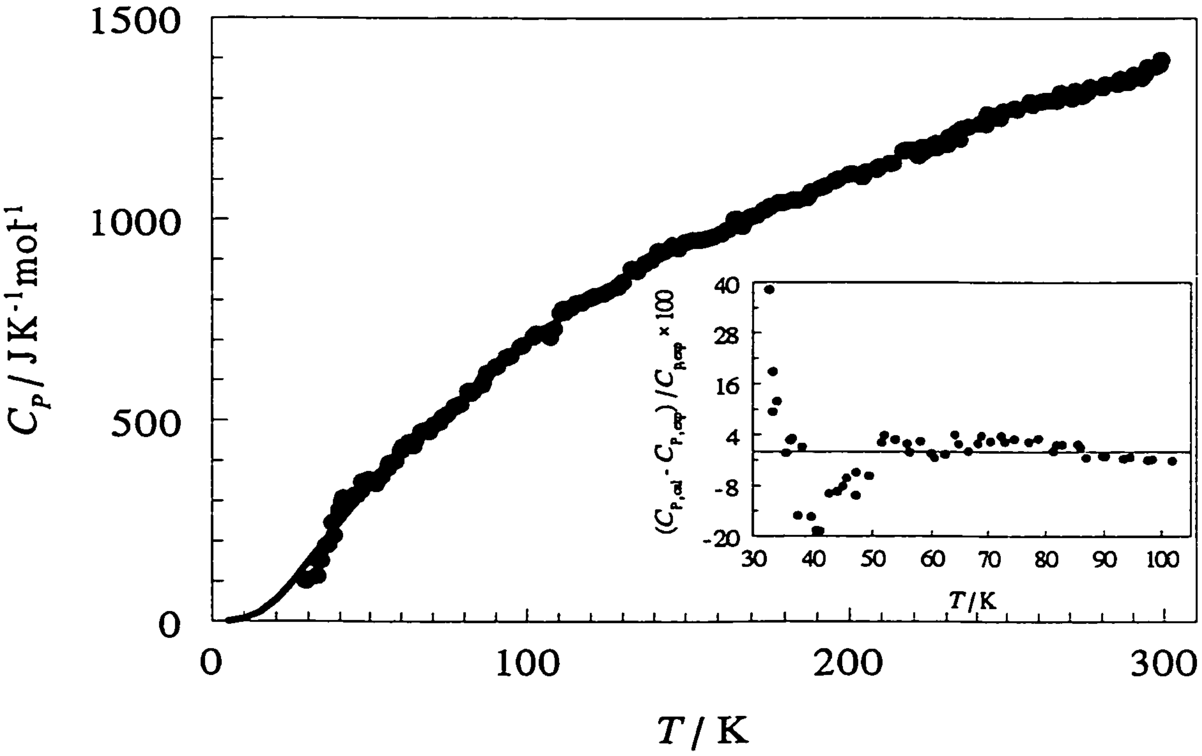

Figure 4.23. Heat capacity of $Ba_8Ga_{16}Si_{30}$. •, experimental results and —, extrapolated values (<100 K) from equation (1.2.27), as indicated in the text. The inset diagram indicates the difference between the experimental and fitted heat capacity data. See text for details.

Table 4.11. Experimental Heat Capacity of $Ba_8Ga_{16}Si_{30}$.

T/K	C_P/J K^{-1} mol^{-1}	T/K	C_P/J K^{-1} mol^{-1}	T/K	C_P/J K^{-1} mol^{-1}
29.11	102	68.77	473	124.13	816
29.52	105	70.41	490	125.68	822
32.63	114	72.28	496	128.43	832
33.25	151	72.94	508	130.05	845
33.90	154	74.53	515	132.73	877
35.43	189	77.08	535	134.44	872
36.13	191	78.68	540	137.01	891
36.40	193	81.31	573	138.82	899
37.36	247	81.88	568	141.30	922
38.07	215	82.84	574	143.21	922
39.67	277	85.58	589	145.65	936
40.57	300	86.05	597	147.60	929
41.10	307	87.01	617	149.93	945
42.69	296	89.86	632	151.98	949
44.04	309	90.25	634	154.22	949
45.00	316	93.33	656	156.35	953
45.63	316	94.45	660	158.50	958
47.20	348	97.58	683	160.81	965
47.22	328	98.44	687	162.79	975
49.44	354	101.86	709	165.21	1003
51.54	345	102.66	716	167.07	983
51.98	344	106.20	719	169.55	1006
53.77	363	106.92	717	171.37	1010
55.77	383	107.23	708	173.88	1024
56.21	394	108.28	728	175.35	1032
58.02	399	110.52	767	178.18	1042
59.87	426	111.21	777	179.55	1042
60.41	434	111.66	769	182.51	1048
62.21	445	113.77	781	183.81	1048
63.91	438	115.51	792	186.85	1054
64.57	452	117.06	794	188.11	1069
66.33	473	119.84	805	191.15	1079
68.10	476	121.35	810	192.37	1083

Continued…

Table 4.11. (continued).

T/K	C_P/J K^{-1} mol^{-1}	T/K	C_P/J K^{-1} mol^{-1}
195.46	1096	247.69	1253
196.53	1101	248.26	1263
199.78	1112	248.77	1270
200.70	1114	252.42	1276
204.01	1106	253.15	1274
204.90	1118	257.24	1292
208.23	1124	257.98	1285
209.06	1131	260.93	1294
212.49	1140	262.05	1296
213.25	1140	262.85	1295
216.69	1170	265.77	1296
217.21	1173	266.91	1315
218.54	1174	270.57	1301
220.80	1170	271.64	1320
221.28	1158	273.98	1308
222.51	1180	275.55	1318
222.67	1167	276.37	1329
224.91	1178	280.19	1329
226.50	1190	281.01	1336
226.79	1178	284.97	1337
229.05	1189	285.64	1349
230.46	1187	288.23	1341
230.85	1205	289.53	1349
233.11	1216	290.13	1360
234.35	1200	292.70	1352
234.80	1225	294.10	1365
237.11	1230	294.51	1379
241.05	1238	297.17	1380
243.18	1237	298.50	1386
243.40	1262	298.92	1396
244.88	1259		

The heat capacity increases smoothly with temperature and approaches the Dulong-Petit value (1347 J K^{-1} mol^{-1}) around 290 K, indicating that all vibrational modes are essentially fully excited. This temperature is lower than that where Na_8Si_{46} is fully excited; it reaches only about 85% of its Dulong-Petit value at room temperature. It is likely that the framework of $Ba_8Ga_{16}Si_{30}$ is not as stiff as Na_8Si_{46} due to the Ga-Si bonds being softer than Si-Si bonds.

The heat capacities[192] of Ba,[154] Ga[258-260] and Si[158] at several temperatures were used to evaluate that of $Ba_8Ga_{16}Si_{30}$ according to the Neumann-Kopp law. The difference between the experimental and calculated Neumann-Kopp value is about 2% at 100 K and increases to 10% at 300 K, which likely reflects from the energy change between the diamond phase and clathrate.

4.6.3.2 Thermodynamic Stability

Thermodynamic properties can be used to determine the thermodynamic stability of $Ba_8Ga_{16}Si_{30}$. They require complete heat capacity at low temperatures. Since the vibrational data and the elastic properties of $Ba_8Ga_{16}Si_{30}$ have not been reported yet, the present experimental heat capacities below 100 K were least squares fit to equation (1.2.27). The best fit parameters were θ_D = 186 K and θ_E = 436 K; m = 24 and n = 30. The fitted heat capacity deviates from experimental values above 40 K by an average of 2%. The heat capacity below 40 K was extrapolated to 0 K according to equation (1.2.27) and is shown in Figure 4.23.

The enthalpy and entropy derived from the experimental C_P are listed Table 4.12.

Table 4.12. Thermodynamic Properties of $Ba_8Ga_{16}Si_{30}$.

T/K	C_P/J K^{-1} mol^{-1}	$(H_T\text{-}H_0)$/kJ mol^{-1}	$(S_T\text{-}S_0)$/J K^{-1} mol^{-1}	$(G_T\text{-}G_0)$/kJ mol^{-1}
5	0.911	0.00227	0.455	0.0000
10	7.29	0.0230	2.73	-0.0043
15	24.5	0.102	8.63	-0.027
20	55.8	0.303	19.7	-0.091
25	99.4	0.69	36.6	-0.22
30	149	1.31	59.0	-0.46
35	200	2.19	85.7	-0.81
40	249	3.31	116	-1.31
45	294	4.67	148	-1.97
50	337	6.25	181	-2.79
55	374	8.02	215	-3.78
60	414	10.0	249	-4.94
65	452	12.2	283	-6.26
70	490	14.5	318	-7.77
75	527	17.1	353	-9.45
80	563	19.8	389	-11.3
85	598	22.7	424	-13.3
90	631	25.8	459	-15.5
95	663	29.0	494	-17.9
100	694	32.4	529	-20.5
105	723	35.9	563	-23.2
110	751	39.6	597	-26.1
115	778	43.4	631	-29.2
120	804	47.4	665	-32.4
125	828	51.5	698	-35.8
130	851	55.7	731	-39.4
135	874	60.0	764	-43.1
140	895	64.4	796	-47.1
145	916	68.9	828	-51.1
150	936	73.6	859	-55.3
155	955	78.3	890	-59.7
160	973	83.1	921	-64.2
165	991	88.0	951	-68.9

Continued ...

Table 4.12. (continued).

T/K	C_P/J K^{-1} mol^{-1}	(H_T-H_0)/kJ mol^{-1}	(S_T-S_0)/J K^{-1} mol^{-1}	(G_T-G_0)/kJ mol^{-1}
170	1009	93.0	981	-73.7
175	1026	98.1	1010	-78.7
180	1043	103	1039	-83.7
185	1059	109	1068	-89.1
190	1075	114	1097	-94.5
195	1092	119	1125	-100
200	1107	125	1153	-106
205	1123	130	1180	-112
210	1139	136	1207	-118
215	1154	142	1234	-124
220	1170	148	1261	-130
225	1185	153	1288	-136
230	1200	159	1314	-143
235	1215	165	1340	-150
240	1230	172	1366	-156
245	1245	178	1391	-163
250	1259	184	1416	-170
255	1273	190	1441	-177
260	1287	197	1466	-185
265	1300	203	1491	-192
270	1313	210	1515	-199
275	1325	216	1540	-207
280	1337	223	1564	-215
285	1349	230	1587	-223
290	1359	237	1611	-231
295	1370	243	1634	-239
298.15	1376	248	1649	-244
300	1379	250	1657	-247

With the assumption $S_0 = 0$, the entropy of formation for $Ba_8Ga_{16}Si_{30}$ at $T = 298.15$ K, determined from the entropies of Ba,[154] Ga,[258-260] and Si[158] is -69 ± 8 J K^{-1} mol^{-1}. The negative entropy change indicates destabilization of the clathrate structure, relative to elements. The complete entropies of Ba below 298.15 K are not available, so the entropies of formation of $Ba_8Ga_{16}Si_{30}$ were not listed in Table 4.12.

4.6.3.3 Apparent Debye Temperature

The apparent Debye temperature, Θ_D, can provide information about anharmonicity of lattice vibrations. The total heat capacity, C_V, discussed in Section 4.6.3.1 was converted to apparent Θ_D through equation (1.2.21). As for most solids, it is a temperature-dependent function and approaches a maximum of 430 K around $T = 160$ K, as shown in Figure 4.24. The apparent Θ_D decreases above 220 K due to anharmonicity of the lattice vibrations. It is apparent that replacement of Ga atoms for Si atoms decreases the stiffness of the silicon clathrate framework and hence the maximum apparent Θ_D because of the weaker Ga-Si bond.

4.6.3.4 Grüneisen Parameter

The Grüneisen parameter is helpful to understand the anharmonicity of lattice vibrations and phonon-phonon interactions for clathrates of Group 14 elements. The required data to estimate the Grüneisen parameter include thermal expansion coefficients and bulk modulus, and present total isochoric heat capacity. The calculations of the first two quantities have been discussed in Section 4.6.3.1. The molar volume was calculated

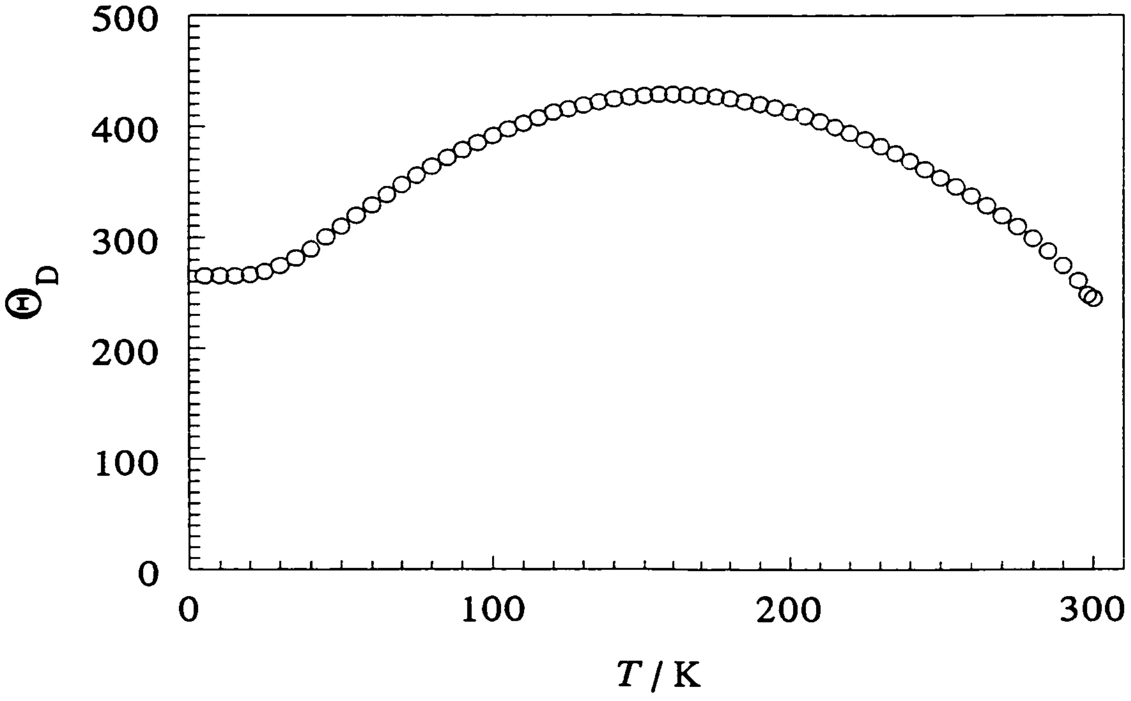

Figure 4.24. Apparent Debye temperature of $Ba_8Ga_{16}Si_{30}$, calculated from the total heat capacity, C_V, discussed in the text.

from the experimental lattice parameter of $Ba_8Ga_{16}Si_{30}$ at 300 K.[227] The results are shown in Figure 4.25. Like most solids, the uncertainty of the Grüneisen parameter largely from thermal expansion. Nevertheless, the estimated Grüneisen parameter still can provide information associated with anharmonicity of the lattice vibrations. At room temperature, the uncertainty of the Grüneisen parameter is around 20%. The increase of Grüneisen parameters at low temperature is from the acoustic phonon scattering by the rattling of guest Ba atoms in the cages, which agrees with the interpretation of experimental thermal conductivity.[227]

4.6.4 Conclusions

The heat capacity of $Ba_8Ga_{16}Si_{30}$ below room temperature was determined. At 298.15 K, C_P, H_T-H_0, $S_T - S_0$ and $\Delta_f S^\circ$ were found to be 1376 J K^{-1} mol^{-1}, 248 kJ mol^{-1}, 1649 J K^{-1} mol^{-1} and -69 J K^{-1} mol^{-1}, rcspectively. The apparent Debye temperature is a temperature-dependent function. At T = 160 K, it has a maximum of 430 K. The replacement of Ga atoms for Si atoms deceases the stiffness of the silicon clathrate framework. An increase of the Grüneisen parameter at low temperatures results from the acoustic phonon scattering by the rattling of guests in the cages.

4.7 Overall Summary for Clathrates

The heat capacities of five Si, Ge, Sn clathrates were determined below ambient temperatures. Their heat capacities, entropies, enthalpies, and entropies of formation at

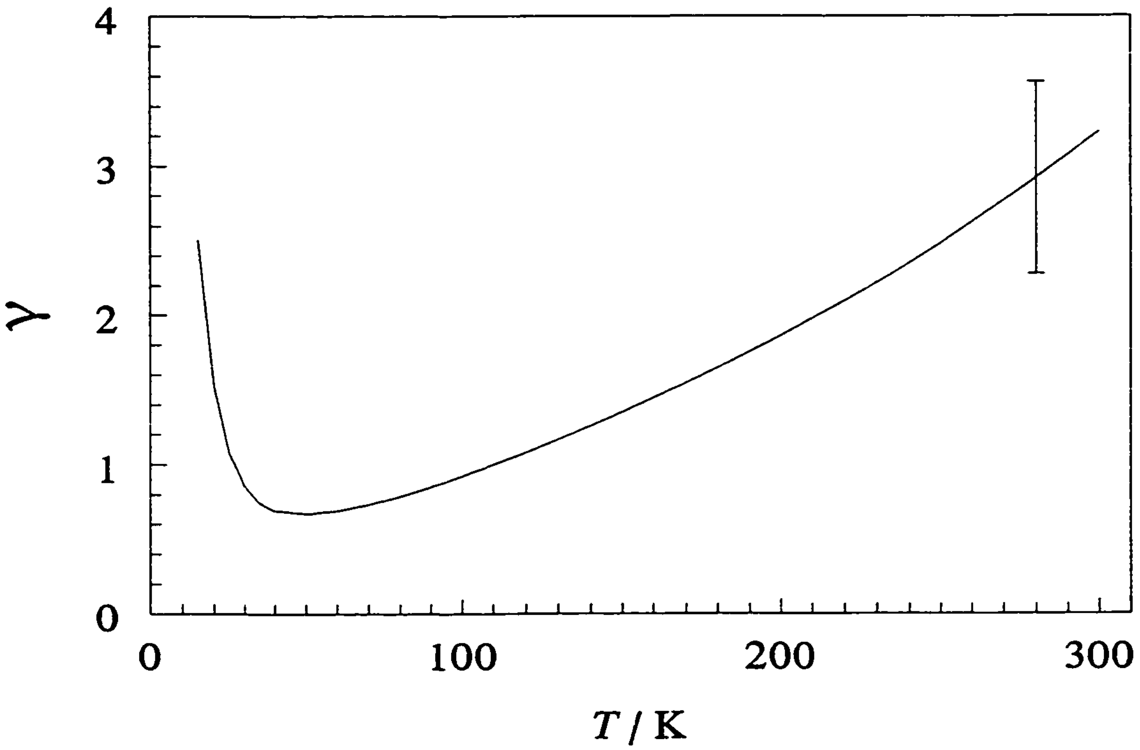

Figure 4.25. Grüneisen parameter of $Ba_8Ga_{16}Si_{30}$, estimated from the thermal expansion and bulk modulus of Na_8Si_{46}, the present total heat capacity, C_V, and the experimental lattice parameter of $Ba_8Ga_{16}Si_{30}$. The error bar represents the uncertainty of γ.

298.15 K are summarized in Table 4.13. The experimental heat capacities for all five clathrates are shown in Figure 4.26.

Table 4.13. Summary of Thermodynamic Properties of Clathrates at $T = 298.15$ K.

Clathrates	C_P/J K^{-1} mol^{-1}	(H_T-H_0)/J mol^{-1}	(S_T-S_0)/J K^{-1} mol^{-1}	$\Delta_f S$/J K^{-1} mol^{-1}
Na_8Si_{46}	1159 ± 6	206 ± 1	1310 ± 7	32 ± 7
$Sr_8Ga_{16}Ge_{30}$	1348 ± 7	279 ± 1	2000 ± 10	-52 ± 10
$Sr_8Zn_8Ge_{38}$	1393 ± 7	283 ± 1	1988 ± 10	18 ± 10
$Cs_8Ga_8Sn_{38}$	1564 ± 8	314 ± 2	2382 ± 10	-570 ± 10
$Ba_8Ga_{16}Si_{30}$	1376± 7	248 ± 2	1649 ± 8	-69 ± 8

Among these clathrates, Na_8Si_{46} has the lowest heat capacity and consequently the highest apparent Debye temperature at room temperature.

In the Sn clathrate examined, it would appear that the stronger host-guest interactions result in more negative entropy of formation at room temperature than for the Si and Ge clathrates.

The Grüneisen parameters of the clathrates investigated were estimated. At very low temperatures, the γ values of the Si and Ge clathrates increased with decrease of temperature while the γ of the Sn clathrate was approximately temperature independent. These results indicate that the anharmonicity of lattice vibrations in Si and Ge clathrates result from the scattering of heat-carrying acoustic phonons by the rattling of guests in the cages. However, such resonant scattering is significantly reduced due to the strong

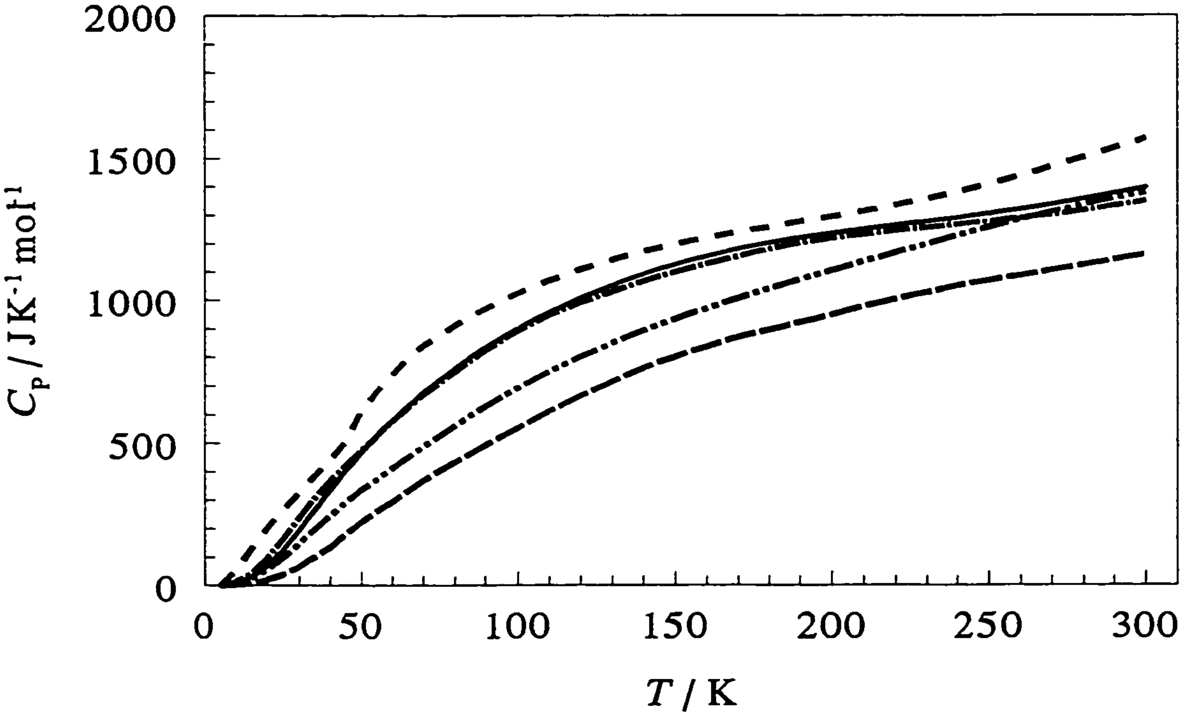

Figure 4.26. Summary of heat capacities of clathrates.
— — —, $Cs_8Ga_8Sn_{38}$, ———, $Sr_8Zn_8Ge_{38}$, — - — -, $Sr_8Ga_{16}Ge_{30}$, — - - —, $Ba_8Ga_{16}Si_{30}$ and — —, Na_8Si_{46}.

host-guest interactions in Sn clathrates. These conclusions agree with both experimental thermal conductivities and lattice dynamic calculations.

Chapter 5 Thermal Properties of 2,6-dimethylbicyclo[3.3.1]nonane-*exo*-2, *exo*-6-diol

5.1 Introduction

In the late 1970's it was found that some organic diols, such as 2,6-dimethylbicyclo[3.3.1]nonane-*exo*-2, *exo*-6-diol[268] abbreviated as diol **1** and shown in Figure 5.1, can form a strong helical channel (or tubuland) structure through intermolecular hydrogen bonds, as shown in Figure 5.2. The most significant difference between these novel materials and many other hosts such as urea and clathrate hydrates is that the hydrogen-bonded helical tubuland frameworks of organic diols do not depend on their guests. By modifying the molecular skeleton of diols, the volume of the unit cell can be changed significantly from 858 to 1150 Å^3 and the cross-section area from 4.7 to 34 Å^2, depending on the shape of the channel.[269]

Diol **1** has the simplest molecular structure of diols that form helical tubuland channels.[270] The host molecules in each channel wall alternatively behave either as a double hydrogen donor pointing inwards or as a double acceptor pointing outwards, as shown in Figure 5.2. Due to the $2c$ pitch of the diol chains, there are two independent helices in each channel wall.[270] Each OH function in diol **1** acts as both hydrogen bond donor and acceptor along the helical spine of hydrogen bonds, Figure 5.3. All the channels are parallel to the c-axis and have an equilateral triangular cross section,[271] which is surrounded by six units of diol **1** with an unobstructed area of about 22 Å^2. The walls of the channels are lined with only hydrogen atoms on the non-polar hydrocarbon functions of the host molecules. In contrast with urea inclusion compounds, the guest molecules in diol **1** are not exposed to the hydroxyl groups and generally strong guest-

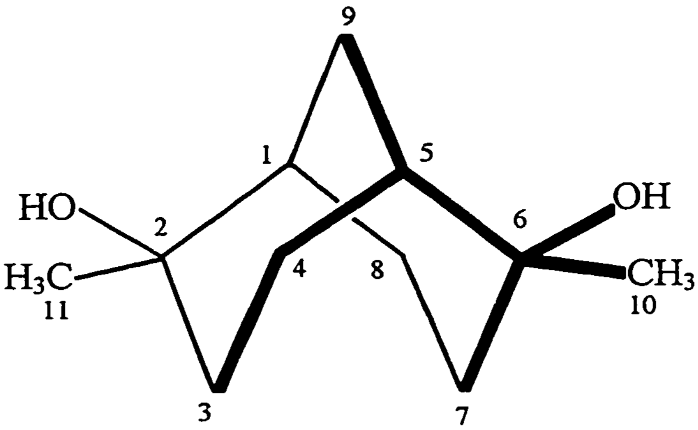

Figure 5.1. 2,6-Dimethylbicyclo[3.3.1]-nonane-*exo*-2, *exo*-6-diol, or diol **1**. It has C_2 symmetry and the bridge is on the same side as the hydroxy groups. These properties of the molecule skeleton are important for diols to form helical tubuland structures.

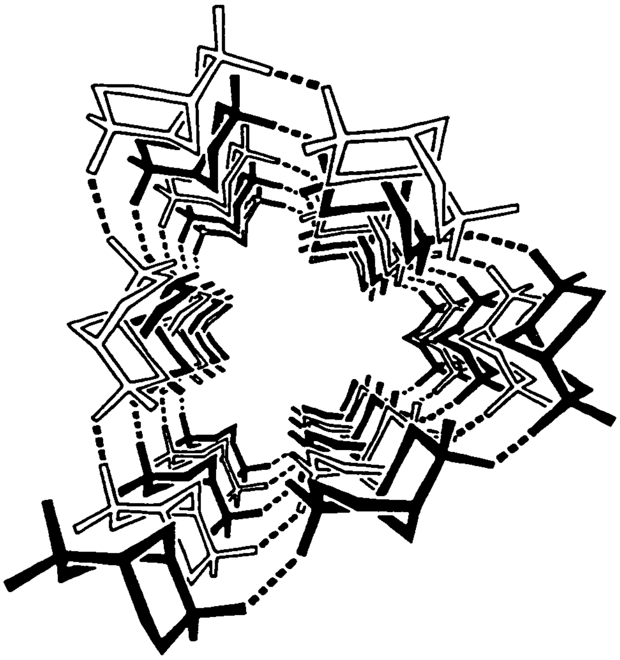

Figure 5.2. Double helical arrangement of diol **1** molecules around one helical tubuland channel with each helix alternatively shaded. Six units of diol **1** are required for one turn around the channel.[270]

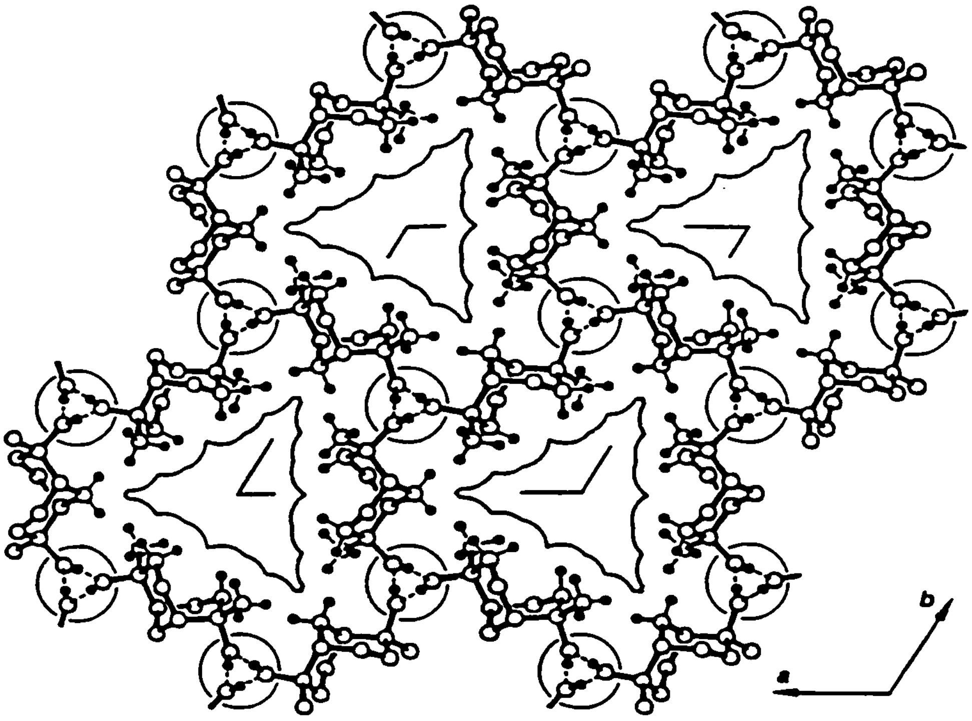

Figure 5.3. A view along the c-axis of the helical tubuland channel of diol **1**. The cross-section of the channel is an equilateral triangular. The helical spines of hydrogen bonds are circled.[271]

host interactions do not exist.

Various guest molecules with different functions and polarities have been included in diol **1**.[272] The typical host to guest ratio is approximately 3:1. Whether a guest can be entrapped in the channels or not depends on its shape and size. For example, chlorobenzene is appropriate but mesitylene is too bulky to be included in the channels. Hence, the latter can be used as a solvent for diol **1**. The framework of diol **1** displays a high elasticity when it entraps the guests. The volume of the unit cell can change from 862 $Å^3$ for the acetonitrile compound to 938 $Å^3$ for the dioxane compound. The unobstructed cross-section area of the channel can be altered as much as 62% by including guests.[270] The inclusion compounds of diol **1** generally are very stable and the removal of guests from the channels requires harsh conditions such as sublimation under low pressure.

As discussed in the previous chapters, the investigation of the thermal properties of materials provides considerable information such as thermodynamic stability and structure-property relationships. The empty host of this diol and its highly stable inclusion compounds provide ideal materials to study guest-guest and guest-host interactions. In this part of the thesis, the heat capacity and the fusion enthalpy of diol **1** were determined and the thermodynamic stability of diol **1** is discussed.

5.2 Experimental

5.2.1 Synthesis

The sample diol **1** was provided by Dr. R. Bishop of the University of New South

Wales. It was prepared by the hydration of 2,6-dimethylenebicyclo-[3.3.1]nonane using the mercuric acetate procedure[268]with a yield of 66%.[270]

The crystalline structure of diol **1** has been investigated[270,271] by X-ray diffraction. The unit cell has a chiral trigonal structure with a space group $P3_121$ or its enantiomer $P3_221$. The room temperature lattice parameters have values of $a = b = 12.165$ Å and $c = 7.001$ Å; $\alpha = \beta = 90^0$ and $\gamma = 120^0$.[270] The O···O distance[271] in the intermolecular hydrogen bond is 2.812 Å. Each unit cell is composed of three diol **1** molecules.

Solid-state ^{13}C NMR showed 5 groups of peaks[273] indicating the equivalence of C-2,6; C-1,5; C-3,7; C-9,4,8 and C-10,11 where the numbers are the positions of carbon atoms in diol **1** as shown in Figure 5.1.

Raman spectra for diol **1** have been determined using a Bruker RFS100 Fourier-transform Raman spectrometer at 83, 163, 217 and 300 K.[274] Low-temperature measurements were carried out in a vacuum-jacket, glass cold-finger, which was cooled by nitrogen gas fed through a coil of copper tubing submerged in liquid nitrogen. The interior of the finger was bathed in this cooled nitrogen. Variable temperatures were achieved through the variation of the flow rate of nitrogen gas. The temperature was determined by copper-constantan thermocouple at the sample site.

A Perkin Elmer Pyris-1 differential scanning calorimeter (DSC) was used to examine a 10.1 mg sample at a scanning rate of 5 K min^{-1}. The apparatus was calibrated with a standard indium sample, which has a melting point of 429.45 K and fusion enthalpy of 28.45 J g^{-1}.[275]

5.2.2 Heat Capacity Measurement

The solvent-free diol **1** (0.8667 g) was loaded in a glove box under a dry nitrogen atmosphere. The vessel of the adiabatic calorimeter was sealed in helium gas to increase thermal equilibrium. The details of operation of the calorimeter have been discussed in Section 2.4. The heat capacity of diol **1** was determined between 30 and 300 K.

5.3 Results and Discussion

5.3.1 Experimental Heat Capacity

The experimental heat capacity of diol **1** increases smoothly with temperature, as shown in Figure 5.4 and Table 5.1. The heat capacity from the sample comprised of about 10% of total heat capacity at 30 K and 15% at 300 K.

The heat capacity of diol **1** increases almost linearly with temperature above 40 K (Figure 5.4) due to the existence of many high-frequency optic modes. At 300 K, the heat capacity is only about 30% of the Dulong-Petit value, 823.1 J K^{-1} mol^{-1} ($3R \times 33$), indicating that most optic modes are not excited yet at room temperature.

The experimental heat capacity, C_P, is under constant pressure. The calculation of the physically more interesting heat capacity, C_V, requires thermal expansions coefficients and compressibility, which are not available presently. Thus it was assumed that $C_P = C_V$ for further analysis.

The apparent Debye temperature, Θ_D, calculated from the total heat capacity, C_P, shown in the Figure 5.5, increases smoothly with temperature and has a temperature-

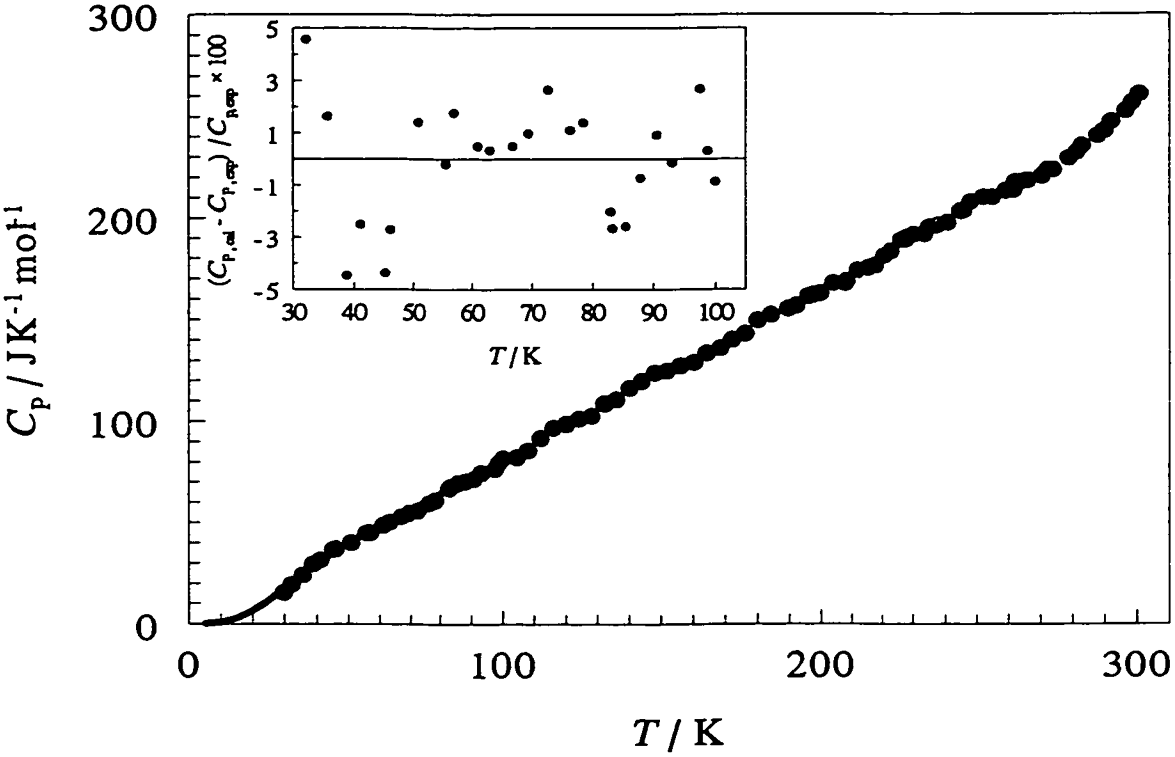

Figure 5.4. Heat capacity for diol **1**. • and — represent the experimental and extrapolated values from equation (1.2.27), as discussed in the text. The inset diagram indicates the difference between the experimental and fitted heat capacity data See text for details.

Table 5.1. Experimental Heat Capacity of Diol **1**.

T/K	C_P/J K^{-1} mol^{-1}	T/K	C_P/J K^{-1} mol^{-1}	T/K	C_P/J K^{-1} mol^{-1}
29.70	15.4	120.01	98.6	226.20	189
32.08	19.3	124.04	101	227.44	189
35.58	24.1	128.09	103	228.12	190
38.77	29.6	132.12	109	230.21	192
41.02	31.6	135.82	111	233.40	192
45.10	36.8	140.00	116	234.87	195
45.97	37.0	143.87	120	237.56	196
50.86	40.1	148.01	124	240.60	198
55.63	44.8	151.93	125	244.73	203
56.97	45.0	156.02	127	245.69	204
60.95	48.6	160.10	129	247.83	208
62.95	50.2	164.05	134	251.90	210
66.77	53.0	168.21	136	254.69	210
69.35	54.6	172.05	140	258.78	213
72.58	56.0	176.15	143	261.46	214
76.28	59.6	179.93	150	261.83	218
78.43	61.1	184.13	152	263.44	218
82.90	66.9	189.63	155	265.85	219
83.21	67.6	192.05	157	270.26	221
85.37	69.4	195.93	161	272.29	224
87.86	70.3	197.48	162	273.88	224
90.58	71.5	199.80	163	278.80	229
93.10	74.5	203.79	168	281.14	232
97.52	76.5	207.58	168	282.86	236
98.74	79.6	208.07	169	287.66	241
99.96	81.7	211.65	174	289.74	243
104.49	82.3	215.21	175	291.82	247
107.99	85.7	217.68	177	296.32	253
111.95	91.7	220.62	181	298.35	257
115.99	96.7	222.78	184	300.56	261

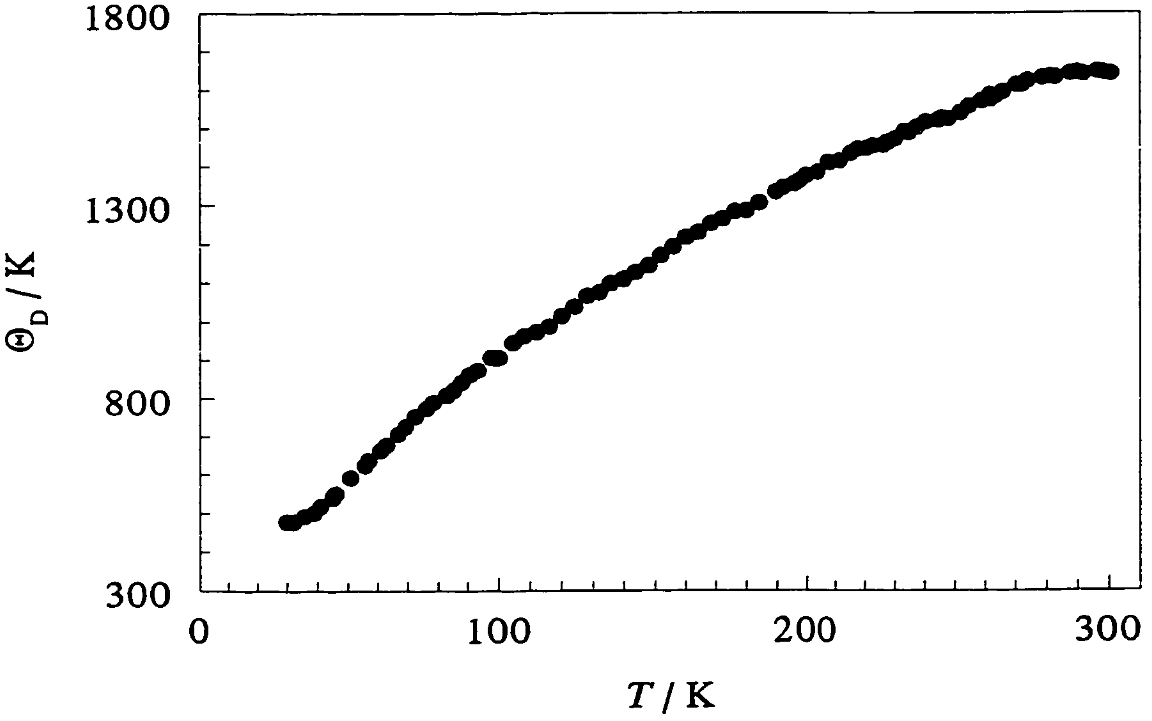

Figure 5.5. Apparent Debye temperature for diol **1**, calculated from the total heat capacity, C_p, as discussed in the text.

profile typical of solids. At 290 K, Θ_D approaches a maximum value of 1600 K. The high Θ_D is related to the large number of high-frequency optic modes in the diol crystal.

5.3.2 Raman Spectroscopy

The Raman spectra of diol **1** are shown in Figure 5.6.[274] Although the intensity of the peaks changes slightly with temperature, the overall variation of the spectra at different temperatures is rather small (Figure 5.6), indicating that diol **1** has a very stiff framework. The peak appearing at 2330 cm^{-1} at 83 K was assigned to that of liquid nitrogen[276] which was found to condense inside the apparatus during the experiment. Most peaks are located in the range 100 ~ 1500 cm^{-1}. Two other regions are 2850 ~ 3000 cm^{-1} and 3220 ~ 3380 cm^{-1}.

In the region 100 ~ 1500 cm^{-1}, especially 200 ~ 500 cm^{-1} (Figure 5.7), pairs of peaks, one pair at ~ 430 cm^{-1} and the other pair at ~ 500 cm^{-1} were clearly resolved at 83 K but severely overlapped at 300 K. In addition, a broad peak around 270 cm^{-1} at 300 K was separated into two at 83 K and one of the peaks has quite strong intensity, likely suggesting some change of lattice vibration.

In the region 2850 ~ 3000 cm^{-1} (Figure 5.8) the intensity of all peaks increases with the decrease of temperature. At 83 K, an additional peak at 2940 cm^{-1} appears which might be smeared at higher temperature.

In the region 3220 cm^{-1} ~ 3380 cm^{-1} (Figure 5.9) each peak shifts down about 10 cm^{-1} when the temperature is decreased by 50 K.

The detailed assignment of the Raman vibrational modes will require further

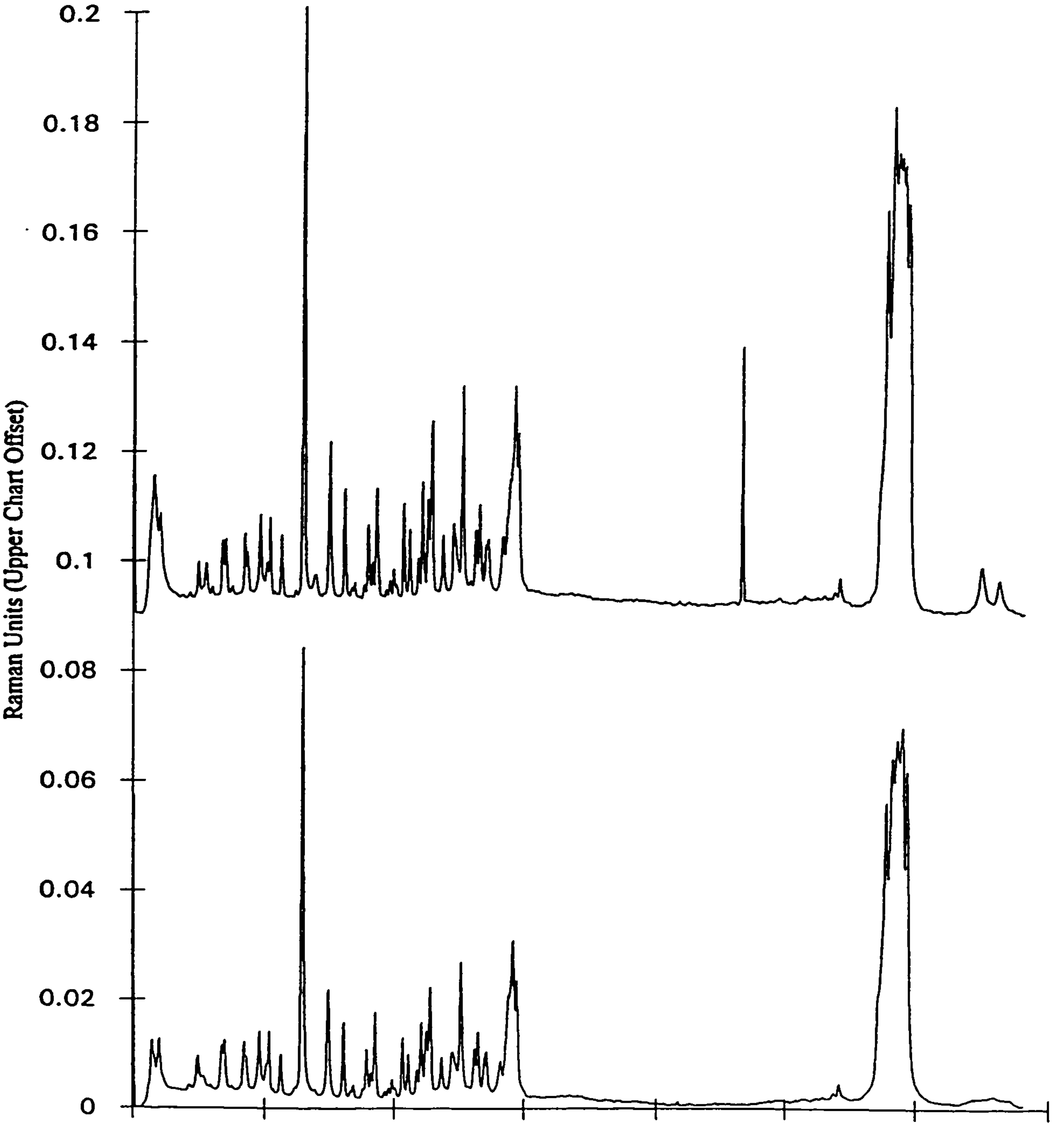

Figure 5.6. The Raman spectrum of diol 1 at 83 K (top) and 300 K (bottom).[274]

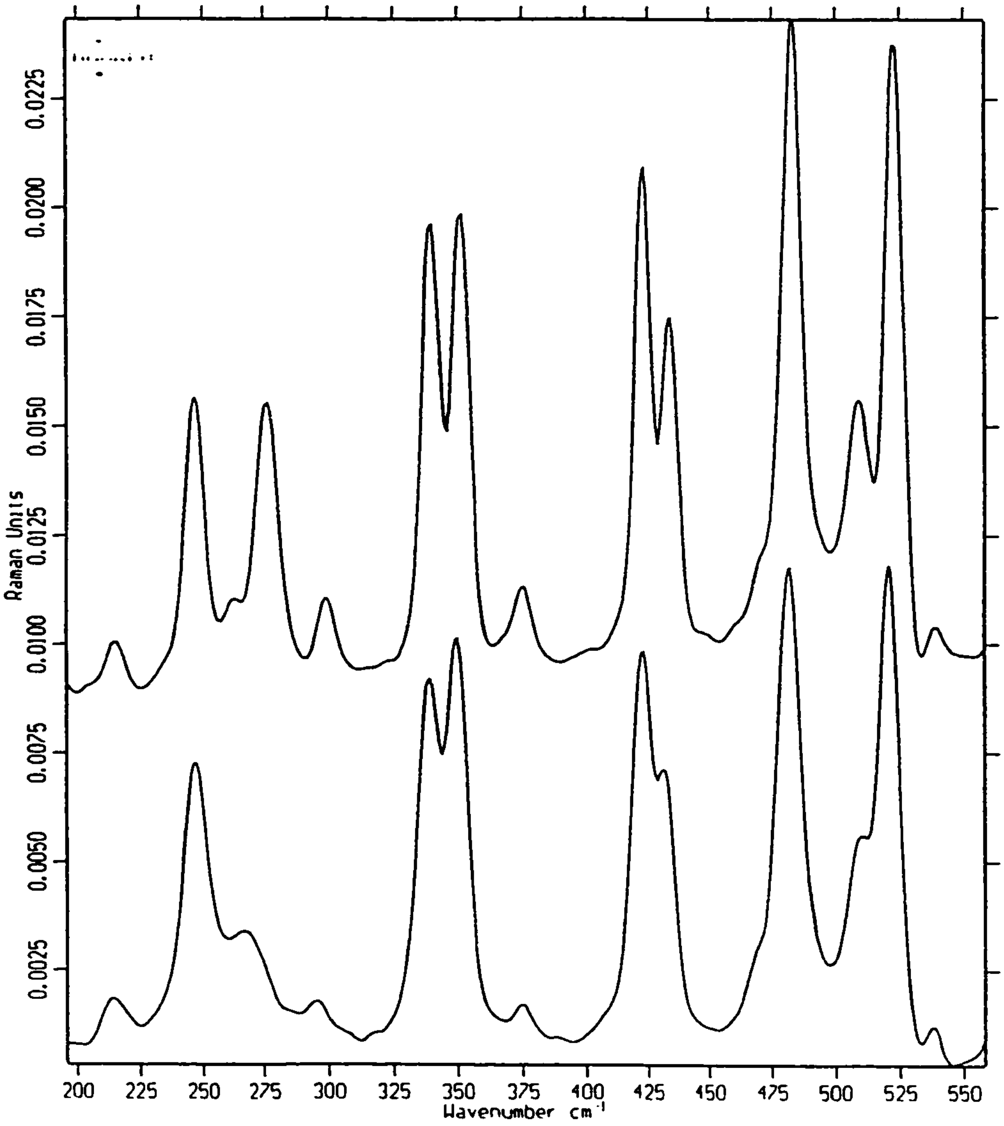

Figure 5.7. The region 200 ~ 550 cm^{-1} of Raman spectrum of diol **1** at 83 K (top) and 300 K (bottom).[274]

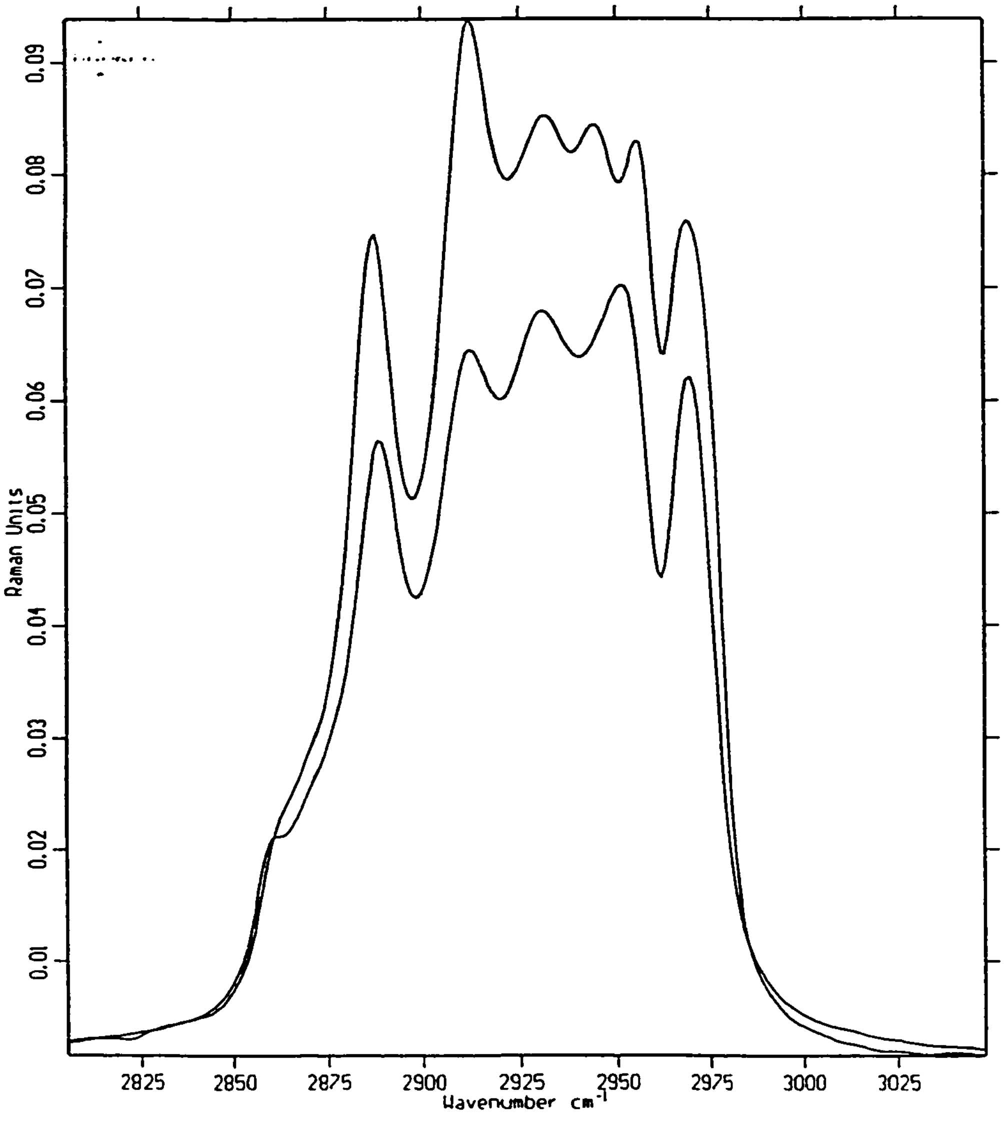

Figure 5.8. The region 2800 ~ 3000 cm^{-1} of Raman spectrum of diol **1** at 83 K (top) and 300 K (bottom).[274]

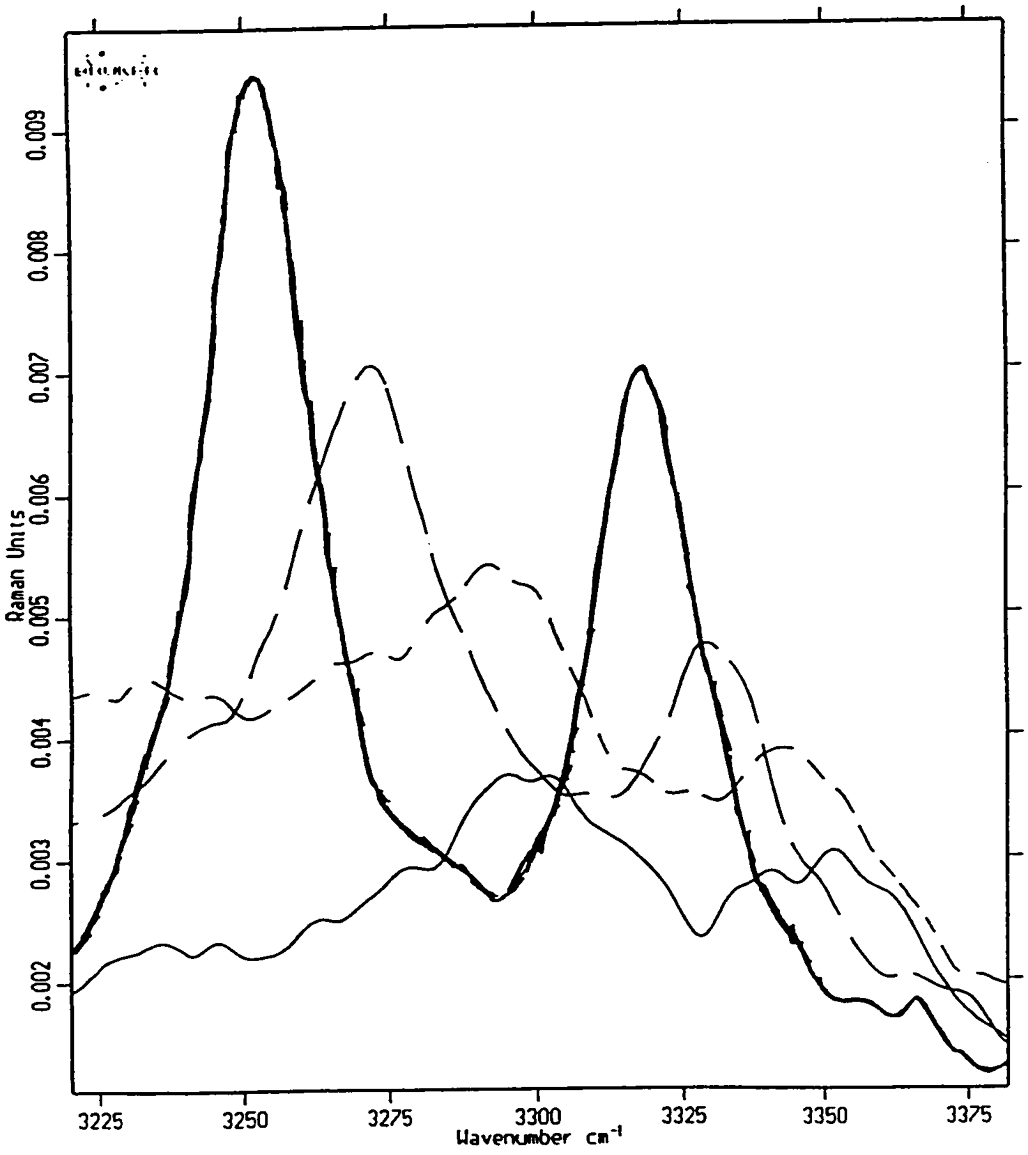

Figure 5.9. The region 3200 ~ 3400 cm^{-1} of Raman spectrum of diol **1**, —, at 83 K, — —, at 163 K, - - at 217 K, and — at 300 K.[274]

work. A test of that assignment would be a good fit between the calculated and experimental heat capacities.

5.3.3 Thermodynamic Stability

Thermodynamic properties are necessary to determine the stability of diol **1**. In order to obtain the complete thermodynamic properties, in absence of a vibrational assignment which would allow calculation of the low-temperature heat capacity, the experimental heat capacities below 100 K were fitted with equation (1.2.27) to extrapolate the heat capacity to $T = 0$ K. The best-fit parameters were $\theta_D = 190$ K and $\theta_E = 618$ K; and $m = 9$ and $n = 27$. The average fitted deviation was 1.6% of the experimental heat capacity. The increments of entropy and enthalpy relative to 0 K were calculated from the heat capacity and are listed in Table 5.2. From the entropies of H_2, O_2, C (graphite)[154] and diol **1**, the standard entropy of formation for diol **1** was determined to be -1377 ± 7 J mol^{-1} K^{-1} at 298.15 K.

The DSC reveals that diol **1** has a long melting path as shown in Figure 5.10. The peak begins to deviate from the baseline around 430 K and ends at 452 K with an onset temperature of 450 ± 1 K, indicating a gradual collapse of the hydrogen-bonded framework upon heating. The present melting point is lower than that reported (462 K) in the literature.[277] The difference is probably due to the fact that the instrument used in the literature report was not calibrated. DSC results reveal that diol **1** has a fusion enthalpy change of 25.9 ± 0.4 kJ mol^{-1} and fusion entropy change of 57.6 ± 0.8 J K^{-1} mol^{-1}.

Table 5.2. Thermodynamic Properties of Diol **1**.

T/K	C_P/J K^{-1} mol^{-1}	$(H_T\text{-}H_0)$/kJ mol^{-1}	$(S_T\text{-}S_0)$/J K^{-1} mol^{-1}	$(G_T\text{-}G_0)$/kJ mol^{-1}
5	0.105	0.000262	0.0524	0.000
10	0.838	0.00262	0.314	0.00052
15	2.82	0.0118	0.993	-0.0031
20	6.47	0.0350	2.27	-0.0105
25	11.6	0.080	4.24	-0.0259
30	17.6	0.153	6.87	-0.0529
35	23.8	0.257	10.0	-0.0946
40	29.7	0.391	13.6	-0.153
45	35.1	0.553	17.4	-0.231
50	39.9	0.740	21.3	-0.327
55	44.2	0.95	25.4	-0.444
60	48.2	1.18	29.4	-0.581
65	51.8	1.43	33.4	-0.737
70	56.1	1.70	37.4	-0.914
75	60.4	1.99	41.4	-1.11
80	64.5	2.30	45.4	-1.33
85	68.7	2.64	49.4	-1.57
90	72.8	2.99	53.5	-1.82
95	76.8	3.37	57.5	-2.10
100	80.9	3.76	61.6	-2.40
105	84.9	4.17	65.6	-2.72
110	89.0	4.61	69.7	-3.05
115	93.0	5.06	73.7	-3.41
120	97.1	5.54	77.7	-3.79
125	101	6.03	81.8	-4.19
130	105	6.55	85.8	-4.61
135	109	7.09	89.9	-5.05
140	114	7.64	93.9	-5.51
145	118	8.22	98.0	-5.99
150	122	8.82	102	-6.49
155	126	9.44	106	-7.00
160	131	10.1	110	-7.55

Continued...

Table 5.2 (continued).

T/K	C_P/J K^{-1} mol^{-1}	$(H_T\text{-}H_0)$/kJ mol^{-1}	$(S_T\text{-}S_0)$/J K^{-1} mol^{-1}	$(G_T\text{-}G_0)$/kJ mol^{-1}
165	135	10.8	114	-8.11
170	139	11.4	118	-8.70
175	144	12.1	123	-9.30
180	148	12.9	127	-9.92
185	152	13.6	131	-10.6
190	156	14.4	135	-11.2
195	161	15.2	139	-11.9
200	165	16.0	143	-12.6
205	169	16.8	147	-13.4
210	173	17.7	151	-14.1
215	177	18.6	155	-14.9
220	181	19.5	160	-15.6
225	186	20.4	164	-16.4
230	190	21.3	168	-17.3
235	194	22.3	172	-18.1
240	198	23.3	176	-19.0
245	202	24.3	180	-19.9
250	206	25.3	184	-20.8
255	210	26.3	188	-21.7
260	214	27.4	193	-22.7
265	218	28.4	197	-23.7
270	223	29.5	201	-24.7
275	228	30.7	205	-25.7
280	233	31.8	209	-26.7
285	238	33.0	213	-27.7
290	244	34.2	217	-28.8
295	251	35.4	222	-29.9
298.15	255	36.2	224	-30.6
300	258	36.7	226	-31.0

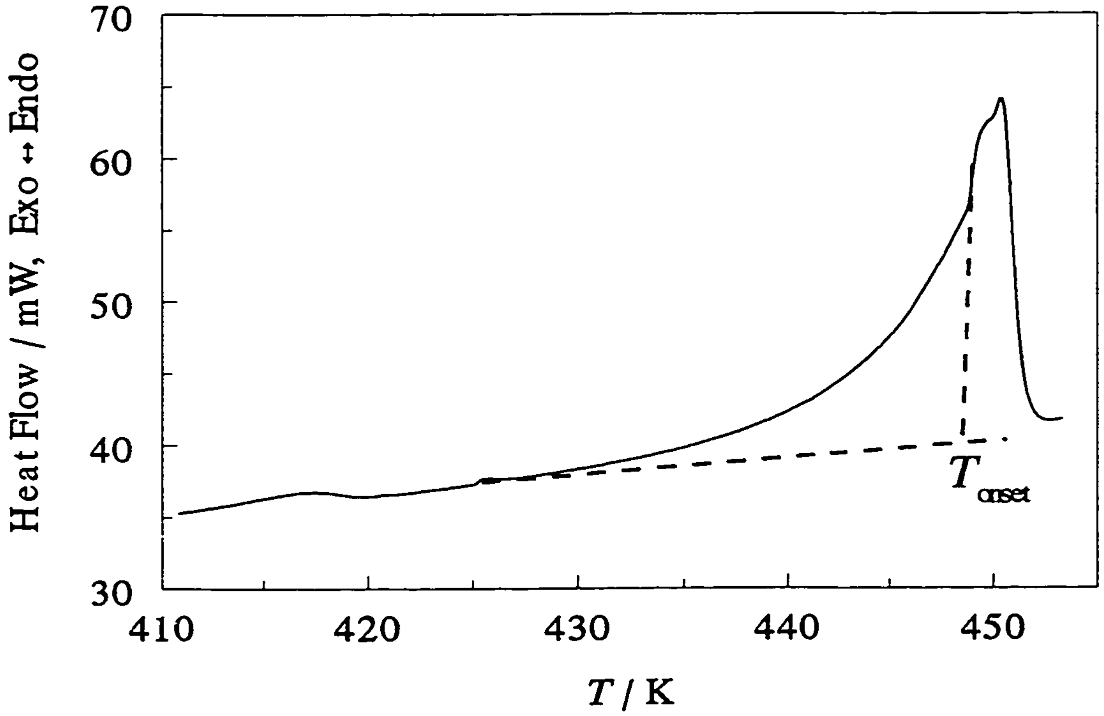

Figure 5.10. The melting of diol **1** in DSC with scanning rate of 5 K min^{-1}. The fusion enthalpy is 25.9 ± 0.4 kJ mol^{-1}. The melting curve is rather unsymmetrical. The melting point is considered as the onset temperature (T_{onset}) which is the intersection between the baseline and tangent line of peak with a maximum slope. It has a value of 450 ± 1 K. Thus the melting entropy is 57.6 ± 0.8 J K^{-1} mol^{-1}.

According to Timmermans,[278] molecular crystals with the fusion entropy change below 2.5 *R* (21 J K^{-1} mol^{-1}) are plastic crystals, and possess orientational disorder before melting and have much higher melting temperatures than molecules with similar molecular weights. However, diol **1** exhibits a much higher melting entropy, 6.9 *R* (57.6 J K^{-1} mol^{-1}), which is close to Walton's Rule[279] (*i.e.*, rigid molecules have a fusion entropy of 6.5 *R*). Gilson[280] also pointed out that molecular crystals that are ordered prior to melting have fusion entropies between 6.0 *R* and 7.2 *R*. The large fusion entropy of diol **1** indicates that its framework is highly ordered in the solid state. This agrees with the investigation of heat capacity and is particularly important for the stabilization of the helical tubuland channels of diol **1**.

Urea also forms inclusion compounds with parallel channels through intermolecular hydrogen bonds. However, pure urea's fusion entropy,[281] 4.38 *R*, is much less than that of diol **1**. Such a difference is ascribed to the formation of hydrogen bonds in liquid urea,[280] which is apparently more difficult for diol **1**, likely because of steric hindrance and relatively random movement of molecules in the liquid state. In the solid state, the hydrogen bond in diol **1** is stronger than that of urea: the O···H distance in diol **1** is around 1.85 Å, assuming that the bond length[273] of O—H is 0.956 Å as in CH_3OH and the O···O distance[271] in the hydrogen bond is 2.812 Å, and this is shorter than the O···H distance of 2.0 Å in either tetragonal or hexagonal urea.[282] The methyl group is also an important factor in the formation of the helical tubuland framework of diol **1**.[271] Hence, diols form the empty helical tubuland channels while urea cannot support an empty channel structure.

The enthalpy of combustion of diol **1** is currently under investigation. With it, the temperature dependent Gibbs energy and enthalpy of formation of diol **1** can be obtained. The heat capacity of diol **1** inclusion compounds with various guests will be investigated in the future. Information about guest-guest and host-guest interactions can be obtained from the study of the heat capacity of these inclusion compounds.

5.4 Conclusions

The heat capacity and the related thermodynamic properties of diol **1**, 2,6-dimethylbicyclo[3.3.1]nonane-*exo*-2, *exo*-6-diol, have been determined below ambient temperature. At 298.15 K, the heat capacity, enthalpy and entropy relative to 0 K are 255 J mol^{-1}, 36.2 kJ mol^{-1} and 224 J mol^{-1} K^{-1}, respectively.

The Raman spectra of diol **1** at different temperatures do not show significant change of vibrational frequencies, indicating that diol **1** has a very stiff framework and no solid-solid phase transitions, in agreement with the findings from adiabatic calorimetry.

Diol **1** has a melting point of 450 ± 1 K, fusion enthalpy of 25.9 ± 0.4 kJ mol^{-1} and fusion entropy of 57.6 ± 0.8 J mol^{-1} K^{-1}. Its fusion entropy is in the region of an ordered molecule crystal rather than that of plastic crystals, suggesting that the framework of diol **1** is highly ordered. The strong helical tubuland framework of diol **1** is related to the intermolecular hydrogen bonding.

Chapter 6 Conclusions and Future Directions

The thermal properties of some selected zeolites, clathrates of Group 14 elements and a channel-forming diol have been investigated and the related thermodynamic properties below 300 K were obtained. These novel materials do not have solid-solid state phase transitions in the examined temperature range.

Around room temperature, the heat capacities of most of the studied clathrates approach the Dulong-Petit value ($3NR$) while the zeolites and the diol have much lower heat capacities, indicating that their optic modes are at high frequencies.

In the zeolites, it was found that the higher the concentration of Al, the more thermodynamically stable the zeolite. The stabilities of zeolites relative to the elements were found to be enthalpic but not entropic and the formation of zeolites from their elements is exothermic.

However, entropic effects would be important for the formation of these clathrates from their elements due to higher energy of clathrate frameworks relative to their diamond phases. Further study of the heat capacity of different guests in the same clathrate framework, and the same guest in the different clathrate frameworks would delineate the role of guest and host in thermodynamic stabilities. Furthermore, if the enthalpies of formation of these clathrates were determined, their Gibbs energies of formation could be obtained.

Structurally, the frameworks of zeolites and clathrates of Group 14 elements are based on covalent bonds while the framework of the diol relies on hydrogen bonds and steric effects. It is expected that the covalent bonds are thermodynamically more stabilizing than the latter. In fact, the framework of the diol begins to collapse near its melting point, 450 K.

The zeolite NaX has a small Grüneisen parameter (much less than 1) and small thermal expansion coefficient (~10^{-6} K^{-1}) at room temperature, revealing that zeolite NaX has a rather stiff framework. At the same temperature, the clathrates examined have Grüneisen parameter values around 2 and thermal expansion coefficients (~10^{-5} K^{-1}) typical of most solids. This is due to the much stiffer Al-O and Si-O bonds than Si-Si, Ge-Ge or Sn-Sn, in agreement with the results obtained from heat capacity investigations.

At very low temperature, the rattling of the guests in the cages of Si and Ge clathrate frameworks couples with acoustic phonons, increasing the Grüneisen parameter as temperature decreases. Such a coupling significantly decreases the mean free path of phonons and results in the amorphous-like thermal conductivities of these Si and Ge clathrates. However, the Grüneisen parameter is a constant for $Cs_8Ga_8Sn_{38}$ below room temperature, indicating that resonant scattering in this Sn clathrate is not important, likely due to the strong guest-host interactions. These results agree well with both experimental thermal conductivities and theoretical calculations.

Although the empty frameworks of these zeolites and diol **1** are stable, the clathrands of Group 14 elements currently are not available except for Si_{136}. The study of thermal properties of the corresponding clathrands certainly would help to develop new framework materials and to understand structure-property relationships. Moreover, the investigation of elastic properties also is important to improve the understanding of thermal properties of these framework materials. Finally, heat capacity determinations of the inclusion compounds of zeolites and diol **1** would be necessary to obtain quantitative information concerning host-guest interactions and to explore their various applications.

References:

1. A. Kent, *Experimental Low Temperature Physics*, API, 1993.
2. J. M. Honig, *Thermodynamics*, 2nd edition, Academic Press, 1999.
3. A. Navrotsky, *Physics and Chemistry of Earth Materials*, Cambridge University Press, 1994, p. 166.
4. *Specific Heat of Solids*, ed. A. Cezairliyan, Hemisphere Publishing Corporation, 1988.
5. E. Grüneisen, *Ann. Phys.* 1912, **39**, 257.
6. R. J. Borg and G. J. Dienes, *The Physical Chemistry of Solids*, Academic Press, 1992.
7. W. Nernst and F. A. Lindemann, *Z. Electrochem.* 1911, **17**, 817.
8. K. Moriya, T. Matsuo and H. Suga, *J. Chem. Thermodyn.* 1988, **20**, 913.
9. A. Inaba, S. Ishida, T. Matsuo, K. Shibata and A. P. Tasi, *Phil. Mag. Lett.* 1996, **74**, 381.
10. C. H. P. Lupis, *Chemical Thermodynamics of Materials*, Elsevier Science Publishing Co., Inc. 1983.
11. K. Takada, O. Yamamuro and H. Suga, *J. Phys. Chem.* 1995, **99**, 1603.
12. O. Haida, T. Matsuo, H. Suga and S. Seki, *J. Chem. Thermodyn.* 1974, **6**, 815.
13. P. W. R. Bessonette, Ph.D. thesis, Dalhousie University, Halifax, 1998.
14. A. P. Ramirez and G. R. Kowach, *Phys. Rev. Lett.* 1998, **80**, 4903.
15. T. Matsuo and O. Yamamuro, *Supramol. Chem.* 1995, **6**, 103.
16. M. A. White, A. Perrott, D. Britten and M. J. M. Van Oort, *J. Chem. Phys.* 1988, **89**, 4346.
17. T. Matsuo, O. Yamamuro, M. Oguni and H. Suga, *J. Thermal Anal.* 1996, **46**, 1167.
18. P. Ehrenfest, *Commun. Kamerlingh Onnes Lab.* Leiden Suppl. 1933, 75b.

19. P. W. R. Bessonettte and M. A. White, *J. Chem. Edu.* 1999, **76**, 220.

20. P. L. Dulong and A. T. Petit, *Ann. Chim. Phys.* 1819, **10**, 395.

21. E. S. R. Gopal, *Specific Heats at Low Temperatures*, Plenum Press, 1966.

22. L. Qiu and M. A. White, *J. Chem. Edu.* 2000, submitted.

23. A. Einstein, *Ann. Phys.* 1907, **22**, 180.

24. P. Debye, *Ann. Phys.* 1912, **39**, 789.

25. P. A. Giguère and M. Boisvert, *Tables des Fonctions Thermodynamiques de Debye*, Les Presses de l'Université Laval, Québec, 1962.

26. T. Ohta, O. Yamamuro, T. Matsuo and H. Suga, *J. Phys. Chem.* 1996, **100**, 2355.

27. Y. Kume, T. Matsuo, Y. Miyazaki and H. Suga, *J. Phys. Chem. Solids* 1992, **53**, 1297.

28. D. Michalski and M. A. White, *J. Chem. Phys.* 1995, **103**, 6173.

29. C. G. Maier and K. K. Kelley, *J. Am. Chem. Soc.* 1932, **54**, 3243.

30. I. N. Levine, *Physical Chemistry*, 3rd edition, McGraw-Hill, Inc. 1988, p. 151.

31. J. L. Haas and J. R. Fisher, *Am. J. Sci.* 1976, **276**, 525.

32. Z. Tan, T. Masuo, H. Suga, Z. Zhang, J. Yin, B. Jiang and T. Sun, *Sci. China B* 1996, **39**, 276.

33. R. C. Newton, A. Navrotsky and B. J. Wood, *Advances in Physical Geochemistry, Vol. 1, Thermodynamics of Minerals and Melts*, Springer-Verlag New York, Inc. 1981.

34. R. G. Berman and T. H. Brown, *Contrib. Mineral Petrol.* 1985, **89**, 168.

35. B. F. Woodfield, J. Boerio-Goates, J. L. Shapiro, R. L. Putnam and A. Navrotsky, *J. Chem. Thermodyn.* 1999, **31**, 245.

36. T. Matsuo, N. Kinami and H. Suga, *Thermochim. Acta* 1995, **267**, 421.

37. J. L. Shapiro, B. F. Woodfield, R. Stevens and J. Boerio-Goates, *J. Chem. Thermodyn.* 1999, **31**, 725.

38. R. J. Bruls, H. T. Hintzen, R. Metselaar and J. C. V. Miltenburrg, *J. Phys. Chem. B* 1998, **102**, 7871.

39. J. E. Callanan, R. D. Weir and E. G. Westrum, Jr. *J. Chem. Thermodyn.* 1998, **30**, 1483.

40. C. Kittel, *Introduction to Solid State Physics*, 6th Edition, John Wiley & Sons, Inc. 1986.

41. W. Abriel, A. Bois, M. Zakrzewski and M. A. White, *Can. J. Chem.* 1990, **68**, 1352.

42. D. Michalski, M. A. White, P. K. Bakshi, T. S. Cameron and I. Swainson, *Can. J. Chem.* 1995, **73**, 513.

43. H. E. Stanley, S. V. Buldyrev, M. Canpolat, O. Mishima, M. R. Sadr-Lahijany, A. Scala and F. W. Starr, *Phys. Chem. Chem. Phys.* 2000, **2**, 1551.

44. N. H. Fletcher, *The Chemical Physics of Ice*, Cambridge University Press, 1970, p. 131.

45. G. K. White, *Cryogenics* 1976, **16**, 487.

46. V. Korthuis, N. Khosrovani, A. W. Sleight, N. Roberts, R. Dupree and W. W. Warren, *Chem. Mater.* 1995, **7**, 412.

47. N. Khosrovani, A. W. Sleight and T. Vogt, *J. Solid State Chem.* 1997, **132**, 355.

48. R. L. Withers, J. S. O. Evans, J. Hanson and A. W. Sleight, *J. Solid State Chem.* 1998, **137**, 161.

49. J. S. O. Evans, T. A. Mary and A. W. Sleight, *J. Solid State Chem.* 1997, **133**, 580.

50. D. A. Woodcock, P. Lightfoot and C. Ritter, *Chem. Commun.* 1998, 107.

51. P. Lightfoot, D. A. Woodcock, J. D. Jorgensen and S. Short, *Int. J. Inorg. Mater.* 1999, **1**, 53.

52. J. S. O. Evans, T. A. Mary and A. W. Sleight, *J. Solid State Chem.* 1998, **137**, 148.

53. P. M. Forster, A. Yokochi and A. W. Sleight, *J. Solid State Chem.* 1998, **140**, 157.

54. D. A. Woodcock, P. Lightfoot and C. Ritter *J. Solid. State Chem.* 2000, **149**, 92.

55. T. G. Amos, A. Yokochi and A. W. Sleight, *J. Solid. State Chem.* 1998, **14**, 303.

56. T. A. Mary, J. S. O. Evans, T. Vogt and A. W. Sleight, *Science* 1996, **272**, 90.

57. G. Ernst, C. Broholm, G. R. Kowach and A. P. Ramirez, *Nature* 1998, **396**, 147.

58. A. W. Sleight, *Annu. Rev. Mater. Sci.* 1998, **28**, 29.

59. W. F. Schlosser, G. M. Graham and P. P. M. Meincke, *J. Phys. Chem. Solids* 1971, **32**, 927.

60. S. Chikazumi, *J. Magn. Magn. Mater.* 1979, **10**, 113.

61. M. A. White, *Properties of Materials*, Oxford University Press, 1999.

62. R. C. Zeller and R. O. Pohl, *Phys. Rev. B* 1971, **4**, 2029.

63. D. Michalski and M. A. White, *J. Phys. Chem.* 1995, **99**, 3774.

64. J. S. Tse and M. A. White, *J. Phys. Chem.* 1988, **92**, 5006.

65. D. Michalski and M. A. White, *J. Chem. Phys.* 1997, **106**, 6202.

66. N. W. Ashcroft and N. D. Merin, *Solid State Physics*, Holt Rinchart and Winston, 1976.

67. J. S. Tse, *J. Physique Coll.* 1987, **48**, 543.

68. N. G. Parsonage and L. A. K. Staveley, *Inclusion Compounds*, ed. J. L. Atwood, J. E. D. Davies and D. D. MacNicol, Academic Press, 1984, Vol. 3, p. 1.

69. M. J. O'Neill, *Anal. Chem.* 1966, **38**, 1331.

70. M. A. White, in *Comprehensive Supramolecular Chemistry*, Elsevier Science Ltd. 1996, Vol. 8, p. 179.

71. T. Hatakeyama, H. Kanetsuna and S. Ichihcra, *Thermochim. Acta* 1989, **146**, 311.

72. J. E. Callanan, H. M. McDermott, R. D. Weir and E. F. Westrum, Jr. *J. Chem. Thermodyn.* 1992, **24**, 233.

73. U. Rahm and E. Gmelin, *J. Therm. Anal.* 1992, **38**, 335.

74. P. F. Sullivan and G. Seidel, *Phys. Rev.* 1968, **173**, 679.

75. G. Bednarz, B. Millier and M. A. White, *Rev. Sci. Instrum.* 1992, **63**, 3944.

76. T. Stoebe, C. C. Hung and J. W. Goodby, *Phys. Rev. Lett.* 1992, **68**, 2994.

77. J. Boerio-Goates, C. W. Garland and R. Shashidhar, *Phys. Rev. A* 1990, **41**, 3192.

78. G. R. Stewart, *Rev. Sci. Instrum.* 1983, **54**, 1.

79. W. Gaede, *Phys. Z.* 1902, **4**, 105.

80. A. Eucken, *Phys. Z.* 1909, **10**, 586.

81. E. Gmelin, *Thermochim. Acta* 1987, **110**, 183.

82. J. B. Ott and W. F. Giauque, *J. Am. Chem. Soc.* 1960, **82**, 1.

83. T. Matsuo and H. Suga, *Thermochim. Acta* 1985, **88**, 149.

84. K. Saito, Y. Yamamura, H. Saitoh, H. Matsuyama, K. Kikuchi and I. Ikemoto, *Solid State Commun.* 1994, **92**, 495.

85. J. C. Lasjaunias, P. Monceau, E. Rememyi, S. Sahling, G. Dhalenne and A. Revcolevschi, *Solid State Commun.* 1997, **101**, 677.

86. M. Sorai, K. Kaji and Y. Kaneko, *J. Chem. Thermodyn.* 1992, **24**, 167.

87. G. N. Lewis and M. Randall, *Thermodynamics*, 2nd edition, McGraw-Hill Book Co. 1961, p. 64.

88. M. J. M. Van Oort and M. A. White, *Rev. Sci. Instrum.* 1987, **58**, 1239.

89. R. Hultgren, R. L. Orr, P. D. Anderson and K. K. Kelly, *Selected Values of Thermodynamic Properties of Metals and Alloys*, Wiley, 1963.

90. F. Grønvold, *J. Therm. Anal.* 1978, **13**, 419.

91. E. F. Westrum, Jr., C. Chou, D. W. Osborne and H. E. Flotow, *Cryogenics*, 1967, 7, 43.

92. G. K. White, *Experimental Techniques in Low Temperature Physics*, 3rd edition, Clarendon Press, 1979, p. 276.

93. L. B. Sand and F. A. Mumpton, *Natural Zeolites: Occurrence, Properties, Use*, Pergamon Press Ltd. 1978.

94. D. A. Howell, G. K. Johnson, I. R. Tasker P, A. G. O'Hare and W. S. Wise, *Zeolites* 1990, **10**, 525.

95. O. Wiegel and E. Steinhof, *Z. Kristallogr.* 1925, **61**, 125.

96. D. E. W. Vaughan, in *Comprehensive Supramolecular Chemistry*, Elsevier Science Ltd. 1996, Vol. 7, p. 381.

97. K. Kessler, in *Comprehensive Supramolecular Chemistry*, Elsevier Science Ltd. 1996, Vol. 7, p. 428.

98. G. A. Ozin, A. Kuperman and A. Stein, *Angew. Chem. Int. Ed. Engl.* 1989, **28**, 359.

99. R. Szostak, *Molecular Sieves: Principles of Synthesis and Identification*, Van Nostrand Reinhold, 1989, p. 3.

100. L. B. McCusker, in *Comprehensive Supramolecular Chemistry*, Elsevier Science Ltd. 1996, Vol. 7, p. 393.

101. W. M. Meier, D. H. Olson and C. Baerlocher, *Zeolites* 1996, **17**, 1.

102. W. M. Meier, D. H. Olson and C. Baerlocher, Eds., *Atlas of Zeolite Structure Types*, 4th revised edition, Elsevier Science Ltd. 1996.

103. T. R. Gaffney, *Curr. Opin. Solid State Mater. Sci.* 1996, **1**, 69.

104. G. K. Johnson, I. R. Tasker, H. E. Flotow, P. A. G. O'Hare and W. S. Wise, *Am. Mineral.* 1992, **85**, 77.

105. A. Navrotsky, *J. Therm. Analy. Calorim.* 1999, **57**, 653.

106. A. Abdoulaye, G. Chabanis, J. C. Giunyini, J. Vanderschueren, J. V. Zanchetta and F. Di Renzo, *J. Phys. Chem. B* 1997, **101**, 1831.

107. X. Lin, J. L. Falconer and R. D. Noble, *Chem. Mater.* 1998, **10**, 3716.

108. D. A. Woodcock, P. Lightfoot, P. A. Wright, L. A. Villaescusa, M. J. D. Cabanas and M. A. J. Camblor, *J. Mater. Chem.* 1999, **9**, 349.

109. T. Asanuma, H. Nakayama, T. Eguchi and N. Nakamura, *J. Chem. Soc. Faraday Trans.* 1998, **94**, 3521.

110. W. Löwenstein, *Am. Mineral.* 1954, **39**, 92.

111. L. Zhu, K. Seff, D. H. Olson, B. J. Cohen and R. B. V. Dreele, *J. Phys. Chem. B.* 1999, **103**, 10365.

112. E. Dempsey, G. H. Kuhl and D. H. Olson, *J. Phys. Chem.* 1969, **73**, 387.

113. T. Takaishi, *J. Chem. Soc. Faraday Trans.* 1998, **94**, 1507.

114. A. R. R. Salvador, D. W. Lewis, J. R. Soneria, G. R. Fuentes, L. R. Sierra and C. R. A. Catlow, *J. Phys. Chem. B* 1998, **102**, 8417.

115. C. Dybowski, *J. Inclus. Phenom. Mol.* 1995, **21**, 113.

116. K. M. Bulanin, R. F. Lobo and M. O. Bulanin, *J. Phys. Chem.* 2000, **104**, 1269.

117. P. P. K. Gerrits, D. E. De Vos, E. J. P. Feijen and P. A. Jacobs, *Microporous Mater.* 1997, **8**, 3.

118. B. Smith, *J. Phys. Chem.* 1995, **99**, 5597.

119. P. Demontis and G. B. Suffritti, *Chem. Rev.* 1997, **97**, 2845.

120. K. A. Iyer and S. J. Singer, *J. Phys. Chem.* 1994, **98**, 12670.

121. J. W. Couves, R. H. Jones, S. C. Parker, P. Tschaufeser and C. R. A. Catlow, *J. Phys.: Condens. Mat.* 1993, **5**, L329.

122. P. Tschaufeser and S. C. Parker, *J. Phys. Chem.* 1995, **99**, 10609.

123. A. Colantuano, S. DalVecchio, G. Mascolo and M. Pansini, *Thermochim. Acta* 1997, **296**, 59.

124. M. P. Attfield and A. W. Sleight, *Chem. Commun.* 1998, 601.

125. D. A Woodcock, P. Lightfoot, P. A. Wright, L. A. Villaescusa, M. Cabanas and M. A. Camblor, *J. Mater. Chem.* 1999, **9**, 349.

126. D. A. Woodcock, P. Lightfoot, L. A. Villaescusa, M. Cabanas, M. A. Camblor and D. Engberg, *Chem. Mater.* 1999, **11**, 2508.

127. M. P. Attfield and A. W. Sleight, *Chem. Mater.* 1998, **10**, 2013.

128. J. S. O. Evans, *J. Chem. Soc. Dalton Trans.* 1999, 3317.

129. A. W. Sleight, *Curr. Opin. Solid State Mater. Sci.* 1998, **3**, 128.

130. V. Ramamurthy, in *Comprehensive Supramolecular Chemistry*, Elsevier Science Ltd. 1996, Vol. 7, p. 693.

131. M. M. Thackeray and J. Coetzer, *Solid State Ionics* 1982, **6**, 135.

132. K. Takemoto and N. Sonoda, in *Inclusion Compounds*, edited by J. L. Atwood, J. E. D. Davies and D. D. MacNicol, Academic Press, 1984, Vol. 2, p. 47.

133. C. F. Mellot, A. M. Davidson, J. Eckert and A. K. Cheetham, *J. Phys. Chem. B.* 1998, **102**, 2530.

134. N. P. Blake and G. D. Stucky, *J. Inclus. Phenom. Mol.* 1995, **21**, 299.

135. N. Herron, *J. Inclus. Phenom. Mol.* 1995, **21**, 283.

136. P. P. Edwards, P. A. Anderson and J. M. Thomas, *Acc. Chem. Res.* 1996, **29**, 23

137. G. K. Johnson, H. E. Flotow and P. A. G. O'Hare, *Am. Mineral.* 1982, **67**, 736.

138. N. Komada, E. F. Westrum Jr., B. S. Hemingway, M. Yu. Zolotov, Y. V. Semono, I. L. Khodakovasky and L. M. Anovitz, *J. Chem. Thermodyn.* 1995, **27**, 1119.

139. I. E. Paukov, I. A. Belitskii and Y. A. Kovalevskaya, *Geochem. International* 1998, **36**, 663.

140. I. E. Paukov, I. A. Belitskii and G. A. Berezovskii, *Geochem. International* 1998, **36**, 565.

141. V. A. Drebushchak, V. N. Naumov, V. V. Nogteva, I. A. Belitsky and I. E. Paukov, *Thermochim. Acta* 1999, **348**, 33.

142. G. K. Johnson, I. R. Tasker, H. E. Flotow, P. A. G. O'Hare and W. S. Wise, *Am. Mineral.* 1985, **70**, 1065.

143. G. K. Johnson, I. R. Taker, H. E. Flotow, P. A. G. O'Hare and W. S. Wise, *Am. Mineral.* 1983, **68**, 1134.

144. I. Hassan and H. D. Grundy, *Acta Cryst.* 1984, **B40**, 6.

145. D. A. Faux, *J. Phys. Chem. B.* 1998, **102**,10658.

146. S. C. Kim, N. R. Keskar, A. V. McCormick, J. R. Chelikowsky and H. T. Davis, *J. Chem. Phys.* 1995, **102**, 8656.

147. V. Subramanian and K. Seff, *J. Phys. Chem.* 1977, **81**, 2249.

148. J. J. Pluth and J. V. Smith, *J. Am. Chem. Soc.* 1980, **102**, 4704.

149. G. Zhu, S. Qiu, J. Yu, Y. Sakamoto, F. Xiao, R. Xu and O. Treasaki, *Chem. Mater.* 1998, **10**, 1483.

150. Correspondence with UOP Canada Inc. 1997.

151. J. M. Bennett, C. S. Blackwell and D. E. Cox, *ACS Symp. Ser.* 1983, **218**, 143.

152. L. A. Bursill, E. A. Lodge, J. M. Thomas and A. K. Cheetham, *J. Phys. Chem.* 1981, **85**, 2409.

153. R. M. Hazen and L. W. Finger, *J. Appl. Phys.* 1984, **56**, 1838.

154. M. W. Chase, Jr. *NIST-JANAF Thermochemical Tables*, Fourth Edition, *J. Phys. Chem. Ref. Data* Monograph 9, 1998, 1.

155. A. La Iglesia and A. J. Aznar, *Zeolites* 1986, **6**, 26.

156. P. P. Caullet, J. L. Guth and R. Wey, *Bull. Mineral.* 1980, **105**, 330.

157. D. B. Downie and J. F. Martin, *J. Chem. Thermodyn.* 1980, **12**, 779.

158. P. Flubacher, A. J. Leadbetter and J. A. Morrison, *Phil. Mag.* 1959, **4**, 275.

159. J. Hilsenrath, C. W. Beckett, W. S. Benedict, L. Fano, H. J. Hoge, J. F. Masi, R. L. Nuttall, Y. S. Touloukian and H. W. Woolley, *Tables of Thermal Properties of Gases, National Bureau of Standards Circular*, **564**, 1955.

160. C. B. Alcok, M. W. Chase and V. P. Itkin, *J. Phys. Chem. Ref. Data* 1994, **23**, 415.

161. R. A. Robie, B. S. Hemingway and J. R. Fisher, *U. S. Geol. Survey Bull.* 1978, 1452.

162. I. Petrovic, A. Navrotsky, M. E. Davis and S. I. Zones, *Chem. Mater.* 1993, **5**, 1805.

163. F. Porcher, M. Souhassou, V. Dusausoy and C. Lecomite, *Eur. J. Mineral.* 1999, **11**, 333.

164. I. Gener, G. Ginestet, G. Buntinx and C. Bremard, *Phys. Chem. Chem. Phys.* 2000, **2**, 1855.

165. P. Pissis and D. Daoukaki-Diamanti, *J. Phys. Chem. Solids* 1993, **54**, 701.

166. S. Zhen and K. Seff, *J. Phys. Chem. B.* 1999, **103**, 10409.

167. L. Zhu and K. Seff, *J. Phys. Chem. B.* 1999, **103**, 9512.

168. D. H. Olson, *Zeolites* 1995, **15**, 439.

169. G. Vitale, C. F. Mellot, L. M. Bull and A. K. Cheetham, J. *Phys. Chem. B.* 1997, **101**, 4559.

170. C. E. A. Kirschhock, B. Hunger, J. Martens and P. A. Jacobs, *J. Phys. Chem. B.* 2000, **104**, 439.

171. I. Petrovic and A. Navrotsky, *Microporous Mater.* 1997, **9**, 1.

172. T. H. K. Barron, *Ann. Phys.* 1957, **1**, 77.

173. M. Blackman, *Proc. Phys. Soc.* 1957, **B70**, 827.

174. M. Igarashi, N. Okubo and R. Yoshizaki, *Z. Naturforsch.* 1997, **53a**, 442.

175. H. A. M. Verhulst, W. J. J. Welters, G. Vorbeck, L. J. M. van der Ven, V. H. J. de Beer, R. A. V. Santen and J. W. D. Haan, *J. Chem. Soc., Chem. Commun.* 1994, 639.

176. A. N. Fitch, H. Jobic and A. Renouprez, *J. Phys. Chem.* 1986, **90**, 1311.

177. G. R. Eulenberger, D. P. Shoemaker and J. G. Keil, *J. Phys. Chem.* 1967, **71**, 1812.

178. E. Geidel, K. Krause, H. Förster and F. Bauer, *J. Chem. Soc. Faraday Trans.* 1997, **93**, 1439.

179. J. Klinowski, S. Ramdas, J. M. Thomas, C. A. Fyfe and J. S. Hartman, *J. Chem. Soc. Faraday Trans.* 2, 1982, **78**, 1025.

180. J. A. Hriljac, M. M. Eddy, A. K. Cheetham, J. A. Donohue and G. J. Ray, *J. Solid State Chem.* 1993, **106**, 66.

181. C. Y. Li and L. V. C. Rees, *Zeolites* 1986, **6**, 60.

182. M. E. Cosgrove and C. Th. Papavassilion, *Marine Geol.* 1979, **33**, M-77.

183. B. S. Hemingway, R. A. Robie and V. Reston, *J. Res. U. S. Geol. Surv.* 1977, **5**, 413.

184. G. K. Johnson, H. E. Flotow, P. A. G. O'Hare and W. S. Wise, *Am. Mineral.* 1982, **67**, 736.

185. B. S. Hemingway, K. M. Krupka and R. A. Robie, *Am. Mineral.* 1981, **66**, 1202.

186. R. Glaccum and K. Bostrom, *Marine Geol.* 1976, **21**, 47.

187. R. A. Robie, B. S. Hemingway and J. R. Fisher, *U. S. Geol. Surv. Bull.* 1979, p. 1452.

188. K. Moriguchi, S. Munetoh and A. Shintani, *Phys. Rev. B* 2000, **62**, 7138.

189. J. Gryko, P. F. McMillan, R. F. Marzke, G. K. Ramachandran, D. Patton, S. K. Deb and O. F. Sankey, *Phys. Rev. B* 2000, **62**, R7707.

190. T. J. Quinn, *Temperature*, Second Edition, Academic Press, 1990, p. 286.

191. G. K. White, *Experimental Techniques in Low-Temperature Physics*, Third Edition, Clarendon Press, 1979, p. 117.

192. F. J. DiSalvo, *Science* 1999, **285**, 703.

193. M. A. White in *Crystal Engineering*, eds. K. R. Seddon and M. Zaworotko, Kluwer Academic Publishers, 1999, p. 273.

194. Y. C. Wang and F. J. DiSalvo, *Chem. Mater.* 2000, **12**, 1011.

195. S. L. Wilkinson, *Chem. Eng. News* 2000, **78**, 31.

196. G. Slack, in "*CRC Handbook of Thermoelectrics*" D. M. Rowe, Ed., CRC Press, 1995, p. 407.

197. G. A. Slack, *Mater. Res. Symp. Proc.* 1997, **478**, 47.

198. B. C. Sales, D. Mandrus and R. K. Williams, *Science* 1996, **272**, 1325.

199. A. Watcharapasorn, R. C. DeMattei, R. S. Feigelson, T. Caillat, A. Borshchevsky, G. J. Snyder and J. P. Fleurial, *J. Appl. Phys.* 1999, **86**, 6213.

200. S. Katsuyama, Y. Shichijo, M. Ito, K. Majima and H. Nagai, *J. Appl. Phys.* 1998, **84**, 6708.

201. G. S. Nolas, M. Kaeser, R. T. Littleton IV and T. M. Tritt, *Appl. Phys. Lett.* 2000, 77, 1855

202. *Gmelin Handbook of Inorganic Chemistry* 1960, **9**(B2), 1102.

203. H. M. Powell, *J. Chem. Soc.* 1948, 61.

204. G. A. Jeffrey in *Inclusion Compounds*, Academic Press, 1984, Vol. 1, p. 135.

205. D. D. MacNicol in *Inclusion Compounds*, Academic Press, 1984, Vol. 2, p. 1.

206. G. K. Ramachandran, P. F. McMillan, S. K. Deb, M. Somayazulu, J. Gryko, J. J. Dong and O. F. Sankey, *J. Phys.: Condens. Mat.* 2000, **12**, 4013.

207. J. S. Kasper, P. Hagenumuller, M. Pouchard and C. Cros, *Science* 1965, **150**, 1713.

208. E. Reny, M. Menetrier, C. Cros, M. Pouchard and J. Senegas, *C. R. Acad. Sci. Paris, t. 1, Serie II c, p.* 1998, 129.

209. P. Mélinon, P. Keghélian, A. Perez, B. Champagnon, Y. Guyot, L. Saviot, E. Reny, C. Cros, M. Pouchard and A. J. Dianoux, *Phys. Rev. B.* 1999, **59**, 10099.

210. C. Cros, E. Reny and M. Pouchard, *Mol. Cry. Liq. Cryst.* 1998, **310**, 199.

211. H. Kawaji, H. Horie, S. Yamanaka and M. Ishikawa, *Phys. Rev. Lett.* 1995, **74**, 1427.

212. C. Cros, M. Pouchard and P. Hagenmuller, *J. Solid State Chem.* 1970, **2**, 570.

213. G. S. Nolas, T. J. R. Weakley and J. L. Cohn, *Chem. Matter.* 1999, **11**, 2470.

214. E. Reny, P. Gravereau, C. Cros and M. Pouchard, *J. Mater. Chem.* 1998, **8**, 2839.

215. D. Kahn and J. P. Lu, *Phys. Rev. B*. 1997, **56**, 13898.

216. J. J. Dong and O. F. Sankey, *J. Phys.: Condens. Mat.*. 1999, **11**, 6129.

217. J. J. Dong, O. F. Sankey and G. Kern, *Phys. Rev. B*. 1999, **60**, 950.

218. R. Kröner, K. Peters, H. G. von Schnering and R. Nesper, *Z. Kristallogr. NCS* 1998, **213**, 667.

219. R. Kröner, K. Peters, H. G. von Schnering and R. Nesper, *Z. Kristallogr. NCS* 1998, **213**, 669.

220. H. G. von Schnering, H. Menke, R. Kröner, E. M. Peters, K. Peters and R. Nesper, *Z. Kristallogr. NCS* 1998, **213**, 673.

221. J. Gryko, P. F. McMillan and O. F. Sankey, *Phys. Rev. B* 1996, **54**, 3037.

222. N. P. Blake, L. Mollnitz, G. Kresse and H. Metiu, *J. Chem. Phys*. 1999, **111**, 3133.

223. B. B. Iversen, A. E. C. Palmqvist, D. E. Cox, G. S. Nolas, G. D. Stucky, N. P. Blake and H. Metiu, *J. Solid State Chem*. 2000, **149**, 455.

224. J. Zhou, A. Buldum, J. P. Lu and C. Y. Fong, *Phys. Rev. B* 1999, **60**, 14177.

225. B. C. Chakoumakos, B. C. Sales, D. G. Mandrus and G. S. Nolas, *J. Alloys Compd.* 2000, **296**, 80.

226. A. San-Minguel, P. Kéghélian, X. Blase, P. Mélinon, A. Perez, J. P. Itié, A. Polian, E. Reny, C. Cros and M. Pouchard, *Phys. Rev. Lett*. 1999, **83**, 5290.

227. J. L. Cohn, G. S. Nolas, V. Fessatidis, T. H. Metcalf and G. A. Slack, *Phys. Rev. Lett*. 1999, **82**, 779.

228. G. S. Nolas, J. L. Cohn and G. A. Slack, *Phys. Rev. B* 1998, **58**, 164.

229. H. G. von Schnering, W. Carrillo-Cabrera, R. Kroner, E. M. Peters, K. Peters and R. Nesper, *Z. Kristallogr. NCS* 1998, **213**, 679.

230. R. Kroner, K. Peters, H. G. von Schnering and R. Nesper, *Z. Kristallogr. NCS* 1998, **213**, 664.

231. G. S. Nolas, T. J. R. Weakley, J. L. Cohn and R. Sharma, *Phys. Rev. B*. 2000, **61**, 3845.

232. M. Zakrzewski and M. A. White, *Phys. Rev. B*. 1992, **45**, 2809.

233. J. S. Tse, V. P. Shpakov, V. Murashov and V. R. Belosludov, *J. Chem. Phys.* 1997, **107**, 9271.

234. B. C. Sales, B. C. Chakoumakos, D. Mandrus and J. W. Sharp, *J. Solid State Chem.* 1999, **146**, 528.

235. G. S. Nolas, J. L. Cohn, G. A. Slack and S. B. Schjuman, *Appl. Phys. Lett.* 1998, **73**, 178.

236. S. Satio and A. Oshiyama, *Phys. Rev. B* 1995, **51**, 2628.

237. A. A. Demkov, O. F. Sankey, K. E. Schmidt, G. B. Adams and M. O'Keeffe *Phys. Rev. B*. 1994, **50**, 17 001.

238. J. S. Tse, K. Uehara, R. Rousseau, A. Ker, C. I. Ratcliffe, M. A. White and G. R. MacKay, *Phys. Rev. Lett.* 2000, **85**, 114.

239. F. Shimizu, Y. Maniwa, K. Kume, H. Kawaji, S. Yamanaka and M. Ishikawa, *Phys. Rev. B*. 1996, **54**, 13242.

240. S. Bobev and S. C. Sevov, *J. Am. Chem. Soc.* 1999, **121**, 3795.

241. S. Yamanaka, E. Enishi, H. Fukuoka and M. Yasukawa, *Inorg. Chem.* 2000, **39**, 58.

242. C. Cros, M. Pouchard and P. Hagenmuller, *Comp. Rend. Acad. Sci. Paris* 1965, **260**, 4764.

243. C. Cros and J. C. Benejat, *Bull. Soc. Chim. France* 1972, **5**, 1739.

244. J. He, D. D. Klug, K. F. Preston, C. I. Ratcliffe, K. Uehara, J. S. Tse and C. A. Tulk, *J. Am. Chem. Soc.* 2000, submitted.

245. M. Menon, E. Richter and K. R. Subbaswamy, *Phys. Rev. B*. 1997, **56**, 12290.

246. Y. Guyot, B. Champagnon, E. Reny, C. Cros, M. Pouchard, P. Melinon, A. Perez and I. Gregora, *Phys. Rev. B*. 1998, 57, R9475.

247. S. L. Fang, L. Grigorian, P. C. Eklund, G. Dresselhaus, M. S. Dresselhaus, H. Kawaji and S. Yamanaka, *Phys. Rev. B*. 1998, 57, 7686.

248. L. Qiu, M. A. White, L. Zhiqiang, J. S. Tse, C. I. Ratcliffe, C. A. Tulk, J. J. Dong and O. F. Sankey, submitted to *Phys. Rev. B*, 2000.

249. R. D. Desattes, *Phys. Rev. Lett.* 1974, **33**, 463.

250. P. Becker, K. Dorenwendt and G. Ebeling, *Phys. Rev. Lett.* 1981, **46**, 1540.

251. F. Brunet, P. Mélinon, A. San Minguel, P. Kéghélian, A. Perez, A. M. Flank, E. Reny, C. Cros and M. Pouchard, *Phys. Rev. B.* 2000, **61**, 16 550.

252. T. H. K. Barron and G. K. White, *Heat Capacity and Thermal Expansion at Low Temperatures*, Kluwer Academic/Plenum Publishers, 1999, p. 86.

253. J. F. Nye, *Physical Properties of Crystals: Their Representation by Tensors and Matrices*, Clarendon Press, 1986.

254. M. A. White, *J. Physique Coll.* 1987, C1-565.

255. M. Zakrzewski and M. A. White, *J. Phys: Condens. Mat.*. 1991, **3**, 6703.

256. S. B. Schujman, G. S. Nolas, R. A. Young, C. Lind, A. P. Wilkinson, G. A. Slack, R. Patschke, M. G. Kanatzidis, M. Ulutagay and S. J. Hwu, *J. Appl. Phys.* 2000, **87**, 1529.

257. J. Boerio and E. F. Westrum, Jr., *J. Chem. Thermodyn.* 1978, **10**, 1.

258. G. B. Adams, Jr., H. J. Johnston and E. C. Kerr, *J. Am. Chem. Soc.* 1952, **74**, 4787.

259. V. W. Eichenauer and M. Schulze, *Z. Naturforsch* 1959, **14a**, 962.

260. G. Seidel and P. H. Kessom, *Phys. Rev.* 1958, **112**, 1083.

261. Private communication with G. S. Nolas, 2000.

262. D. L. Martin, *Phys. Rev.* 1968, **167**, 640.

263. M. G. Zabetakis, Ph. D. Thesis, Univ. Pittsburg. 1956.

264. G. S. Nolas, B. C. Chakoumakos, B. Mahieu, G. J. Long and T. J. R. Weakley, *Chem. Mater.* 2000, **12**, 1947.

265. G. S. Nolas and C. A. Kendziora, *Phys. Rev. B* 2000, **62**, 7157.

266. D. D. Wagman, W. H. Evans, V. B. Parker, R.H. Schumm, I. Halow, S. M Bailey, K. L. Churney and R. L Nuttall, *J. Phys. Chem. Ref. Data* 1982, **11**,1.

267. Private communication with J. S. Tse, 2000.

268. R. Bishop and I. Dance, *J. Chem. Soc. Chem. Comm.* 1979, 992.

269. I. G. Dance, R. Bishop, S. C. Hawkins, T. Lipari, N. L. Scudder and D. C. Craig, *J. Chem. Soc. Perkin Trans. II* 1986,1299.

270. R. Bishop in *Comprehensive Supramolecular Chemistry*, Pergamon, 1996, Vol. 6, p. 85.

271. R. Bishop and I. G. Dance in *Inclusion Compounds*, Vol. 4, eds. J. L. Attwood, J. E. D. Davies and D. D. MacNicol, Oxford University Press, 1991, p. 1.

272. A. T. Ung, R. Bishop, D. C. Craig, I. G. Dance and M. L. Scudder, *J. Chem. Soc. Perkin Trans. II* 1992, 861.

273. D. Gizachew, L. C. M. van Gorkom, I. G. Dance, J. V. Hanna and M. A. Wilson, *Solid State Magn. Reson.* 1994, 3, 67.

274. D. Morrison, *Properties of Inclusion Compounds*, B. Sc. Thesis, Dalhousie University, 1996.

275. R. C. Weast and M. J. Astle, *Handbook of Chemistry and Physics, 61th*, CRC Press, Inc. 1981.

276. G. A. Ozin, in *Vibrational Spectroscopy of Trapped Species*, ed. H. E. Hallam, London, John Wiley & Sons, 1973, p. 408.

277. I. G. Dance, R. Bishop, S. C. Hawkins, T. Lipari, M. L. Scudder and D. C. Craig, *J. Chem. Soc. Perkins Trans. II* 1986, 1309.

278. J. Timmermans, *J. Phys. Chem. Solids* 1961, **18**, 1.

279. P. Walton, *Z. Electrochem.* 1908, **14**, 713.

280. D. F. R. Gilson, *J. Chem. Educ.* 1992, **69**, 23.

281. G. Della Gatta and D. Ferro, *Thermochim. Acta* 1987, **122**,143.

282. M. D. Hollingsworth and K. D. M. Harris, in *Comprehensive Supramolecular Chemistry*, Pergamon, 1996, Vol. 6, p. 177.